

**Journal of  
Mechanics of  
Materials and Structures**

**Volume 12, No. 5**

**December 2017**



# JOURNAL OF MECHANICS OF MATERIALS AND STRUCTURES

[msp.org/jomms](http://msp.org/jomms)

Founded by Charles R. Steele and Marie-Louise Steele

## EDITORIAL BOARD

ADAIR R. AGUIAR	University of São Paulo at São Carlos, Brazil
KATIA BERTOLDI	Harvard University, USA
DAVIDE BIGONI	University of Trento, Italy
YIBIN FU	Keele University, UK
IWONA JASIUK	University of Illinois at Urbana-Champaign, USA
MITSUTOSHI KURODA	Yamagata University, Japan
C. W. LIM	City University of Hong Kong
THOMAS J. PENCE	Michigan State University, USA
GIANNI ROYER-CARFAGNI	Università degli studi di Parma, Italy
DAVID STEIGMANN	University of California at Berkeley, USA
PAUL STEINMANN	Friedrich-Alexander-Universität Erlangen-Nürnberg, Germany

## ADVISORY BOARD

J. P. CARTER	University of Sydney, Australia
D. H. HODGES	Georgia Institute of Technology, USA
J. HUTCHINSON	Harvard University, USA
D. PAMPLONA	Universidade Católica do Rio de Janeiro, Brazil
M. B. RUBIN	Technion, Haifa, Israel

**PRODUCTION** [production@msp.org](mailto:production@msp.org)

SILVIO LEVY Scientific Editor

Cover photo: Wikimedia Commons

---

See [msp.org/jomms](http://msp.org/jomms) for submission guidelines.


---

JoMMS (ISSN 1559-3959) at Mathematical Sciences Publishers, 798 Evans Hall #6840, c/o University of California, Berkeley, CA 94720-3840, is published in 10 issues a year. The subscription price for 2017 is US \$615/year for the electronic version, and \$775/year (+\$60, if shipping outside the US) for print and electronic. Subscriptions, requests for back issues, and changes of address should be sent to MSP.

---

JoMMS peer-review and production is managed by EditFLOW<sup>®</sup> from Mathematical Sciences Publishers.

PUBLISHED BY

 **mathematical sciences publishers**  
nonprofit scientific publishing

<http://msp.org/>

© 2017 Mathematical Sciences Publishers

# NONLINEAR IMPACTING OSCILLATIONS OF PIPE CONVEYING PULSATING FLUID SUBJECTED TO DISTRIBUTED MOTION CONSTRAINTS

WANG YIKUN, NI QIAO, WANG LIN, LUO YANGYANG AND YAN HAO

The nonlinear dynamics of a simply supported pipe conveying pulsating fluid is investigated by introducing distributed motion constraints along the pipe axis. The constraints are modeled by trilinear springs. The flowing fluid in the pipe is pulsatile, which is assumed to have a time-dependent harmonic component superposed on the steady fluid flow. Attention is concentrated on the potential performance of the pipe/impacting system with various pulsating frequencies. To investigate the short-wave buckling, the behaviors of the simply supported pipe with steady internal flow velocities are presented first. The partial differential equations (PDEs) are formulated and then transformed into a set of ordinary differential equations (ODEs) using the Galerkin's method. The nonlinear dynamical responses are presented in the form of bifurcation diagrams, time histories, phase portraits, Poincaré maps and power spectrums. Some interesting and sometimes unexpected results have been observed under various system parameters.

## 1. Introduction

The dynamical problem of pipes conveying fluid is an important academic topic with broad industrial applications, e.g., pump discharge lines, oil pipelines, propellant lines, reactor system components, microfluidic devices and so forth [Païdoussis 1998; Hu et al. 2016; Wang et al. 2016]. Their oscillation behavior is also one of the most troublesome problems in engineering applications. These industries usually utilize high thermal efficiency shell and heat exchanger designs to avoid failure. Some practical cases often require the devices to be able to work with high flow velocities, which in turn could cause pipes to experience complicated flow-induced vibrations.

A large number of studies have been devoted to the flow-induced vibrations of pipes due to their rich dynamical behavior [Païdoussis 1983; Chen 1991; Weaver et al. 2000; Pettigrew et al. 1978; Dai et al. 2014a]. Many researchers focused on the flow-induced vibrations of pipes to get better understanding of the mechanisms of the system. Studies related to this topic seem to have started in the 1960s. The stabilities and nonlinear dynamics of pipes conveying fluid were investigated both theoretically and experimentally. A very comprehensive introduction to the flow-induced vibrations and the associated linear stability problems can be found in [Chen 1987]. Nonlinear behaviors of slender structures subjected to axial fluid flows were discussed in details in [Païdoussis 1998]. Indeed, the pipe system exhibits a wide range of interesting dynamical behaviors under different boundary conditions and motion constraints. These cases cover a number of factors, such as the parametric excitations in the form of flow fluctuation, external excitations, various loose supports, articulated or continuous configuration, additional system

---

The financial support of the National Natural Science Foundation of China (Nos. 11672115 and 11622216) is gratefully acknowledged.

*Keywords:* nonlinear dynamics, chaotic motion, pipe conveying pulsating fluid, distributed motion constraints, impacting.

configurations like lumped mass, attached nozzles, elastic foundations, elastic constraints, and various forms of nonlinearities in the system arising from different aspects.

In the literature many studies have considered either pulsating fluid flows or motion constraints at one or finite number of locations on the pipe. The dynamics of a pipe conveying fluid was explored when the flow velocity is harmonically perturbed about a mean value in [Païdoussis and Sundararajan 1975]. Cantilevered and clamped-clamped models were investigated, in which the parametric and combination resonances were included. The method of averaging is adapted to examine the nonlinear dynamics of supported pipes conveying pulsating fluid in the vicinity of subharmonic resonances in [Sri Namachchivaya 1989; Chen 1971]. Several other notable papers on linear analytical models for these parametric instability problems of simply supported pipes were conducted in [Païdoussis and Issid 1974; Ginsberg 1973; Ariaratnam and Sri Namachchivaya 1986]. They have studied the parametric and combination resonances and evaluated the instability regions using Bolotin's method and numerical Floquet analysis. The nonlinear dynamics of supported pipes conveying pulsating fluid were discussed in [Sri Namachchivaya 1989; Jayaraman and Narayanan 1996; Chang and Chen 1994; Yoshizawa et al. 1986; Dai et al. 2014b]. From these studies, it is clear that the basic system of a pipe conveying pulsating fluid could lose stability at sufficiently high flow velocities. Thus, the analysis of subharmonic and combination resonances was the main interest for simply supported pipes conveying pulsating fluid, yielding the stability boundaries in the parameter space. For a perspective on the whole field of pipes conveying pulsating fluid, the interested reader is referred to [Païdoussis 1998].

In [Panda and Kar 2007; 2008; Wang 2009], a simply supported pipe conveying pulsating fluid was analyzed, in which the nonlinear force considered is associated with the axial extension of the pipe. By accounting for the nonlinearity resulted from the pipe's mean axial extension, the combination, principal parametric and internal resonances of supported pipes were investigated in the first two of these references. Nonlinear analysis of a cantilevered pipe conveying steady fluid with motion constraints was conducted in [Païdoussis and Semler 1993]. Two impact models representing the effect of motion constraints, i.e., cubic and trilinear springs, were introduced in the physical model and taken into account when deriving the nonlinear equation of motion. Results were obtained numerically in the form of bifurcation diagrams, phase plots, power spectral diagrams and time traces. Hassan et al. [2005] provided a means of representing the restraining force by a combination of edge and segmental contacts. The location of the contact segment during impact was unknown and determined artificially according to the researchers' interests in their studies. The location of the contact segment may greatly affect the performance of the system. The nonlinear dynamics of a simply supported pipe conveying pulsating fluid was further studied in [Wang 2009] by considering the effect of motion constraints modeled by cubic springs; the mean value of the pulsating velocity was assumed to be higher than the critical one for buckling instability, compared to the lower values of mean flow velocity used by [Sri Namachchivaya 1989; Sri Namachchivaya and Tien 1989]. Quasiperiodic and chaotic motions were obtained by using the Galerkin method with a two-mode approximation ( $N = 2$ ). In [Xia and Wang 2010], an improved theoretical model for the dynamics of tube arrays subjected to cross flow was developed, with consideration of the nonlinearity associated with the mean axial extension of the tube array. The restraining forces were modeled either by cubic or trilinear springs. In [Tang et al. 2014] another theoretical model was developed to analyze the fluid-elastic vibration of a single flexible curved pipe, surrounded by rigid cylinders and subjected to cross-flow as well as loose supports.



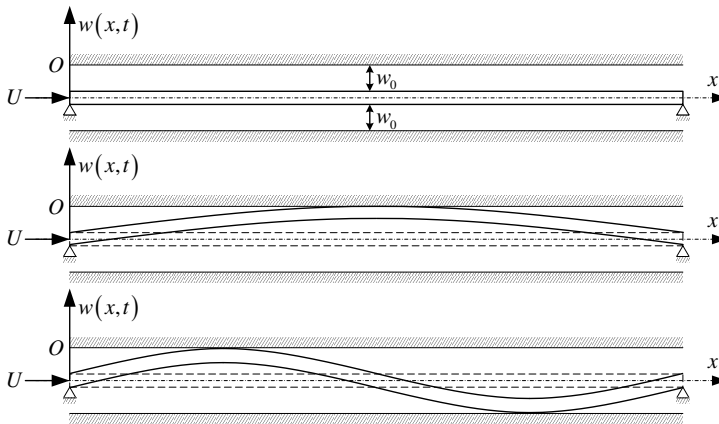


**Figure 1.** Schematic of the simply supported pipe conveying pulsating fluid with distributed motion constraints.

The present study initiates to investigate the dynamics of simply supported pipes with both internal pulsating fluid flow and distributed motion constraints imposed on the pipe. The simply supported pipe would impact the distributed motion constraints once the oscillation amplitude becomes sufficiently large. The constraints are modeled as trilinear springs and further improved as distributed constraints acting on the pipe along its axis. The pulsating internal flow has a time-dependent harmonic component superposed on the steady flow, such that  $u = u_0(1 + \sigma \sin \omega \tau)$ , where  $u_0$  is the mean flow velocity of the internal fluid,  $\sigma$  is the pulsating amplitude, and  $\omega$  is defined as the pulsating frequency of internal fluid flow. Particular attention is focused on the possible behaviors of the system by varying the values of pulsating frequencies of the unsteady internal fluid. Some interesting and sometimes unexpected results will be shown. The bifurcation diagrams, phase portraits, Poincaré maps and power spectral density diagrams will be constructed to present the dynamical behavior of the pipe system.

### 2. Equations of motion

In the current work, the simply supported pipe conveying pulsating fluid in the presence of distributed motion constraints is of length  $L$ , cross section area  $A$ , flexural rigidity  $EI$ , density  $\rho_p$ , mass per unit length  $m$  and coefficient of visco-elastic damping  $E^*$ . The internal flowing fluid is of density  $\rho_f$ , mass per unit length  $M$  and flow velocity  $U$ . The distributed motion constraints are modeled by trilinear springs along the pipe axis, as depicted in Figure 1.

The governing equation of a simply supported pipe in the absence of motion constraints has been obtained before [Panda and Kar 2007; Panda and Kar 2008; Jin and Song 2005]. The governing equation will be modified here to describe the behavior of the pipe with motion constraints. It is

$$EI \frac{\partial^4 w}{\partial x^4} + E^* I \frac{\partial^5 w}{\partial t \partial x^4} + 2MU \frac{\partial^2 w}{\partial t \partial x} + (M + m) \frac{\partial^2 w}{\partial t^2} + \left[ MU^2 + M \frac{\partial U}{\partial t} (l - x) - \left( E + E^* \frac{\partial}{\partial t} \right) \frac{A}{2l} \int_0^l \left( \frac{\partial w}{\partial x} \right)^2 dx \right] \frac{\partial^2 w}{\partial x^2} + F(w) = 0, \quad (1)$$

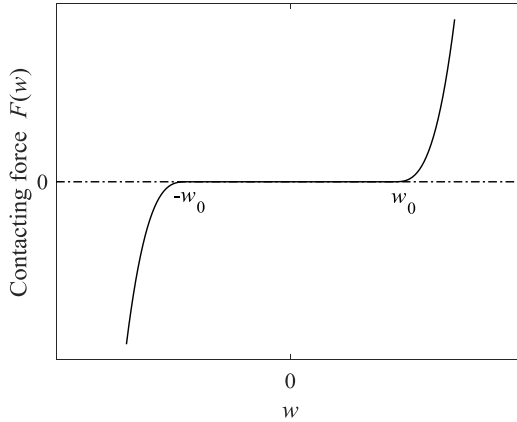


**Figure 2.** Diagrammatic view of the contacting force  $F(w)$  vs. the transverse displacement  $w$ .

in which  $F(w)$  represents the effect of the nonlinear motion constraints acting on the pipe. Following [Païdoussis and Semler 1993], the nonlinear restraining force is given by

$$F(w) = K\left(w - \frac{1}{2}(|w + w_0| - |w - w_0|)\right)^3, \tag{2}$$

in which  $w_0$  is the free gap between the pipe wall and the edge of the motion constraints;  $K$  is the stiffness of the trilinear springs. As suggested by [Païdoussis and Semler 1993], this expression of nonlinear force  $F(w)$  agrees well with the experimental tests. A qualitative relation of the nonlinear spring force and the transverse displacement  $w$  is shown in Figure 2. There is no contact when  $|w| < w_0$  and there is nonzero restraining force once  $|w| > w_0$ .

Introducing the following nondimensional quantities,

$$\eta = \frac{w}{L}, \quad \xi = \frac{x}{L}, \quad d = \frac{w_0}{L}, \quad \tau = \sqrt{\frac{EI}{m + M}} \frac{t}{L^2}, \quad u = \sqrt{\frac{M}{EI}} LU, \quad k = \frac{K_{spr} L^5}{EI},$$

$$\alpha = \sqrt{\frac{EI}{m + M}} \frac{E^*}{L^2}, \quad \beta = \frac{M}{m + M}, \quad \kappa = \frac{AL^2}{2I}$$

Equation (1) can be rewritten in a dimensionless form as

$$\alpha \frac{\partial^5 \eta}{\partial \tau \partial \xi^4} + \frac{\partial^4 \eta}{\partial \xi^4} + [u^2 + \sqrt{\beta} \dot{u}(1 - \xi)] \frac{\partial^2 \eta}{\partial \xi^2} + 2\sqrt{\beta} u \frac{\partial^2 \eta}{\partial \tau \partial \xi} + \frac{\partial^2 \eta}{\partial \tau^2} - \kappa \frac{\partial^2 \eta}{\partial \xi^2} \int_0^1 \left(\frac{\partial \eta}{\partial \xi}\right)^2 d\xi - 2\alpha \kappa \frac{\partial^2 \eta}{\partial \xi^2} \int_0^1 \frac{\partial \eta}{\partial \xi} \frac{\partial^2 \eta}{\partial \tau \partial \xi} d\xi + f(\eta) = 0. \tag{3}$$

The nondimensional restraining force is expressed as

$$f(\eta) = k\left(\eta - \frac{1}{2}(|\eta + d| - |\eta - d|)\right)^3. \tag{4}$$

The nondimensional pulsating fluid velocity is described by a sinusoidal fluctuation in  $\tau$ :

$$u = u_0(1 + \sigma \sin \omega \tau), \tag{5}$$

where  $u_0$  is the mean flow velocity,  $\sigma$  is the pulsating magnitude and  $\omega$  the pulsating frequency.

The infinite dimensional model can be discretized via Galerkin’s technique, with the simply supported beam eigenfunctions  $\phi_j(\xi)$ . These eigenfunctions are used as a suitable set of base functions with  $q_j(\tau)$  being the corresponding generalized coordinates; thus

$$\eta(\xi, \tau) = \sum_{j=1}^N \phi_j(\xi)q_j(\tau), \tag{6}$$

where  $N$  is the number of modes taken into calculations. Substituting (6) into (3), multiplying by  $\phi_i(\xi)$  and integrating from 0 to 1 leads to

$$\{\ddot{q}\} + [C]\{\dot{q}\} + [K]\{q\} + \{f(q)\} + \{g(q, \dot{q})\} = \{0\}. \tag{7}$$

$[C]$ ,  $[K]$ ,  $\{f(q)\}$  and  $\{g(q, \dot{q})\}$  represent the stationary damping and stiffness matrices, column vectors of the nonlinear restraining forces and geometrically nonlinear terms, respectively. The elements of  $[C]$ ,  $[K]$ ,  $\{f(q)\}$  and  $\{g(q, \dot{q})\}$  are given by

$$C_{ij} = \alpha c_{ij}^1 + 2\sqrt{\beta}u_0(1 + \sigma \sin \omega\tau)c_{ij}^2, \quad K_{ij} = k_{ij}^1 + u_0^2(1 + \sigma \sin \omega\tau)^2k_{ij}^2 + \sqrt{\beta}u_0\sigma\omega \cos \omega\tau k_{ij}^3, \tag{8}$$

$$f_i = \int_0^1 \phi_i(\xi)f\left(\sum_{j=1}^N \phi_j(\xi)q_j\right)d\xi, \quad g_i = g_{ijkl}^1q_jq_kq_l + g_{ijkl}^2q_jq_k\dot{q}_l,$$

where

$$c_{ij}^1 = \lambda_i^4\delta_{ij}, \quad c_{ij}^2 = \int_0^1 \phi_i\phi_j'd\xi, \quad k_{ij}^1 = \lambda_1\delta_{ij}, \quad k_{ij}^2 = -\lambda_i^2\delta_{ij}, \quad k_{ij}^3 = \int_0^1 (1 - \xi)\phi_i\phi_j''d\xi, \tag{9}$$

$$g_{ijkl}^1 = g_{ijkl}^2 = \int_0^1 \phi_1\phi_j'' \int_0^1 \phi_k'\phi_l'd\xi d\xi.$$

The calculation of the values of  $f_i$  in (8) deserves special attention. As can be seen in (4), the impacting force  $f(\eta)$  is a function of  $\eta$ . In the numerical algorithm, the values of  $q_i(\tau)$  for arbitrary time  $\tau$  can be calculated from (7) provided that the initial conditions were given, and then the displacement  $\eta(\xi, \tau)$  is obtained using (6). The instantaneous values of  $\eta(\xi, \tau)$  are further substituted into (4), yielding the values of distributed impacting force along the pipe axis at that time. Finally, the values of  $f_i$  can be obtained using the third expression of (8). The interested reader can get the matrix forms of the other coefficients ( $C_{ij}$ ,  $K_{ij}$ ,  $g_i$ ) from [Ni et al. 2015]. For the purpose of numerical computation, we define  $\mathbf{p} = \dot{\mathbf{q}}$  and  $\mathbf{z} = [\mathbf{q}; \mathbf{p}]$ ; equation (9) is then reduced to its first-order form:

$$\dot{\mathbf{z}} = \mathbf{A}\mathbf{z} + \mathbf{F} + \mathbf{G}, \tag{10}$$

where

$$\mathbf{A} = \begin{bmatrix} \mathbf{0} & \mathbf{I} \\ -\mathbf{K} & -\mathbf{C} \end{bmatrix}, \quad \mathbf{G} = \begin{bmatrix} \mathbf{0} \\ -\mathbf{g} \end{bmatrix}, \quad \mathbf{F} = \begin{bmatrix} \mathbf{0} \\ -\mathbf{f} \end{bmatrix}. \tag{11}$$

It follows from (10) that  $\mathbf{A}$ ,  $\mathbf{G}$  and  $\mathbf{F}$  are  $2N \times 2N$ ,  $2N \times 1$  and  $2N \times 1$  matrices, respectively.

### 3. Results and discussion

In the following, the dynamical behaviors of the simply supported pipe conveying pulsating fluid with distributed motion constraints will be investigated numerically. To the author’s knowledge, the nonlinear responses of a supported pipe conveying pulsating fluid with relatively high mean flow velocity in the presence of distributed motion constraints have not yet been explored. Therefore, we analyze the nonlinear vibrations of hinged–hinged pipes conveying fluid regarding this topic.

As is known that for a simply-supported pipe conveying fluid with a steady flow velocity, divergence in the first mode occurs at a dimensionless critical flow velocity  $u_c = \pi$  [Païdoussis 1998]. The main aim of this paper is to explore the effects of the pulsating frequency  $\omega$  with higher mean flow velocity  $u_0$  and the introduction of distributed motion constraints. For that reason, solutions of (10) are obtained by using the fourth-order Runge–Kutta method, with the following initial conditions employed,  $z(1) = \dots = z(N) = -0.001$  and  $z(N + 1) = \dots = z(2N) = 0$ .

The results to be presented are obtained with  $N = 4$  since this choice is sufficient for predicting the nonlinear responses of supported pipes, provided that the pulsating frequency is relatively small [Ni et al. 2014]. In the following calculations, some of the physical parameters are chosen to be

$$\alpha = 0.005, \quad \beta = 0.64, \quad \kappa = 5000, \quad k = 5.6 \times 10^6, \quad d = 0.044, \quad \sigma = 0.4. \quad (12)$$

**3.1. Validation of the algorithm.** In order to illustrate the effectiveness of the present algorithm, we first consider the model of a simply supported pipe conveying pulsating fluid without motion constraints. The system parameters are selected to be those used in [Wang 2009; Ni et al. 2014], i.e.,  $\alpha = 0.005$ ,  $\beta = 0.64$  and  $\kappa = 5000$ . The mean flow velocity is chosen to be  $u_0 = 4.5$  and the pulsating amplitude is  $\sigma = 0.4$ . It is noted that the bifurcation diagram for  $N = 2$  shown in Figure 3 without motion constraints are in good agreement with those obtained in those references. This validates the correctness of the present numerical scheme used in the following analysis.

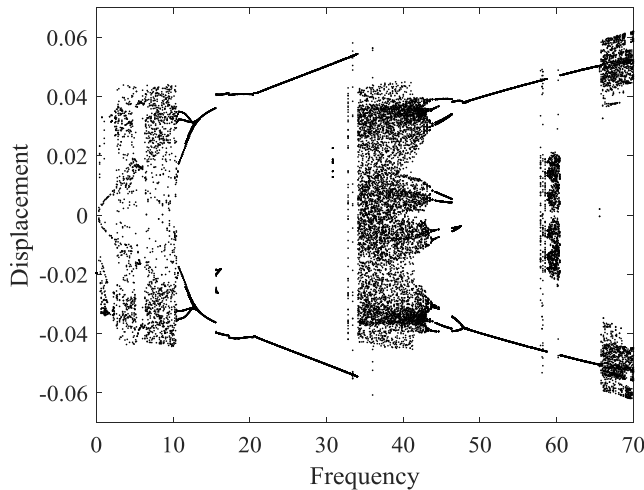


**Figure 3.** Bifurcation diagram of the mid-point displacement, for  $N = 2$ ,  $u_0 = 4.5$ ,  $\sigma = 0.4$ ,  $\alpha = 0.005$ ,  $\beta = 0.64$  and  $\kappa = 5000$ .

**3.2. Buckling of the pipe with motion constraints for  $\sigma = 0$  and  $\omega = 0$ .** To investigate the static short-wave buckling, results will be presented first with the flow velocity assumed to be constant. The pipe is placed between the two-sided motion constraints, which are described by a trilinear-spring contact model. As mentioned in the foregoing, [Ni et al. 2014] have proved the effectiveness of the truncating number  $N = 4$  in the presence of nonlinear motion constraints. So, the buckling analyses are conducted by truncating (8) at  $N = 4$ . To get a good understanding of the buckling style, bifurcation diagrams for displacements of three points on the pipe will be performed, i.e., for  $\eta(0.25, \tau)$ ,  $\eta(0.5, \tau)$  and  $\eta(0.75, \tau)$ . That is, whenever the oscillation velocity is zero (i.e.,  $\dot{\eta}(0.25, \tau)$ ,  $\dot{\eta}(0.5, \tau)$  or  $\dot{\eta}(0.75, \tau)$  are equal to zero), the corresponding displacement will be recorded.

Numerical results shown in Figure 4 are based on the trilinear-spring model. Inspecting Figure 4, it is easy to find that, with the increasing of flow velocity, the pipe exhibits different types of buckling instability. For  $0 < u_0 < 3.14$ , the pipe stays at the equilibrium position. This is because the flow-induced effect cannot overcome the damping effect of the system. For  $3.15 < u_0 < 15.7$ , the pipe is buckled with a half-wave configuration. However, as  $u_0$  is further increased, the half-wave configuration becomes flatter in the vicinity of peak displacement, which means more and more parts of the pipe tend to contact the motion constraints. In this case, the contact ratio between the pipe and the distributed motion constraints becomes larger. The restraining force acts on the pipe and cuts the wave crest of the buckling configuration. The configuration of the pipe is symmetrical although it is not exactly a sinusoidal one. For  $15.8 < u_0 < 19.7$ , the pipe along the axial direction behaves like a “W” shape. Interestingly, the two half-waves occur at the same side of the straight equilibrium position. Moreover, another region of  $19.8 < u_0 < 25$  generates a buckling shape similar to the curve of one period of a sinusoidal function. Several typical buckling configurations of the pipe for various flow velocities are shown in Figure 5. These results show the significant influence of motion constraints on the behavior of the pipe system.

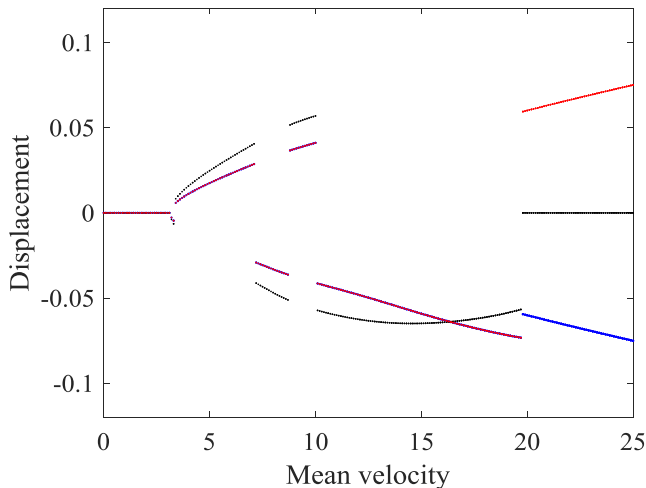


**Figure 4.** Bifurcation diagram for  $\eta(0.25, \tau)$  (blue),  $\eta(0.5, \tau)$  (black) and  $\eta(0.75, \tau)$  (red), as the mean velocity  $u_0$  varies. (Overlapping red and blue points when  $u_0 < 19.7$  indicate symmetry of the pipe shape).



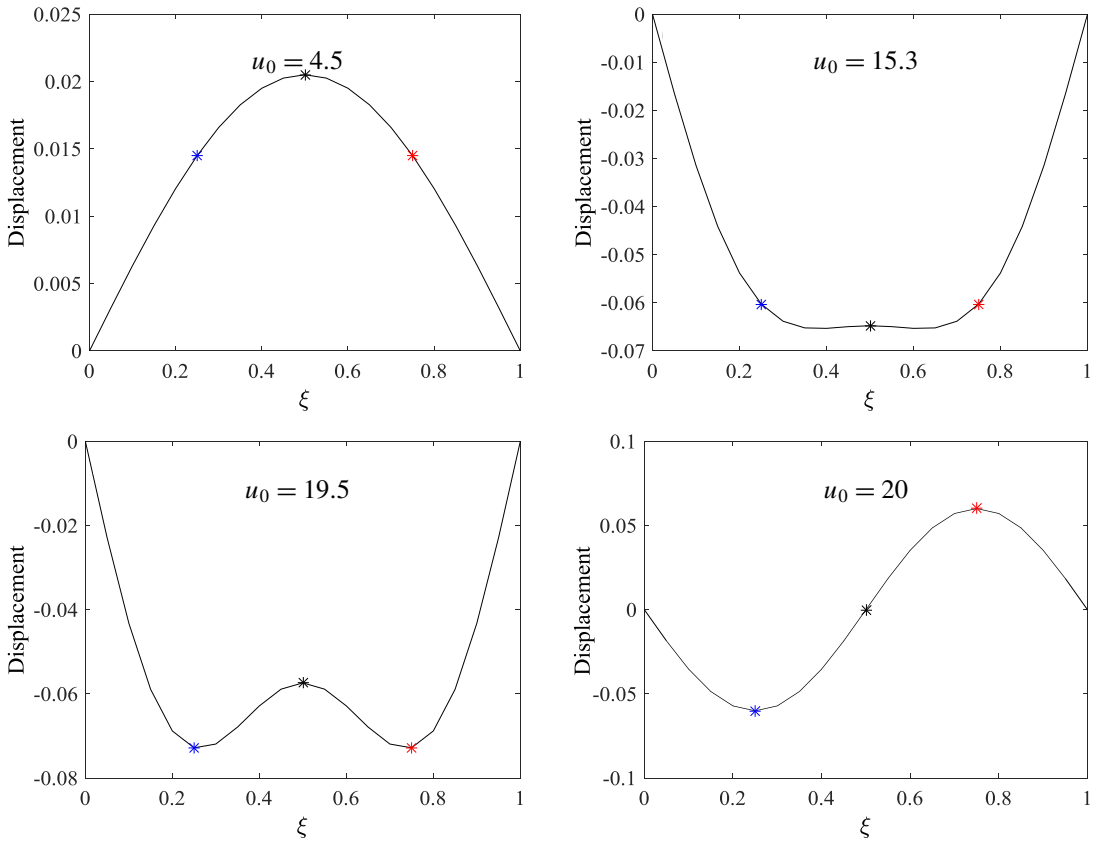


**Figure 5.** Buckling configurations of the pipe conveying steady fluid flow for various flow velocities  $u_0$ .

**3.3. Responses of the pipe with pulsating internal flows.** In this subsection, the effects of pulsating internal flows on the responses of the pipe system will be explored. As mentioned in the foregoing, in some working conditions, the mean flow velocity may be much higher than  $u_c = \pi$ . Therefore, in this paper, the flow velocity is chosen to be higher than  $u_c$ . We consider the cases of  $u_0 = 4.5$  and  $u_0 = 6$ , respectively. Bifurcation diagrams for the midpoint displacement of the pipe are conducted, as the pulsating frequency  $\omega$  is varying.

It can be seen from Figure 6 that, for  $u_0 = 4.5$  and  $0 < \omega < 20$ , the dynamics of the pipe/impacting system are similar to those of the pipe in the absence of motion constraints. This can be expected since the vibration amplitude of the mid-point of the pipe does not exceed the gap of the motion constraints in such case. Moreover, the contact force is small at the onset of impacting. Thus, in the range of  $0 < \omega < 20$ , the pipe has an occurrence of ‘free flight’ between the two-sided constraints. And periodic motions are detected in the range of  $20 < \omega < 38.7$ . Compared with the amplitude shown in Figure 3, the displacement amplitude is limited to be smaller and is slightly larger than the gap distance, indicating that contact between the motion constraints and pipe occurs. The oscillation of the pipe further evolves to become chaotic for  $\omega > 38.8$ , while for a pipe without motion constraints the threshold for chaos is about  $\omega = 32.8$ . In fact, in the range of  $\omega > 38.8$ , quasiperiodic motion might also occur.

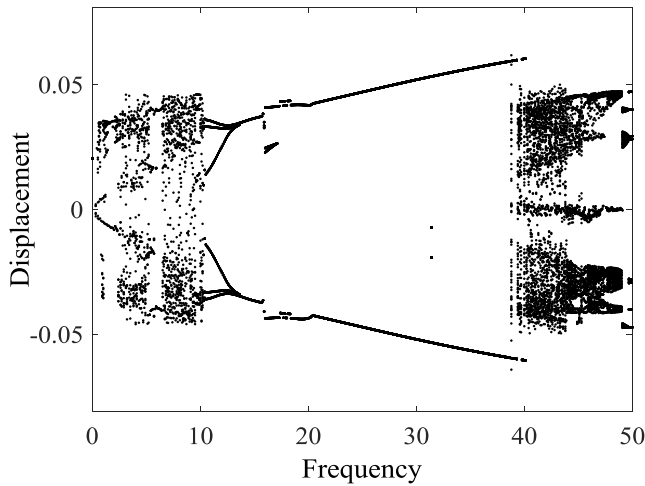


**Figure 6.** Bifurcation diagram for the constrained pipe system with  $u_0 = 4.5$  at  $\xi = 0.5$ .

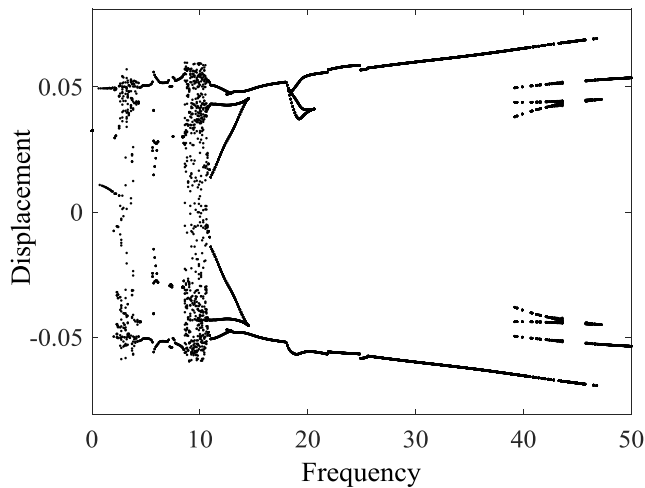


**Figure 7.** Bifurcation diagram for the constrained pipe system with  $u_0 = 6$  at  $\xi = 0.5$ .

Considering the case with relatively high mean flow velocity, i.e.,  $u_0 = 6$ , a quite different result is obtained, as presented in Figure 7. For  $u_0 = 6$ , impact between the pipe and constraints would occur for all pulsating frequencies considered, since the displacement amplitude in the absence of constraints reaches at a value of 0.494, which is larger than the gap distance between the pipe and constraints. As the pulsating frequency increases, it follows from Figure 7 that the response of the pipe may be periodic, quasiperiodic or chaotic. When the pulsating frequency is larger than  $\omega = 10.9$ , different types of periodic motion (with periods 1, 2 and 3) might occur.

Sample results of phase plots and power spectral density diagrams for the system with  $u_0 = 4.5$  and  $u_0 = 6$  are further presented in Figures 8 and 9. It can be seen that the pipe vibrates regularly or irregularly

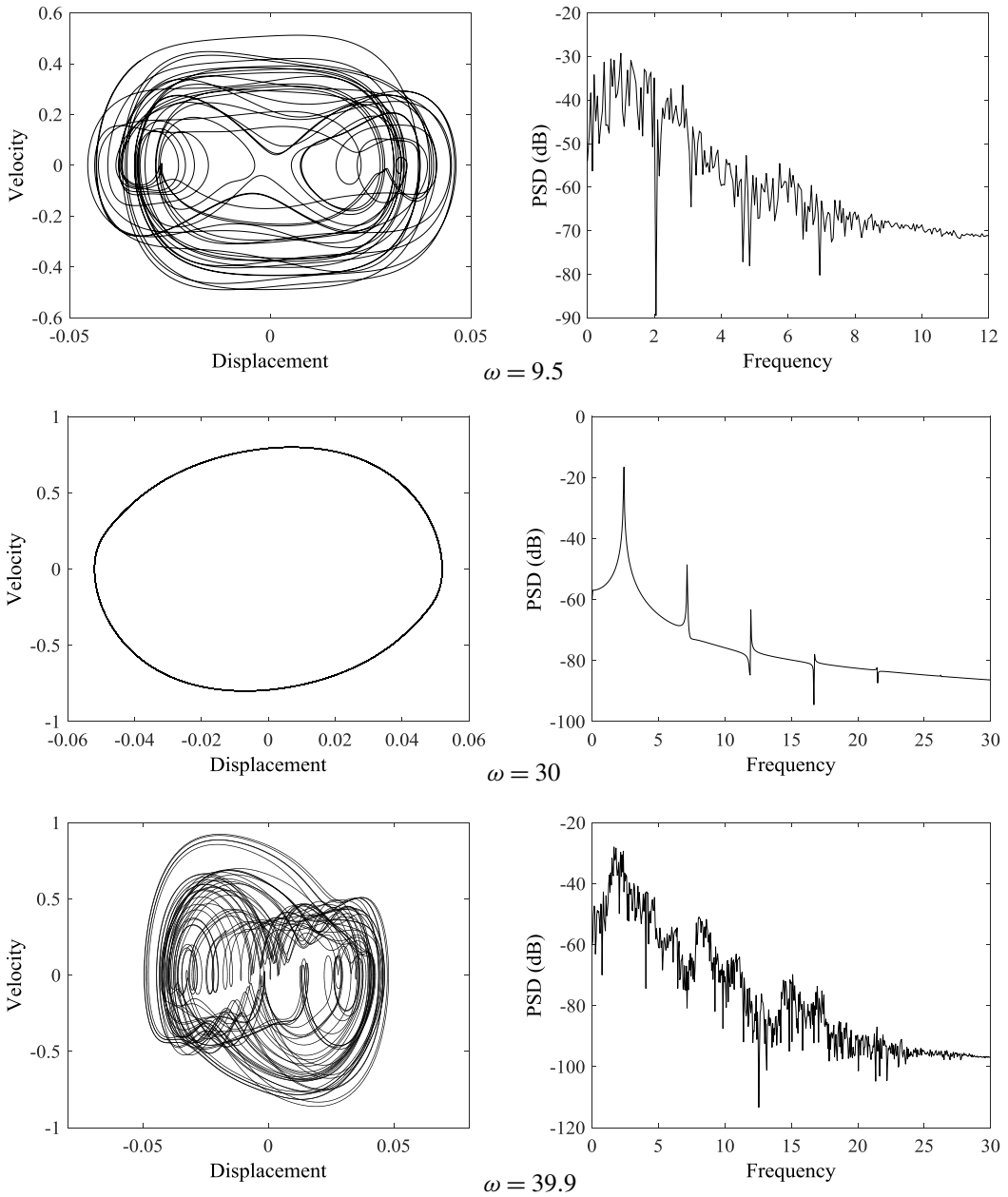


**Figure 8.** Phase plots and PSD diagrams for the system with motion constraints for  $u_0 = 4.5$  and three values of  $\omega$ .

back and forth within the gap, showing periodic motions (Figure 8, middle, and Figure 9, middle and bottom), chaotic-like motions (top parts of Figures 8 and 9) and transition motions (Figure 8, bottom) at some particular pulsating frequencies. The Poincaré maps for period-1 and multiperiod motions, as well as chaotic motions are constructed and shown in Figure 10. In this figure, the number of points in

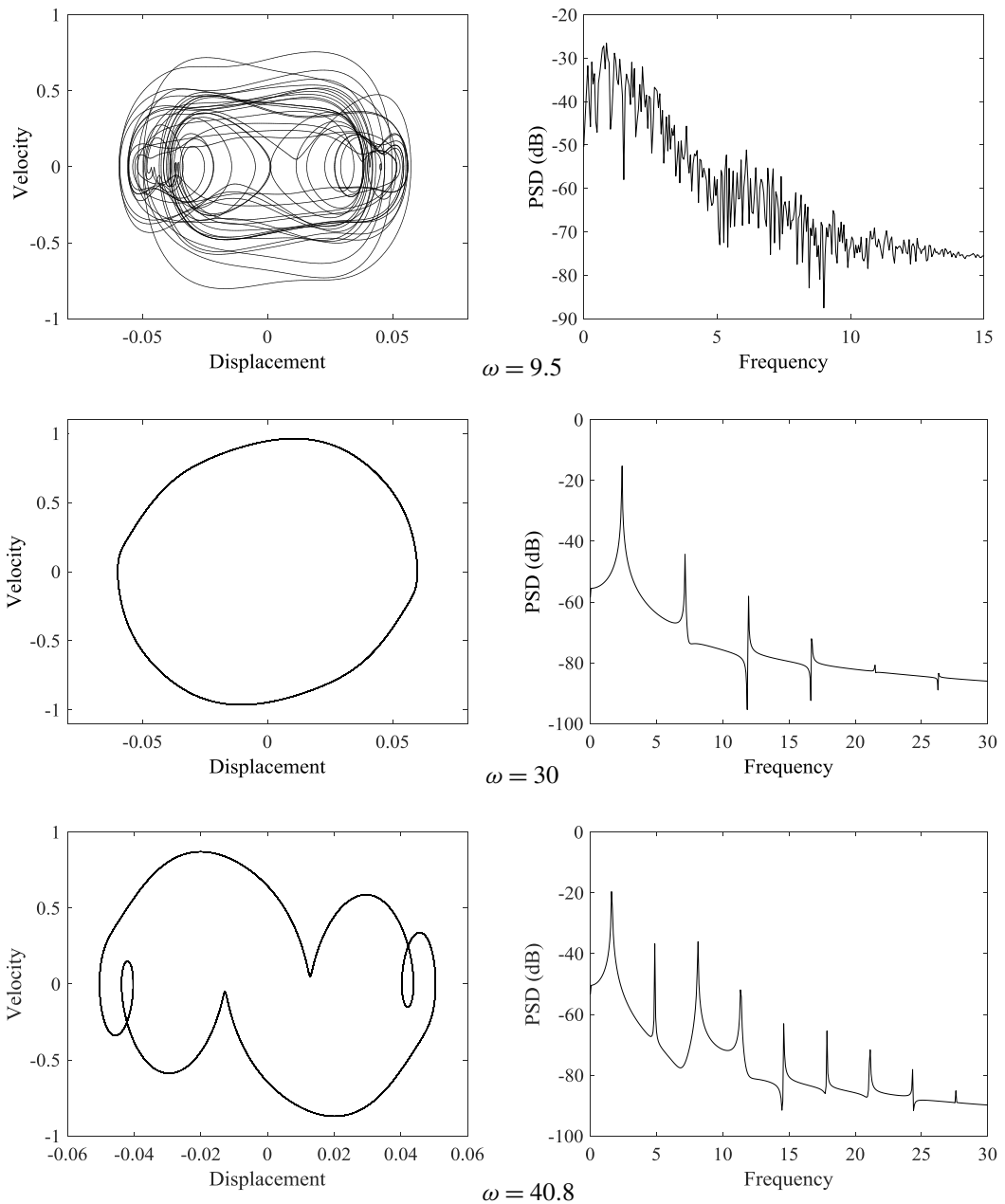


**Figure 9.** Phase plots and PSD diagrams for the system with motion constraints for  $u_0 = 6$  and three values of  $\omega$ .

Poincaré maps is twice as big as the number of pulsating period [Cai and Chen 1993]. Thus, the Poincaré maps for period-1, period-2, and chaotic motions consist of two points, four points, and infinitely many points, respectively, as seen in Figure 10. It is seen that the Poincaré map for chaos shows a complex fractal structure.

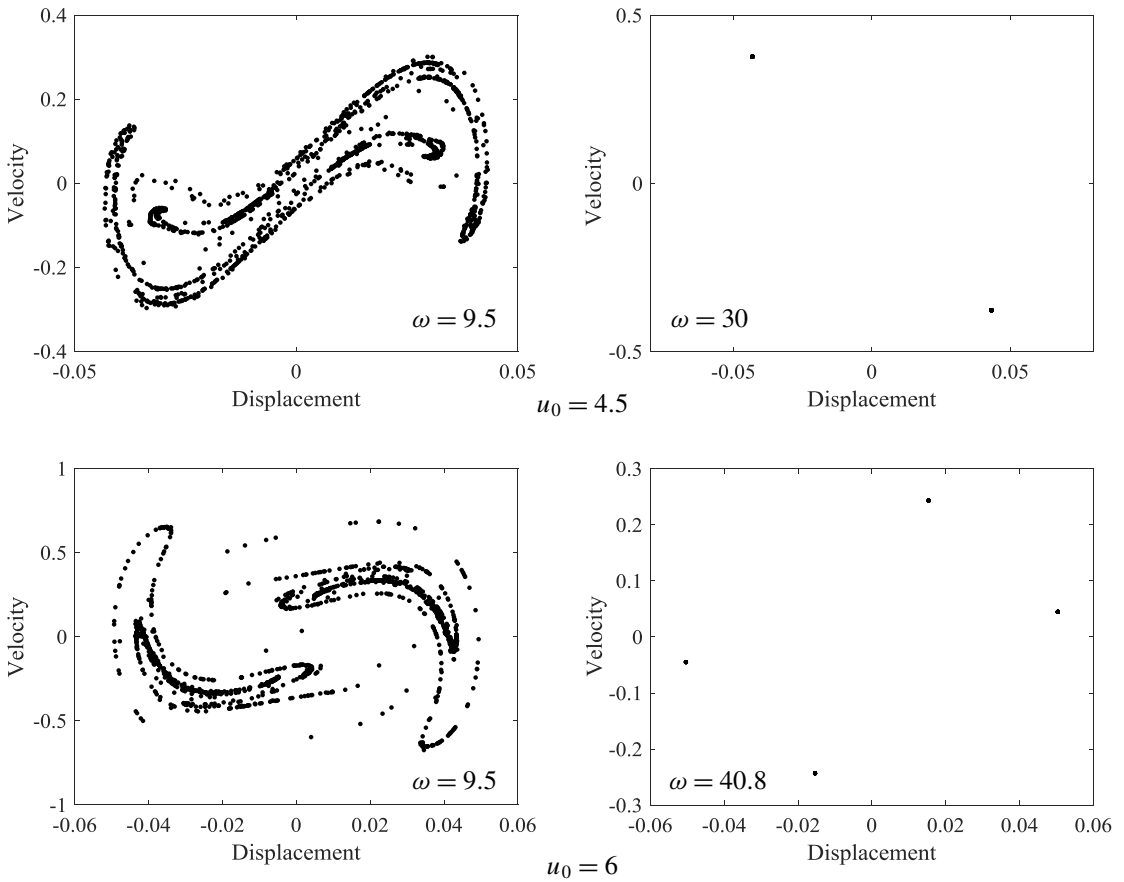


**Figure 10.** Poincaré maps for chaotic, period-1 and multiperiod motions.

Figure 11 shows mode shapes of the pipe for two sets of system parameters with different mean flow velocities and pulsating frequencies. To make the oscillation style clearer, only half-period of the motion is presented since it is a periodic vibration. We can see two phenomena from these mode shapes. The first is that the pipe deflects like a sinusoidal function in a period when it crosses the straight equilibrium position. The second is when the pipe bangs on one constraint, the impacting force makes the pipe rebound from it. Thus, the mode shape also changes at this moment. The time traces shown in Figure 11, right, imply that the difference between the cases of low and high mean flow velocities is obvious.

**3.4. Evolution of the impacting forces between the pipe and constraints.** The previous three subsections have focused on the dynamical behavior of the pipe. We now turn our attention to the evolution of the impacting forces as the pipe is impacting on the constraints. In Figure 1, two contact modes have been shown and there may be some other types in describing the contact behavior. Since the aforementioned two types of contact behavior have been realized in the numerical computation, the impacting force will be presented. The impacting forces may vary dynamically with time since the contact process changes quickly as time progresses.



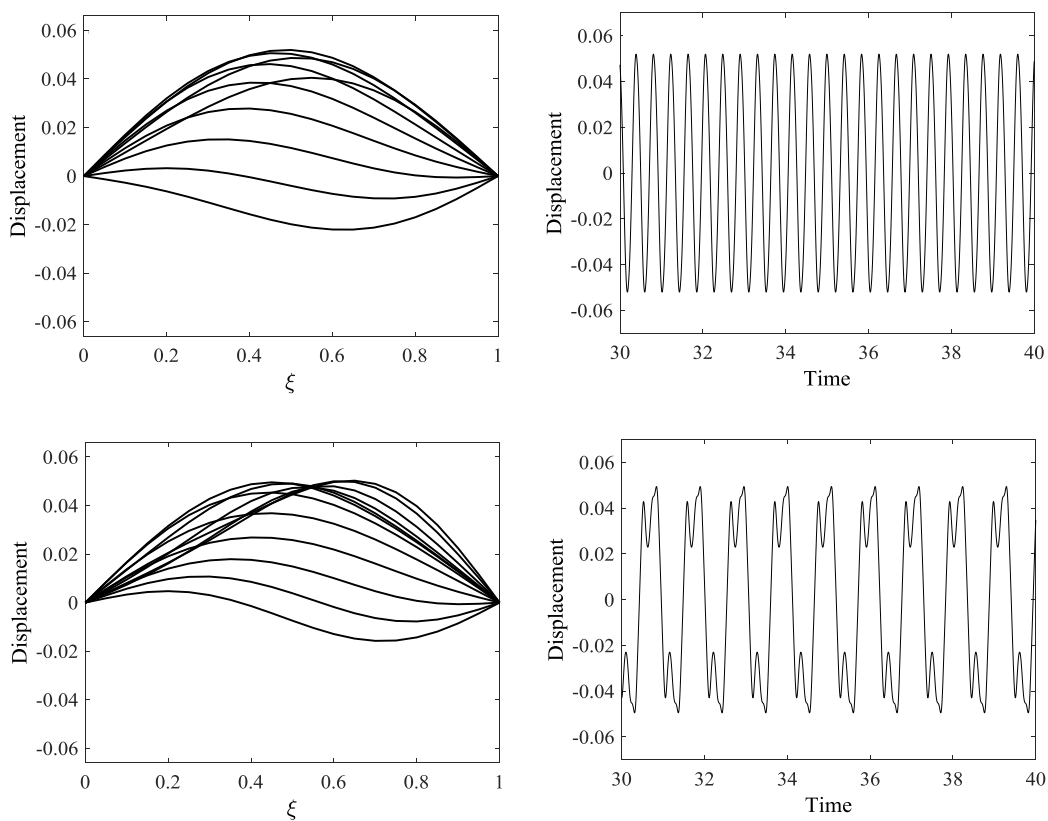


**Figure 11.** Special vibration shapes and displacement responses at the mid-point of the pipe under various load cases. (a) vibration shape for  $u_0 = 4.5, \omega = 30$ ; (b) vibration shape for  $u_0 = 6, \omega = 11.9$ ; (c) displacement for  $u_0 = 4.5, \omega = 30$ ; (d) displacement for  $u_0 = 6, \omega = 11.9$ .

Inspecting [Figure 5](#), top left, it is found that the buckling amplitude is smaller than the gap between the pipe and constraints and hence no contact occurs in this case. For the results shown in the rest of [Figure 5](#), however, there exist contact forces between the pipe and constraints. These contact forces are further illustrated in [Figure 12](#). As seen in part (a) of the figure, that impacting force appears at one side of the pipe, indicating that the pipe sticks to one of the motion constraints, as also schematically shown in [Figure 1](#), middle. The mode shape of the pipe schematically shown in [Figure 1](#), bottom might be linked to the distributed impacting force represented in [Figure 12\(c\)](#). The distributed impacting force shown in [Figure 12\(b\)](#), however, can be regarded as the transition state from [Figure 12\(a\)](#) to [Figure 12\(c\)](#). As the flow velocity increases from 19.5 to 20, therefore, buckling style of the pipe would change.

#### 4. Conclusions

In this paper, the nonlinear dynamics of a simply supported pipe conveying pulsating fluid is numerically investigated, with consideration of the effect of distributed motion constraints along the axial direction.

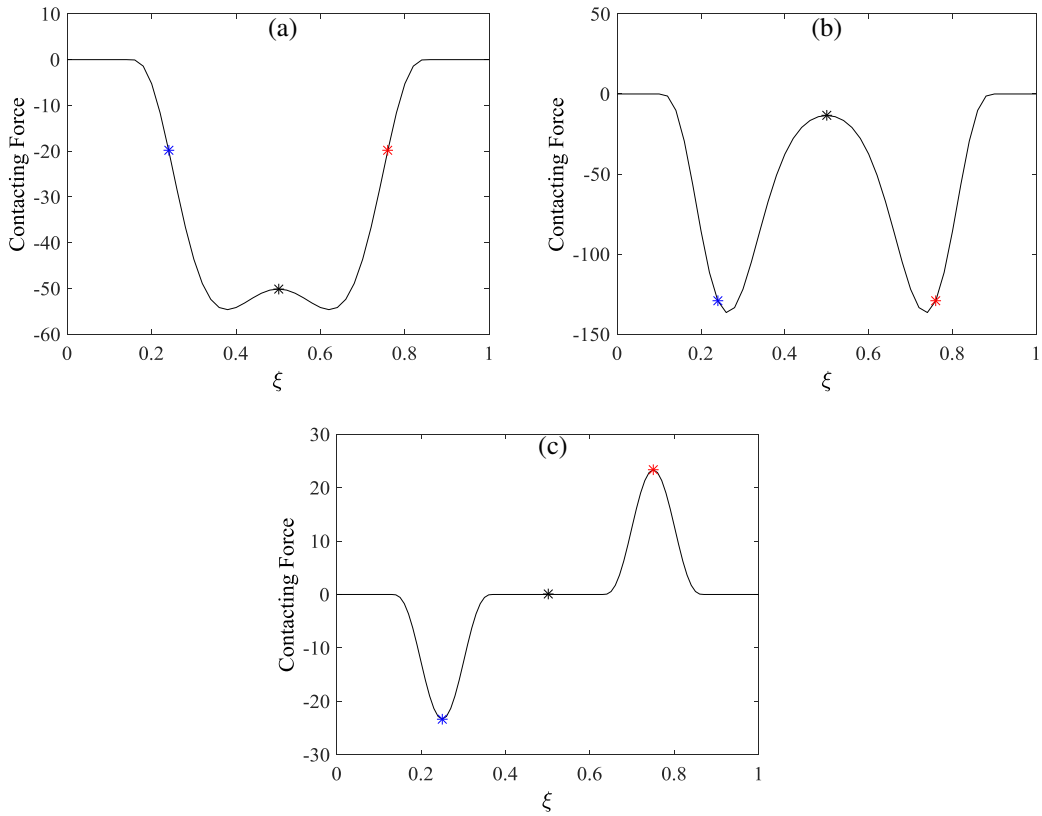


**Figure 12.** Contacting forces of the distributed motion constraints corresponding to the buckling styles shown in the middle and bottom parts of Figure 1.

The motion constraints are modeled by trilinear springs. The flow velocity is assumed to be pulsatile. A parametric analysis is conducted of the effect of the pulsating frequency and motion constraints on the dynamical behavior of the pipe.

Buckling analysis for a pipe conveying steady fluid flow is conducted first in the presence of distributed motion constraints. The pipe represents four different buckling types within the considered range of flow velocity. Then the significant effect of motion constraints on the flow-induced vibration of the pipe with pulsating fluid is explored. It is shown that the pipe is capable of displaying both periodic and chaotic motions with increasing the pulsating frequency. It is of particular interest to note that the distributed impacting force between the pipe and constraints may be associated with the buckling types of the system. Thus, the present configuration of pipes conveying pulsating fluid flow in the presence of distributed motion constraints serves as an example of a physical system on which the kaleidoscopic dynamical behavior could be observed.

## References

- [Ariaratnam and Sri Namachchivaya 1986] S. T. Ariaratnam and N. Sri Namachchivaya, “Dynamic stability of pipes conveying pulsating fluid”, *J. Sound Vib.* **107**:2 (1986), 215–230.

- [Cai and Chen 1993] Y. Cai and S.-S. Chen, “Chaotic vibrations of nonlinearly supported tubes in cross-flow”, *J. Press. Vessel Technol. (ASME)* **115**:2 (1993), 128–134.
- [Chang and Chen 1994] C. O. Chang and K. C. Chen, “Dynamics and stability of pipes conveying fluid”, *J. Press. Vessel Technol. (ASME)* **116**:1 (1994), 57–66.
- [Chen 1971] S.-S. Chen, “Dynamic stability of tube conveying fluid”, *J. Eng. Mech. Div. (ASCE)* **97**:5 (1971), 1469–1485.
- [Chen 1987] S.-S. Chen, *Flow-induced vibration of circular cylindrical structures*, Hemisphere, Washington, DC, 1987.
- [Chen 1991] S.-S. Chen, “A review of dynamic tube-support interaction in heat exchanger tubes”, pp. 111–120 in *Flow induced vibrations* (Brighton, UK, 1991), IMechE Conf. Publ. **1991-6**, Mech. Engin. Publ., Suffolk, 1991.
- [Dai et al. 2014a] H. L. Dai, A. Abdelkefi, and L. Wang, “Modeling and nonlinear dynamics of fluid-conveying risers under hybrid excitations”, *Int. J. Eng. Sci.* **81** (2014), 1–14.
- [Dai et al. 2014b] H. L. Dai, L. Wang, Q. Qian, and Q. Ni, “Vortex-induced vibrations of pipes conveying pulsating fluid”, *Ocean Eng.* **77** (2014), 12–22.
- [Ginsberg 1973] J. H. Ginsberg, “The dynamic stability of a pipe conveying a pulsatile flow”, *Int. J. Eng. Sci.* **11**:9 (1973), 1013–1024.
- [Hassan et al. 2005] M. A. Hassan, D. S. Weaver, and M. A. Dokainish, “A new tube/support impact model for heat exchanger tubes”, *J. Fluid. Struct.* **21**:5-7 (2005), 561–577.
- [Hu et al. 2016] K. Hu, Y. K. Wang, H. L. Dai, L. Wang, and Q. Qian, “Nonlinear and chaotic vibrations of cantilevered micropipes conveying fluid based on modified couple stress theory”, *Int. J. Eng. Sci.* **105** (2016), 93–107.
- [Jayaraman and Narayanan 1996] K. Jayaraman and S. Narayanan, “Chaotic oscillations in pipes conveying pulsating fluid”, *Nonlinear Dyn.* **10**:4 (1996), 333–357.
- [Jin and Song 2005] J. D. Jin and Z. Y. Song, “Parametric resonances of supported pipes conveying pulsating fluid”, *J. Fluid. Struct.* **20**:6 (2005), 763–783.
- [Ni et al. 2014] Q. Ni, Z. Zhang, L. Wang, Q. Qian, and M. Tang, “Nonlinear dynamics and synchronization of two coupled pipes conveying pulsating fluid”, *Acta Mech. Solida Sin.* **27**:2 (2014), 162–171.
- [Ni et al. 2015] Q. Ni, Y. Wang, M. Tang, Y. Luo, H. Yan, and L. Wang, “Nonlinear impacting oscillations of a fluid-conveying pipe subjected to distributed motion constraints”, *Nonlinear Dyn.* **81**:1-2 (2015), 893–906.
- [Païdoussis 1983] M. P. Païdoussis, “A review of flow-induced vibrations in reactors and reactor components”, *Nucl. Eng. Des.* **74**:1 (1983), 31–60.
- [Païdoussis 1998] M. P. Païdoussis, *Fluid-structure interactions: slender structures and axial flow, I*, Academic Press, San Diego, 1998.
- [Païdoussis and Issid 1974] M. P. Païdoussis and N. T. Issid, “Dynamic stability of pipes conveying fluid”, *J. Sound Vib.* **33**:3 (1974), 267–294.
- [Païdoussis and Semler 1993] M. P. Païdoussis and C. Semler, “Nonlinear and chaotic oscillations of a constrained cantilevered pipe conveying fluid: a full nonlinear analysis”, *Nonlinear Dyn.* **4**:6 (1993), 655–670.
- [Païdoussis and Sundararajan 1975] M. P. Païdoussis and C. Sundararajan, “Parametric and combination resonances of a pipe conveying pulsating fluid”, *J. Appl. Mech. (ASME)* **42**:4 (1975), 780–784.
- [Panda and Kar 2007] L. N. Panda and R. C. Kar, “Nonlinear dynamics of a pipe conveying pulsating fluid with parametric and internal resonances”, *Nonlinear Dyn.* **49**:1-2 (2007), 9–30.
- [Panda and Kar 2008] L. N. Panda and R. C. Kar, “Nonlinear dynamics of a pipe conveying pulsating fluid with combination, principal parametric and internal resonances”, *J. Sound Vib.* **309**:3-5 (2008), 375–406.
- [Pettigrew et al. 1978] M. J. Pettigrew, Y. Sylvestre, and A. O. Campagna, “Vibration analysis of heat exchanger and steam generator designs”, *Nucl. Eng. Des.* **48**:1 (1978), 97–115.
- [Sri Namachchivaya 1989] N. Sri Namchchivaya [sic], “Non-linear dynamics of supported pipe conveying pulsating fluid, I: Subharmonic resonance”, *Int. J. Non-Linear Mech.* **24**:3 (1989), 185–196.
- [Sri Namachchivaya and Tien 1989] N. Sri Namchchivaya [sic] and W. M. Tien, “Non-linear dynamics of supported pipe conveying pulsating fluid, II: Combination resonance”, *Int. J. Non-Linear Mech.* **24**:3 (1989), 197–208.

- [Tang et al. 2014] M. Tang, Q. Ni, Y. Luo, Y. Wang, and L. Wang, “Flow-induced vibration of curved cylinder arrays subject to loose support”, *Nonlinear Dyn.* **78**:4 (2014), 2533–2545.
- [Wang 2009] L. Wang, “A further study on the non-linear dynamics of simply supported pipes conveying pulsating fluid”, *Int. J. Non-Linear Mech.* **44**:1 (2009), 115–121. Correction in **45**:3 (2010) 331–335.
- [Wang et al. 2016] L. Wang, Y. Z. Hong, H. L. Dai, and Q. Ni, “Natural frequency and stability tuning of cantilevered CNTs conveying fluid in magnetic field”, *Acta Mech. Solida Sin.* **29**:6 (2016), 567–576.
- [Weaver et al. 2000] D. S. Weaver, S. Ziada, M. K. Au-Yang, S.-S. Chen, M. P. Paidoussis, and M. J. Pettigrew, “Flow-induced vibrations in power and process plant components: progress and prospects”, *J. Press. Vessel Technol. (ASME)* **122**:3 (2000), 339–348.
- [Xia and Wang 2010] W. Xia and L. Wang, “The effect of axial extension on the fluidelastic vibration of an array of cylinders in cross-flow”, *Nucl. Eng. Des.* **240**:7 (2010), 1707–1713.
- [Yoshizawa et al. 1986] M. Yoshizawa, H. Nao, E. Hasegawa, and Y. Tsujioka, “Lateral vibration of a flexible pipe conveying fluid with pulsating flow”, *Bull. Jpn. Soc. Mech. Eng.* **29**:253 (1986), 2243–2250.

Received 4 Jun 2016. Revised 24 May 2017. Accepted 27 May 2017.

WANG YIKUN: [wykfang1053@hust.edu.cn](mailto:wykfang1053@hust.edu.cn)

Department of Mechanics, Huazhong University of Science and Technology, Wuhan, 430074, China

NI QIAO: [niqiao@hust.edu.cn](mailto:niqiao@hust.edu.cn)

Department of Mechanics, Huazhong University of Science and Technology, Wuhan, 430074, China

WANG LIN: [wanglindds@hust.edu.cn](mailto:wanglindds@hust.edu.cn)

Department of Mechanics, Huazhong University of Science and Technology, Wuhan, 430074, China

LUO YANGYANG: [123443887@qq.com](mailto:123443887@qq.com)

Department of Mechanics, Huazhong University of Science and Technology, Wuhan, 430074, China

YAN HAO: [824174017@qq.com](mailto:824174017@qq.com)

Department of Mechanics, Huazhong University of Science and Technology, Wuhan, 430074, China

## MICRO AND MACRO CRACK SENSING IN TRC BEAM UNDER CYCLIC LOADING

YISKA GOLDFELD, TILL QUADFLIEG, STAV BEN-AAROSH AND THOMAS GRIES

This paper studies the ability of self-sensory carbon/glass textile reinforced concrete (TRC) beams to distinguish between micro- and macrocracking. In the proposed configuration, continuous carbon rovings knitted into the textile mesh serve both as the structural reinforcement and as the sensory system. The paper faces the challenge of detecting structural damage within the TRC structure. In this study, damage is defined as the formation of macroscopic cracks, which lead to the accumulation of significant irreversible residual deflection and to a reduction of the relative stiffness of the component. We explore experimentally the correlation between the electrical resistance change and the change of the structural properties and suggests crack detection parameters in order to identify, and mainly to distinguish, between micro- and macrostructural phenomena. Carbon rovings are found to provide electromechanical sensing capabilities, having the ability to distinguish between inner micromechanical structural phenomena and macroscopic ones. These observations are a step towards the applications of SHM techniques by intelligent carbon-based TRC elements.

### 1. Introduction

Multifunctional textile reinforced concrete (TRC) structures combine the advantages of high performance material and structural systems with those of integrated structural health monitoring system. The technology is based on a biaxial warp knitted fabric made of continuous fiber rovings (glass and carbon), which are embedded within thin-walled concrete structures, and serve two purposes simultaneously: reinforcement and monitoring. In this structural configuration, the textile reinforcement can easily follow a curved geometry of the structure. It also allows the reduction of wall thickness, mainly by means of the superior corrosion resistance of the reinforcement material that makes minimum concrete coverage obsolete.

TRC structures can be found in various applications such as pipes, tanks and shell like structures [Silva et al. 2011; Shams et al. 2014]. Such structures are inherently susceptible to internal or external damage such as cracks and material degradation. Yet, such structures are usually characterized by limited accessibility and inspection possibilities. Unless detected early, such damage would increase maintenance cost, disrupt operations and possibly lead to a catastrophic failure.

As opposed to reinforced concrete structural elements with steel rebar, which are allowed to be cracked during their service life, in the case of TRC structures, an adequate design allows for distributed multiple microcracks along the structures. In the latter case, due to the mechanism of the bonding and stress transfer between the concrete and the filaments in the roving, macroscopic cracks considerably degrade the reinforcement roving and reduce its load carrying capacity. The filaments of the roving that are located along the interface with the concrete (called the sleeve filaments [Bartos 1987; Zhu and Bartos 1997]) break due to the macroscopic cracking and only a reduced number of filaments that are located at

*Keywords:* crack detection, textile reinforced concrete, carbon rovings, electrical resistivity.



the core of the roving can further carry the loading (see, for example, [Bentur et al. 2010; Yardimci et al. 2011]). It is therefore essential to explore the damage sensing capabilities of TRC structures in order to further develop a reliable monitoring routine for early detection and rectification of structural damage.

Damage identification and structural health monitoring (SHM) techniques for reinforced concrete elements range from traditional methods such as visual inspection or tap tests, to modern techniques based on embedded or surface mounted strain sensors. The latter are either localized (such as resistor strain gauges and fiber Bragg grating) or distributed (such as time domain reflectometry in fiber optics; see, for example, [Khotiaintsev et al. 2013; Klar et al. 2010; Goldfeld and Klar 2013; Antunes et al. 2011; Majumder et al. 2008; Li et al. 2004; Lee 2003]). In the context of sensory TRC elements, there is a range of research works reporting on the implementation of the sensory devices in the textile grid, such as optic fibers (e.g., [Krebber et al. 2012; Montanini et al. 2012]). These methods are usually based on implementing the sensing system in a structural element, which requires physical accommodation in the load-bearing element. The potential degradation of the effective properties of the host element, and the clear distinction between the structural system and the sensory one (which is not a part of the load bearing system) are drawbacks of this approach. Also, stemming from the concept of joining two separate systems together, the interface between the structural and the sensory systems and the corresponding ability to maintain a coordinated action of the two are potential weak aspects. Finally, the sensory system itself is commonly expensive and its implementation is costly, time-consuming, and it requires specially trained personnel.

Using hybrid carbon fiber textiles as reinforcement for a TRC element and utilizing the electrostructural characteristics of the carbon rovings as a basis for its sensory feature offers a preferred alternative that overcomes some of the aforementioned drawbacks. The sensory TRC element is based on using the same array of continuous carbon rovings for the reinforcement required for the load resisting system and, at the same time, using them as the component providing the structure with the self-sensory feature. For the case of glass/carbon textile configurations, some carbon rovings replace glass fiber rovings and they are embedded in a glass textile grid as part of the production process of the textile. The implementation of the textile in the concrete element is a straightforward act, which is not different than the production process of standard textile reinforcement within TRC elements. The self-sensing capacity of the sensory textile is gained by correlating between the electrical response of the carbon rovings and the structural response of the TRC element. Therefore, the cost and labor inputs needed for converting the standard TRC component into a sensory one are almost eliminated.

Studies on the use of the electrical conductivity features of carbon fibers for sensing purposes can be found in the literature; see, for example, [Chen and Chung 1993; McCarter et al. 2007; Vaidya and Allouche 2011; Wang and Chung 1996; Christner et al. 2012; Horoschenkoff and Christner 2012; Angelidis et al. 2004; Todoroki and Yoshida 2004; Wen and Chung 1999; Wen et al. 2000; Goldfeld et al. 2016a; 2016b; Quadflieg et al. 2016]. There is a clear distinction between strain sensing and damage sensing. Strain can be reversible and it is generally monitored within the linear elastic regime of the structure. Therefore, it is not necessarily accompanied by macroscopic cracks or damage. While in the case of damage sensing, the mechanism of the electrical response is inherently different. Damage leads to an irreversible change in the electrical resistance. The more severe the damage is, the greater the irreversible component of the electrical resistance becomes. The hypothesis of this study is that the irreversibility of the electrical resistance can be correlated to the structural health. The goal is therefore to correlate between the electrical response and the structural health. Understanding the correlation in

the damaged regime is essential for the development of intelligent carbon-based TRC structural elements with inherent SHM capabilities in the future.

The piezoresistivity (the effect of strain on the resistivity) of short carbon fibers embedded in a cement matrix has been extensively investigated in the literature (see, for example, [Chen and Chung 1993; McCarter et al. 2007; Vaidya and Allouche 2011]). The carbon fibers in such applications are an additive for rendering detectable piezoresistive properties to the concrete mixture by improving the electrical conductivity of the cast concrete element. Therefore, in this case, the fibers are not the sensor itself.

An alternative sensing concept is obtained by detecting changes to the electrical resistivity of continuous carbon rovings. In this case, the carbon rovings, made of thousands of carbon filaments, serve both as the structural reinforcement and as the sensory agent. The sensory capability is obtained by monitoring changes to the electrical resistance of the roving due to straining. Investigations of this concept were mainly focused on carbon-based polymer or epoxy matrix composites (see, for example, [Wang and Chung 1996; Christner et al. 2012; Horoschenkoff and Christner 2012; Angelidis et al. 2004; Todoroki and Yoshida 2004]). Relatively few studies have investigated the piezoresistivity effect of continuous carbon fiber embedded in a cement matrix. Wen and Chung [1999] and Wen et al. [2000] investigated the correlation of the changes to the electrical resistance with the straining of a continuous carbon fiber embedded in cement paste under uniaxial tension. They concluded that the electrical resistance increases upon tension and that the electrical resistance increase is mostly reversible. Goldfeld et al. [2016a; 2016b] investigated the piezoresistive effect of hybrid glass/carbon TRC beam elements under monotonic loading and under cyclic loading, respectively. These two studies moved from the fundamental single roving or bundle of fibers scale to the integrative TRC structural element scale. It was reported that along the linear-elastic regime, the integrative electrical resistance can be correlated to the distributed strain, and since the electrical resistance is mostly reversible, a gauge factor can be defined. Slight irreversibility was attributed to inner irreversible micromechanical processes, such as degradation of the fiber-concrete bond strength and breakage of single filaments [Banholzer and Brameshuber 2004; Banholzer et al. 2006; Bentur et al. 2010; Yardimci et al. 2011].

Damage sensing, which differs from strain sensing, is essential in the case of thin walled TRC structures. It has been mainly reported for the case of short carbon-based cement composites; see, for example, [Wen and Chung 2007; Ding et al. 2013; Teomete 2015; Meehan et al. 2010; Yao et al. 2003; Peled et al. 2001; Bontea et al. 2000; Reza et al. 2003]. In the case of damage sensing, the mechanism of the electrical response is different. Damage leads to irreversible changes in the electrical resistance, depending on the severity of the damage [Bontea et al. 2000; Reza et al. 2003].

In the case of damage sensing with continuous carbon fibers, most of the studies were focused on carbon fiber reinforced polymers; see, for example, [Wang and Chung 2006; Chung 2007]. In these studies, it was reported that the accumulation of damage and irreversible structural response triggered irreversible changes to resistance.

Studies on damage sensing with continuous carbon rovings embedded in concrete elements were only focused on the correlation between internal microstructural phenomena, such as the degradation of the interface between the fiber and the concrete matrix, and the measured electrical resistance; see [Wen and Chung 1999; Wen et al. 2000; Goldfeld et al. 2016a]. These microstructural phenomena characterize the linear-elastic regime of the response, which is considered as the healthy state of the structure and therefore is attributed to the strain sensing. Damage sensing, which extends beyond the

aforementioned strain sensing concepts is, on the other hand, the most crucial monitoring capability of thin-walled TRC structures. The goal of the current study is therefore to investigate the structural and the electrical response of a damaged TRC element. As opposed to [Goldfeld et al. 2016a], which focused on the piezoresistive behavior of the carbon-based textile along the linear-elastic regime, the present study focuses on the essential capabilities of the carbon-based textile to sense structural damage in terms of macroscopic crack and to quantitatively distinguish between micro- and macrostructural phenomena. The goal is therefore to explore and characterize the correlation between the structural and electrical responses of a TRC beam before and after cracking.

In this study, the damage state is defined by the formation of a macroscopic crack. In TRC composites, since the reinforcing rovings are made of thousands of filaments, the bonding and stress mechanism between the filaments and concrete matrix play a significant role in the load carrying capacity of the roving and, as a result, of the whole component. Due to increased tension loading, and after formation of the first matrix crack, the sleeve filaments of the roving break and filaments in the core of the roving can further carry on the increasing load providing strain hardening behavior. It is commonly modeled by a telescopic pull-out mechanism (see, for example, [Bartos 1987; Zhu and Bartos 1997; Bentur et al. 2010; Yardimci et al. 2011]) with microcracks being smaller than 100 microns in width during the strain hardening stage, where significant load can be transferred across the microcrack. Therefore, an adequate design allows for distributed multiple microcracks along the structures to be considered here as being in the healthy state. When a macrocrack opens, at the cracked zone all sleeve filaments break, including progressive breakage of core filaments, as well as extensive displacement in the core filaments, leading to a significant reduction in the load carrying capacity. Thus, as a result of the widening of one (or several) of the microcracks into a macrocrack (significantly wider than 100 microns), the strain hardening behavior turns into a marked softening one, with significant reduction in the load bearing capacity of the TRC component. The formation of the macrocrack can be seen by a drop of the load-deflection curve, as in the present study. Therefore, the formation of a macrocrack is defined as the damaged state in this study.

The hypothesis of this study claims that the micro- and macrostructural response are reflected by the measured electrical response of the carbon rovings. Therefore, the goal is to correlate between the structural response and the electrical measure, and consequently estimate the structural health.

In order to support the hypothesis of the study, the structural and electrical response of a TRC beam are experimentally investigated under cyclic loading at the healthy and at the cracked state. The loading cycles extend the predamaged loading process presented in [Goldfeld et al. 2016a] to the damaged cracked-state. For the sake of completeness, the relevant data from [Goldfeld et al. 2016a] are shortly presented. The preliminary information regarding the structural and electrical setups is mentioned here again, and selected results for the healthy state are presented as a reference in order to compare, distinguish and highlight the differences between the strain and damage sensing capabilities of the carbon rovings.

## 2. Experimental investigation

The experimental investigation focuses on the crack sensing capabilities of the carbon rovings. It uses the cyclic loading test conducted in [Goldfeld et al. 2016a] in the precracked range as reference and extends the cyclic loading to the cracked regime. The generic setups and properties of the sensory textile, the beam sample, the electrical layout, the testing scheme and the procedure for the compensation for the effect of the temperature on the sensing system are presented in [Goldfeld et al. 2016a], and (for clarity

and completeness) will be briefly presented here. In the previous work, the strain sensing capability at the healthy state was investigated, while the current study focuses on the structural and the sensing responses of the beam at the cracked regime.

**2.1. Sensory textiles.** The sensory textile is based on two types of rovings: rovings made of glass, which are the main reinforcement platform, and rovings made of carbon, which are also used as the sensory system (see also [Goldfeld et al. 2016a; 2016b]); see Figure 1. The material properties of the glass and the carbon rovings are given in Table 1.

The reinforcing textile structure consists of a warp-knitted grid of alkali-resistant (AR) glass rovings and sensory carbon rovings, which are spaced 7–8 mm from each other. The weft direction consists only

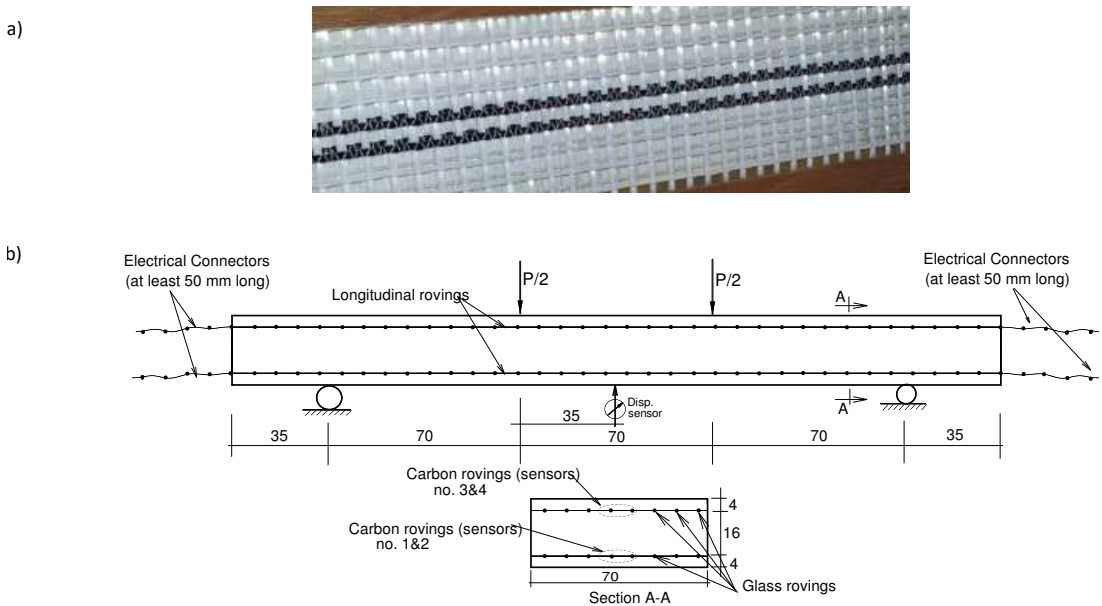


**Figure 1.** (a) The reinforcement sensory textile; (b) schematic drawing, cross section, geometrical parameters and loading scheme of the TRC specimen (dimensions in mm) [Goldfeld et al. 2016a].

	glass roving	carbon roving
density [tex]	2400	3300
specific mass density [kg/m <sup>3</sup> ]	2680	1800
modulus of elasticity [GPa]	72	240
filament tensile strength [MPa]	1700 (elongation 2.4%)	4000 (elongation 1.7%)
filament diameter [μm]	19	7
filament count	–	50000
equivalent cross-sectional area [mm <sup>2</sup> ]	0.9	1.81
electrical resistance [Ω/m]	∞	13

**Table 1.** Material properties of the glass and the carbon rovings.

of AR glass rovings. In the warp direction, some of AR-glass rovings were replaced by sensory carbon rovings in a symmetric layout. Placing the carbon rovings only in one direction avoids potential electrical linking between perpendicular rovings, but limits the sensing capabilities to one chosen direction. The rovings are knitted with warp-knitting yarns made of polypropylene. The type of knitting stitch is pillar; its influence on the tensile properties of the roving within the concrete has been investigated in [Stolyarov et al. 2015a]. The cross-sectional area of the rovings as given in Table 1 is a theoretical value and relates to the cross section of all filaments counted together and is used for the stress calculation. The cross section and occupied space of the roving is much bigger, due to the spaces between the filaments. The shape of the roving cross section also depends in the stitch type, e.g., pillar stitch forms a more circular shaped cross section, while the tricot stitch forms a more elliptical shaped cross section; see [Stolyarov et al. 2015b]. The textile used had a roving width of 1–2 mm. The production of the glass/carbon textile uses a conventional process with no specific or special treatment of the textile. The electrical integration of the carbon fiber rovings into the data acquisition (DAQ) system uses a cast connector, made of conductive epoxy, at the ends of each carbon roving; see [Goldfeld et al. 2016a].

**2.2. TRC beam samples.** Beam samples reinforced with the glass/carbon textile have been designed and manufactured. The specimens are 280 mm long, 70 mm wide and 24 mm thick, according to the loading setup used in this research (four point bending), and they were reinforced with two layers of the sensory textile located 4 mm from the upper and lower faces of the element. The thickness was determined in order to capture both microstructural behavior (so it should not be too thick), as well as macrostructural behavior (so it should not be too thin). Therefore, the distance between the textiles is determined as 16 mm, and the total thickness of the beams is 24 mm. The width (70 mm) is determined according to the textile grid (the interval between the rovings is about 7 mm–8 mm). The carbon rovings are located at the middle of the beam and the influence of the added stiffness of the carbon rovings with respect to the glass rovings can be averaged along the beam width. The length of the beam (280 mm) is determined in accordance to the loading scheme and the estimated bending capacity of the beam's cross section.

Each textile layer includes six longitudinal ( $0^\circ$ ) glass rovings and two longitudinal carbon rovings. The transverse ( $90^\circ$ ) rovings are all made of glass fibers; see Figure 1. Special molds were developed in attempt to maintain a preliminary low level of pretensioning in all four directions to both layers of the sensory smart textile. The pretensioning was performed manually; see [Goldfeld et al. 2016a]. In Figure 1, the layout of the beam and its cross sectional properties are given.

A commercial grout mixture (Sika Grout 214) was used for the concrete matrix, which was prepared with a water per dry material ratio of 0.125. The concrete matrix was not modified with any electrical conductive component and therefore is considered as an isolating dielectric. The TRC beams were cured at room temperature for 48 hours. According to EN 196-1:2005, after 28 days, the tensile strength and the compression strength of the grout were determined. The mean values  $\pm$  standard deviation are  $f_t = 11.71 \pm 0.49$  MPa and  $f_c = 66.9 \pm 2.77$  MPa.

**2.3. Sensing concept.** The hypothesis of this study is that the measured electrical change of the carbon rovings embedded in the concrete beam has the capabilities to distinguish between internal microstructural phenomena and macroscopic ones. In particular, it aims to explore the correlation of the electrostructural response to the evaluation of damage.



In the examined layout, the bending moment diagram is not constant and thus the stress as well as the damage are not uniformly distributed along the roving. This becomes particularly critical after the formation of the macroscopic crack. On the other hand, the measured electrical resistance is integrally attributed to the entire roving monitored from one end to another. Thus, the measured electrical resistance along each roving is considered as an integrative index. This means that only an integrative value of the electrical resistance  $R_x$  and resistance change  $\Delta R$  can be evaluated. The integrative electrical resistance of the roving is given in an integral form, (see also [Goldfeld et al. 2016a]):

$$R_x = \int_0^L r(x) dx, \quad (1)$$

where  $r(x)$  represents the electrical resistance per unit length depending on the strain distribution, the damage distribution and on the temperature change, and  $L$  is the length of the beam. Consequently, the resistance change  $\Delta R$  due to damage can be defined by

$$\Delta R^{\text{measured}} = (R_x^{\text{damage}} - R_x^0) + \Delta R_x^{\text{temperature}} = \int_0^L r(f(\varepsilon(x), \text{damage}(x))) dx - R_x^0 + \int_0^L r(\Delta T) dx. \quad (2)$$

In the above equations,  $\varepsilon(x)$  designates the distribution of the strain. In the case of a healthy state it depends exclusively on the loading scheme and the moment distribution. At the damaged state,  $\varepsilon(x)$  is also influenced by the location and severity of the damage along the structure, especially in statically indeterminate structures. The function  $\text{damage}(x)$  designates the distribution of the damage along the structures. Therefore,  $r(f(\varepsilon(x), \text{damage}(x)))$  is the electrical resistance along the roving, which is both strain and damage dependent, and  $r(\Delta T)$  is the distributed resistance due to temperature change. In the current study, it is assumed that there is no coupling between the temperature and structural effects. Therefore, in order to correlate the electrical resistance change to the structural response, linear temperature compensation is performed; further details are given in Section 2.5.  $R_x^0$  is the reference electrical resistance, measured before the mechanical loading was applied. The damage sensing capabilities can be performed by comparing the electrical resistance at the healthy state  $\text{damage}(x) = 0$  and at the damaged state  $\text{damage}(x)$ , or by comparing the electrical resistance change at a specific unknown state before  $\varepsilon(x) = 0$  and after loading  $\varepsilon(x)$ . Both possibilities are discussed in Section 3.3 by means of crack detection parameters.

From the structural point of view, the distinction between strain sensing and damage sensing is governed by the micromechanism of the structural response, which is characterized by the bonding mechanism of the roving and the concrete matrix. A simplified constitutive model of the stress-strain diagram of TRC structures is presented in Figure 2 (see [Mobasher et al. 2014]). The constitutive model of the roving under internal tensioned loading (Figure 2a) is characterized by a linear strain-stress relationship up to the macroscopic cracking strain  $\varepsilon_{cr}$ . This part can be represented by the tensile stiffness  $E$ . Along this phase multiple microcracks are formed. Then, after the formation of a macroscopic crack, a postcracking modulus  $E_{cr}$  can be defined.  $E_{cr}$  is lower than  $E$  and its sign depends whether strain softening or strain hardening characterize the postcracking response. The reduction in the elastic modulus is due to the breakage of all sleeve filaments at the cracked zone (see, for example, [Bartos 1987; Zhu and Bartos 1997; Bentur et al. 2010; Yardimci et al. 2011]). Along the last phase, only the core filaments within the rovings are able to carry the tensioned load along the structure, which can be represented by a constant

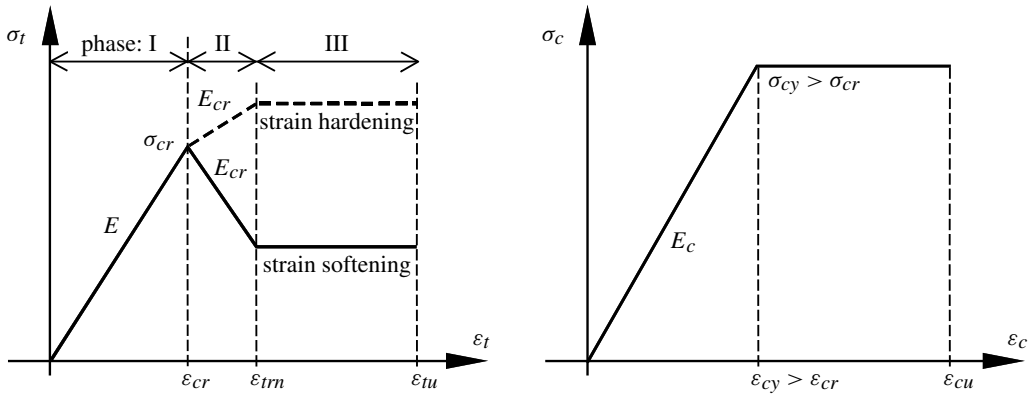


**Figure 2.** Fiber reinforced concrete model: left, tension model; right, compression model; according to [Mobasher et al. 2014].

lower tensile strength and perfectly plastic behavior, phase III in Figure 2a. In the compression model (Figure 2b), the stress increases linearly up to the yield strain  $\varepsilon_{cy}$ , and then remains perfectly plastic. In the current study it is assumed that the strain sensing is represented by the first phase (indicated in Figure 2). This phase is characterized by internal microstructural process associated to the slight degradation of the bonding mechanism and therefore by generally linear-elastic behavior. The damage sensing, on the other hand, is attributed to the second and third phases, after a macrocrack has been formed and only the core filaments within the roving carry on the load. The hypothesis is that both phases, the pre- and postcracking, are reflected by the measured electrical resistance.

The inevitable shift from the distributed effect reflected by changes to  $r(f(\varepsilon(x), \text{damage}(x)))$  and the integrative one reflected by changes in  $R_x$  (equations (1) and (2)) establishes the ability to identify structural events but eliminates the ability to identify its exact location along the roving. Moreover, distributed small cracks and one severe crack can eventually lead to the same integrative electrical measure. This means that the exact location of the damage and its pattern cannot be identified by the integrative measure but only its overall effect in terms of global-integrative indexes. This drawback can be handled by using various approaches (e.g., segmentation of the TRC elements), which are beyond the scope of the present paper. Nevertheless, the study will demonstrate the capability of the integrative electrical resistance to clearly distinguish between a healthy state and a damaged state (after cracking has been formed).

The measurement methodology takes advantage of the continuous configuration of the carbon rovings within each structural segment. Following the experimental setup outlined in detail in [Goldfeld et al. 2016a; 2016b], the electrical setup uses a Wheatstone bridge scheme; the general layout is illustrated in Figure 3. In this configuration, the carbon roving is serially implemented along with the external resistor in the bridge and the voltage change across the bridge is measured. Since the properties of all other resistors are known, and since only the carbon roving triggers the bridge out of balance, the voltage change across the bridge can be converted into changes to the integrated electrical resistance of the carbon fiber roving,  $R_x$  as follows:

$$R_x = \frac{V_{in} R_c}{V_b + \alpha V_{in}} - R_c - R_d, \quad (3)$$

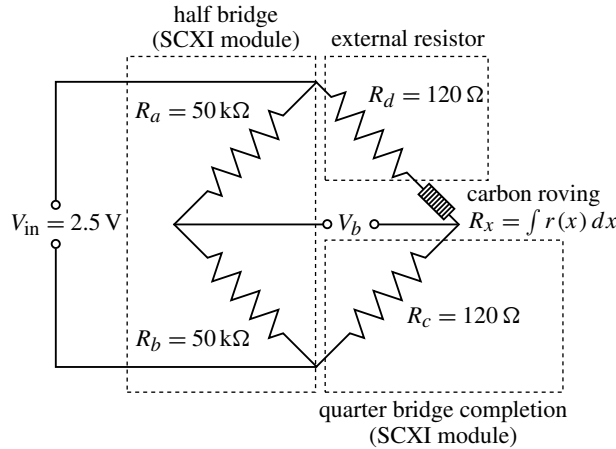


**Figure 3.** Wheatstone bridge circuit setup (generic setup); see also [Goldfeld et al. 2016a]. ( $R_x$  designate the resistance of the carbon roving,  $V_b$  is the measured voltage.)

where  $V_{in}$  is the excitation voltage,  $V_b$  is the signal voltage,  $\alpha = R_b / (R_a + R_b)$ , and  $R_a$ ,  $R_b$ ,  $R_c$  and  $R_d$  are known resistors.

In order to measure the resistance according to the above methodology, carbon rovings were connected to a National Instruments (NI) signal conditioning module (NI-SCXI-1521B) installed in a NI-SCXI-1000 chassis; see Figure 3. The data acquisition system (DAQ) is NI-USB-6361. Therefore, the resistance of the resistors of half of the bridge, which are an integrated part of the SCXI module, are  $R_a = R_b = 50 \text{ k}\Omega$ , the resistance of the resistor of the quarter bridge completion, which is also an integrated part of the module, is  $R_c = 120 \text{ }\Omega$ ; the external resistor is therefore determined to be  $R_d = 120 \text{ }\Omega$  (VISHAY PTF56120R00BZEK), and thus  $\alpha = 0.5$  and  $V_{in} = 2.5 \text{ V}$ . The DAQ system has 24 channels, which allows simultaneous measurement of all four rovings within the loaded beam as well as the one of the carbon roving within the reference beam (used for the temperature compensation, see Section 2.5).

Due to the resistance of the carbon roving  $R_x$ , which is approximately  $3.1 \text{ }\Omega$  before the loading process, the bridge is not balanced. The initial base value is therefore  $V_b = 20 \text{ mV}$ . In the presented configuration, the maximum change to  $V_b$  was measured as  $50 \text{ }\mu\text{V}$  corresponding to a change of  $9.6 \text{ m}\Omega$  in the resistance of the carbon roving.

**2.4. Loading and external monitoring.** The experimental investigation is based on the cyclic loading of TRC beam samples. The mechanical testing uses the cyclic testing scheme presented in [Goldfeld et al. 2016a] and extends the loading and the response to the damaged regime. As opposed to the previous work, which focused on the piezoresistive behavior of the carbon-based textile along the linear-elastic regime, the present study focuses on the essential capabilities of the carbon-based textile to sense structural damage in terms of a macroscopic crack. In order to compare, distinguish and characterize the electrostructural response before and after cracking, the structural response at the healthy state [Goldfeld et al. 2016a] is presented here as a reference.

The mechanical testing of the beam was conducted in a displacement control mode. The beam was tested under a four-points flexural bending scheme with span lengths of 70 mm and 210 mm between loading and supporting, respectively; see Figure 1. In order to examine the ability of the sensory carbon rovings to monitor damage, the first five loading cycles were conducted along the healthy state (see

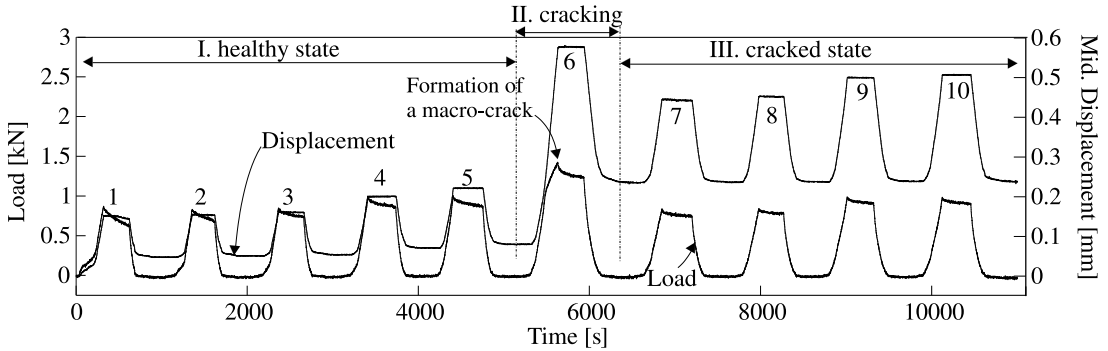


**Figure 4.** Ten load cycles of the TRC beam: load and displacement measured at the middle of the beam vs. time. The healthy state data is from [Goldfeld et al. 2016a].

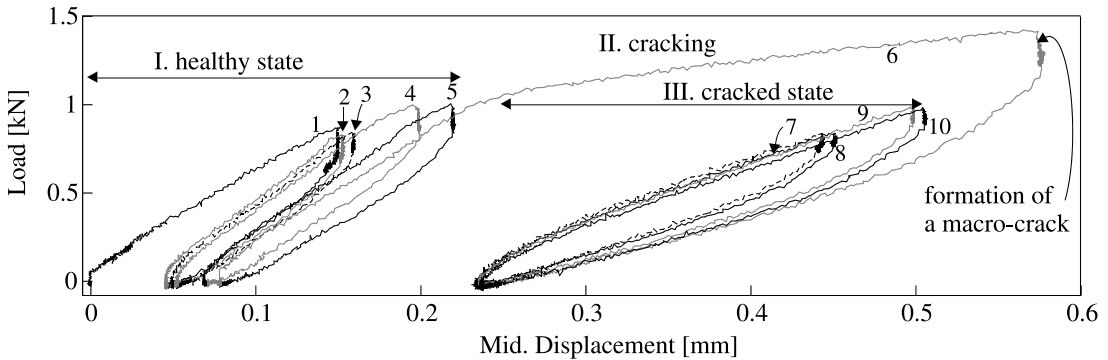


**Figure 5.** Load versus displacement (along the ten loading cycles). Healthy state data is from [Goldfeld et al. 2016a].

the discussion in [Goldfeld et al. 2016a]). Then, an additional loading cycle was conducted up to the formation of macrocracking, which was indicated by a drop in the measured load. Finally, four additional loading cycles were conducted at lower load levels. All loading cycles were conducted under a uniform loading, unloading and reloading rate of 0.1 mm/min.

The test setup also includes monitoring the load, the crosshead movement and the vertical displacement at the middle of the beam. The load and the displacement versus time curves appear in Figure 4, and the load versus prescribed displacement curves are shown in Figure 5. The loading pattern includes ten loading cycles. The load for cycles 1–3 was 0.85 kN, and the load for loading cycles 4–5 was 1 kN. Additional details of these first five loading cycles, which corresponded to a healthy state of the TRC beam, are given in [Goldfeld et al. 2016a]. The load level of the sixth loading cycle was determined by the formation of the macroscopic flexural crack, indicated by a drop in the measured load. It was observed at a load level of 1.25 kN; see Figures 4 and 5. After the experiment was terminated and the beam was removed from the loading machine, the width of the crack was measured to be about 0.25 mm.

Therefore, the first three loading cycles refer to load levels that are about 68% of the cracking load, and the next three loading cycles refer to load levels that are about 80% of the cracking load. Then, four additional loading cycles were applied. Two (loading cycles 7–8) at a load level of 68% of the cracking

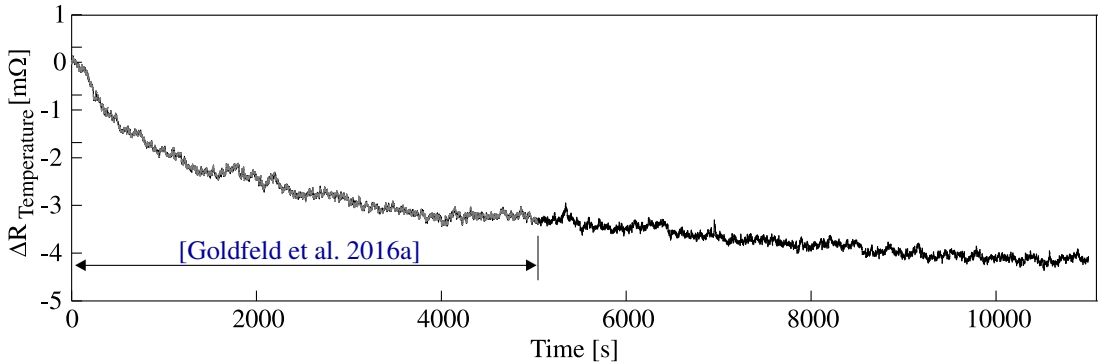


**Figure 6.** Resistance change of the sensory carbon roving embedded in the unloaded reference beam vs. time (up to  $t = 5200$  s; see [Goldfeld et al. 2016a]).

load and two (loading cycles 9–10) at a load level of 80% of the cracking load. These four loading cycles are the ones that will be attributed to the detection procedure.

Selecting the same mechanical pattern of loading-unloading-reloading at the healthy state and at the damaged state is motivated by several aspects. First, the phase of loading and then holding the displacement for 4–5 minutes, for related loading cycles, aims to examine the scenario of exposing the structure to a short term low load level, which is considered to be the monitoring load level for the damage identification procedure. The selected pattern is not intended to trigger and detect long term time dependent behavior, but it can shed light on the short term relaxation effects at the healthy and at the damaged regimes. This is relevant to the sustained loading period as well as to the period between one loading cycle, and another and it aims to simulate a real monitoring scenario. Second, it aims to compare the response at the healthy state and at the damaged state. Choosing the same pattern of loading cycles before and after damage enables the comparison of structural and electrical responses, therefore determining whether damage has occurred and to what extent. Third, it enables the correlation of the electrical response and the load-deflection response, and thus allowing the investigation of the repeatability of the electrical measure with respect to the structural health, and the possible evolution of irrecoverable processes at the damaged state.

**2.5. Temperature compensation.** Parallel to the effect of the mechanical-structural behavior, a change in temperature also triggers changes to the electrical resistance of the carbon rovings. It was reported that as the temperature increases, the resistance of the carbon fiber decreases [Xu et al. 2011; Wen et al. 1999; Crasto and Kim 1993; Yang et al. 2009]. Since the carbon rovings are exposed to a continuous electrical current, the temperature of the rovings increases, leading to resistance change. Therefore, temperature compensation should be performed in order to exclusively correlate the structural response and the measured resistance. In this study, the resistance change due to temperature is measured by a carbon roving embedded in a reference TRC beam (identical to the examined beam) which is not subjected to a mechanical load. Both beams (the loaded beam and the reference beam) were connected to the same DAQ system, and the voltage change in the reference beam was simultaneously measured along the entire process; see [Goldfeld et al. 2016a]. The electrical resistance change in the reference beam is given in Figure 6. It is solely attributed to the temperature effect, and it is subtracted from the response of

the beam subjected to the mechanical loading. Note that [Figure 6](#) extends the results given in [[Goldfeld et al. 2016a](#)] beyond the healthy state of the loaded beam (from about  $t = 5200$  s) to the damage state.

### 3. Results and discussion

**3.1. Structural response and temperature effect.** The structural behavior for all loading cycles (healthy and damaged) is presented in [Figures 4 and 5](#), and the effect of temperature on the electrical resistance is presented in [Figure 6](#). The residual displacement at the end of each load cycle and the relative stiffness, calculated by the change of the measured load per unit deflection and represented by the slope of the loading branches in [Figure 5](#), for each load cycle are summarized in [Table 2](#).

The first macroscopic visible flexural crack was detected at a load level of 1.25 kN at the sixth load cycle (indicated in [Figures 4 and 5](#)). It is reflected by a drop in the measured load and by a gradual residual deflection, as can be seen in [Figures 4 and 5](#) and [Table 2](#). A picture of the beam with its macroscopic crack (of about 0.25 mm width) is given in [Figure 7](#). The picture was taken after the experiment was terminated and the beam was removed from the loading machine. It should be noted that this is the only visible macrocrack that was detected. The lower strain gauge which appears in the figure, and used in [[Goldfeld et al. 2016a](#)], was broken due to the cracking. Immediately after detecting the formation of the crack, the displacement was held for 300 s. The next loading cycles mimic the loading cycles of the healthy state. Usually for structural health monitoring purposes, the load level used is much lower than the load level that actually causes the damage. In the present study, the load levels are the same as the ones applied at the healthy state, although it is relatively high for monitoring purposes. Choosing the same load level for the damaged and for the healthy states enables us to investigate and compare the structural and the electrical responses of the TRC beam, and therefore characterize the discrepancies in terms of damage sensing parameters.

Based on the load and displacement results, the structural response can be divided into three main states. The first one (cycles 1–5) corresponds to the generally linear-elastic state. It was thoroughly investigated in [[Goldfeld et al. 2016a](#)] and is considered here again to reference the structural and electrical response of the damaged state. The second state (sixth cycle) corresponds to the cracking load. The third state (cycles 7–10) corresponds to the cracked-damaged structural behavior of the beam. The three states are indicated in [Figures 4 and 5](#).

The structural response of the first state is characterized by a linear-elastic behavior with a negligible level of hysteresis. The load is slightly relaxed under the prescribed displacement and a small gradual residual deflection is accumulated after each load cycle (see also [Figure 5](#) and [Table 2](#)). This is an outcome of internal microstructural phenomena related to the interaction between the concrete mixture and the

	healthy state (I)					cracking	cracked state (III)			
loading cycle	1	2	3	4	5	6	7	8	9	10
residual displacement [mm]	0.046	0.049	0.052	0.069	0.079	0.234	0.234	0.237	0.237	0.237
relative stiffness [kN/m]	5531	7553	7316	6761	6373	6058	3627	3695	3491	3404

**Table 2.** Residual displacements and relative stiffness measured at the end of each loading cycle.



textile mesh [Bentur et al. 2010; Yardimci et al. 2011; Banholzer and Brameshuber 2004; Banholzer et al. 2006] and especially to the degradation and breakage of the outer filaments of the rovings.

Since the response of the first cycle of the healthy state is different from the next four cycles, and is mainly due to the initial part of the loading that is attributed to the settlement and the slight self-organization of the test setup [Goldfeld et al. 2016a], it is not considered in the following discussion.

The sixth loading cycle, the second state, defines the formation of multiple microcracks along the loading brunch. The loading phase of this cycle ends with a gradual load drop as a result of the widening of one (or several) of these microcracks (formation of a macrocrack), indicated in Figures 4 and 5. Due to that, the entire filament of the roving along the interface with the concrete matrix at the cracking zone breaks, which leads to irreversible gradual deflection and to lower stiffness. Once there was indication of formation of the macrocrack, the displacement was held for about 4–5 minutes and then unloaded.

After the formation of the macroscopic crack, the loading cycles of the third state (cycles 7–10) are characterized by a new linear-elastic state and the global response is governed by the macroscopic crack. The structural behavior is linear with almost no hysteresis, load relaxation or accumulation of additional gradual deflection. In spite of the relatively high levels of load after damage (68% and 80% of the cracking load), the four cycles at the damaged state reveal a repetitive pattern. It is reflected by the load-deflection curve (Figure 5) as well. This state is characterized by a lower and consistent slope of the loading brunches compared to the healthy state (Table 2), which corresponds to the new relative stiffness of the TRC beam. The reduced stiffness is an outcome of the presence of the macroscopic crack and its consistent pattern is related to the new linear state. These phenomena define quantitative indicators for the accumulation of mechanical damage in the beam. Furthermore, it enables one to distinguish between reversible microstructural phenomena to irreversible macroscopic ones, which is reflected by the electrical response of the new state. It also allows us to consider loading cycles 7–10 as the monitoring loading cycles (i.e., the cycles that are of interest), even though they were conducted at a relatively high load level with respect to the cracking load.

Another aspect that supports the consistent and repeatable structural response in the damaged state is the residual deflection after each cycle; see Table 2. After the sixth load cycle, the residual deflection measured at the middle of the beam increases from 0.079 mm (at the end of the first state) to 0.234 mm

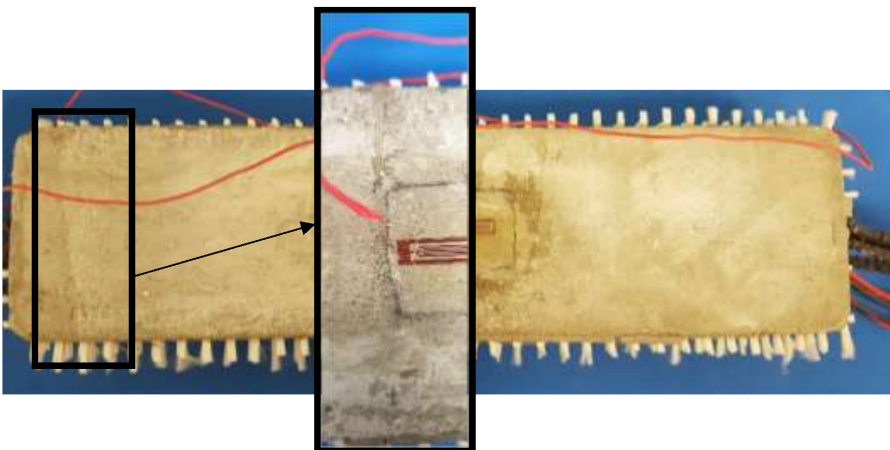


**Figure 7.** Picture of the cracked TRC beam.

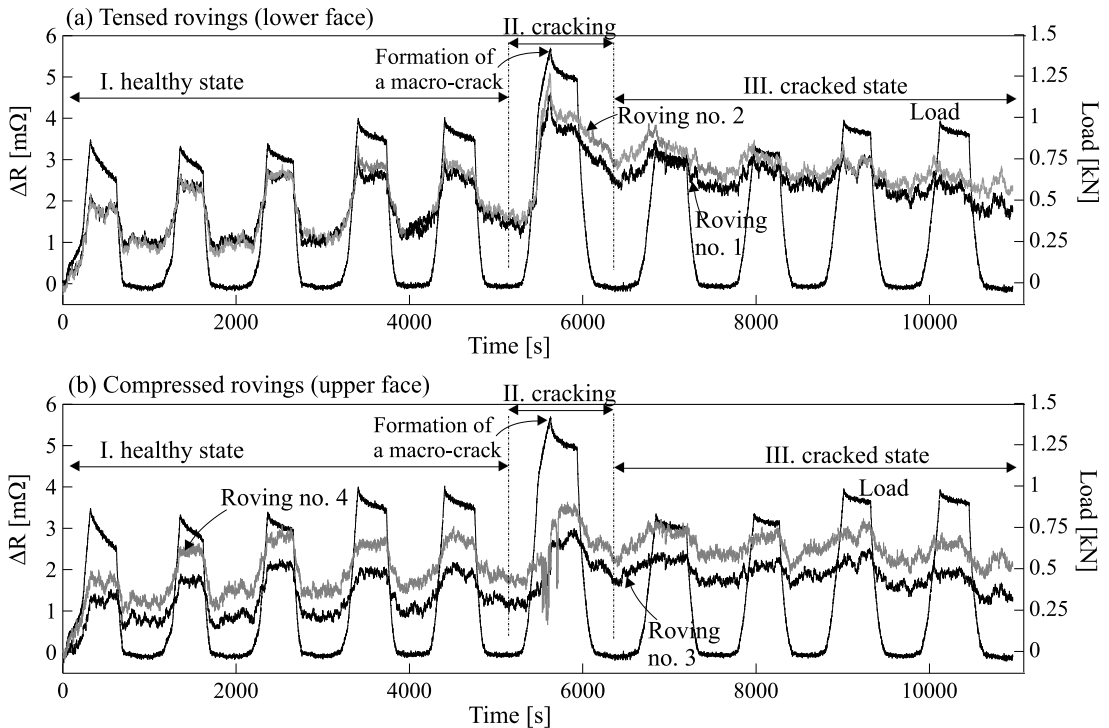


**Figure 8.** Resistance change (after temperature compensation) of the sensory carbon rovings of the loaded beam vs. time. Initial resistance  $R_0 = 3.1 \Omega$ . Healthy state data is from [Goldfeld et al. 2016a].

(after cracking). This value remains almost constant after each of the last four cycles. Before cracking, the mechanical behavior is characterized by the microstructural mechanism of the bonding between the textile and the concrete matrix. After cracking, the structural response is completely different and it is governed by the mechanism of the macroscopic crack. Any additional internal microstructural process, if occurred, has almost no effect on the global structural response. The macrostructural response at the damaged state is repeatable as reflected by the constant residual deflection after each loading cycle and is more consistent compared to the response at the healthy state. The gradual residual deflection and its consistent values can define another quantitative indicator for the accumulation of mechanical damage in the TRC beam.

**3.2. Sensing micro- and macrocracks.** In order to support the hypothesis of this study, the sensing capabilities of the carbon rovings is first demonstrated. The sensing methodology and the associated crack detection approach focus on the electrical response due to mechanical loading before and after a macrocrack has formed. The changes to the electrical resistance of the carbon rovings during all ten loading cycles are plotted versus time in Figure 8. The results were temperature compensated using the results outlined in Figure 6. The results for the two tensed rovings (1 and 2) are presented in Figure 8a and those for the two compressed rovings (3 and 4) are presented in Figure 8b.



The reference electrical resistance of the rovings before the loading process was approximately  $3.1 \Omega$ . The resistance change was measured with respect to this value. The averaged initial resistance values  $R_x^0$  for each load cycle (for the healthy state and for the damage state) are given in Table 3. It is taken as the average measured resistance along the unloaded phase before each loading cycle. Note that the actual electrical resistance along the roving is the reference resistance ( $3.1 \Omega$ ) plus the resistance given in Table 3.

The curves and the results outlined in Figure 8 and Table 3 highlight several observations regarding the sensing capabilities of the carbon rovings along both the healthy and the damage regimes:

- (1) It reveals a clear correlation between the electrical readings of the rovings (Figure 8) and the structural response of the beam (Figures 4 and 5). The sensory system is repeatable and characterized by a generally constant quality of the readings along all ten loading cycles. Even after the formation of the macroscopic crack, the electrical readings of the rovings still reflect a sound sensory capability.
- (2) It implies that along all loading cycles the correlation is relatively linear. In terms of its mathematical representation, only a shift of the reference values and a linear scaling are needed in order to correlate between the structural and the electrical response.
- (3) It reveals that the electrical response of the tensed and of the compressed rovings is generally repeatable along the entire loading process. It is observed that the readings of the two independent rovings located at the same height (rovings 1 and 2 in Figure 8a and rovings 3 and 4 in Figure 8b) are very similar. The constant difference between the compressed rovings was attributed to the initial loading phase of the first load cycle [Goldfeld et al. 2016a].
- (4) It reveals that the electrical resistance increases also when the rovings are compressed. This issue has been discussed in [Goldfeld et al. 2016a] for the linear-elastic state (state I). The negative correlation of the compressed rovings is consistent for the healthy and the cracked state. A dimensional change without a resistivity change would have caused  $R_x$  to decrease under compression. In contrast,  $R_x$  increases. The reason for the increase in resistance, and as a result, to the negative correlation, is attributed to changes to the specific resistivity  $\rho$  at the roving level rather than to dimensional changes. For strain sensing [Goldfeld et al. 2016a] it was assumed that since each carbon roving is comprised of a large number of filaments (about 50000), under compression, the fiber to fiber interface degrades as the bundle of fibers slightly separates. In addition, the inner fibers, which are not sufficiently supported by the cement matrix or by the fiber to fiber contact stresses, are expected to be mostly affected by the compressive stresses. The latter may increase the misalignment of the fibers, cause localized rotation and deviation from the roving's axis, and even cause localized buckling of the fibers. Therefore, it was assumed that all the above phenomena eventually yield an increase in the specific resistivity at the roving level. Regardless of the dimensional changes, these effects increase the overall electrical resistance, and yield an increase in resistance under compressive loading growth and to a negative correlation. The above hypothesis is also supported by the observation that the negative correlation is stable along the entire load cycle for all loading cycles (healthy and cracked states).
- (5) An interesting observation is related to the electrical resistance change at the moment when the macrocrack is formed. The structural response is characterized by a drop of the measured load and the electrical response is characterized by a rapid reduction with several oscillations of the resistance. It is observed at the tensed rovings and at the compressed rovings; see Figure 8.

The above observations clearly demonstrate the sensing capabilities of the carbon roving at the linear-elastic state of the beam, as well as at the damaged state of the beam, which is associated to the formation of cracking. The comparison between the electrical response of the carbon rovings before the formation of the cracks and their responses after the formation of the cracks reveals the following observations:

- (1) It is observed that in the cracked state the measured electrical resistance is relatively high compared to the healthy state. After the accumulation of the macroscopic crack at the sixth loading cycle, the measured electrical resistance increases significantly, and the increase is irreversible. It is mainly visible at the unloaded state at the beginning of each load cycle; see [Table 3](#). This observation is in good agreement with the structural responses due to the formation of the macroscopic crack and is correlated well to the irreversible residual deflection accumulated after the sixth loading cycle.
- (2) At the healthy state (state I), a slight irreversible increase of the resistance is observed at the unloaded phase at the beginning of each load cycle. It is influenced by the accumulation of internal microstructural cracks [[Goldfeld et al. 2016a](#)] and is correlated to the increase of the residual deflection after each load cycle. On the other hand, the electrical response of the cracked state (state III), which is characterized by a significant irreversible increase in the electrical resistance, is consistent and repeatable along the loading cycles. It is correlated to the gradual increase of the residual deflection after the formation of the macrocrack and its constant value along the unloaded phase of the next loading cycles. From the microstructural point of view, at the healthy state, the irreversible electrical response is correlated to the slight hysteretic behavior of the micromechanical response, which was attributed to internal mechanical phenomena during loading. At the cracked state, the mechanical response is governed by the presence of the macroscopic crack and no hysteresis or load relaxation is recorded (see [Figures 4 and 5](#)), which is ultimately reflected by the electrical response; see [Figure 8](#).
- (3) It is observed that the electrical resistance change due to loading is more pronounced at the healthy state. At the cracked state the correlation between the pattern of the structural response and the electrical measure is still valid, but the relative change of the resistance is much lower compared to the healthy state.

The above observations support the hypothesis of the current study that carbon rovings can sense macrostructural damage and can even distinguish between reversible and irreversible structural phenomena associated to micro- and macrocracks, respectively. This is mainly since the electrical signal is strongly affected by the microstructural mechanism of the carbon rovings within the concrete matrix. This study demonstrates these capabilities by assuming an ideal microstructural modeling of the roving within the concrete. Further investigation — which involves the effect of interfacial damage, its influence on the shear strength with respect to the fiber strength and with respect to the electrostructural response — in the context of the influence of the microscale effects on the macroscopic behavior reflected by the electrical setup define an interesting and relevant direction for additional exploration of the problem at hand.

The next section demonstrates this ability by quantitative crack identification parameters.

**3.3. Macrocrack detection.** The observations concluded from [Figure 8](#) and [Table 3](#) were used to determine macrocrack detection parameters. Two are related to the electrical resistance at the unloaded phase, and one is related to the relative change of the resistance and its pattern during the loading process.

**3.3.1. Macrocrack sensing by the electrical resistance at the unloaded phase.** It is clearly seen that at unloaded phases after cracking, the electrical resistance significantly increases, and this increase is

roving # ↓ load cycle →	healthy state (I)				cracking	cracked state (III)			
	2	3	4	5	6	7	8	9	10
1 (tensed)	1.007	1.069	1.294	1.313	1.448	2.557	2.315	2.422	2.124
2 (tensed)	0.923	0.982	1.239	1.462	1.636	3.040	2.658	2.663	2.426
3 (compressed)	0.760	0.872	0.995	1.066	1.210	1.871	1.728	1.867	1.576
4 (compressed)	1.215	1.505	1.612	1.712	1.786	2.428	2.353	2.497	2.217

**Table 3.** Initial electrical resistance change measured at the beginning of each load cycle [ $m\Omega$ ].

irreversible. Moreover, compared to the healthy state, this value is kept almost constant. Therefore, the study suggests to use the magnitude of the irreversible component of the electrical resistance as an indicator for the presence of macrocrack.

To correlate the electrical response to the structural response at the healthy state, it is noted that the internal microstructural phenomena lead to mechanical hysteresis of the load-deflection response (Figure 4) and to the accumulation of residual deflection after each load cycle (Figures 5 and 2). This effect is clearly reflected by the electrical response as slight increases of the resistance in the unloaded state after each load cycle is observed (Figure 8 and Table 2).

The formation of the macroscopic crack at the sixth loading cycle is indicated by a significant increase of the residual deflection and by a reduction of the relative stiffness. At the beginning of the sixth loading cycle, the residual deflection measured at the middle of the beam is 0.079 mm and the relative flexural stiffness of the beam (represented by the slope of the load deflection curve in Figure 5) is 6373 kN/m, whereas after the formation of the macrocrack the residual deflection increases to 0.234 mm and the relative flexural stiffness reduces to 3627 kN/m. This behavior is clearly reflected by the measured electrical resistance. The degradation of the structural health ultimately increases the measured electrical resistance. The average integrative electrical resistance of the four carbon rovings before the sixth loading cycle is 1.52  $m\Omega$ , whereas after this cycle the value increases to 2.47  $m\Omega$ .

In the literature, the characteristic behavior of the electrical resistance and the structural response of continuous carbon rovings was mainly reported and focused on the linear-elastic regime [Wen and Chung 1999; Wen et al. 2000; Goldfeld et al. 2016a]; the slight irreversibility that was observed in the resistance was correlated to internal microstructural phenomena. In the current study, it is seen that the formation of a macroscopic crack increases the electrical resistance significantly, and that this change is irreversible. Therefore, the resistance measured at an unloaded phase can be used as a crack indicator; it has the ability to distinguish between internal microstructural processes to external macrostructural events. In this case, initial information of the resistance of the healthy element at an unloaded phase is used as a reference value.

Without prior information of the healthy state, the resistance change at the unloaded phases from one loading cycle to another can be used by itself as a crack indicator. At the linear elastic state (cycles 1–5), the mechanical response during the loading cycles is governed by microstructural phenomena, leading to a slight increase in the measured residual deflection after each load cycle (the average increase is 14.6%; see Table 2). It is well reflected by the measured electrical resistance, which increases after each load cycle by about 20%; see Table 3. At the cracked state (cycles 7–10), the structural response is

governed by the macroscopic crack and the effect of microstructural behavior is diminished. This leads to a consistent structural response reflected by an almost constant residual deflection, and as a result, to a consistent electrical response. For the cracked state, the resistance measured at the unloaded phase between adjacent loading cycles is in the range from  $-13\%$  to  $8\%$ . Therefore, even without prior data of the resistance at a reference healthy state, the relative resistance change at an unloaded phase between two adjacent loading cycles can be used as a crack indicator. That is, a small reduction in the resistance along the unloaded phase between adjacent loading cycles can lead to the conclusion that the beam has macroscopically cracked.

The electrical resistance change has a strong correlation with the micromechanical behavior and the bonding mechanism of the carbon rovings and the concrete matrix. The micromechanical behavior along the loading cycles can be explained by the telescopic pull-out mechanism in a bundled reinforcement within brittle matrix [Bartos 1987; Zhu and Bartos 1997; Bentur et al. 2010; Yardimci et al. 2011]. It is assumed that the carbon rovings are not fully bonded to the concrete matrix, meaning that only the external sleeve filaments are well bonded to the concrete matrix while the inner core ones are largely free. Due to mechanical tension loading, the external filaments formed a sleeve in which the filaments are tightly bonded to the matrix and fail, while the inner core filaments, which are not well bonded, can engage in slip and provide the stiffness to the concrete. This process is irreversible and is reflected here by the integrative electrical resistance.

Before the macroscopic crack has been formed (state I in Figures 4, 5 and 8), a gradual bonding degradation between the concrete and the carbon rovings due to loading occurs, which is mainly influenced by the external sleeve filaments. This leads to a slight irreversible increase in the resistance after each load cycle. At the damaged state (state III in Figures 4, 5 and 8), due to the formation of the macroscopic crack, the external sleeve filaments are completely degraded and broken and only the core filaments are mechanically and electrically connected, which eventually leads to a considerable irreversible increase in the measured resistance.

**3.3.2. Macrocrack sensing by an electrical resistance change along loading cycle.** The resistance profile along the loading cycle can also be used as a damage indicator. Comparing the resistance change of a similar loading profile before and after macroscopic crack formation can be used to identify the structural health state. Such results are given in Figures 9 and 10 for four couples of similar loading cycles of healthy and damaged states and for the tensed and compressed rovings, respectively. The four couples of similar loading cycles are indicated in the Figures 9 and 10 (cycles 2 and 7 are presented in Figures 9a and 10a; cycles 3 and 8 are presented in Figures 9b and 10b; cycles 4 and 9 are presented in Figures 9c and 10c; cycles 5 and 10 are presented in Figures 9d and 10d). In order to consider each load cycle independently, the resistance change and the load profile along each load cycle are plotted; the starting values of the resistance are given in Table 3. The results in Figures 9 and 10 show that the electrical readings follow the structural response for the healthy and for the damaged states. It is clearly observed that the relative change of the resistance at the damaged state is much lower than the relative change of the resistance at the healthy state. The maximum values of the relative resistance change  $\Delta R/R_0$  for the eight loading cycles are given in Table 4. The maximum values of the resistance were evaluated by averaging the resistance measured along the loading phase. It is seen that for the same loading level, the relative resistance change of the healthy beam is more than three times higher than the relative resistance change

roving # ↓ load cycle →	healthy state (I)				cracked state (III)			
	2	3	4	5	7	8	9	10
1 (tensed)	0.0432	0.0497	0.0424	0.0410	0.0128	0.0152	0.0142	0.0054
2 (tensed)	0.0447	0.0532	0.0519	0.0421	0.0085	0.0115	0.0072	0.0048
3 (compressed)	0.0313	0.0393	0.0302	0.0285	0.0124	0.0123	0.0121	0.0100
4 (compressed)	0.0395	0.0408	0.0324	0.0328	0.0158	0.0143	0.0124	0.0118

**Table 4.** Maximum relative electrical resistance change  $\Delta R/R_0$ .

of the damaged beam. The low relative change in resistance after damage is mainly due to the high initial resistance at the beginning of each load cycle, which has been increased considerably due to macrocrack; see Figure 8 and Table 3. Therefore, it can be concluded that comparing the resistance change of similar loading profiles before and after cracking can be used as an indicator of macrocrack accumulation.

Here again, the electrical resistance can be directly correlated to the micromechanical behavior and the bonding mechanism of the carbon rovings and the concrete matrix. The telescopic pull-out mechanism, discussed in the previous section, is well reflected by the integrative resistance change. At the healthy state, the gradual bonding degradation of the sleeve filaments leads to the slight irreversible increase in the resistance after each load cycle and to a relatively high resistance change due to loading. At the damaged state, the external sleeve filaments are completely degraded and broken and only the core filaments, which comprises 20% of the total filaments [Bentur et al. 2010; Yardimci et al. 2011], are mechanically and electrically connected. The effect of the matrix penetration on the number of broken filaments in multifilament fiber composites has been investigated in [Yardimci et al. 2012]. This phenomenon ultimately leads to a considerable increase in the measured resistance, and as a result, the relatively small change of the resistance during loading.

#### 4. Summary and conclusions

This paper has taken a step towards exploring the concept of using carbon/glass fiber based textile reinforcement for self-sensory TRC structural elements. Specifically, it has looked into the sensing capabilities of the carbon rovings to detect damage, which in the case of TRC structures is defined as the formation of macrocracking. It was found that the sensory textile can make a clear distinction between internal microstructural phenomena to external macroscopic structural ones. The micromechanism of the roving within the concrete matrix governed by the macrostructural response of the TRC element, which is ultimately reflected by the electrical readings.

The study offered three qualitative crack detection parameters that distinguish between the healthy state and after the formation of a macrocrack. The parameters are based on the characteristic behavior of the reversibility of the electrical response with respect to the structural behavior. It was found that at the linear-elastic regime, the slight mechanical degradation leads to a slight electronically irrecoverable response. At the damaged state, on the other hand, once the electrical resistance irreversibly increases after the formation of the macrocrack, it remains repeatable and stable. However, the relative change of the electrical resistance during the loading cycles at the cracked state is much lower than that of the

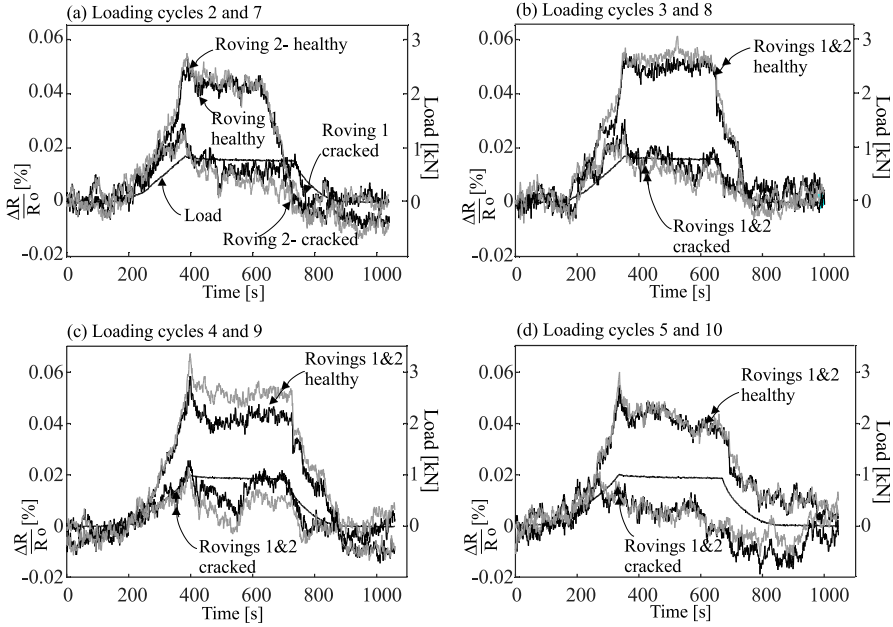


**Figure 9.** Resistance of the tensed carbon rovings vs. time for each loading cycle: (a) loading cycles 2 and 7; (b) loading cycles 3 and 8; (c) loading cycles 4 and 9; (d) loading cycles 5 and 10.

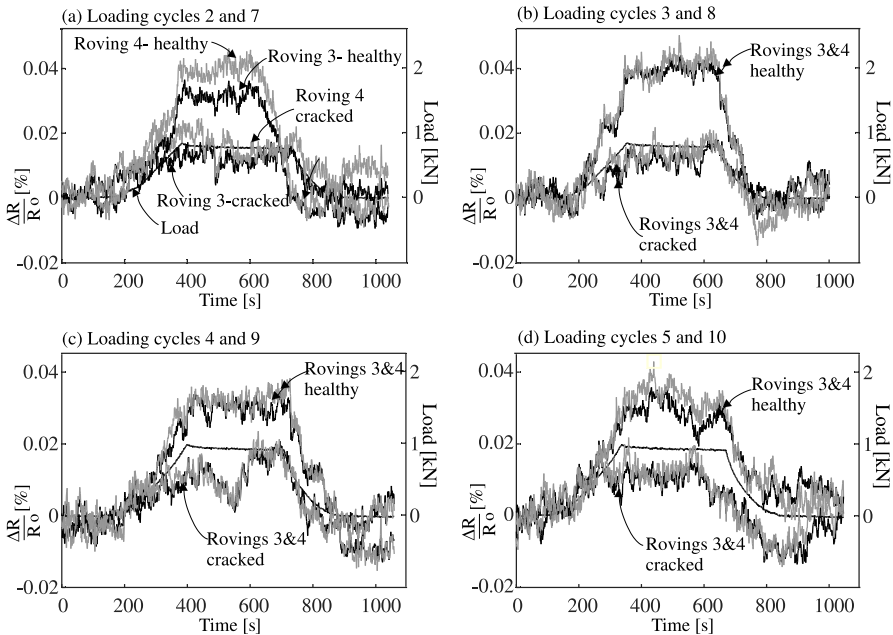


**Figure 10.** Resistance of the compressed carbon rovings vs. time for each loading cycle: (a) loading cycles 2 and 7; (b) loading cycles 3 and 8; (c) loading cycles 4 and 9; (d) loading cycles 5 and 10.



healthy state. It is mainly due to significant reduction in the number of filaments within the roving that continues to carry on the loading as well as to pass electrical current.

The findings of this study and the above conclusions validate the idea that the carbon/glass fiber textile can be used as reinforcement and as a damaged sensory device at the same time. The present study has focused on the ability of the textile to sense macrocracks during cyclic structural response in a TRC structural element and to distinguish between healthy to damaged state. The experimental demonstration of this aspect has taken us one step further towards the development of smart TRC structures.

### Acknowledgements

The authors are grateful for the help of Barak Ofir, Elhanan Yitzhak, and the technical and administrative staff of the National Building Research Institute at the Technion.

### References

- [Angelidis et al. 2004] N. Angelidis, C. Y. Wei, and P. E. Irving, “The electrical resistance response of continuous carbon fibre composite laminates to mechanical strain”, *Compos. A Appl. Sci. Manuf.* **35**:10 (2004), 1135–1147.
- [Antunes et al. 2011] P. Antunes, H. Lima, N. Alberto, L. Bilro, P. Pinto, A. Costa, H. Rodrigues, J. L. Pinto, R. Nogueira, H. Varum, and P. S. André, “Optical sensors based on fiber Bragg gratings for structural health monitoring”, pp. 253–295 in *New developments in sensing technology for structural health monitoring*, edited by S. C. Mukhopadhyay, Lecture Notes in Electrical Engineering **96**, Springer, Berlin, 2011.
- [Banholzer and Brameshuber 2004] B. Banholzer and W. Brameshuber, “Tailoring of AR-glass filament/cement based matrix-bond: analytical and experimental techniques”, pp. 1443–1452 in *Sixth RILEM Symposium on Fibre-Reinforced Concretes (BEFIB)* (Varenna, Italy, 2004), edited by M. di Prisco et al., RILEM Proceedings **Pro 039**, RILEM Publ., Bagneux, France, 2004.
- [Banholzer et al. 2006] B. Banholzer, T. Brockmann, and W. Brameshuber, “Material and bonding characteristics for dimensioning and modelling of textile reinforced concrete (TRC) elements”, *Mater. Struct.* **39** (2006), 749–763.
- [Bartos 1987] P. Bartos, “Brittle-matrix composites reinforced with bundles of fibres”, pp. 539–546 in *From materials science to construction materials engineering, II: Combining materials: design, production and properties* (Versailles, 1987), edited by J. C. Maso, Chapman and Hall, London, 1987.
- [Bentur et al. 2010] A. Bentur, R. Tirosh, M. Yardimci, M. Puterman, and A. Peled, “Controlling bond characteristics by impregnation”, pp. 23–33 in *Textile reinforced concrete (2nd ICTRC)* (Aachen, 2010), edited by W. Brameshuber, RILEM Proceedings **Pro 075**, RILEM Publ., Bagneux, France, 2010.
- [Bontea et al. 2000] D.-M. Bontea, D. D. L. Chung, and G. C. Lee, “Damage in carbon fiber reinforced concrete, monitored by electrical resistance measurement”, *Cem. Concr. Res.* **30**:4 (2000), 651–659.
- [Chen and Chung 1993] P.-W. Chen and D. D. L. Chung, “Carbon fiber reinforced concrete as an electrical contact material for smart structures”, *Smart Mater. Struct.* **2**:3 (1993), 181–188.
- [Christner et al. 2012] C. Christner, A. Horoschenkoff, and H. Rapp, “Longitudinal and transverse strain sensitivity of embedded carbon fibre sensors”, *J. Compos. Mater.* **47**:2 (2012), 155–167.
- [Chung 2007] D. D. L. Chung, “Damage detection using self-sensing concepts”, *Proc. Inst. Mech. Eng. G, J. Aerosp. Eng.* **221**:4 (2007), 509–520.
- [Craeto and Kim 1993] A. S. Craeto and R. Y. Kim, “Using carbon fiber piezoresistivity to measure residual stresses in composites”, pp. 162–173 in *Composite materials, mechanics, and processing* (Cleveland, 1993), Proceedings of the American Society for Composites Technical Conference **8**, Technomic, Lancaster, PA, 1993.
- [Ding et al. 2013] Y. Ding, Z. Chen, Z. Han, Y. Zhang, and F. Pacheco-Torgal, “Nano-carbon black and carbon fiber as conductive materials for the diagnosing of the damage of concrete beam”, *Constr. Build. Mater.* **43** (2013), 233–241.



- [Goldfeld and Klar 2013] Y. Goldfeld and A. Klar, “Damage identification in reinforced concrete beams using spatially distributed strain measurements”, *J. Struct. Eng. (ASCE)* **139**:12 (2013), art. id. 04013013.
- [Goldfeld et al. 2016a] Y. Goldfeld, S. Ben-Aarosh, O. Rabinovitch, T. Quadflieg, and T. Gries, “Integrated self-monitoring of carbon based textile reinforced concrete beams under repeated loading in the un-cracked region”, *Carbon* **98** (2016), 238–249.
- [Goldfeld et al. 2016b] Y. Goldfeld, O. Rabinovitch, B. Fishbain, T. Quadflieg, and T. Gries, “Sensory carbon fiber based textile-reinforced concrete for smart structures”, *J. Intell. Mater. Syst. Struct.* **27**:4 (2016), 469–489.
- [Horoschenkoff and Christner 2012] A. Horoschenkoff and C. Christner, “Carbon fibre sensor: theory and application”, pp. 357–376 in *Composites and their applications*, edited by N. Hu, InTech, Rijeka, Croatia, 2012.
- [Khotiaintsev et al. 2013] S. Khotiaintsev, A. Beltrán-Hernández, J. González-Tinoco, H. Guzmán-Olguín, and G. Aguilar-Ramos, “Structural health monitoring of concrete elements with embedded arrays of optical fibers”, art. id. 869513 in *Health monitoring of structural and biological systems* (San Diego, 2013), edited by T. Kundu, Proceedings of SPIE **8695**, SPIE, Bellingham, WA, 2013.
- [Klar et al. 2010] A. Klar, Y. Goldfeld, and Z. Charas, “Measures for identifying cracks within reinforced concrete beams using BOTDR”, art. id. 764721 in *Sensors and smart structures technologies for civil, mechanical, and aerospace systems* (San Diego, 2010), edited by M. Tomizuka, Proceedings of SPIE **7647**, SPIE, Bellingham, WA, 2010.
- [Krebber et al. 2012] K. Krebber, P. Lenke, S. Liehr, N. Nöther, M. Wendt, A. Wosniok, and W. Daum, “Structural health monitoring by distributed fiber optic sensors embedded into technical textiles”, *Tech. Messen* **79**:7-8 (2012), 337–347.
- [Lee 2003] B. Lee, “Review of the present status of optical fiber sensors”, *Opt. Fiber Tech.* **9**:2 (2003), 57–79.
- [Li et al. 2004] H.-N. Li, D.-S. Li, and G.-B. Song, “Recent applications of fiber optic sensors to health monitoring in civil engineering”, *Eng. Struct.* **26**:11 (2004), 1647–1657.
- [Majumder et al. 2008] M. Majumder, T. K. Gangopadhyay, A. K. Chakraborty, K. Dasgupta, and D. Bhattacharya, “Fibre Bragg gratings in structural health monitoring: present status and applications”, *Sens. Actuators A Phys.* **147**:1 (2008), 150–164.
- [McCarter et al. 2007] W. J. McCarter, G. Starrs, T. M. Chrisp, and P. F. G. Banfill, “Activation energy and conduction in carbon fibre reinforced cement matrices”, *J. Mater. Sci.* **42**:6 (2007), 2200–2203.
- [Meehan et al. 2010] D. G. Meehan, S. Wang, and D. D. L. Chung, “Electrical-resistance-based sensing of impact damage in carbon fiber reinforced cement-based materials”, *J. Intell. Mater. Syst. Struct.* **21**:1 (2010), 83–105.
- [Mobasher et al. 2014] B. Mobasher, V. Dey, Z. Cohen, and A. Peled, “Correlation of constitutive response of hybrid textile reinforced concrete from tensile and flexural tests”, *Cem. Concr. Compos.* **53** (2014), 148–161.
- [Montanini et al. 2012] R. Montanini, F. De Domenico, F. Freni, N. Maugeri, and A. Recupero, “Structural health monitoring of reinforced concrete beams by means of embedded fiber Bragg grating sensors”, art. id. 8421AW in *22nd International Conference on Optical Fiber Sensors (OFS2012)* (Beijing, 2012), edited by Y. Liao et al., Proceedings of SPIE **8421**, SPIE, Bellingham, WA, 2012.
- [Peled et al. 2001] A. Peled, J. M. Torrents, T. O. Mason, S. P. Shah, and E. J. Garboczi, “Electrical impedance spectra to monitor damage during tensile loading of cement composites”, *ACI Mater. J.* **98**:4 (2001), 313–322.
- [Quadflieg et al. 2016] T. Quadflieg, O. Stolyarov, and T. Gries, “Carbon rovings as strain sensors for structural health monitoring of engineering materials and structures”, *J. Strain Anal. Eng. Des.* **51**:7 (2016), 482–492.
- [Reza et al. 2003] F. Reza, G. B. Batson, J. A. Yamamuro, and J. S. Lee, “Resistance changes during compression of carbon fiber cement composites”, *J. Mater. Civ. Eng. (ASCE)* **15**:5 (2003), 476–483.
- [Shams et al. 2014] A. Shams, M. Horstmann, and J. Hegger, “Experimental investigations on textile-reinforced concrete (TRC) sandwich sections”, *Compos. Struct.* **118** (2014), 643–653.
- [Silva et al. 2011] F. D. A. Silva, M. Butler, V. Mechtcherine, D. Zhu, and B. Mobasher, “Strain rate effect on the tensile behaviour of textile-reinforced concrete under static and dynamic loading”, *Mater. Sci. Eng. A* **528**:3 (2011), 1727–1734.
- [Stolyarov et al. 2015a] O. Stolyarov, T. Quadflieg, and T. Gries, “Effects of fabric structures on the tensile properties of warp-knitted fabrics used as concrete reinforcements”, *Textile Res. J.* **85**:18 (2015), 1934–1945.
- [Stolyarov et al. 2015b] O. Stolyarov, T. Quadflieg, and T. Gries, “A study of warp-knitted fabric structure parameters affecting the mechanical properties of textile-reinforced concrete”, art. id. 3111–2 in *Proceedings of the 20th International Conference on Composite Materials* (Copenhagen, 2015), International Committee on Composite Materials, 2015.

- [Teomete 2015] E. Teomete, “Measurement of crack length sensitivity and strain gage factor of carbon fiber reinforced cement matrix composites”, *Measurement* **74** (2015), 21–30.
- [Todoroki and Yoshida 2004] A. Todoroki and J. Yoshida, “Electrical resistance change of unidirectional CFRP due to applied load”, *JSME Int. J. A Mech. M.* **47**:3 (2004), 357–364.
- [Vaidya and Allouche 2011] S. Vaidya and E. N. Allouche, “Strain sensing of carbon fiber reinforced geopolymer concrete”, *Mater. Struct.* **44**:8 (2011), 1467–1475.
- [Wang and Chung 1996] X. Wang and D. D. L. Chung, “Continuous carbon fibre epoxy-matrix composite as a sensor of its own strain”, *Smart Mater. Struct.* **5**:6 (1996), 796–800.
- [Wang and Chung 2006] S. Wang and D. D. L. Chung, “Self-sensing of flexural strain and damage in carbon fiber polymer-matrix composite by electrical resistance measurement”, *Carbon* **44**:13 (2006), 2739–2751.
- [Wen and Chung 1999] S. Wen and D. D. L. Chung, “Piezoresistivity in continuous carbon fiber cement-matrix composite”, *Cem. Concr. Res.* **29**:3 (1999), 445–449.
- [Wen and Chung 2007] S. Wen and D. D. L. Chung, “Electrical-resistance-based damage self-sensing in carbon fiber reinforced cement”, *Carbon* **45**:4 (2007), 710–716.
- [Wen et al. 1999] S. Wen, S. Wang, and D. D. L. Chung, “Carbon fiber structural composites as thermistors”, *Sens. Actuators A Phys.* **78**:2-3 (1999), 180–188.
- [Wen et al. 2000] S. Wen, S. Wang, and D. D. L. Chung, “Piezoresistivity in continuous carbon fiber polymer-matrix and cement-matrix composites”, *J. Mater. Sci.* **35**:14 (2000), 3669–3675.
- [Xu et al. 2011] S. L. Xu, W. T. Yu, and S. D. Song, “Numerical simulation and experimental study on electrothermal properties of carbon/glass fiber hybrid textile reinforced concrete”, *Sci. China Tech. Sci.* **54** (2011), 2421–2428.
- [Yang et al. 2009] C. Yang, Z. Wu, and H. Huang, “Development of carbon fiber-based piezoresistive linear sensing technique”, art. id. 72930T in *Smart sensor phenomena, technology, networks, and systems* (San Diego, 2009), edited by N. G. Meyendorf et al., Proceedings of SPIE **7293**, SPIE, Bellingham, WA, 2009.
- [Yao et al. 2003] W. Yao, B. Chen, and K. Wu, “Smart behavior of carbon fiber reinforced cement-based composite”, *Mater. Sci. Technol.* **19**:3 (2003), 239–242.
- [Yardimci et al. 2011] M. Y. Yardimci, R. Tirosh, P. Larianovsky, M. Puterman, and R. Bentur, “Improving the bond characteristics of AR-glass strands by microstructure modification technique”, *Cem. Concr. Compos.* **33**:1 (2011), 124–130.
- [Yardimci et al. 2012] M. Y. Yardimci, B.-G. Kang, and W. Brameshuber, “Quantitative measurement of filament ruptures of a multi-filament AR-glass yarn embedded in concrete”, *Mater. Struct.* **45**:4 (2012), 599–607.
- [Zhu and Bartos 1997] W. Zhu and P. J. M. Bartos, “Assessment of interfacial microstructure and bond properties in aged GRC using a novel microindentation method”, *Cem. Concr. Res.* **27**:11 (1997), 1701–1711.

Received 3 Sep 2016. Revised 23 May 2017. Accepted 23 May 2017.

YISKA GOLDFELD: [yiska@technion.ac.il](mailto:yiska@technion.ac.il)

Department of Civil and Environmental Engineering, Technion, Israel Institute of Technology, Haifa, Israel

TILL QUADFLIEG: [till.quadflieg@ita.rwth-aachen.de](mailto:till.quadflieg@ita.rwth-aachen.de)

Institut fuer Textiltechnik, RWTH Aachen University, Aachen, Germany

STAV BEN-AAROSH: [stavba@tx.technion.ac.il](mailto:stavba@tx.technion.ac.il)

Department of Civil and Environmental Engineering, Technion, Israel Institute of Technology, Haifa, Israel

THOMAS GRIES: [thomas.gries@ita.rwth-aachen.de](mailto:thomas.gries@ita.rwth-aachen.de)

Institut fuer Textiltechnik, RWTH Aachen University, Aachen, Germany



## STATIC ANALYSIS OF NANOBEAMS USING RAYLEIGH–RITZ METHOD

LAXMI BEHERA AND S. CHAKRAVERTY

Boundary characteristic orthogonal polynomials have been used as shape functions in the Rayleigh–Ritz method for static analysis of nanobeams. The formulation is based on Euler–Bernoulli and Timoshenko beam theories in conjunction with nonlocal elasticity theory of Eringen. Application of Rayleigh–Ritz method converts the problem into a system of linear equations. Some of the parametric studies have been carried out. The novelty of the method is that it can handle any set of classical boundary conditions (viz., clamped, simply supported and free) with ease. Although the assumed shape functions need to satisfy the geometric boundary condition only, the final solution is for the targeted boundary condition of the problem or domain. Deflection and rotation shapes for some of the boundary conditions have also been illustrated.

### 1. Introduction

Nanosized structures such as nanobeams, nanoplates and nanoshells are commonly used as components in nanoelectromechanical systems (NEMS) devices. The most distinct characteristic of nanostructures is that their mechanical properties are size dependent [Ansari et al. 2013; Miller and Shenoy 2000; Xu et al. 2010]. Fundamental knowledge of their mechanical behavior is needed for proper design and application of nanostructured materials; however, conducting experiments at nanoscale size is quite difficult. In this regard, size dependent continuum theories came into existence. Among these theories, nonlocal elasticity theory, pioneered by Eringen [1972], has received much attention in modeling small sized structures. According to this theory, the stress at a specific point depends on the strain tensors of the entire body. As such, the nonlocal stress tensor  $\sigma$  at a point  $x$  is expressed as [Reddy 2007]

$$\sigma = \int_V K(|x' - x|, \tau) t(x') dx',$$

where  $V$  is the volume occupied by the elastic body,  $\tau$  the material constant which depends on both internal length (lattice spacing) and external characteristic length (wavelength) and  $K(|x' - x|, \tau)$  denotes the nonlocal modulus. Also,  $|x' - x|$  is the Euclidean distance and  $t(x)$  is the classical macroscopic stress tensor at a point  $x$  and is related to strain  $\varepsilon(x)$  by Hooke's law:

$$t(x) = C(x) : \varepsilon(x),$$

where  $C$  is the fourth-order elasticity tensor.

Since it is difficult to solve the integral constitutive relation, an equivalent differential form was proposed [Reddy 2007],

$$(1 - \tau^2 L^2 \nabla^2) \sigma = t, \quad \tau = e_0 a / L,$$

*Keywords:* Rayleigh–Ritz method, boundary characteristic orthogonal polynomial, nonlocal elasticity theory.

where  $e_0$  is material constant,  $a$  the internal characteristic length and  $L$  the external characteristic length.

Nonlocal effects considered in the nonlocal elasticity theory play an important role in the analysis and is determined by the magnitude of nonlocal parameter  $e_0a$ . The parameter  $e_0a$  is the scale coefficient that incorporates the small scale [Wang et al. 2006]. When the nonlocal parameter is zero, we obtain the constitutive relations of the local theories. Since classical continuum theories do not consider size effects arising from the small scale, so application of classical continuum theory is not appropriate for the nanostructures. In this regard, nonlocal elasticity theory has been widely used in the analysis of nanostructures.

Researchers have applied nonlocal elasticity theory in buckling [Wang et al. 2006; Mohammadi and Ghannadpour 2010] and vibration [Peddieson et al. 2003; Xu 2006] analyses of beams. Few authors have also applied nonlocal elasticity theory in bending analysis of beams. Some of them have been cited below.

Reddy and Pang [2008] presented analytical solutions for bending analysis of beams subjected to four sets of boundary conditions. Aydogdu [2009] developed a general nonlocal beam theory to derive governing equations from which all the well-known beam theories may be obtained. A nonlocal shear deformation beam theory has been proposed by Thai [2012]. Analytical solutions have also been presented for nonlocal sinusoidal shear deformation beam theory [Thai and Vo 2012]. Şimşek and Yurtcu [2013] examined bending and buckling of functionally graded (FG) nanobeams. Bending solutions have been presented analytically by Wang et al. [2008] for nanobeams. Some of the numerical methods such as the Ritz [Ghannadpour et al. 2013], the differential quadrature [Civalek and Demir 2011] and the finite element method [Alshorbagy et al. 2013; Eltaher et al. 2013] have also been developed for the bending analysis of nanobeams. Civalek and Akgöz [Civalek et al. 2009] presented deflection shapes and bending moments for nonlocal Euler–Bernoulli beams subjected to different boundary conditions.

The literature reveals that few works have been done on bending analysis of nanobeams based on Euler–Bernoulli and Timoshenko beam theories. It is also revealed that few numerical methods have also been developed for the above mentioned problem. In this article, authors have implemented Rayleigh–Ritz method with orthogonal polynomials as basis functions. The novelty of the method is that it may handle any set of boundary conditions with ease. Though this method has been used in classical beams and plates [Civalek et al. 2009; Behera and Chakraverty 2014; Bhat 1985; 1991; Chakraverty et al. 1999; 2007; Chakraverty and Petyt 1997; Singh and Chakraverty 1994; Hu et al. 2004], no works have been done in bending analysis of nanobeams. Boundary characteristic orthogonal polynomials have been applied in the Rayleigh–Ritz method to analyze effects of nonlocal, boundary condition and slenderness ratio on the deflection. Nondimensional deflection and rotation shapes have also been shown for three sets of boundary conditions.

## 2. Problem formulation

The study is carried out on the basis of Euler–Bernoulli and Timoshenko beam theories in conjunction with nonlocal elasticity theory of Eringen.

A straight uniform beam with the length  $L$  and a rectangular cross-section of thickness  $h$  is considered, as shown in Figure 1. A Cartesian coordinate system  $(x, y, z)$  is fixed on the central axis of the beam, where  $x$ ,  $y$  and  $z$  coordinates are taken along the length, width and thickness of the beams [Ansari et al. 2013]. The Rayleigh–Ritz method has been employed for bending analysis. To apply the present method,

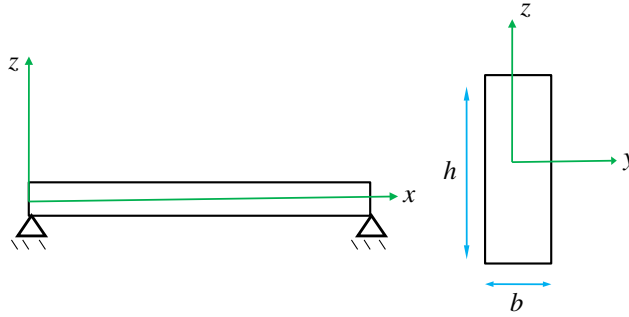


**Figure 1.** Uniform beam with rectangular cross section and its coordinate system [Ansari et al. 2013].

we have given a summary of the energies of the structures based on Euler–Bernoulli and Timoshenko beam theories.

**2.1. Euler–Bernoulli beam theory (EBT).** The strain energy  $u_s$  may be written as [Wang et al. 2000]

$$u_s = \frac{1}{2} \int_0^L \int_A \sigma_{xx} \varepsilon_{xx} \, dA \, dx, \tag{1}$$

where  $L$  is the length of nanobeam,  $A$  is the cross sectional area,  $\sigma_{xx}$  is the axial stress and  $\varepsilon_{xx}$  is the normal strain.

Normal strain  $\varepsilon_{xx}$  is given by the relation

$$\varepsilon_{xx} = -z \frac{d^2 w}{dx^2}, \tag{2}$$

where  $w$  is the transverse deflection at the point  $(x, 0)$  on the midplane of the beam.

Substituting (2) into (1), we get

$$u_s = -\frac{1}{2} \int_0^L M \frac{d^2 w}{dx^2} \, dx, \tag{3}$$

where  $M$  is the bending moment and is defined as

$$M = \int_A z \sigma_{xx} \, dA. \tag{4}$$

Assuming that the beam is subjected to a transverse load  $q(x)$ , the potential energy  $u_p$  may be given as [Wang et al. 2000]

$$u_p = -\frac{1}{2} \int_0^L q w \, dx. \tag{5}$$

Applying the principle of virtual displacement, we may obtain the following governing equation:

$$\frac{d^2 M}{dx^2} + q = 0. \tag{6}$$

According to Eringen's nonlocal elasticity theory, the moment-curvature relation has the following form:

$$M - (e_0a)^2 \frac{d^2M}{dx^2} = -EI \frac{d^2w}{dx^2}, \quad (7)$$

where  $a$  is the internal characteristic length (e.g., lattice parameter, C-C bond length and granular distance) and  $e_0$  is a constant appropriate to each material. The magnitude of  $e_0$  is determined experimentally or approximated by matching the dispersion curves of plane waves with those of atomic lattice dynamics. Here  $e_0a$  is the scale coefficient that incorporates the small scale effect [Wang et al. 2007]. Also  $E$  is the Young's modulus and  $I$  the second moment of area.

Using (6) and (7),  $M$  may be obtained as

$$M = -EI \frac{d^2w}{dx^2} - \mu q, \quad (8)$$

where  $\mu = (e_0a)^2$  is the nonlocal parameter.

Combining (3) and (5), the total potential energy of the system may be written as

$$U = \frac{1}{2} \int_0^L \left( EI \left( \frac{d^2w}{dx^2} \right)^2 + \mu q \frac{d^2w}{dx^2} - qw \right) dx. \quad (9)$$

**2.2. Timoshenko beam theory.** Based on Timoshenko beam theory, the strain energy  $u_s$  may be given as [Ansari et al. 2013]

$$u_s = \frac{1}{2} \int_0^L \int_A (\sigma_{xx} \varepsilon_{xx} + \sigma_{xz} \gamma_{xz}) dA dx, \quad (10)$$

where  $\sigma_{xx}$  is the normal stress,  $\sigma_{xz}$  is the transverse shear stress,  $L$  is the length of the beam and  $A$  is the cross sectional area of the beam.

In (10),  $\varepsilon_{xx}$  and  $\gamma_{xz}$  are the normal and transverse shear strains respectively and are given by

$$\varepsilon_{xx} = z \frac{d\phi}{dx}, \quad (11)$$

$$\gamma_{xz} = \phi + \frac{dw}{dx}, \quad (12)$$

where  $\phi$  is the rotation due to bending and  $w$  the transverse displacement.

Substituting (11) and (12) into (10), one may obtain

$$u_s = \frac{1}{2} \int_0^L \left( M \frac{d\phi}{dx} + Q \left( \phi + \frac{dw}{dx} \right) \right) dx, \quad (13)$$

where  $M$  and  $Q$  are the bending moment and shear force respectively and are defined as

$$M = \int_A \sigma_{xx} z dA, \quad Q = \int_A \sigma_{xz} dA.$$

The potential energy of the transverse load  $u_p$  may be described as [Ansari et al. 2013]

$$u_p = -\frac{1}{2} \int_0^L qw dx. \quad (14)$$



Based on nonlocal elasticity theory, nonlocal constitutive equations are as follows:

$$M - (e_0a)^2 \frac{d^2 M}{dx^2} = EI \frac{d\phi}{dx} \tag{15}$$

$$Q = k_s GA \left( \phi + \frac{dw}{dx} \right), \tag{16}$$

where  $I$  is the second moment of area,  $E$  is the Young’s modulus,  $G$  is the shear modulus and  $k_s$  is the shear correction factor in the Timoshenko beam theory to compensate the for error in assuming a constant shear strain (stress) through the thickness of the beam.

Applying the principle of virtual displacement, one may obtain the following governing equations for bending analysis:

$$\frac{dM}{dx} = Q, \tag{17}$$

$$\frac{dQ}{dx} = -q. \tag{18}$$

Using (15)–(18), bending moment  $M$  may be obtained as

$$M = EI \frac{d\phi}{dx} - (e_0a)^2 q. \tag{19}$$

Combining (13) and (14), the total potential energy of the system may be written as

$$U = \frac{1}{2} \int_0^L \left( EI \left( \frac{d\phi}{dx} \right)^2 - \mu q \frac{d\phi}{dx} + k_s GA \left( \phi + \frac{dw}{dx} \right)^2 - qw \right) dx. \tag{20}$$

### 3. Solution methodology

Since conducting experiments at nanoscale size is quite difficult, the development of mathematical models has become quite important. In this paper, we have studied bending of beams based on Euler–Bernoulli and Timoshenko beam theories in conjunction with nonlocal elasticity theory. For doing so, we have applied the Rayleigh–Ritz method with boundary characteristic orthogonal polynomials as shape functions. Thus, displacement and rotation functions are represented by a series of admissible functions. Substituting the unknown functions and minimizing the potential energy of the system as a function of constants, one may find the system of linear equations. The above system of linear equations has been solved by using MATLAB and the solutions give the deflection parameter.

We define the nondimensional variable  $X$  as

$$X = x/L.$$

Each of the unknown functions  $w$  and  $\phi$  may be expressed as the sum of series of polynomials, viz.,

$$w(X) = \sum_{k=1}^n c_k \hat{\varphi}_k(X), \tag{21}$$

$$\phi(X) = \sum_{k=1}^n d_k \hat{\psi}_k(X), \tag{22}$$

where  $n$  is the number of terms taken for computation,  $c_k$ ,  $d_k$  are unknowns and  $\hat{\varphi}_k$ ,  $\hat{\psi}_k$  are orthonormal polynomials. First, orthogonal polynomials  $\varphi_k$  have been obtained from a linearly independent set of functions  $\theta_k = F_u l_k$ ,  $k = 1, 2, 3 \dots, n$  with  $l_k = X^{k-1}$  using the Gram–Schmidt process as follows [Chakraverty and Petyt 1997]:

$$\varphi_1 = \theta_1, \quad \varphi_k = \theta_k - \sum_{j=1}^{k-1} \beta_{kj} \varphi_j, \quad (23)$$

where

$$\beta_{kj} = \frac{\langle \theta_k, \varphi_j \rangle}{\langle \varphi_j, \varphi_j \rangle}, \quad k = 2, 3, \dots, n, \quad j = 1, 2, \dots, k-1.$$

Here,  $\langle \cdot, \cdot \rangle$  denotes the inner product of two functions and we define inner product of two functions, say  $\varphi_i$  and  $\varphi_k$ , as

$$\langle \varphi_i, \varphi_k \rangle := \int_0^1 \varphi_i(X) \varphi_k(X) dX. \quad (24)$$

Similarly, the norm of the function  $\varphi_k$  is defined as

$$\|\varphi_k\| = \sqrt{\int_0^1 \varphi_k^2(X) dX}.$$

Then normalized functions  $\hat{\varphi}_k$  may be obtained by using the following relation:

$$\hat{\varphi}_k = \frac{\varphi_k}{\|\varphi_k\|}$$

One may note that same procedure may be followed to obtain  $\hat{\psi}_k$ .  $F_u$  and  $F_v$  are the boundary functions corresponding to unknown functions  $w$  and  $\phi$ , respectively. It may be noted that the boundary polynomial specifies support conditions, particularly essential boundary conditions. Since  $\hat{\varphi}_k$  and  $\hat{\psi}_k$  are sets of orthogonal polynomials in the interval  $[0, 1]$ , more rapid convergence and better stability in the numerical computation may be accomplished.

In Euler–Bernoulli beam theory,  $F_u = X^r(1-X)^s$ , where  $r$  will take values of 0, 1, 2 accordingly as the edge  $X = 0$  is free, simply supported or clamped, respectively. The same justification can be given to  $s$  for the edge  $X = 1$ . For Timoshenko beam theory, the following conditions should be satisfied by the boundary conditions; as such, the boundary functions used for the above said boundary conditions are given in Table 1:

- $W = M = 0$  at  $X = 0$  and 1 for simply supported–simply supported (SS),
- $W = \phi = 0$  at  $X = 0$  and 1 for clamped–clamped (CC), and
- $W = \phi = 0$  at  $X = 0$  and  $W = M = 0$  at  $X = 1$  for clamped–simply supported (CS).

Substituting (21) into (9) and minimizing the potential energy of the system as a function of constants (i.e.,  $\partial U / \partial c_j = 0$ ), one may obtain following system of linear equations for EBT:

$$\sum_{j=1}^n a_{ij} c_j = P b_i, \quad (25)$$

boundary condition	$F_u$	$F_v$
S-S	$X(1 - X)$	1
C-S	$X(1 - X)$	$X$
C-C	$X(1 - X)$	$X(1 - X)$

**Table 1.** Boundary functions used for different edge conditions (TBT).

where  $a_{ij} = \int_0^1 \hat{\varphi}_i'' \hat{\varphi}_j'' dX$ ,  $b_i = \int_0^1 \hat{\varphi}_i - \mu/L^2 \hat{\varphi}_i'' dX$ ,  $i = 1, 2, \dots, n$  and  $P = qL^4/(EI)$

Similarly, substituting (21) and (22) into (20) and minimizing the potential energy of the system as a function of constants (i.e.,  $\partial U/\partial c_j = 0$  and  $\partial U/\partial d_j = 0$ ;  $j = 1, 2, \dots, n$ ), one may find the following system of linear equations for Timoshenko beam theory:

$$[K]\{Y\} = P\{B\}, \quad \text{where} \quad K = \begin{bmatrix} k_1 & k_2 \\ k_3 & k_4 \end{bmatrix}. \tag{26}$$

Here,  $k_1, k_2, k_3$  and  $k_4$  are submatrices and are given by

$$k_1(i, j) = \int_0^1 2k_s GA \hat{\varphi}_i' \hat{\varphi}_j' dX, \quad k_2(i, j) = \int_0^1 2k_s GAL \hat{\varphi}_i' \hat{\psi}_j dX,$$

$$k_3(i, j) = \int_0^1 2k_s GAL \hat{\psi}_i \hat{\varphi}_j' dX, \quad k_4(i, j) = \int_0^1 (2k_s GAL^2 \hat{\psi}_i \hat{\psi}_j + 2EI \hat{\psi}_i' \hat{\psi}_j') dX.$$

In (26),  $Y = \{c_1 c_2 \dots c_n d_1 d_2 \dots d_n\}^T$  and  $B = \{b_1 b_2\}^T$ , where

$$b_1(i) = \int_0^1 \varphi_i dX, \quad b_2(i) = \int_0^1 \mu qL \psi_i' dX.$$

### 4. Results and discussions

A numerical code has been developed in MATLAB to compute numerical results. Material and geometric properties of the carbon nanotubes are taken from [Alshorbagy et al. 2013], and are given in Table 2. A uniformly distributed load ( $q = 1$ ) has been taken into consideration for three different boundary conditions. The letters C, S and F refer to clamped, simply supported and free edge conditions, respectively. It is a well-known fact that nondimensional maximum deflection is evaluated at the center of the beam, which is given by  $W_{\max} = -w \times 10^2(EI/(qL^4))$ . Before presenting and discussing the new results, it is necessary to perform a convergence study and also to validate the present method with other methods presented in the literature.

Therefore, a convergence study has been carried out for the nondimensional maximum deflection  $W_{\max}$  of the EBT nanobeam with C-S support. As such, Figure 2 shows convergence of the nanobeam with  $L/h = 10$  and  $\mu = 1.5 \text{ nm}^2$ . As can be seen from the figure,  $n = 4$  is sufficient for converged results. It may be noted that previous published results [Ghannadpour et al. 2013] also show the same number of terms required for computation.

In order to validate the results obtained by the present method, the nondimensional maximum deflection is compared in Table 3 with those reported in [Alshorbagy et al. 2013]. In this table, the results are presented for nonlocal beams with boundary conditions at two ends which are of a variety of combinations

properties	value
$E$	$30 \cdot 10^6$
$h$	1
$ks$	5/6
$\nu$	0.19

**Table 2.** Material properties of the carbon nanotubes.

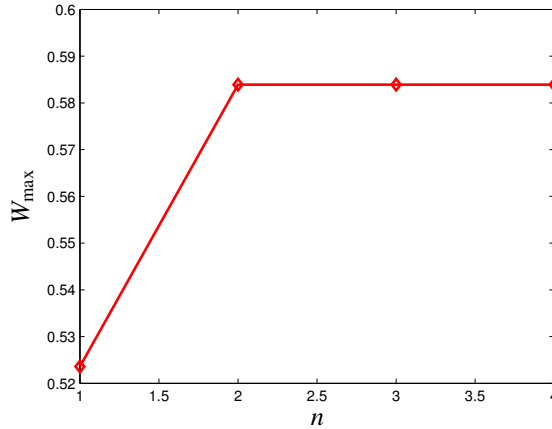


**Figure 2.** Convergence of nondimensional maximum center deflection for EBT.

$\mu$	C-S		C-C	
	present	[Alshorbagy et al. 2013]	present	[Alshorbagy et al. 2013]
0	0.50	0.54	0.24	0.26
1	0.52	0.58	0.24	0.26
2	0.59	0.61	0.24	0.26
3	0.60	0.65	0.24	0.26

**Table 3.** Comparison of nondimensional maximum center deflection ( $W_{max}$ ) for C-S and C-C boundary conditions.

such as C-S and C-C. Results have been shown for different values of a nonlocal parameter. It is noted that the results reported by Alshorbagy et al. [2013] are obtained by the finite element model. It can be seen that there is an excellent agreement between the obtained results in this paper and those reported in the previous work.

Next, we have carried out some of the parametric studies which are discussed below. One may note unless mentioned that deflection and rotation would refer to nondimensional maximum center deflection and nondimensional maximum center rotation respectively.

**4.1. Effect of slenderness ratio.** Figure 3 illustrates the effect of the slenderness ratio ( $L/h$ ) on the deflection of nanobeams. In this figure, we have shown the variation of deflection with slenderness ratio

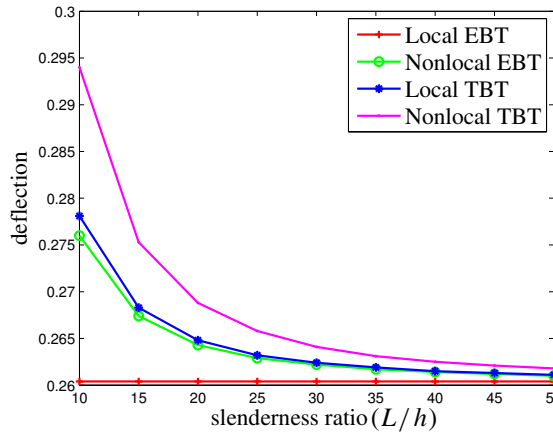


**Figure 3.** Effect of the slenderness ratio on the dimensionless deflection.

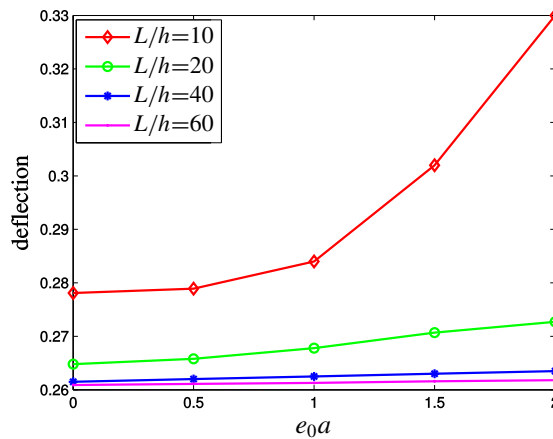


**Figure 4.** Effect of the nonlocal parameter on the dimensionless deflection.

for both local and nonlocal theories. Here, the slenderness ratio varies from 10 to 50 and the boundary condition is considered as C-S. Local results may be computed by taking the nonlocal parameter ( $\mu$ ) as zero. One may note that nonlocal results have been computed for  $\mu = 1 \text{ nm}^2$ . We have presented the graphical results for nanobeams based on both EBT and TBT beam theories. One may observe that in the case of nanobeams based on local EBT, the slenderness ratio has no effect on the beam deflection whereas in nonlocal EBT, deflection is dependent on the slenderness ratio. It may also be noticed that in case of nanobeams based on both local and nonlocal TBT, deflection is dependent on the slenderness ratio. The dependency of the responses on the slenderness ratio for local TBT is uniquely due to the effect of shear deformation and this dependency becomes strong with the effect of small scale. As slenderness ratio decreases, the difference between the solutions of EBT and TBT becomes highly important.

**4.2. Nonlocal parameter effect.** In order to investigate the effect of the nonlocal parameter on the deflection, variation of deflection with the scale coefficient has been demonstrated in Figure 4 for different values of the slenderness ratio ( $L/h$ ). In this figure, we have considered TBT nanobeams with the C-S edge condition. Graphical results have been shown for different values of slenderness ratio. It is seen

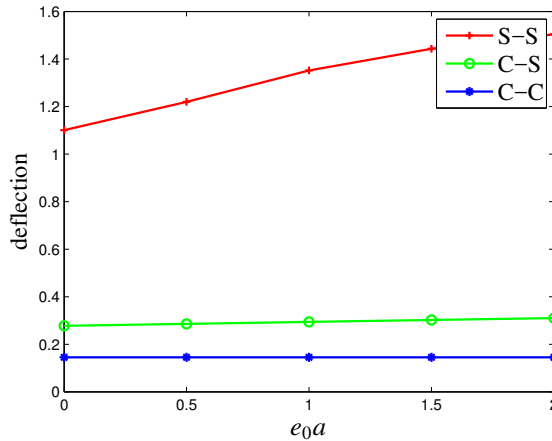


**Figure 5.** Effect of the nonlocal parameter on the dimensionless deflection for different boundary conditions.

from the figure that deflection varies nonlinearly with the scale coefficient. One may also observe that all responses of nanobeams with lower aspect ratios are strongly affected by the nonlocal parameter than those of nanobeams with relatively higher aspect ratios. From these computations, it may be explained that modeling based on the local beam models may not be suitable, whereas the nonlocal beam models show an adequate approximation for the nanosized structures [Şimşek and Yurtcu 2013]. It is also noticed that deflection increases with the scale coefficient, while it is not true in case of buckling and vibration [Şimşek and Yurtcu 2013]. One may conclude here that the nonlocal beam model produces a larger deflection than the classical (local) beam model. Therefore, the small scale effects (or nonlocal effects) should be considered in the analysis of the mechanical behavior of nanostructures.

**4.3. Boundary condition effect.** Deflections of nanobeams under uniform load have been computed for different boundary conditions and are shown in Figure 5. In this figure, the effect of deflection on the scale coefficient has been shown for three sets of boundary conditions, viz., S-S, C-S and C-C. In doing so, we have taken the slenderness ratio as 10. We observe that C-C has the smallest deflection for a particular value of the nonlocal parameter. One may note that in the case of C-C edge condition, there is no effect of the nonlocal parameter on the deflection, whereas in the case of S-S and C-S supports, deflection increases with an increase in the nonlocal parameter. Hence, the effect of the nonlocal parameter on the deflection is inconsistent for different boundary conditions. We state some other observations in Section 4.4.

**4.4. Deflection and rotation shapes.** In this subsection, we examine the behavior of deflection and rotation shapes of nanobeams along its length for different boundary conditions. Figures 6–8 show variation of deflection with length for S-S, C-S and C-C edge conditions, respectively. It is observed from the figures that deflection of S-S and C-S nanobeams increases with increases in the nonlocal parameter. It is due to the fact that increasing nonlocal parameter causes an increase in the bonding force of atoms and this force is constrained by its boundaries, which increases deflection. Another observation is seen in that the nonlocal parameter has no effect on the deflection of C-C nanobeams because of its constrained nature [Alshorbagy et al. 2013]. Next, we have shown variation of rotation with length for S-S, C-S and C-C edge conditions, respectively in Figures 9–11. It may be noticed that the rotation behaves differently

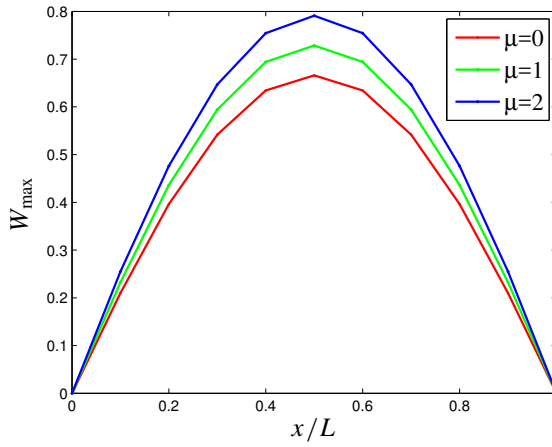


**Figure 6.** Static deflection of S-S nanobeams for different nonlocal parameters.

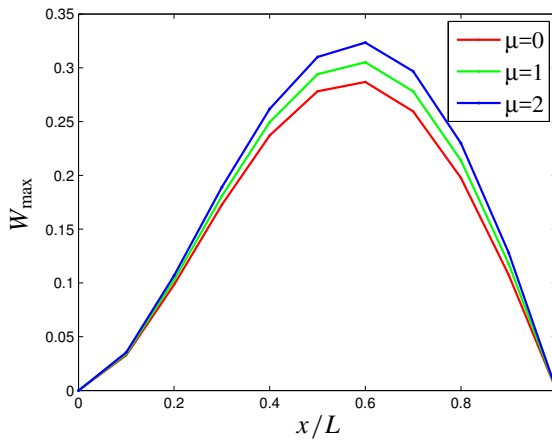


**Figure 7.** Static deflection of C-S nanobeams for different nonlocal parameters.

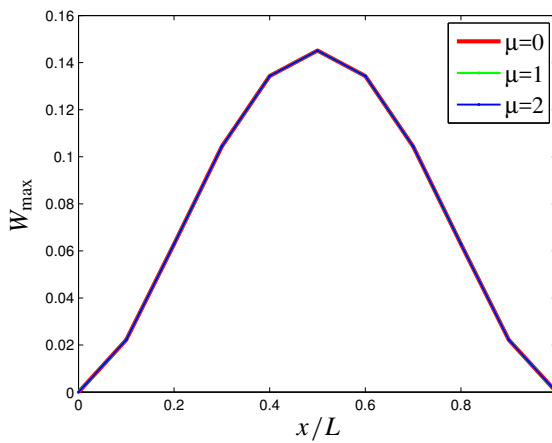


**Figure 8.** Static deflection of C-C nanobeams for different nonlocal parameters.



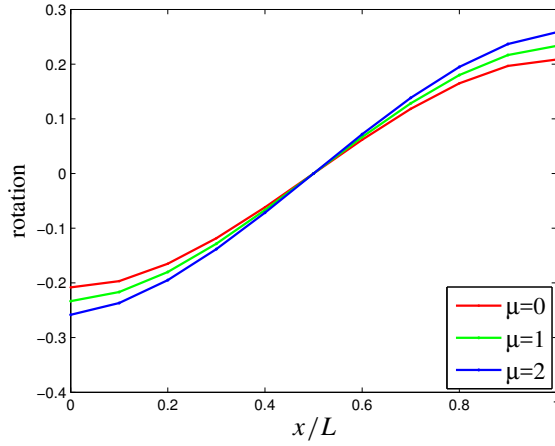


**Figure 9.** Static rotation of S-S nanobeams for different nonlocal parameters.

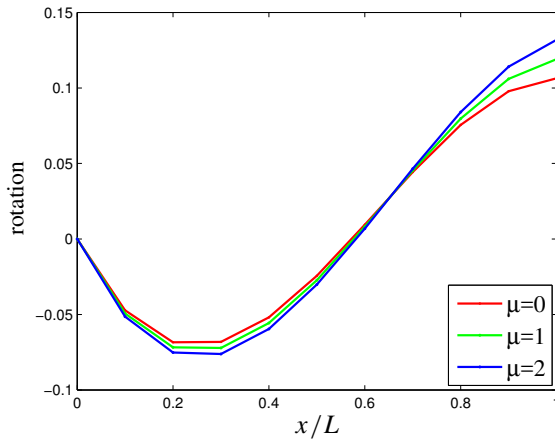


**Figure 10.** Static rotation of C-S nanobeams for different nonlocal parameters.

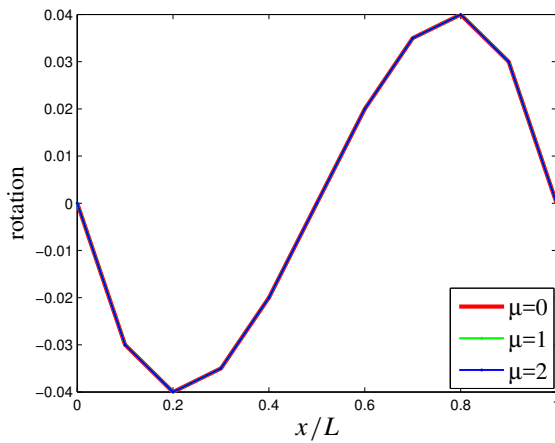


**Figure 11.** Static rotation of C-C nanobeams for different nonlocal parameters.

than that of deflection. Increasing the nonlocal parameter decreases rotation of S-S and C-C nanobeams up to midlength and afterwards increases in the nonlocal parameter increases rotation. One may also notice that the nonlocal parameter has no effect on the rotation of C-C nanobeams.

## 5. Concluding remarks

Boundary characteristic orthogonal polynomials as shape functions have been implemented in the Rayleigh–Ritz method for static analysis of nanobeams. The formulation is based on both Euler–Bernoulli and Timoshenko beam theories in conjunction with nonlocal elasticity of Eringen. A system of linear equations is formed by the applying the present method. The following conclusions may be derived from the present analysis:

- Slenderness ratio has no effect on the beam deflection in the case of local EBT, whereas in the case of nonlocal EBT, deflection is dependent on the slenderness ratio.
- It is seen that bending responses vary nonlinearly with the nonlocal parameter. One may also observe that bending responses of nanobeams with lower aspect ratios are strongly affected by the nonlocal parameter than those of the nanobeams with relatively higher aspect ratios.
- The nonlocal parameter has no effect on the deflection of C-C nanobeams, whereas in case of S-S and C-S supports, deflection increases with increases in the nonlocal parameter.

## References

- [Alshorbagy et al. 2013] A. E. Alshorbagy, M. A. Eltahir, and F. F. Mahmoud, “Static analysis of nanobeams using nonlocal FEM”, *J. Mech. Sci. Technol.* **27**:7 (2013), 2035–2041.
- [Ansari et al. 2013] R. Ansari, K. Hosseini, A. Darvizeh, and B. Daneshian, “A sixth-order compact finite difference method for non-classical vibration analysis of nanobeams including surface stress effects”, *Appl. Math. Comput.* **219**:10 (2013), 4977–4991.
- [Aydogdu 2009] M. Aydogdu, “A general nonlocal beam theory: its application to nanobeam bending, buckling and vibration”, *Physica E* **41**:9 (2009), 1651–1655.
- [Behera and Chakraverty 2014] L. Behera and S. Chakraverty, “Free vibration of Euler and Timoshenko nanobeams using boundary characteristic orthogonal polynomials”, *Appl. Nanosci.* **4**:3 (2014), 347–358.
- [Bhat 1985] R. B. Bhat, “Plate deflections using orthogonal polynomials”, *J. Eng. Mech. (ASCE)* **111**:11 (1985), 1301–1309.
- [Bhat 1991] R. B. Bhat, “Vibration of rectangular plates on point and line supports using characteristic orthogonal polynomials in the Rayleigh–Ritz method”, *J. Sound Vibration* **149** (1991), 170–172.
- [Chakraverty and Petyt 1997] S. Chakraverty and M. Petyt, “Natural frequencies for free vibration of nonhomogeneous elliptic and circular plates using two-dimensional orthogonal polynomials”, *Appl. Math. Model.* **21**:7 (1997), 399–417.
- [Chakraverty et al. 1999] S. Chakraverty, R. B. Bhat, and I. Stiharu, “Recent research on vibration of structures using boundary characteristic orthogonal polynomials in the Rayleigh–Ritz method”, *Shock Vib. Digest* **31**:2 (1999), 187–194.
- [Chakraverty et al. 2007] S. Chakraverty, R. Jindal, and V. K. Agarwal, “Effect of non-homogeneity on natural frequencies of vibration of elliptic plates”, *Meccanica (Milano)* **42**:6 (2007), 585–599.
- [Civalek and Demir 2011] Ö. Civalek and C. Demir, “Buckling and bending analyses of cantilever carbon nanotubes using the Euler–Bernoulli beam theory based on non-local continuum model”, *Asian J. Civil Engng. Build.* **12**:5 (2011), 651–661.
- [Civalek et al. 2009] Ö. Civalek, Ç. Demir, and B. Akgöz, “Static analysis of single walled carbon nanotubes (SWCNT) based on Eringen’s nonlocal elasticity theory”, *International Journal of Engineering and Applied Sciences* **2**:1 (2009), 47–56.
- [Şimşek and Yurtcu 2013] M. Şimşek and H. H. Yurtcu, “Analytical solutions for bending and buckling of functionally graded nanobeams based on the nonlocal Timoshenko beam theory”, *Compos. Struct.* **97** (2013), 378–386.

- [Eltaher et al. 2013] M. A. Eltaher, S. A. Emam, and F. F. Mahmoud, “Static and stability analysis of nonlocal functionally graded nanobeams”, *Compos. Struct.* **96** (2013), 82–88.
- [Eringen 1972] A. C. Eringen, “Nonlocal polar elastic continua”, *Int. J. Eng. Sci.* **10** (1972), 1–16.
- [Ghannadpour et al. 2013] S. A. M. Ghannadpour, B. Mohammadi, and J. Fazilati, “Bending, buckling and vibration problems of nonlocal Euler beams using Ritz method”, *Compos. Struct.* **96** (2013), 584–589.
- [Hu et al. 2004] X. X. Hu, T. Sakiyama, C. W. Lim, Y. Xiong, H. Matsuda, and C. Morita, “Vibration of angle-ply laminated plates with twist by Rayleigh–Ritz procedure”, *Comput. Methods Appl. Mech. Eng.* **193**:9-11 (2004), 805–823.
- [Miller and Shenoy 2000] R. E. Miller and V. B. Shenoy, “Size-dependent elastic properties of nanosized structural elements”, *Nanotechnology* **11**:3 (2000), 139–147.
- [Mohammadi and Ghannadpour 2010] B. Mohammadi and S. A. M. Ghannadpour, “Buckling analysis of micro- and nanorods/tubes based on nonlocal timoshenko beam theory using Chebyshev polynomials”, pp. 619–622 in *Multi-Functional materials and structures* (Jeonju, 2010), vol. III, part 1, edited by J. H. Lee, Advanced Materials Research **123**, Trans Tech Publications, 8 2010.
- [Peddieson et al. 2003] J. Peddieson, G. R. Buchanan, and R. P. McNitt, “Application of nonlocal continuum models to nanotechnology”, *Int. J. Eng. Sci.* **41**:3 (2003), 305–312.
- [Reddy 2007] J. N. Reddy, “Nonlocal theories for bending, buckling and vibration of beams”, *Int. J. Eng. Sci.* **45**:2-8 (2007), 288–307.
- [Reddy and Pang 2008] J. N. Reddy and S. D. Pang, “Nonlocal continuum theories of beams for the analysis of carbon nanotubes”, *J. Appl. Phys.* **103**:2 (2008), art. id. 023511.
- [Singh and Chakraverty 1994] B. Singh and S. Chakraverty, “Boundary characteristic orthogonal polynomials in numerical approximation”, *Commun. Numer. Methods Eng.* **10**:12 (1994), 1027–1043.
- [Thai 2012] H.-T. Thai, “A nonlocal beam theory for bending, buckling, and vibration of nanobeams”, *Int. J. Eng. Sci.* **52** (2012), 56–64.
- [Thai and Vo 2012] H.-T. Thai and T. P. Vo, “A nonlocal sinusoidal shear deformation beam theory with application to bending, buckling, and vibration of nanobeams”, *Int. J. Eng. Sci.* **54** (2012), 58–66.
- [Wang et al. 2000] C. M. Wang, J. N. Reddy, and K. H. Lee, *Shear deformable beams and plates: relationships with classical solutions*, Elsevier, 2000.
- [Wang et al. 2006] C. M. Wang, Y. Y. Zhang, S. S. Ramesh, and S. Kitipornchai, “Buckling analysis of micro- and nanorods/tubes based on nonlocal Timoshenko beam theory”, *J. Phys. D Appl. Phys.* **39**:17 (2006), 3904–3909.
- [Wang et al. 2007] C. M. Wang, Y. Y. Zhang, and X. Q. He, “Vibration of nonlocal Timoshenko beams”, *Nanotechnology* **18**:10 (2007), art. id. 105401.
- [Wang et al. 2008] C. M. Wang, S. Kitipornchai, C. W. Lim, and M. Eisenberger, “Beam bending solutions based on nonlocal Timoshenko beam theory”, *J. Eng. Mech. (ASCE)* **134**:6 (2008), 475–481.
- [Xu 2006] M. Xu, “Free transverse vibrations of nano-to-micron scale beams”, *Proc. R. Soc. Lond. A* **462**:2074 (2006), 2977–2995.
- [Xu et al. 2010] F. Xu, Q. Qin, A. Mishra, Y. Gu, and Y. Zhu, “Mechanical properties of ZnO nanowires under different loading modes”, *Nano Res.* **3**:4 (2010), 271–280.

Received 11 Nov 2016. Revised 2 Jun 2017. Accepted 13 Jun 2017.

LAXMI BEHERA: [laxmibehera25@gmail.com](mailto:laxmibehera25@gmail.com)

Department of Mathematics, National Institute of Technology, Rourkela, India

S. CHAKRAVERTY: [sne\\_chak@yahoo.com](mailto:sne_chak@yahoo.com)

Department of Mathematics, National Institute of Technology, Rourkela, India

# ANALYSIS OF PEDESTRIAN-INDUCED LATERAL VIBRATION OF A FOOTBRIDGE THAT CONSIDERS FEEDBACK ADJUSTMENT AND TIME DELAY

JIA BUYU, CHEN ZHOU, YU XIAOLIN AND YAN QUANSHENG

Research on pedestrian-bridge dynamic interaction has intensified in recent years after the occurrence of several footbridge accidents caused by pedestrian-induced vibration. This study focuses on the analysis of pedestrian-induced lateral vibration of footbridges by considering the time delay and feedback adjustment that occur in the interaction between the pedestrians and the footbridge. A detailed nonlinear lateral vibration model is first established. Then, the bifurcation and stability of this model around the critical value of time delay is discussed using a qualitative method. Moreover, response amplitude and the critical number of pedestrians are evaluated using a multiscale method. Analysis of the results shows that the time delay and feedback adjustment play important roles in controlling the lateral vibration of the footbridge.

## 1. Introduction

Pedestrian load is considerably smaller than vehicle load; consequently, pedestrian-induced vibration of footbridges has not aroused considerable attention until the occurrence of the Millennium Bridge accident in London, which was caused by large lateral vibration. Unlike a running vehicle, a pedestrian creates an alternating motion as they walk with their two legs; this does not only produce a vertical force but also lateral and longitudinal forces. The normal pedestrian walking frequency ranges from 1.6 Hz to 2.4 Hz in the vertical direction, from 0.8 Hz to 1.2 Hz in the lateral direction, and from 0.8 Hz to 1.2 Hz in the longitudinal direction [Živanović et al. 2005]. Meanwhile, the fundamental frequencies of most flexible footbridges are less than 3.0 Hz, which indicates that the walking frequency of pedestrians falls within the range of the fundamental frequency of most footbridges. That is, the walking action of a pedestrian may easily cause resonance on a footbridge. Accidents caused by large vibrations have occurred in recent years. For example, a steel suspension footbridge in the Sichuan Province in China collapsed in 2010 because of a large lateral vibration caused by walking tourists; the accident left over 28 people injured [Qin 2013]. Apart from causing collapse failure, the footbridge vibration frequently leads to discomfort among pedestrians. Pedestrians are highly sensitive to footbridge vibration; therefore, a large footbridge vibration can make pedestrians feel uncomfortable and even cause panic in a crowd. The large lateral vibration of the Millennium Bridge is a famous example [Dallard et al. 2001a]. The Millennium Bridge

---

This research was supported by the National Natural Science Foundation of China (Nos. 51478193), the China Postdoctoral Science Foundation (Nos. 2016M592490), the Fundamental Research Funds for the Central Universities (Nos. 2015ZM114), and the Open Fund of State Key Laboratory of Bridge Engineering Structural Dynamics (Nos. 201507).

*Keywords:* footbridge, nonlinear vibration, lateral displacement, time delay, feedback adjustment.

was temporarily closed for 20 months until the vibration was reduced by implementing several temporary solutions. This incident has become a symbol of pedestrian-induced vibration of footbridges.

Since the occurrence of large lateral vibration of the London Millennium Bridge during its inauguration, experts have started to study the involved mechanisms. In recent years, a number of tests and theoretic models have been investigated to explain the large lateral vibration of footbridges.

Prior to the retrofit of the Millennium Bridge, a full scale test was implemented [Dallard et al. 2001a]. The test showed that there exists a critical number of pedestrians needed to trigger a divergence of lateral vibration. The test also showed that the pedestrian-induced lateral force is proportional to the velocity of bridge, which means the action of pedestrians could be treated as negative viscous dampers. Brownjohn et al. [2004a; 2004b] performed a test on pedestrians circumambulating on a bridge in the Singapore Changi Airport. According to the test, pedestrians might slow down or stop moving forward, depending on the state of bridge vibration. The test also showed that the critical number of pedestrians cannot be determined in a repeatable way due to the randomness of pedestrian walking characteristics.

While walking on a lateral vibrating footbridge, pedestrians continually adjust their states to walk comfortably, and the phenomenon of “lock-in” (pedestrians synchronizing their steps with the bridge’s movement) may occur when the walking frequency of pedestrians is close to the bridge’s lateral natural frequency, which further enhances the lateral vibration. Dallard et al. [2001a] defined this kind of mechanism as Synchronous Lateral Excitation (SLE). To explain the large pedestrian-induced lateral vibration, several models have been proposed and classified into linear response models and nonlinear response models [Ingólfsson et al. 2012]. Linear response models can also be regarded as direct resonance models, where the lateral vibrations are caused by direct resonance; namely, the pedestrian walking frequency is in resonance with the natural frequency of one or more lateral vibration modes. Fujino et al. [1993] considered the direct resonance as the source that excites the large pedestrian-induced lateral vibration and used a linear monodimensional damped dynamical system to analyze the lateral vibration of the T-Bridge. The test on the Millennium Bridge [Dallard et al. 2001a] showed that the first lateral frequency of the central span is 0.48 Hz, which does not fall in the range of pedestrian lateral walking frequencies. This means the direct resonance is not able to explain the large vibration of the first lateral mode of the central span of the Millennium Bridge. It is interesting to note that the second lateral frequency of the central span is around 1 Hz, which may lead to a mixed resonant-parametric excitation. However, such higher mode excitation will not be considered here, as the research’s object is the large vibration of the first lateral mode.

For the nonlinear response model, there are several remarkable models. Based on the Dallard model [Dallard et al. 2001a], which is widely used as a stability criterion to estimate the number of pedestrians needed to trigger large lateral vibration, Nakamura [2004] proposed a refined model by multiplying the lateral force with a modulated function. The modulated function represents the self-limiting nature of the pedestrian synchronization: pedestrians will reduce their walking speed, or completely stop, when the bridge’s velocity becomes large. Yuan [2006] proposed an empirical model, in which the dynamic load factor and the probability of synchronization depend on the vibration amplitude. In this model, both of the self-excited effect caused by the synchronized pedestrians and the forced vibration effect caused by the unsynchronized pedestrians are considered, and a nonlinear equation for stability criterion is derived to estimate the critical number of pedestrians. Blekherman [2005] proposed an autoparametric resonance model to explain the large lateral vibration. Based on the model of Blekherman, the large lateral vibration

in the footbridge can be attributed to the existence of an integer ratio between vertical and lateral mode frequencies. For example, there is a 2 : 1 ratio between the third vertical mode frequency (1.89 Hz) and the second lateral mode frequency (0.95 Hz) in central span of the Millennium Bridge, as well as a 2 : 1 ratio between the third vertical mode frequency (2.0 Hz) and the first lateral mode frequency (1.0 Hz) in the T-Bridge. Besides the autoparametric resonance model, there is another parametric resonance nonlinear model proposed by Piccardo and Tubino [2008], which is based on a displacement-dependent nonlinear lateral force model. According to this model, the large lateral vibration in the flexible footbridge can be attributed to the parametric resonance in which the lateral natural frequency is equivalent to half of the pedestrian lateral walking frequency. For example, in the Millennium Bridge, the first lateral frequency (0.48 Hz) is nearly half of the pedestrian lateral walking frequency (1.0 Hz).

As mentioned previously, pedestrians will make a feedback adjustment according to the bridge vibration. During the process of adjustment, there exists a time delay among the pedestrian-bridge interaction. Based on the Nakamura model, Liu and Xie [2013] proved that the time delay has a great influence on the lateral vibration of footbridge. Newland [2004] assumed that pedestrian movement was composed of two parts. The first part is the natural movement of a pedestrian while walking on a stationary pavement; the second part is the movement caused by the bridge vibration, which is proportional to the bridge amplitude with a time delay. However, Newland did not conduct a specific study on the effect of time delay.

The Millennium Bridge is used as the background in this study. A qualitative analytical method and a multiscale method are used to analyze pedestrian-induced lateral vibration of a footbridge by considering the time delay and feedback adjustment. In addition, the effects of time delay and feedback adjustment on the critical number of pedestrians and response amplitude are discussed.

**2. Basic nonlinear vibration model**

A footbridge is modeled as a beam under the action of pedestrians. A segment with length  $ds$ , which is  $x$  distance from the beam support, is considered (Figure 1).

The cross sections are assumed to remain normal to the deformed axis. Using the displacement method, the equilibrium equation of lateral motions at the centroid is obtained as [Chopra 1981]

$$(\rho_s A + m_p) \frac{\partial^2 w}{\partial t^2} ds + \mu_2 \frac{\partial w}{\partial t} ds = \frac{\partial}{\partial s} (N \sin \theta - Q \cos \theta) ds + f_l ds, \tag{1}$$

where  $\rho_s$  is the density of the footbridge,  $A$  is the section area,  $m_p$  is the crowd mass per meter along the bridge,  $w(x, t)$  is the lateral displacement,  $\mu_2$  is the lateral damping coefficient of the footbridge,  $\theta$  is the

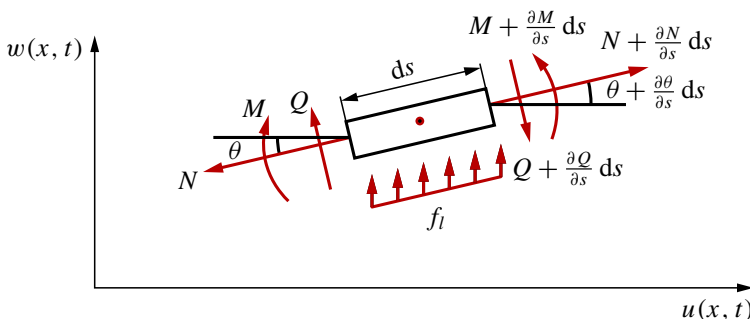


**Figure 1.** Segment equilibrium.

section angle,  $N(x, t)$  is the axial force,  $Q(x, t)$  is the shear force, and  $f_l$  is the lateral force of pedestrians. Realizing that the pedestrian motion is harmonic and that there exists a time delay (the footbridge vibration does not vary immediately) between the bridge and the pedestrians when the pedestrians-bridge action takes place, the expression of  $f_l$  with consideration of a time delay  $\tau$  can be written as

$$f_l(t - \tau) = \lambda \alpha_l m_p g \cos(\omega_p(t - \tau)), \tag{2}$$

where  $\lambda$  is the pedestrian synchronous coefficient (according to Piccardo and Tubino [2008], the value of  $\lambda$  in the Millennium Bridge is set as  $\lambda = 0.3$ ),  $g$  is the acceleration of gravity,  $\omega_p$  is the pedestrian walking frequency, and  $\alpha_l$  is the lateral dynamic loading factor of the first harmonic (the ratio between the lateral dynamic force and the pedestrian weight).

According to the measured data from the literature [Dallard et al. 2001a], it can be found that the pedestrian lateral force is proportional to the lateral velocity of footbridge. Thus, it is assumed that there is a linear relationship between the pedestrian lateral force and the lateral velocity of footbridge, and  $\alpha_l$  can be defined as

$$\alpha_l = \alpha_{l1} + \alpha_{l2} \frac{\partial w(x, t - \tau)}{\partial t}, \tag{3}$$

where  $\alpha_{l1}$  is the dynamic load coefficient while walking on stationary pavement and  $\alpha_{l2}$  is the dynamic load coefficient related to the lateral velocity of footbridge. Subsequently, the pedestrian lateral force can be rewritten as

$$f_l(t - \tau) = \lambda \left[ \alpha_{l1} + \alpha_{l2} \frac{\partial w(x, t - \tau)}{\partial t} \right] m_p g \cos(\omega_p(t - \tau)). \tag{4}$$

The fit method is used to approximate the linear relationship between the dynamic load coefficient and the lateral velocity of footbridge (Figure 2). The fitting results show that the values of  $\alpha_{l1}$  and  $\alpha_{l2}$  in the Millennium Bridge are  $\alpha_{l1} = 0.04$  and  $\alpha_{l2} = 0.7$ .

Assuming that shear force  $Q(x, t)$  and moment  $M(x, t)$  exhibit the relationship  $Q = \partial M / \partial s = \cos \theta (\partial M / \partial x)$ , then (1) can be rewritten as

$$(\rho_s A + m_p) \frac{\partial^2 w}{\partial t^2} + \mu_2 \frac{\partial w}{\partial t} = \frac{\partial}{\partial x} \left( N \sin \theta - \frac{\partial M}{\partial x} \cos^2 \theta \right) \cos \theta + f_l(t - \tau). \tag{5}$$

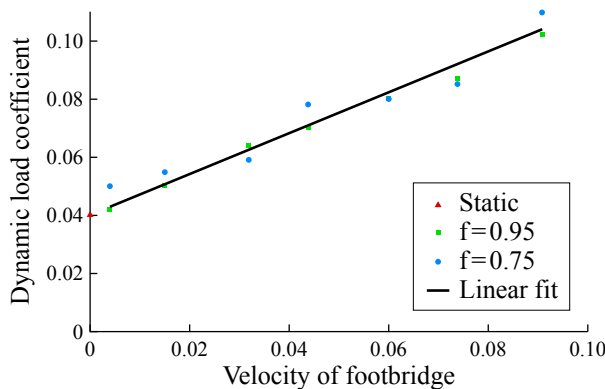


**Figure 2.** Dynamic load coefficient versus lateral velocity of footbridge.



Through the stress integration on the section, the axial force caused by lateral bend is obtained as

$$N(x, t) = \iint E \varepsilon_N dA = E \iint \frac{\partial \left[ \int_0^x \sqrt{1 + (\partial w / \partial x)^2} dx - x \right]}{\partial s} dA, \quad (6)$$

where  $\varepsilon_N$  is the normal strain caused by lateral bend.  $N(x, t)$  is rewritten (based on the first-order Taylor Series expansion of  $\varepsilon_N$  and  $\cos \theta$ ) as

$$\begin{aligned} N(x, t) &\approx E \iint \frac{\partial \left[ \int_0^x \left[ 1 + \frac{1}{2} (\partial w / \partial x)^2 \right] dx - x \right]}{\partial s} \cos \theta dA \\ &= E \iint \frac{1}{2} \left( \frac{\partial w}{\partial x} \right)^2 \cos \theta dA \approx \frac{1}{2} EA \left( \frac{\partial w}{\partial x} \right)^2. \end{aligned} \quad (7)$$

The moment caused by section rotation is obtained as

$$M(x, t) = EI \frac{\partial \theta}{\partial x} = EI \frac{\partial^2 w}{\partial x^2}. \quad (8)$$

Taking the first-order Taylor series expansion of  $\sin \theta$  yields  $\sin \theta \approx \theta = \partial w / \partial x$ . Accordingly, one has  $\cos \theta \approx 1 - (\partial w / \partial x)^2$ . Then substituting (7) and (8) into (5), the dynamic equation that contains the only unknowns of the lateral displacement is obtained as

$$\begin{aligned} (\rho_s A + m_p) \frac{\partial^2 w}{\partial t^2} + \mu_2 \frac{\partial w}{\partial t} + EI \frac{\partial^4 w}{\partial x^4} \\ = \frac{3}{2} EA \left( \frac{\partial w}{\partial x} \right)^2 \frac{\partial^2 w}{\partial x^2} + EI \frac{\partial^4 w}{\partial x^4} \left( \frac{\partial w}{\partial x} \right)^2 + 6EI \frac{\partial^3 w}{\partial x^3} \frac{\partial^2 w}{\partial x^2} \frac{\partial w}{\partial x} + 2EI \left( \frac{\partial^2 w}{\partial x^2} \right)^3 + f_l(t - \tau). \end{aligned} \quad (9)$$

When walking on a lateral vibrating footbridge, pedestrians would adjust their strides to walk comfortably, according to the feedback of vibration. The action exerted by the pedestrians on the bridge changes with the bridge vibration. During the early stage of adjustment, the pedestrians' action based on the feedback of vibration may continually enhance the vibration. However, when the lateral vibration amplitude of bridge becomes large enough to make the pedestrians feel uncomfortable, pedestrians will reduce their walking speed or stop walking to lower their actions on the bridge, and then the bridge vibration decreases. These findings suggest that the pedestrians' feedback adjustment is a very complicated process. The mechanism of pedestrians' feedback adjustment involves some uncertain influencing factors, such as pedestrians' psychology, bridge deck typology, human-human interaction, etc. Unfortunately, there is no model or law so far that can precisely describe the pedestrians' feedback adjustment. In this study, a factor  $\zeta$  is used to comprehensively represent these influencing factors. Then the term  $\zeta w(t - \tau)$ , which is obtained by multiplying the factor  $\zeta$  with the lateral displacement of the bridge that allows for the time delay, is introduced to describe the action of feedback adjustment. By adding the term  $\zeta w(t - \tau)$  into the (9), we obtain the following:

$$\begin{aligned} (\rho_s A + m_p) \frac{\partial^2 w}{\partial t^2} + \mu_2 \frac{\partial w}{\partial t} + EI \frac{\partial^4 w}{\partial x^4} \\ = \frac{3}{2} EA \left( \frac{\partial w}{\partial x} \right)^2 \frac{\partial^2 w}{\partial x^2} + EI \frac{\partial^4 w}{\partial x^4} \left( \frac{\partial w}{\partial x} \right)^2 + 6EI \frac{\partial^3 w}{\partial x^3} \frac{\partial^2 w}{\partial x^2} \frac{\partial w}{\partial x} + 2EI \left( \frac{\partial^2 w}{\partial x^2} \right)^3 + f_l(t - \tau) + \zeta w(t - \tau). \end{aligned} \quad (10)$$



This study intends to explain the large first lateral vibration of the central span of the Millennium Bridge on the basis of parametric vibration. The second-order factor will not be considered in this study, because the second-order factor corresponds to a direct resonance at second lateral mode (the second lateral frequency of the central span is close to the pedestrian lateral walking frequency). Therefore, the first-order mode  $w(x, t) = \psi(x)w_1(t)$  is only considered, where the mode shape function is considered as

$$\phi(x) = \sin(\pi x/l). \tag{11}$$

By using the Galerkin method to execute a discretization, the corresponding modal differential equation is given as

$$\ddot{w}_1(t) + \zeta_1 \dot{w}_1(t) + \omega_1^2 w_1(t) - \zeta_2 \cos(\omega_p(t - \tau)) \dot{w}_1(t - \tau) + \beta w_1^3(t) - h w_1(t - \tau) - F_0 \cos(\omega_p(t - \tau)) = 0, \tag{12}$$

where  $\zeta_1 = 2\zeta_0\omega_1$  ( $\zeta_0$  is the damping ratio of a footbridge), and

$$\omega_1 = \sqrt{\frac{EI\pi^4}{l^4(\rho_s A + m_p)}}, \quad \zeta_2 = \frac{\lambda\alpha_{l2}m_p g}{\rho_s A + m_p}, \quad \beta = \frac{10EI\pi^6 + 3\pi^4 l^2 EA}{8l^6(\rho_s A + m_p)},$$

$$F_0 = \frac{4\lambda\alpha_{l1}m_p g}{\pi(\rho_s A + m_p)}, \quad \text{and} \quad h = \frac{4\zeta}{\pi(\rho_s A + m_p)}.$$

### 3. Critical values of time delay

Let  $q_1(t) = w_1(t)$  and  $q_2(t) = \dot{w}_1(t)$ . Equation (12) can be rewritten as

$$\begin{aligned} \dot{q}_1(t) &= q_2(t), \\ \dot{q}_2(t) &= -\zeta_1 q_2(t) + \zeta_2 \cos(\omega_p(t - \tau)) q_2(t - \tau) \\ &\quad - \omega_1^2 q_1(t) - \beta q_1^3(t) + h q_1(t - \tau) + F_0 \cos(\omega_p(t - \tau)). \end{aligned} \tag{13}$$

Let  $\bar{\zeta}_2 = \zeta_2 \cos(\omega_p(t - \tau))$ . The following characteristic equation that corresponds to (13) can be obtained by adopting a linearization method [Zhen et al. 2013]:

$$\lambda^2 + \zeta_1 \lambda + \omega_1^2 - \bar{\zeta}_2 \lambda e^{-\lambda\tau} - h e^{-\lambda\tau} = 0. \tag{14}$$

Let  $\lambda = \kappa + i\nu$  and substitute it into (14). The real part and the imaginary part can be respectively expressed by

$$\kappa^2 - \nu^2 + \zeta_1 \kappa + \omega_1^2 - \bar{\zeta}_2 e^{-\lambda\tau} [\kappa \cos(\nu\tau) + \nu \sin(\nu\tau)] - h e^{-\kappa\tau} \cos(\nu\tau) = 0, \tag{15}$$

$$2\kappa\nu + \zeta_1\nu - \bar{\zeta}_2 e^{-\lambda\tau} [\nu \cos(\nu\tau) - \kappa \sin(\nu\tau)] + h e^{-\kappa\tau} \sin(\nu\tau) = 0. \tag{16}$$

Hopf bifurcation may occur near the origin of (14) when  $\kappa$  changes within a small range around zero; thus, (15) and (16) can be respectively rewritten as

$$-\nu^2 + \omega_1^2 = \bar{\zeta}_2 \nu \sin(\nu\tau) + h \cos(\nu\tau), \tag{17}$$

$$\zeta_1 \nu = \bar{\zeta}_2 \nu \cos(\nu\tau) - h \sin(\nu\tau). \tag{18}$$

Combining (17) with (18) and considering the elimination of time delay  $\tau$  yields

$$\nu^4 - (2\omega_1^2 + \bar{\zeta}_2^2 - \zeta_1^2)\nu^2 + \omega_1^4 - h^2 = 0. \tag{19}$$

According to (17) and (19), we have

$$v_k = \sqrt{\frac{2\omega_1^2 + \bar{\zeta}_2^2 - \zeta_1^2 \pm \sqrt{4h^2 + (\bar{\zeta}_2^2 - \zeta_1^2)^2 + 4\omega_1^2(\bar{\zeta}_2^2 - \zeta_1^2)}}{2}}, \quad k = 1, 2; \quad (20)$$

$$\tau_{n,k} = \frac{1}{v_{1,2}} \left[ \arcsin\left(\frac{\omega_1^2 - v_{1,2}^2}{\sqrt{\bar{\zeta}_2^2 v_{1,2}^2 + h^2}}\right) - \arctan\left(\frac{h}{\bar{\zeta}_2 v_{1,2}}\right) + 2n\pi \right], \quad n = 0, 1, 2, 3, \dots \quad k = 1, 2. \quad (21)$$

When  $\tau = \tau_{n,k}$ , the complex conjugate roots of (14) may cross the imaginary axis if the following conditions are satisfied:

- (1) a real root of (19) exists, and
- (2) the real part of  $d\lambda/d\tau$  is not equal to zero.

The stability and bifurcation of (14) is considered in this study. Note that  $\kappa$  and  $v$  in (15) and (16) are functions of  $\tau$ ; hence, the solutions with the form of  $\kappa(\tau) \pm i\nu(\tau)$  are considered. Let  $\kappa(\tau_{n,k}) = 0$ ,  $v_k = v_k(\tau_{n,k})$ , and  $n = 0, 1, 2, 3, \dots$ ,  $k = 1, 2$ . Implementing the partial derivative with (15) and (16) yields

$$\begin{aligned} & [\zeta_1 + h\tau \cos(v_k \tau) - \bar{\zeta}_2 \cos(v_k \tau) + \bar{\zeta}_2 \tau v_k \sin(v_k \tau)] \frac{d\kappa}{d\tau} \\ & + [-2v_k + h\tau \sin(v_k \tau) - \bar{\zeta}_2 \sin(v_k \tau) - \bar{\zeta}_2 \tau v_k \cos(v_k \tau)] \frac{dv_k}{d\tau} \\ & = -h v_k \sin(v_k \tau) + \bar{\zeta}_2 v_k^2 \cos(v_k \tau), \quad k = 1, 2; \quad (22) \end{aligned}$$

$$\begin{aligned} & [2v_k - h\tau \sin(v_k \tau) + \bar{\zeta}_2 \sin(v_k \tau) + \bar{\zeta}_2 \tau v_k \cos(v_k \tau)] \frac{d\kappa}{d\tau} \\ & + [\zeta_1 + h\tau \cos(v_k \tau) - \bar{\zeta}_2 \cos(v_k \tau) + \bar{\zeta}_2 \tau v_k \sin(v_k \tau)] \frac{dv_k}{d\tau} \\ & = -h v_k \sin(v_k \tau) - \bar{\zeta}_2 v_k^2 \sin(v_k \tau), \quad k = 1, 2. \quad (23) \end{aligned}$$

Combining (22) with (23) yields

$$\frac{d\kappa}{d\tau} = \frac{L_1}{L_2}, \quad (24)$$

where

$$\begin{aligned} L_1 &= -v_k [\zeta_2^2 v_k + (2\bar{\zeta}_2 v_k^2 + \zeta_1 h) \sin(v_k \tau) + (2h v_k - \zeta_1 \bar{\zeta}_2 v_k) \cos(v_k \tau)], \\ L_2 &= [\zeta_1 + h\tau \cos(v_k \tau) - \bar{\zeta}_2 \cos(v_k \tau) + \bar{\zeta}_2 \tau v_k \sin(v_k \tau)]^2 \\ &+ [2v_k - h\tau \sin(v_k \tau) + \bar{\zeta}_2 \sin(v_k \tau) + \bar{\zeta}_2 \tau v_k \cos(v_k \tau)]^2, \quad k = 1, 2. \end{aligned}$$

Substituting  $\tau = \tau_{n,1}$  and  $\tau = \tau_{n,2}$  ( $\tau_{n,1} < \tau_{n,2}$ ) into (24) yields

$$\left. \frac{d\kappa}{d\tau} \right|_{\tau=\tau_{n,1}} < 0, \quad n = 0, 1, 2, 3, \dots; \quad (25)$$

$$\left. \frac{d\kappa}{d\tau} \right|_{\tau=\tau_{n,2}} > 0, \quad n = 0, 1, 2, 3, \dots \quad (26)$$

According to (25) and (26), the stable and unstable regions can be obtained as follows:

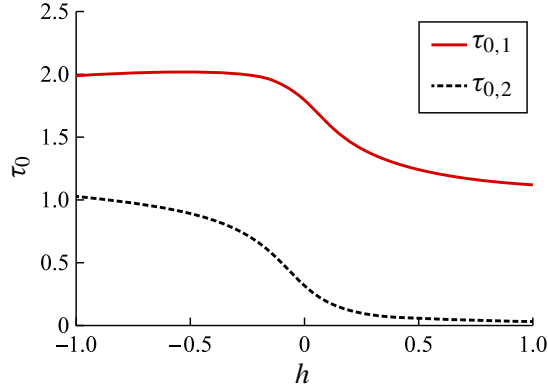


**Figure 3.** Relationship between the critical value of time delay and the feedback adjustment factor.

- (1) When  $d\kappa/d\tau|_{\tau=\tau_{n,1}} < 0$ , a pair of eigenvalues cross the imaginary axis, and the real part of the eigenvalues changes from positive to negative. At that moment, the system tends to be stable with an increase in time delay.
- (2) When  $d\kappa/d\tau|_{\tau=\tau_{n,2}} > 0$ , a pair of eigenvalues cross the imaginary axis, and the real part of the eigenvalues changes from negative to positive. At that moment, the system tends to be unstable with an increase in time delay.

Hence, when  $h$  has a certain value, time delay  $\tau$  will have two corresponding critical values, i.e.,  $\tau_{n,1}$  and  $\tau_{n,2}$ , and bifurcations will occur near  $\tau_{n,1}$  and  $\tau_{n,2}$ . Given that  $\tau_{n,1} < \tau_{n,2}$ , the system is initially stable. When  $\tau$  arrives at  $\tau_{n,2}$ , bifurcation occurs, and the system has no real solution. Subsequently, when  $\tau$  arrives at  $\tau_{n,1}$ , bifurcation occurs again; at that moment, the system has real solutions. These findings suggest that the lateral vibration of the bridge at first decreases in amplitude as the time delay increases, then it stops altogether when the time delay is in the range  $[\tau_{n,1}, \tau_{n,2}]$ , and then its amplitude starts increasing again with time delay when the time delay exceeds  $\tau_{n,2}$ .

Figure 3 shows the relationship between the critical value of time delay and the feedback adjustment factor under  $n = 0$  and  $\bar{\zeta}_2 = 0.8\zeta_2$ . Some conclusions can be derived from Figure 3 as follows:

- (1) When the feedback adjustment factor is fixed at a certain value, the variation of time delay will make the system shift from a balanced state to an unbalanced state and then to another balanced state.
- (2) The critical values of time delay depend on whether the feedback adjustment factor  $h$  is positive (pedestrian exerts a feedback adjustment action in an opposite direction to the displacement) or negative (pedestrian exerts a feedback adjustment action in the same direction to the displacement).
- (3) The critical values of time delay vary dramatically around the point of  $h = 0$ , which denotes that a small feedback adjustment factor will have a relatively large influence on the critical values of time delay.

The aforementioned analysis belongs to the qualitative analysis domain. In the next section, we will adopt a quantitative analysis theory (multiscale method) to discuss the influences of time delay and feedback adjustment on pedestrian-induced lateral vibration of a footbridge.

#### 4. Nonlinear parametric resonance

Back to (12), since the pedestrian modal mass is usually small compared with the structural modal mass,  $\zeta_2$  is naturally small, which can be represented by a small parameter  $\varepsilon$ ; moreover, the terms  $\zeta_1$ ,  $\beta$ ,  $h$  and  $F_0$  are also small, and they are assumed small enough to be of the same order as  $\varepsilon$ . Hence, these parameters mentioned above are rewritten as follows:

$$\zeta_2 = \varepsilon, \quad \zeta_1 = \varepsilon \tilde{\zeta}_1, \quad \beta = \varepsilon \tilde{\beta}, \quad h = \varepsilon \tilde{h}, \quad F_0 = \varepsilon \tilde{F}_0. \quad (27)$$

Letting  $r(t) = w_1(t)$  and substituting (27) into (12) yields

$$\ddot{r}(t) + \varepsilon \tilde{\zeta}_1 \dot{r}(t) - \varepsilon \cos(\omega_p(t - \tau)) \dot{r}(t - \tau) \omega_1^2 r(t) + \varepsilon \tilde{\beta} r^3(t) - \varepsilon \tilde{h} r(t - \tau) - \varepsilon \tilde{F}_0 \cos(\omega_p(t - \tau)) = 0. \quad (28)$$

The multiscale method is used to solve (28). The first-order approximation with two time scales is introduced as

$$\begin{aligned} r(t) &= r_0(T_0, T_1) + \varepsilon r_1(T_0, T_1) + O(\varepsilon^2), \quad T_n = \varepsilon^n t, \quad n = 0, 1; \\ r_\tau(t) &= r_{0\tau}(T_0, T_1) + \varepsilon r_{1\tau}(T_0, T_1) + O(\varepsilon^2). \end{aligned} \quad (29)$$

Consider the following differential operators:

$$\begin{aligned} \frac{d}{dT} &= \frac{\partial}{\partial T_0} + \varepsilon \frac{\partial}{\partial T_1} + O(\varepsilon^2) \equiv D_0 + \varepsilon D_1 + O(\varepsilon^2), \\ \frac{d^2}{dT^2} &= D_0^2 + 2\varepsilon D_0 D_1 + O(\varepsilon^2). \end{aligned} \quad (30)$$

Substituting (29) and (30) into (28), and equating the same power of  $\varepsilon$  yields

$$\varepsilon^0 : D_0^2 r_0 + \omega_1^2 r_0 = 0, \quad (31)$$

$$\begin{aligned} \varepsilon^1 : D_0^2 r_1 + \omega_1^2 r_1 &= -2D_0 D_1 r_0 - \tilde{\zeta}_1 D_0 r_0 + D_0 r_{0\tau} \cos(\omega_p(t - \tau)) \\ &\quad - \tilde{\beta} r_0^3 + \tilde{h} r_{0\tau} + \tilde{F}_0 \cos(\omega_p(t - \tau)). \end{aligned} \quad (32)$$

The solution to (31) is

$$r_0(T_0, T_1) = A(T_1) e^{j\omega_1 T_0} + \bar{A}(T_1) e^{-j\omega_1 T_0}. \quad (33)$$

The time delay term can then be written as

$$r_{0\tau}(T_0, T_1) = A_\tau(T_1) e^{j\omega_1(T_0 - \tau)} + \bar{A}_\tau(T_1) e^{-j\omega_1(T_0 - \tau)}, \quad (34)$$

where  $A(T_1)$  and  $A_\tau(T_1)$  denote the complex functions with respect to  $T_1$ , which will be determined later; and  $\bar{A}(T_1)$  and  $\bar{A}_\tau(T_1)$  denote the complex conjugate of  $A(T_1)$  and  $A_\tau(T_1)$ , respectively.

Substituting (33) and (34) into (32) yields

$$\begin{aligned} D_0^2 r_1 + \omega_1^2 r_1 &= -(2D_1 A j\omega_1 + \tilde{\zeta}_1 A j\omega_1) e^{j\omega_1 T_0} + \frac{1}{2} j\omega_1 (A_\tau e^{j(\omega_p + \omega_1)(T_0 - \tau)} - \bar{A}_\tau e^{j(\omega_p - \omega_1)(T_0 - \tau)}) \\ &\quad - \tilde{\beta} (A^3 e^{3j\omega_1 T_0} + 3A^2 \bar{A} e^{j\omega_1 T_0}) + \tilde{h} A_\tau e^{j\omega_1(T_0 - \tau)} + \frac{1}{2} \tilde{F}_0 e^{j(\omega_p T_0 - \omega_p \tau)} + cc, \end{aligned} \quad (35)$$

where  $cc$  denotes the complex conjugate of all the preceding terms on the right side. On the basis of (35), parametric vibration will occur when  $\omega_p \approx 2\omega_1$ , whereas forced vibration will occur when  $\omega_p \approx \omega_1$ . Parametric vibration and forced vibration cannot occur simultaneously under the action of pedestrian

lateral force when considering the first lateral mode of bridge; thus, only parameter vibration  $\omega_p \approx 2\omega_1$  is considered in this section. A detuning parameter  $\sigma$  is added, and the equation is assumed as

$$\omega_p = 2\omega_1 + \varepsilon\sigma. \quad (36)$$

Eliminating the secular terms in (35) yields

$$2D_1Aj\omega_1 + \bar{\zeta}_1Aj\omega_1 + \frac{1}{2}j\omega_1\bar{A}_\tau e^{j\sigma T_1} e^{-j(\omega_1+\varepsilon\sigma)\tau} - \tilde{h}A_\tau e^{-j\omega_1\tau} + 3\tilde{\beta}A^2\bar{A} = 0. \quad (37)$$

When the time delay is not large and  $\varepsilon$  is extremely small,  $\bar{A}_\tau$  and  $A_\tau$  can be respectively rewritten by using Taylor expansion as follows:

$$\bar{A}_\tau(T_1) = \bar{A}(T_1 - \varepsilon\tau) = \bar{A}(T_1) - \varepsilon\tau\bar{A}'(T_1) + \frac{1}{2}\varepsilon^2\tau^2\bar{A}''(T_1) \approx \bar{A}(T_1), \quad (38)$$

$$A_\tau(T_1) = A(T_1 - \varepsilon\tau) = A(T_1) - \varepsilon\tau A'(T_1) + \frac{1}{2}\varepsilon^2\tau^2 A''(T_1) \approx A(T_1). \quad (39)$$

Then, (37) becomes

$$2D_1Aj\omega_1 + \bar{\zeta}_1Aj\omega_1 + \frac{1}{2}j\omega_1\bar{A}(T_1)e^{j\sigma T_1} e^{-j(\omega_1+\varepsilon\sigma)\tau} - \tilde{h}A(T_1)e^{-j\omega_1\tau} + 3\tilde{\beta}A^2\bar{A} = 0. \quad (40)$$

For convenience, the complex function  $A(T_1)$  is written in polar form as

$$A(T_1) = \frac{1}{2}a_1(T_1)e^{j\phi_1(T_1)}, \quad (41)$$

where  $a_1(T_1)$  and  $\phi_1(T_1)$  are real functions of  $T_1$ . By substituting (41) into (40) and separating the resulting equation into real and imaginary parts, we obtain the following:

$$D_1a_1 = -\frac{1}{2}\tilde{\zeta}_1a_1 - \frac{1}{4}a_2 \cos \psi \cos((\omega_1 + \varepsilon\sigma)\tau) - \frac{1}{4}a_1 \sin \psi \sin((\omega_1 + \varepsilon\sigma)\tau) - \frac{\tilde{h}a_1}{2\omega_1} \sin(\omega_1\tau), \quad (42)$$

$$D_1\psi = \sigma + \frac{1}{2} \sin \psi \cos((\omega_1 + \varepsilon\sigma)\tau) - \frac{1}{2} \cos \psi \sin((\omega_1 + \varepsilon\sigma)\tau) - \frac{3\tilde{\beta}a_1^2}{4\omega_1} + \frac{\tilde{h}}{\omega_1} \cos(\omega_1\tau), \quad (43)$$

where  $\psi = \sigma T_1 - 2\phi_1$ . For a steady primary resonance,  $D_1a_1 = D_1\psi = 0$ , which leads to the following equations with consideration of (27):

$$\frac{1}{2}\tilde{\zeta}_1 + \frac{h}{2\omega_1} \sin(\omega_1\tau) = -\frac{1}{4}\tilde{\zeta}_2 \cos \psi \cos((\omega_1 + \varepsilon\sigma)\tau) - \frac{1}{4}\tilde{\zeta}_2 \sin \psi \sin((\omega_1 + \varepsilon\sigma)\tau), \quad (44)$$

$$\varepsilon\sigma - \frac{3\beta a_1^2}{4\omega_1} + \frac{h}{\omega_1} \cos(\omega_1\tau) = \frac{1}{2}\tilde{\zeta}_2 \cos \psi \sin((\omega_1 + \varepsilon\sigma)\tau) - \frac{1}{2}\tilde{\zeta}_2 \sin \psi \cos((\omega_1 + \varepsilon\sigma)\tau). \quad (45)$$

By squaring both sides of (44) and (45) and adding the resulting equations, the amplitude-frequency equation and the phase-frequency equation can be respectively obtained as

$$\left(\tilde{\zeta}_1 + \frac{h}{\omega_1} \sin(\omega_1\tau)\right)^2 + \left(\varepsilon\sigma - \frac{3\beta a_1^2}{4\omega_1} + \frac{h}{\omega_1} \cos(\omega_1\tau)\right)^2 = \frac{1}{4}\tilde{\zeta}_2^2, \quad (46)$$

$$\tan \psi = \frac{\frac{3\beta a_1^2}{4\omega_1} - \frac{h}{\omega_1} \cos(\omega_1\tau) - \varepsilon\sigma - \left[\tilde{\zeta}_1 + \frac{h}{\omega_1} \cos(\omega_1\tau)\right] \tan((\omega_1 + \varepsilon\sigma)\tau)}{\left[\sigma - \frac{3\beta a_1^2}{4\omega_1} + \frac{h}{\omega_1} \cos(\omega_1\tau)\right] \tan((\omega_1 + \varepsilon\sigma)\tau) - \left[\tilde{\zeta}_1 + \frac{h}{\omega_1} \cos(\omega_1\tau)\right]}. \quad (47)$$

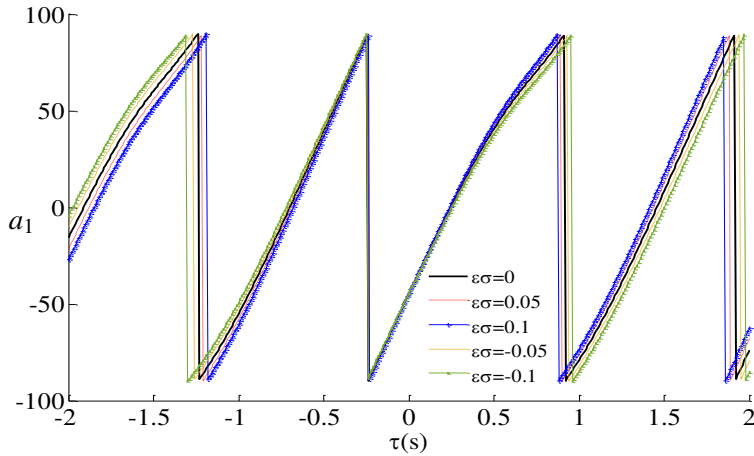


**Figure 4.** Relationship between phase angle and time delay ( $h = 0.05$ ).

From (46), it can be known that  $[\zeta_1 + h/\omega_1 \sin(\omega_1 \tau)]^2 \leq \frac{1}{4}\zeta_2^2$ . Note that  $\zeta_2$  is probably very small, hence a physical limit range of  $h$  can be obtained as  $|h| \leq \omega_1 \zeta_1$ .

According to (46) and (47), the time delay and feedback adjustment have made a difference in both amplitude and phase.

Figure 4 shows the relationship between phase angle and time delay under different detuning parameters when  $h = 0.05$  (rad/s)<sup>2</sup>. As shown in the figure, phase angle changes with time delay, and it has the envelope amplitudes around  $\pm 90$ . Moreover, the curves of  $\varepsilon\sigma > 0$  and the curves of  $\varepsilon\sigma < 0$  are distributed symmetrically on the opposite two sides of the curve of  $\varepsilon\sigma = 0$ . It is noted that, when time delay is near the region centered around  $\tau = -0.23$ , the difference between the curve of  $\varepsilon\sigma > 0$  and that of  $\varepsilon\sigma < 0$  is slight, whereas the difference increases as the time delay becomes farther from the center point.

Solving (46) yields

$$a_1 = \sqrt{\frac{4h}{3\beta} \cos(\omega_1 \tau) + \frac{4\omega_1}{3\beta} \varepsilon\sigma \pm \frac{4\omega_1}{3\beta} \sqrt{\frac{1}{4}\zeta_2^2 - \left(\zeta_1 + \frac{h}{\omega_1} \sin(\omega_1 \tau)\right)^2}}. \quad (48)$$

According to (48), the effect of time delay on response amplitude will be periodic because the time delay is embedded into the triangular functions.

## 5. Effects of displacement feedback adjustment and time delay on response amplitude

The central span of the Millennium Bridge is used as the background. According to previous works [Dallard et al. 2001b; Piccardo and Tubino 2008], the structural parameters are set as  $\omega_1 = 2\pi n_1$  ( $n_1 = 0.48$  Hz),  $\lambda = 0.3$ ,  $m_s = 2000$  kg/m,  $m_{ps} = 70$  kg,  $\zeta_0 = 0.007$ , and  $\alpha_{l2} = 0.7$ . It is assumed that 200 pedestrians are walking on the bridge. The response of the Millennium Bridge under parametric resonance (i.e.,  $\varepsilon\sigma = 0$ ) is analyzed. Figure 5 shows the effects of the time delay (within a certain period) and feedback adjustment on the response amplitude, in which the feedback adjustment factors are set as  $h = \pm 0.05$ ,  $h = \pm 0.1$ , and  $h = \pm 0.1273$  (the limit range of  $h$  is calculated as  $[-0.1273, 0.1273]$ ).

In Figure 5, the solid lines denote stable periodic solutions, whereas the dashed lines denote unstable solutions. Note that no real solution region, which is shown as zero in the figures, exists because the

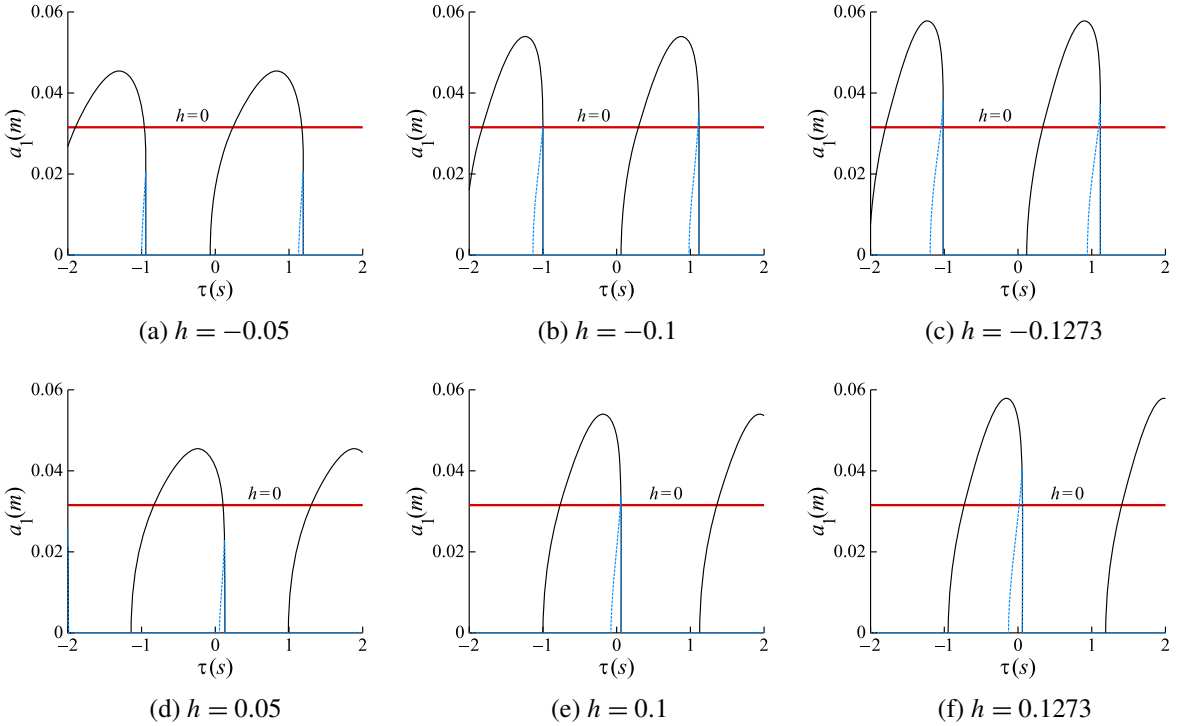


**Figure 5.** Effects of the time delay and feedback adjustment on response amplitude.

pedestrian-induced vibration of the Millennium Bridge will have a crossing phenomenon caused by the time delay.

The time delay and feedback adjustment significantly affect the response amplitude. As shown in Figure 5, the maximum response amplitude by considering the time delay and feedback adjustment is nearly 0.06, which is almost twice that without feedback adjustment.

A comparison between Figures 5a–5c and Figures 5d–5f shows that the distribution of bridge amplitude with regard to the time delay strongly depends on whether the feedback adjustment factor is positive or negative. Besides, the feedback adjustment factor also affects the maximum response amplitude. The maximum response amplitude increases with the absolute value of feedback adjustment factor.

Meanwhile, the trend of bridge amplitude depends on the time delay. In some time delay regions, the bridge vibration that considers the effect of the feedback adjustment is less than that without feedback adjustment, which means that the feedback adjustment of pedestrians would tend to reduce the bridge vibration, whereas in some other time delay regions, the feedback adjustment of pedestrians would tend to raise the bridge vibration.

### 6. Effects of the time delay and feedback adjustment on the critical number of pedestrians

Note that amplitude  $a_1$  should be a real number, as given by

$$\frac{4h}{3\beta} \cos(\omega_1 \tau) + \frac{4\omega_1}{3\beta} \varepsilon \sigma \pm \frac{4\omega_1}{3\beta} \sqrt{\frac{1}{4}\zeta_2^2 - \left(\zeta_1 + \frac{h}{\omega_1} \sin(\omega_1 \tau)\right)^2} \geq 0. \tag{49}$$



Subsequently, (49) results in

$$\zeta_2 \leq \zeta_{2\text{lim}}, \quad (50)$$

where

$$\zeta_{2\text{lim}} = 2\sqrt{\left(\frac{\varepsilon\omega_1\sigma + h \cos(\omega_1\tau)}{\omega_1}\right)^2 + \left(\zeta_1 + \frac{h}{\omega_1} \sin(\omega_1\tau)\right)^2}. \quad (51)$$

According to (51), it can be found that the critical value  $\zeta_{2\text{lim}}$  of  $\zeta_2$  is related to the time delay and feedback adjustment factor.

The pedestrians on the bridge are assumed to be uniformly distributed and the same as the mass distribution of the bridge. This assumption supports the following equation:

$$m_p L = N m_{ps}, \quad (52)$$

where  $N$  denotes the number of pedestrians on the bridge, and  $m_{ps}$  denotes the mass of a single pedestrian. Combining (50) with (52) yields

$$N \leq \frac{2L\rho_s A \sqrt{\left(\frac{\varepsilon\omega_1\sigma + h \cos(\omega_1\tau)}{\omega_1}\right)^2 + \left(\zeta_1 + \frac{h}{\omega_1} \sin(\omega_1\tau)\right)^2}}{\lambda\alpha_{12} m_{ps} g - 2m_{ps} \sqrt{\left(\frac{\varepsilon\omega_1\sigma + h \cos(\omega_1\tau)}{\omega_1}\right)^2 + \left(\zeta_1 + \frac{h}{\omega_1} \sin(\omega_1\tau)\right)^2}}. \quad (53)$$

Figures 6a and 6b present the  $N - \tau$  curve under different values of  $h$ ; Figures 6c and 6d present the  $N - h$  curve under different values of  $\tau$ . Considering the fact that the time delay varies within a certain range under the practical situation, the following analysis will focus on the time delay that is within the range of  $[-1, 1]$ .

The critical number of pedestrians  $N$  depends on different combinations of  $h$  and  $\tau$ . For example, Figure 6a shows that, when  $\tau \in [0.37, 0.67]$  and  $h < 0$ ,  $N$  decreases with an increase of the absolute value of  $h$ . In other words, when the time delay stays within the range of  $[0.37, 0.67]$ , the action of the negative feedback adjustment may tend to cause large bridge vibration. While for the case of  $[0.52, 1]$  and  $h < 0$ ,  $N$  increases with  $\tau$ , denoting that the increase of time delay may tend to reduce the bridge vibration. Meanwhile, the results corresponding to  $h > 0$ , as shown in Figure 6b, exhibits a trend that is opposite to that of  $h < 0$ .

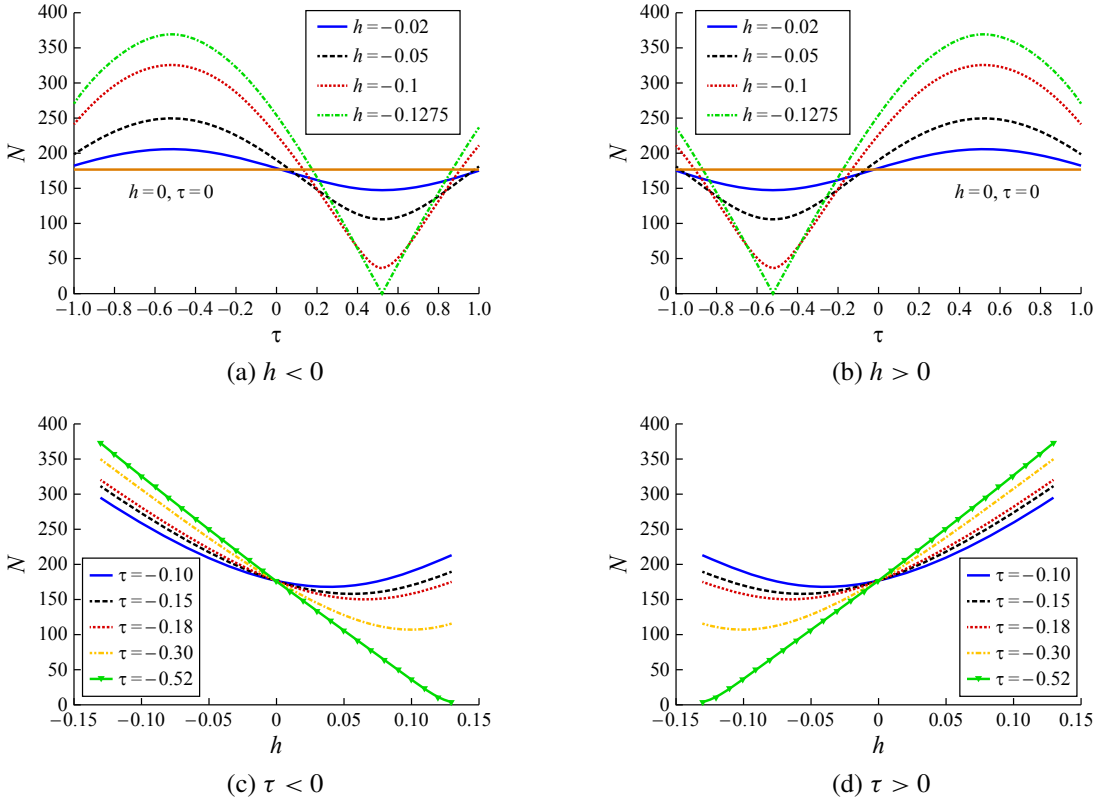
Figures 6c and 6d show that, when under the case of  $\tau \in [-0.18, 0]$  and  $h \in [0, 0.11]$ , or the case of  $\tau \in [0, 0.18]$  and  $h \in [-0.11, 0]$ , the corresponding critical number of pedestrians  $N$  is consistent with experimental observation (165 ~ 185) on the Millennium Bridge.

It is worth noting that in the case of  $h = -0.1273$  and  $\tau = 0.52$ , or the case of  $h = 0.1273$  and  $\tau = -0.52$ , the critical number of pedestrians  $N$  achieves a physical limit of nearly zero. This finding also demonstrates that the limited range of  $h$  is about  $[-0.1273, 0.1273]$  from another perspective.

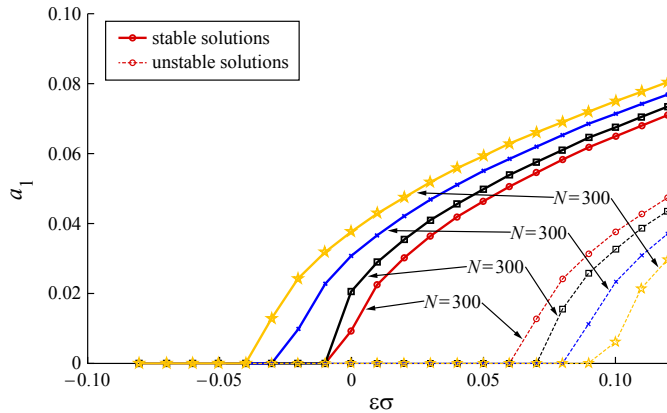
## 7. Amplitude-frequency response curves

Figure 7 shows the amplitude-frequency response curves of the Millennium Bridge under different numbers of pedestrians by assuming that  $h = -0.11$  and  $\tau = 0.18$ .

Some following conclusions can be derived from Figure 7:



**Figure 6.** Relationships between the critical number of pedestrians and time delays and feedback adjustment factors.



**Figure 7.** Amplitude-frequency response curves

- (1) The response amplitude has two different solutions, including the stable solution with a large value and the unstable solution with a small value. The curves of the two solutions are characterized by the rightward inclined shapes which are asymmetrically distributed around  $\epsilon\sigma = 0$ . This suggests

that bifurcations would occur at the point that is more than twice the first lateral frequency of bridge causing the divergent lateral vibration amplitudes.

- (2) When the number of pedestrians on the bridge decreases, the two solutions become closer to  $\varepsilon\sigma = 0$  and the interval between them becomes smaller. This suggests that the number of pedestrians required to trigger the large lateral vibration decreases as the walking frequency arrives closer to the point that is twice the first lateral frequency of bridge.
- (3) The amplitude increases with the detuning parameter  $\varepsilon\sigma$ , suggesting that the amplitude would be larger as the walking frequency becomes greater than twice the bridge's first lateral frequency. Moreover, it is also observed that the curve tends to be more linear with the increase of  $\varepsilon\sigma$ , suggesting that the degree of nonlinearity would be weaker when the pedestrians' walking frequency becomes more than twice the bridge's first lateral frequency.

## 8. Conclusions

This study has used the Millennium Bridge as the background for an analysis of pedestrian-induced lateral vibration of a footbridge by considering the time delay and feedback adjustment that occur in the pedestrian-footbridge interaction. The main contributions of the present study can be summarized as follows:

- (1) The results of the qualitative analysis show that the time delay significantly affects the stability of the lateral vibration of footbridge. Moreover, the critical value of the time delay depends on the sign of the feedback adjustment factor.
- (2) The influences of time delay and feedback adjustment on response amplitude are significant. The time delay and feedback adjustment may cause a larger bridge amplitude than that without considering the time delay and feedback adjustment. The sign of feedback adjustment factor affects the distribution of bridge amplitude, while the time delay affects the trend of bridge amplitude.
- (3) The critical number of pedestrians depends on different combinations of time delay and feedback adjustment. In some cases, the time delay and feedback adjustment may cause a small value for the critical number of pedestrians, while in some other cases, the time delay and feedback adjustment may cause a large value for the critical number of pedestrians. By comparing with the experimental observation on the Millennium Bridge, the feedback adjustment factor and time delay corresponding to the large vibration of the Millennium Bridge may be the case of  $\tau \in [-0.18, 0]$  and  $h \in [0, 0.11]$ , or the case of  $\tau \in [0, 0.18]$  and  $h \in [-0.11, 0]$ .
- (4) When the walking frequency approaches the doubled first lateral frequency of bridge, a relatively small number of pedestrians is required to cause large lateral vibration.

## References

- [Blekhman 2005] A. N. Blekhman, "Swaying of pedestrian bridges", *J. Bridge Eng.* **10**:2 (2005), 142–150.
- [Brownjohn et al. 2004a] J. M. W. Brownjohn, P. Fok, M. Roche, and P. Moyo, "Long span steel pedestrian bridge at Singapore Changi Airport, I: Prediction of vibration serviceability problems", *Struct. Eng.* **82**:16 (2004), 21–27.
- [Brownjohn et al. 2004b] J. M. W. Brownjohn, P. Fok, M. Roche, and P. Omenzetter, "Long span steel pedestrian bridge at Singapore Changi Airport, II: Crowd loading tests and vibration mitigation measures", *Struct. Eng.* **82**:16 (2004), 28–34.

- [Chopra 1981] A. K. Chopra, *Dynamics of structures: a primer*, Earthquake Eng. Res. Inst., Oakland, CA, 1981.
- [Dallard et al. 2001a] P. Dallard, A. J. Fitzpatrick, A. Flint, S. L. Bourva, A. Low, R. M. Ridsdill Smith, and M. Willford, “The London Millennium Footbridge”, *Struct. Eng.* **79**:22 (2001), 17–33.
- [Dallard et al. 2001b] P. Dallard, T. Fitzpatrick, A. Flint, A. Low, R. M. Ridsdill Smith, M. Willford, and M. Roche, “London Millennium Bridge: pedestrian-induced lateral vibration”, *J. Bridge Eng.* **6**:6 (2001), 412–417.
- [Fujino et al. 1993] Y. Fujino, B. M. Pacheco, S.-I. Nakamura, and P. Warnitchai, “Synchronization of human walking observed during lateral vibration of a congested pedestrian bridge”, *Earthq. Eng. Struct. Dyn.* **22**:9 (1993), 741–758.
- [Ingólfsson et al. 2012] E. T. Ingólfsson, C. T. Georgakis, and J. Jönsson, “Pedestrian-induced lateral vibrations of footbridges: a literature review”, *Eng. Struct.* **45** (2012), 21–52.
- [Liu and Xie 2013] L. Liu and W.-P. Xie, “Influence of time delay on the lateral vibration of footbridges induced by pedestrians”, *J. Civ. Eng. Manag.* **30**:1 (2013), 6–9, 15. In Chinese.
- [Nakamura 2004] S.-I. Nakamura, “Model for lateral excitation of footbridges by synchronous walking”, *J. Struct. Eng. (ASCE)* **130**:1 (2004), 32–37.
- [Newland 2004] D. E. Newland, “Pedestrian excitation of bridges”, *Proc. Inst. Mech. Eng. C, J. Mech. Eng. Sci.* **218**:5 (2004), 477–492.
- [Piccardo and Tubino 2008] G. Piccardo and F. Tubino, “Parametric resonance of flexible footbridges under crowd-induced lateral excitation”, *J. Sound Vib.* **311**:1-2 (2008), 353–371.
- [Qin 2013] J. W. Qin, *Human-structure interaction based on the bipedal walking model*, Ph.D. thesis, Beijing Jiaotong University, 2013. In Chinese.
- [Yuan 2006] X. Yuan, *Pedestrian-induced vibration characteristics of footbridges*, Ph.D. thesis, Tongji University, 2006. In Chinese.
- [Zhen et al. 2013] B. Zhen, W. Xie, and J. Xu, “Nonlinear analysis for the lateral vibration of footbridges induced by pedestrians”, *J. Bridge Eng.* **18**:2 (2013), 122–130.
- [Živanović et al. 2005] S. Živanović, A. Pavic, and P. Reynolds, “Vibration serviceability of footbridges under human-induced excitation: a literature review”, *J. Sound Vib.* **279**:1-2 (2005), 1–74.

Received 19 Jan 2017. Revised 25 May 2017. Accepted 30 May 2017.

JIA BUYU: [ctjby@scut.edu.cn](mailto:ctjby@scut.edu.cn)

School of Civil Engineering and Transportation, South China University of Technology, Guangzhou, China

CHEN ZHOU: [cznew123@126.com](mailto:cznew123@126.com)

College of Transportation & Civil Engineering and Architecture, Foshan University, Foshan, China

YU XIAOLIN: [xlyu1@scut.edu.cn](mailto:xlyu1@scut.edu.cn)

School of Civil Engineering and Transportation, South China University of Technology, Guangzhou, China

YAN QUANSHENG: [cvqshyan@scut.edu.cn](mailto:cvqshyan@scut.edu.cn)

School of Civil Engineering and Transportation, South China University of Technology, Guangzhou, China

# NEARLY EXACT AND HIGHLY EFFICIENT ELASTIC-PLASTIC HOMOGENIZATION AND/OR DIRECT NUMERICAL SIMULATION OF LOW-MASS METALLIC SYSTEMS WITH ARCHITECTED CELLULAR MICROSTRUCTURES

MARYAM TABATABAEI, DY LE AND SATYA N. ATLURI

Additive manufacturing has enabled the fabrication of lightweight materials with intricate cellular architectures. These materials are interesting due to their properties which can be optimized upon the choice of the parent material and the topology of the architecture, making them appropriate for a wide range of applications including lightweight aerospace structures, energy absorption, thermal management, metamaterials, and bioscaffolds. In this paper we present the simplest initial computational framework for the analysis, design, and topology optimization of low-mass metallic systems with architected cellular microstructures. A very efficient elastic-plastic homogenization of a repetitive Representative Volume Element (RVE) of the microlattice is proposed. Each member of the cellular microstructure undergoing large elastic-plastic deformations is modeled using only one nonlinear three-dimensional (3D) beam element with 6 degrees of freedom (DOF) at each of the 2 nodes of the beam. The nonlinear coupling of axial, torsional, and bidirectional-bending deformations is considered for each 3D spatial beam element. The plastic hinge method, with arbitrary locations of the hinges along the beam, is utilized to study the effect of plasticity. We derive an explicit expression for the tangent stiffness matrix of each member of the cellular microstructure using a mixed variational principle in the updated Lagrangian corotational reference frame. To solve the incremental tangent stiffness equations, a newly proposed Newton homotopy method is employed. In contrast to the Newton's method and the Newton–Raphson iteration method, which require the inversion of the Jacobian matrix, our homotopy methods avoid inverting it. We have developed a code called CELLS/LIDS (CELLular Structures/Large Inelastic DeformationS), which provides the capabilities to study the variation of the mechanical properties of the low-mass metallic cellular structures by changing their topology. Thus, due to the efficiency of this method we can employ it for topology optimization design and for impact/energy absorption analyses.

## 1. Introduction

A lot of natural structures, such as hornbill bird beaks and bird wing bones, are architected cellular materials, which provide optimum strength and stiffness at low density. Humankind, over the past few years, has also fabricated cellular materials with more complex architectures in comparison with previously developed synthetic materials like open-cell metallic foams and honeycombs [Schaedler and Carter 2016]. Properties of these cellular structures are determined based on their parent materials and the topology of the microarchitecture. Additive manufacturing technologies and progress in three-dimensional (3D) printing techniques enable the design of materials and structures with complex cellular

*Keywords:* architected cellular microstructures, large deformations, plastic hinge approach, nonlinear coupling of axial-torsional-bidirectional bending deformations, mixed variational principle, homotopy methods.

microarchitectures, optimized for specific applications. In fact, one of the most interesting characteristics of cellular structures with pore networks is that they can be designed with desirable properties, making them appropriate for lightweight structures, metamaterials, energy absorption, thermal management, and bioscaffolds [Schaedler et al. 2014]. For example, efforts are under way to fabricate bioscaffolds to repair and replace tissue, cartilage, and bone [Hutmacher 2000; Mota et al. 2015; Valentin et al. 2006; Han and Gouma 2006]. These architected materials should be fabricated in such a way that they can meet biocompatibility requirements in addition to the mechanical properties of the tissues at the site of implantation. Therefore, presentation of a highly efficient computational method to predict and optimize the mechanical properties of such structures is of interest. Herein, we present a nearly exact and highly efficient computational method to predict the elastic-plastic homogenized mechanical properties of low-mass metallic systems with architected cellular microstructures. The framework of the methods presented in this paper is also germane to the analysis under static as well as impact loads, design, and topology optimization of cellular solids.

The ultralow-density metallic cellular microlattices have been recently fabricated at HRL Laboratories [Schaedler et al. 2011; Torrents et al. 2012], suitable for thermal insulation, battery electrodes, catalyst supports, and acoustic, vibration, or shock energy damping [Gibson and Ashby 1988; Evans et al. 2010; Lu et al. 2005; Valdevit et al. 2011; Ashby et al. 2000; Wadley 2002]. They produced nickel cellular microlattices, consisting of hollow tubular members, by preparing a sacrificial polymeric template for electroless Ni deposition, and then chemically etching the sacrificial template [Schaedler et al. 2011].

Using this process, they fabricated novel nickel-based microlattice materials with structural hierarchy spanning three different length scales: nm,  $\mu\text{m}$  and mm. They obtained a 93% Ni–7% P composition by weight for microlattices using energy dispersive spectroscopic analysis. They employed quasistatic axial compression experiments to measure macroscopic mechanical properties such as Young’s moduli of nickel microlattices. The load  $P$  was measured by SENSOTEC load cells, and the displacement  $\delta$  was measured using an external LVDT for modulus extraction. Strain-stress curves were obtained based on engineering stress and strain defined, respectively, as  $\sigma = P/A_0$  and  $\varepsilon = \delta/L_0$ .  $A_0$  and  $L_0$  are the initial cross-sectional area and length of the sample, respectively.

Salari-Sharif and Valdevit [2014] extracted the Young’s modulus of a series of nickel ultralight microlattices by coupling experimental results obtained using laser Doppler vibrometry with finite element (ABAQUS) simulations. Salari-Sharif and Valdevit [2014] fabricated a sandwich configuration by attaching carbon/epoxy face sheets as the top and bottom layers of the ultralight nickel hollow microlattice thin film [Schaedler et al. 2011]. Furthermore, Salari-Sharif and Valdevit [2014] detected the resonant frequencies by scanning laser vibrometry and ABAQUS simulations and extracted the relation between Young’s modulus and the natural frequencies. Then, the effective Young’s moduli of samples were obtained in the direction normal to the face sheets [Salari-Sharif and Valdevit 2014]. It is worth noting that for finite element (FE) modeling, a representative volume element (RVE) consisting of only four members of the cellular microlattice with at least ten thousand of 4-node shell FEs was employed [Salari-Sharif and Valdevit 2014], resulting in at least ten thousand nodes and, thus, sixty thousand degrees of freedom (DOF). We should emphasize that in our methodology each member can be modeled by a single spatial beam element. In other words, to perform a 4-member RVE analysis, we use only four spatial beam elements and five nodes, with a total of 30 DOF and, thus, at least 2000 times less DOF than in [Salari-Sharif and Valdevit 2014]. Since the cost of computation in a FE nonlinear analysis varies as the

$n$ -th power ( $n$  between 2 and 3) of the number of DOF, it is clear that we seek to present a far more efficient analysis procedure than any available commercial software. This provides the capability to simulate the cellular microstructure using repetitive RVEs consisting of an arbitrary number of members, enabling a very efficient homogenization and/or direct numerical simulation (DNS) of a cellular macrostructure.

In addition, Schaedler et al. [2011] and Torrents et al. [2012] showed experimentally that nickel-phosphorous cellular microlattices undergo large effective compressive strains through extensive rotations about remnant node ligaments. Unfortunately, there are no computational studies in the literature on the large-deformation elastic-plastic analysis of such metallic cellular structures, which is the major concern of the present study, although there is a vast variety of studies on the large deformation analysis of space-frames [Besseling 1986; Geradin and Cardona 1988; Mallett and Berke 1966; Izzuddin 2001] from the era of large space structures for use in outer space. In the realm of space-frame analyses, numerous studies have been devoted to deriving an explicit expression for the tangent stiffness matrix of each element, accounting for arbitrarily large rigid rotations, moderately large nonrigid point-wise rotations, and the stretching-bending coupling [Bathe and Bolourchi 1979; Punch and Atluri 1984; Lo 1992; Kondoh et al. 1986; Kondoh and Atluri 1987]. Some researchers employed displacement-based approaches using variants of a Lagrangian for either geometrically or materially nonlinear analyses of frames [Bathe and Bolourchi 1979; Punch and Atluri 1984; Lo 1992]. Kondoh et al. [1986] extended the displacement approach to evaluate explicitly the tangent stiffness matrix without employing either numerical or symbolic integration for a beam element undergoing large deformations. Later, Kondoh and Atluri [1987] presented a formulation on the basis of assumed stress resultants and stress couples, satisfying the momentum balance conditions in the beam subjected to arbitrarily large deformations.

In order to study the elastic-plastic behavior of cellular members undergoing large deflections, we employ the mechanism of plastic hinge developed by Hodge [1959], Ueda et al. [1968], and Ueda and Yao [1982]. In this mechanism, a plastic hinge can be generated at any point along the member as well as its end nodes, anywhere the plasticity condition in terms of generalized stress resultants is satisfied. It is worthwhile to mention that contours of the von Mises stress given in [Salari-Sharif and Valdevit 2014] for the 4-member RVE with PBCs show a very high concentration of stress at the junction of four members. The stress contours were obtained based on linear elastic FE simulations [Salari-Sharif and Valdevit 2014]. Therefore, it clearly mandates an elastic-plastic analysis, which is undertaken in the present study. A complementary energy approach in conjunction with the plastic hinge method has been previously utilized to study elasto-plastic large deformations of space-framed structures [Kondoh and Atluri 1987; Shi and Atluri 1988]. Shi and Atluri [1988] derived the linearized tangent stiffness matrix of each finite element in the corotational reference frame in an explicit form and showed that this approach based on assumed stresses is simpler in comparison with assumed-displacement type formulations. In contrast to [Shi and Atluri 1988], which presents the linearized tangent stiffness, the current work derives explicitly the tangent stiffness matrix under the nonlinear coupling of axial, torsional, and bidirectional-bending deformations.

One of the extensively employed approaches in the literature for the analysis of nonlinear problems with large deformations or rotations is based on variational principles. For instance, Cai et al. [2009a; 2009b] utilized the primal approach as well as the mixed variational principle [Reissner 1953] in the updated Lagrangian corotational reference frame to obtain an explicit expression for the tangent stiffness matrix of the elastic beam elements. Cai et al. [2009a] showed that the mixed variational principle in



comparison to the primal approach, which requires  $C^1$  continuous trial functions for displacements, needs simpler trial functions for the transverse bending moments and rotations. In fact, the authors assumed linear trial functions within each element and obtained much simpler tangent stiffness matrices for each element than those previously presented in the literature [Lo 1992; Kondoh et al. 1986; Simo 1985]. While Cai et al. [2009a] considered only a few macromembers, our analysis is applicable to metallic cellular microlattices with an extremely large number of repetitive RVEs. Since plasticity and buckling occur in many members of the microlattice, we found that the Newton-type algorithm that was utilized in [Cai et al. 2009a] fails. In the present study, we discovered that only our Newton homotopy method provides convergent solutions in the presence of the plasticity and buckling in a large number of members of the microlattice.

To solve tangent stiffness equations, we use a Newton homotopy method recently developed to solve a system of fully coupled nonlinear algebraic equations (NAEs) with as many unknowns as desired [Liu et al. 2009; Dai et al. 2014]. By using these methods, displacements of the equilibrium state are iteratively solved without the inversion of the Jacobian (tangent stiffness) matrix. Newton homotopy methods are advantageous, particularly when the effect of plasticity is going to be studied. It is well known that the simple Newton's method as well as the Newton–Raphson iteration method require the inversion of the Jacobian matrix, which fail to pass the limit load as the Jacobian matrix becomes singular, and require arc-length methodology which are commonly used in commercial off-the-shelf software such as ABAQUS. Furthermore, homotopy methods are useful in the following cases: when the system of algebraic equations is very large in size, when the solution is sensitive to the initial guess, and when the system of nonlinear algebraic equations is either over- or under-determined [Liu et al. 2009; Dai et al. 2014].

The paper is organized as follows. The theoretical background including the nonlinear coupling of axial, torsional, and bidirectional-bending deformations for a typical cellular member under large deformation; mixed variational principle in the corotational updated Lagrangian reference frame; the plastic hinge method; and the equation-solving algorithm accompanying Newton homotopy methods are summarized in Section 2. Section 3 is devoted to the validation of our methodology: a three-member rigid-knee frame, the Williams toggle problem, and a right-angle bent including the effect of plasticity are compared with the corresponding results given in the literature. Section 4 analyzes the mechanical behavior of two different cellular microlattices subjected to tensile, compressive, and shear loading. Throughout this section, it is shown that our calculated results (Young's modulus and yield stress) under compressive loading are very comparable with those measured experimentally by Schaedler et al. [2011] and Torrents et al. [2012]. Moreover, the progressive development of plastic hinges in the cellular microlattice as well as its deformed structure are presented. Finally, a summary and conclusion are given in Section 5. Appendices A, B, C, and D follow.

## 2. Theoretical background

Throughout this section, the concepts employed to derive nearly exact and highly efficient elastic-plastic homogenization of low-mass metallic systems with architected cellular microstructures are given. Nonlinear coupling of axial, torsional, and bidirectional-bending deformations; strain-displacement; and stress-strain relations in the updated Lagrangian corotational frame are described in Section 2.1. Section 2.2 is devoted to deriving an explicit expression for the tangent stiffness matrix of each member of the cellular

structure, accounting for large rigid rotations, moderate relative rotations, the bending-twisting-stretching coupling and elastic-plastic deformations. A solution algorithm is also given in Section 2.3.

**2.1. The nonlinear coupling of axial, torsional, and bidirectional-bending deformations for a spatial beam element with a tubular cross-section.** A typical 3D member of a cellular structure is considered, spanning between nodes 1 and 2 as illustrated in Figure 1. The element is initially straight with arbitrary cross section and is of the length  $l$  before deformation. As seen from Figure 1, three different coordinate systems are introduced:

- (1) the global coordinates (fixed global reference)  $\bar{x}_i$  with the orthonormal basis vectors  $\bar{e}_i$ ,
- (2) the local coordinates for the member in the undeformed state  $\tilde{x}_i$  with the orthonormal basis vectors  $\tilde{e}_i$ , and
- (3) the local coordinates for the member in the deformed state (current configuration)  $x_i$  with the orthonormal basis vectors of  $e_i$  ( $i = 1, 2, 3$ ).

Local displacements at the centroidal axis of the deformed member along  $e_i$ -directions are denoted as  $u_{i0}$ , ( $i = 1, 2, 3$ ). Rotation about  $x_1$ -axis (angle of twist) is denoted by  $\hat{\theta}$ , and those about  $x_i$ -axes,  $i = 2, 3$ , (bend angle) are denoted by  $\theta_{i0}$ ,  $i = 2, 3$ , respectively. It is assumed that nodes 1 and 2 of the member undergo arbitrarily large displacements, and rotations between the undeformed state of the member and its deformed state are arbitrarily finite. Moreover, it is supposed that local displacements in the current configuration ( $x_i$  coordinates system) are moderate and the axial derivative of the axial deflection at the centroid,  $\partial u_{10}/\partial x_1$  is small in comparison with that of the transverse deflections at the centroid,  $\partial u_{i0}/\partial x_1$  ( $i = 2, 3$ ).

We examine large deformations for a cylindrical member with an unsymmetrical cross section around  $x_2$ - and  $x_3$ -axes and constant cross section along  $x_1$ -axis subjected to torsion  $T$  around  $x_1$ -axis and bending moments  $M_2$  and  $M_3$  around  $x_2$ - and  $x_3$ -axes, respectively. It is assumed that the warping displacement  $u_{1T}(x_2, x_3)$  due to the torsion  $T$  is independent of  $x_1$  variable, the axial displacement at the centroid is  $u_{10}(x_1)$ , and the transverse bending displacements at the origin ( $x_2 = x_3 = 0$ ) are  $x_{20}(x_1)$  and

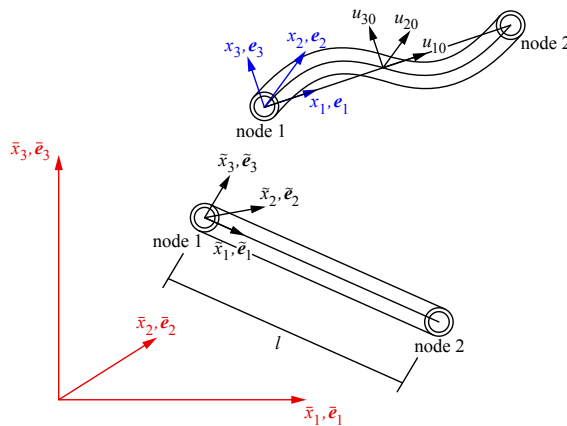


**Figure 1.** Nomenclature for the reference frames corresponding to the global, undeformed, and deformed states.

$x_3(x_1)$  along  $e_2$ - and  $e_3$ -directions, respectively. The reason for the consideration of the nonlinear axial, torsional, and bidirectional-bending coupling for each spatial beam element is the frame-like behavior of these cellular metallic microlattices. The scanning electron microscopy (SEM) images of microlattices given by Torrents et al. [2012] show the formation of partial fracture at nodes (for a microlattice with  $t = 500$  nm), localized buckling (for a microlattice with  $t = 1.3$   $\mu\text{m}$ ), and plastic hinging at nodes (for a microlattice with  $t = 26$   $\mu\text{m}$ ). Therefore, the 3D displacement field for each spatial beam element in the current configuration is considered as follows using the normality assumption of the Bernoulli–Euler beam theory:

$$\begin{aligned} u_1(x_1, x_2, x_3) &= u_{1T}(x_2, x_3) + u_{10}(x_1) - x_2 \frac{\partial u_{20}(x_1)}{\partial x_1} - x_3 \frac{\partial u_{30}(x_1)}{\partial x_1}, \\ u_2(x_1, x_2, x_3) &= u_{20}(x_1) - \hat{\theta} x_3, \\ u_3(x_1, x_2, x_3) &= u_{30}(x_1) + \hat{\theta} x_2. \end{aligned} \quad (1)$$

The Green–Lagrange strain components in the updated Lagrangian corotational frame  $e_i$  ( $i = 1, 2, 3$ ) are

$$\varepsilon_{ij} = \frac{1}{2}(u_{i,j} + u_{j,i} + u_{k,i}u_{k,j}), \quad (2)$$

where the index notation  $\bullet_{,i}$  denotes  $\partial \bullet / \partial x_i$  and  $k$  is a dummy index. Replacement of (1) into (2) results in the following strain components:

$$\begin{aligned} \varepsilon_{11} &= u_{1,1} + \frac{1}{2}(u_{1,1})^2 + \frac{1}{2}(u_{2,1})^2 + \frac{1}{2}(u_{3,1})^2 \approx u_{10,1} + \frac{1}{2}(u_{20,1})^2 + \frac{1}{2}(u_{30,1})^2 - x_2 u_{20,11} - x_3 u_{30,11}, \\ \varepsilon_{22} &= u_{2,2} + \frac{1}{2}(u_{1,2})^2 + \frac{1}{2}(u_{2,2})^2 + \frac{1}{2}(u_{3,2})^2 = \frac{1}{2}(u_{1T,2} - u_{20,1})^2 + \frac{1}{2}\hat{\theta}^2 \approx 0, \\ \varepsilon_{33} &= u_{3,3} + \frac{1}{2}(u_{1,3})^2 + \frac{1}{2}(u_{2,3})^2 + \frac{1}{2}(u_{3,3})^2 \approx 0, \\ \varepsilon_{12} &= \frac{1}{2}(u_{1,2} + u_{2,1}) + \frac{1}{2}u_{3,1}u_{3,2} \approx \frac{1}{2}(u_{1T,2} - \hat{\theta}_{,1}x_3), \\ \varepsilon_{13} &= \frac{1}{2}(u_{1,3} + u_{3,1}) + \frac{1}{2}u_{2,1}u_{2,3} \approx \frac{1}{2}(u_{1T,3} + \hat{\theta}_{,1}x_2), \\ \varepsilon_{23} &= \frac{1}{2}(u_{2,3} + u_{3,2}) + \frac{1}{2}u_{1,2}u_{1,3} \approx 0. \end{aligned} \quad (3)$$

By defining the following parameters:

$$\begin{aligned} \Theta &= \hat{\theta}_{,1}, \quad \mathfrak{N}_{22} = -u_{20,11}, \quad \mathfrak{N}_{33} = -u_{30,11}, \\ \varepsilon_{11}^0 &= u_{10,1} + \frac{1}{2}(u_{20,1})^2 + \frac{1}{2}(u_{30,1})^2 = \varepsilon_{11}^{0L} + \varepsilon_{11}^{0NL}, \end{aligned} \quad (4)$$

and employing them into (3), strain components can be rewritten as

$$\begin{aligned} \varepsilon_{11} &= \varepsilon_{11}^0 + x_2 \mathfrak{N}_{22} + x_3 \mathfrak{N}_{33}, \quad \varepsilon_{12} = \frac{1}{2}(u_{1T,2} - \Theta x_3), \\ \varepsilon_{13} &= \frac{1}{2}(u_{1T,3} + \Theta x_2), \quad \varepsilon_{22} = \varepsilon_{33} = \varepsilon_{23} = 0, \end{aligned} \quad (5)$$

and in the matrix notation as

$$\boldsymbol{\varepsilon} = \boldsymbol{\varepsilon}^L + \boldsymbol{\varepsilon}^N, \quad (6)$$

in which

$$\boldsymbol{\varepsilon}^L = \begin{bmatrix} \varepsilon_{11}^L \\ \varepsilon_{12}^L \\ \varepsilon_{13}^L \end{bmatrix} = \begin{bmatrix} u_{10,1} + x_2 \mathfrak{N}_{22} + x_3 \mathfrak{N}_{33} \\ \frac{1}{2}(u_{1T,2} - \Theta x_3) \\ \frac{1}{2}(u_{1T,3} + \Theta x_2) \end{bmatrix}, \quad (7)$$

$$\boldsymbol{\varepsilon}^N = \begin{bmatrix} \varepsilon_{11}^N \\ \varepsilon_{12}^N \\ \varepsilon_{13}^N \end{bmatrix} = \begin{bmatrix} \frac{1}{2}(u_{20,1})^2 + \frac{1}{2}(u_{30,1})^2 \\ 0 \\ 0 \end{bmatrix}. \quad (8)$$

Similarly, the member generalized strains are determined in the matrix form as

$$\mathbf{E} = \mathbf{E}^L + \mathbf{E}^N = \begin{bmatrix} \varepsilon_{11}^0 \\ \mathfrak{N}_{22} \\ \mathfrak{N}_{33} \\ \Theta \end{bmatrix}, \quad (9)$$

where  $\mathbf{E}^L = [u_{10,1} \ -u_{20,11} \ -u_{30,11} \ \hat{\theta}_{,1}]^T$  and  $\mathbf{E}^N = [\frac{1}{2}(u_{20,1})^2 + \frac{1}{2}(u_{30,1})^2 \ 0 \ 0 \ 0]^T$ .

We consider for now that the member material is linear elastic, thus the total stress tensor (the second Piola–Kirchhoff stress tensor)  $\mathbf{S}$  is calculated as

$$\mathbf{S} = \mathbf{S}^1 + \boldsymbol{\tau}^0. \quad (10)$$

Here  $\boldsymbol{\tau}^0$  is the preexisting Cauchy stress tensor, and  $\mathbf{S}^1$  is the incremental second Piola–Kirchhoff stress tensor in the updated Lagrangian corotational frame  $\mathbf{e}_i$  given by

$$\begin{aligned} S_{11}^1 &= E \varepsilon_{11}, & S_{12}^1 &= 2\mu \varepsilon_{12}, \\ S_{13}^1 &= 2\mu \varepsilon_{13}, & S_{22}^1 &= S_{33}^1 = S_{23}^1 \approx 0, \end{aligned} \quad (11)$$

in which  $\mu$  is the shear modulus,  $\mu = E/(2(1 + \nu))$ ,  $E$  is the elastic modulus, and  $\nu$  is the Poisson's ratio. Using (5) and (11), the generalized nodal forces for the member shown in Figure 1 subjected to the twisting and bending moments are calculated as

$$\begin{aligned} N_{11} &= \int_A S_{11}^1 \, dA = E(A\varepsilon_{11}^0 + I_2 \mathfrak{N}_{22} + I_3 \mathfrak{N}_{33}), \\ M_{22} &= \int_A S_{11}^1 x_2 \, dA = E(I_2 \varepsilon_{11}^0 + I_{22} \mathfrak{N}_{22} + I_{23} \mathfrak{N}_{33}), \\ M_{33} &= \int_A S_{11}^1 x_3 \, dA = E(I_3 \varepsilon_{11}^0 + I_{23} \mathfrak{N}_{22} + I_{33} \mathfrak{N}_{33}), \\ T &= \int_A (S_{13}^1 x_2 - S_{12}^1 x_3) \, dA = \mu I_{rr} \Theta, \end{aligned} \quad (12)$$

where  $A$  is the area of the cross section;  $I_i$  and  $I_{ij}$  ( $i, j = 2, 3$ ) are the first moment and the second moment of inertia of the cross section, respectively;  $I_2 = \int_A x_2 \, dA$ ,  $I_3 = \int_A x_3 \, dA$ ,  $I_{22} = \int_A x_2^2 \, dA$ ,  $I_{33} = \int_A x_3^2 \, dA$ ,  $I_{23} = \int_A x_2 x_3 \, dA$ , and  $I_{rr}$  is the polar moment of inertia,  $I_{rr} = \int_A (x_2^2 + x_3^2) \, dA$ . Using

the element generalized strains  $\mathbf{E}$  the element generalized stresses  $\boldsymbol{\sigma}$  are also determined in the matrix form as

$$\boldsymbol{\sigma} = \mathbf{D}\mathbf{E}, \tag{13}$$

in which

$$\boldsymbol{\sigma} = \begin{bmatrix} N_{11} \\ M_{22} \\ M_{33} \\ T \end{bmatrix}, \tag{14}$$

$$\mathbf{D} = \begin{bmatrix} EA & EI_2 & EI_3 & 0 \\ EI_2 & EI_{22} & EI_{23} & 0 \\ EI_3 & EI_{23} & EI_{33} & 0 \\ 0 & 0 & 0 & \mu I_{rr} \end{bmatrix}. \tag{15}$$

**2.2. Explicit derivation of tangent stiffness matrix undergoing large elasto-plastic deformation.** In this section, the mixed variational principle in the corotational updated Lagrangian reference frame and a plastic hinge method are employed to obtain explicit expressions for the tangent stiffness matrix of each member shown in Figure 1. The stiffness matrix is calculated for each member by accounting for large rigid rotations; moderate relative rotations; the nonlinear coupling of axial, torsional, and bidirectional-bending deformations; and the effect of plasticity. The functional of the mixed variational principle in the corotational updated Lagrangian reference frame and the trial functions for the stress and displacement fields within each element are given in Section 2.2.1. Plastic analysis using the plastic hinge method is described in Section 2.2.2. The explicit expression of the stiffness matrix in the presence of plasticity for each cellular member is also presented in Section 2.2.3.

**2.2.1. Mixed variational principle in the corotational updated Lagrangian reference frame.** Consideration of  $S_{ij}^1$  and  $u_i$ , respectively, as the components of the incremental second Piola–Kirchhoff stress tensor and the displacement field in the updated Lagrangian corotational frame, the functional of the mixed variational principle in the same reference frame with orthonormal basis vectors  $\mathbf{e}_i$  is obtained as

$$\mathcal{H}_R = \int_V \left\{ -B[S_{ij}^1] + \frac{1}{2}\tau_{ij}^0 u_{k,i} u_{k,j} + \frac{1}{2}S_{ij}(u_{i,j} + u_{j,i}) - \rho b_i u_i \right\} dV - \int_{S_\sigma} \bar{T}_i u_i dS, \tag{16}$$

where  $V$  is the volume in the current corotational reference state,  $S_\sigma$  is the part of the surface with the prescribed traction,  $\bar{T}_i = \bar{T}_i^0 + \bar{T}_i^1$  ( $i = 1, 2, 3$ ) are the components of the boundary tractions, and  $b_i = b_i^0 + b_i^1$  ( $i = 1, 2, 3$ ) are the components of body forces per unit volume in the current configuration. The displacement boundary conditions prescribed at the surface  $S_u$  are also considered as  $\bar{u}_i$  ( $i = 1, 2, 3$ ), assumed to be satisfied a priori. Equation (16) is a general variational principle governing stationary conditions, which with respect to variations  $\delta S_{ij}^1$  and  $\delta u_i$  results in the following incremental equations in the corotational updated Lagrangian reference frame:

$$\frac{\partial B}{\partial S_{ij}^1} = \frac{1}{2}(u_{i,j} + u_{j,i}), \tag{17}$$

$$[S_{ij}^1 + \tau_{ik}^0 u_{j,k}]_{,j} + \rho b_i^1 = -\tau_{ij,j}^0 - \rho b_i^0, \tag{18}$$

$$n_j[S_{ij}^1 + \tau_{ik}^0 u_{j,k}] - \bar{T}_i^1 = -n_j \tau_{ij}^0 + \bar{T}_i^0 \quad \text{on } S_\sigma, \quad (19)$$

where  $\mathbf{n}$  is the outward unit normal on the surface  $S_\sigma$ . For a group of members  $V_m$  ( $m = 1, 2, \dots, N$ ) with common surfaces  $\rho_m$ , (16) can be written as

$$\mathcal{H}_R = \sum_m \left( \int_{V_m} \left\{ -B[S_{ij}^1] + \frac{1}{2} \tau_{ij}^0 u_{k,i} u_{k,j} + \frac{1}{2} S_{ij} (u_{i,j} + u_{j,i}) - \rho b_i u_i \right\} dV - \int_{S_{\sigma_m}} \bar{T}_i u_i dS \right), \quad m = 1, 2, \dots, N. \quad (20)$$

If the trial function  $u_i$  and the test function  $\partial u_i$  for each member  $V_m$  ( $m = 1, 2, \dots, N$ ) are chosen in such a way that the interelement displacement continuity condition is satisfied at  $\rho_m$  a priori, then stationary conditions of  $\mathcal{H}_R$  for a group of finite elements lead to

$$\partial B / \partial S_{ij}^1 = \frac{1}{2} (u_{i,j} + u_{j,i}) \quad \text{in } V_m, \quad (21)$$

$$[S_{ij}^1 + \tau_{ik}^0 u_{j,k}]_{,j} + \rho b_i^1 = -\tau_{ij,j}^0 - \rho b_i^0 \quad \text{in } V_m, \quad (22)$$

$$[n_i (S_{ij}^1 + \tau_{ik}^0 u_{j,k})]^+ + [n_i (S_{ij}^1 + \tau_{ik}^0 u_{j,k})]^- = -[n_i \tau_{ij}^0]^+ - [n_i \tau_{ij}^0]^- \quad \text{at } \rho_m, \quad (23)$$

$$n_j [S_{ij}^1 + \tau_{ik}^0 u_{j,k}] - \bar{T}_i^1 = -n_j \tau_{ij}^0 + \bar{T}_i^0 \quad \text{on } S_{\sigma_m}. \quad (24)$$

Here,  $+$  and  $-$  denote the outward and inward quantities at the interface, respectively. The continuity of the displacement at the common interface  $\rho_m$  between elements is determined by

$$u_i^+ = u_i^- \quad \text{on } \rho_m. \quad (25)$$

Applying (5) and (13) into (20) and integrating over the cross sectional area of each element gives

$$\mathcal{H}_R = \sum_{m=1}^N \left\{ \int_l \left( -\frac{1}{2} \boldsymbol{\sigma}^T \mathbf{D}^{-1} \boldsymbol{\sigma} \right) dl + \int_l N_{11}^0 \frac{1}{2} (u_{20,1}^2 + u_{30,1}^2) dl + \int_l (\hat{N}_{11} \varepsilon_{11}^{0L} + \hat{M}_{22} \mathfrak{N}_{22} + \hat{M}_{33} \mathfrak{N}_{33} + \hat{T} \Theta) dl - \bar{\mathbf{Q}} \mathbf{q} \right\}, \quad (26)$$

in which  $\boldsymbol{\sigma}^0 = [N_{11}^0 \ M_{22}^0 \ M_{33}^0 \ T^0]^T$  is the initial member generalized stress in the corotational reference coordinates  $\mathbf{e}_i$ ,  $\hat{\boldsymbol{\sigma}} = \boldsymbol{\sigma} + \boldsymbol{\sigma}^0 = [\hat{N}_{11} \ \hat{M}_{22} \ \hat{M}_{33} \ \hat{T}]^T$  is the total member generalized stress in the coordinates  $\mathbf{e}_i$ ,  $\bar{\mathbf{Q}}$  is the nodal external generalized force vector in the global reference frame  $\bar{\mathbf{e}}_i$ , and  $\mathbf{q}$  is the nodal generalized displacement vector in the coordinates  $\bar{\mathbf{e}}_i$ . Equation (26) can be simplified by applying integration by parts to the third integral term on the right-hand side of the equation. More details on how to perform the integration are given in Appendix A. Stationary conditions for  $\mathcal{H}_R$  given in (26) result in

$$\begin{aligned} \mathbf{D}^{-1} \boldsymbol{\sigma} &= \mathbf{E}, \\ \hat{N}_{11,1} &= 0 \quad \text{in } V_m, \\ \hat{T}_{,1} &= 0 \quad \text{in } V_m, \\ \hat{M}_{22,11} + [N_{11}^0 u_{20,1}]_{,1} &= 0 \quad \text{in } V_m, \\ \hat{M}_{33,11} + [N_{11}^0 u_{30,1}]_{,1} &= 0 \quad \text{in } V_m, \end{aligned} \quad (27)$$

and the nodal equilibrium equations are obtained from the following relation:

$$\sum_{m=1}^N \{ \hat{N}_{11} \delta u_{10}|_0^l + \hat{M}_{22,1} \delta u_{20}|_0^l - \hat{M}_{22} \delta u_{20,1}|_0^l + \hat{M}_{33,1} \delta u_{30}|_0^l - \hat{M}_{33} \delta u_{30,1}|_0^l + \hat{T} \delta \hat{\theta}|_0^l + (N_{11}^0 u_{20,1}) \delta u_{20}|_0^l + (N_{11}^0 u_{30,1}) \delta u_{30}|_0^l - \bar{\mathbf{Q}} \delta \mathbf{q} \} = 0. \quad (28)$$

Herein, the trial functions for the stress and displacement fields within each member  $V_m$  ( $m = 1, 2, \dots, N$ ) are discussed. We assume that the components of the member generalized stress  $\sigma$  obey the following relation:

$$\sigma = \mathbf{P}\beta, \quad (29)$$

where

$$\mathbf{P} = \begin{bmatrix} 1 & 0 & 0 & 0 & 0 & 0 \\ 0 & -1 + x_1/l & -x_1/l & 0 & 0 & 0 \\ 0 & 0 & 0 & 1 - x_1/l & x_1/l & 0 \\ 0 & 0 & 0 & 0 & 0 & 1 \end{bmatrix}, \quad (30)$$

$$\beta = [n \quad {}^1m_3 \quad {}^2m_3 \quad {}^1m_2 \quad {}^2m_2 \quad m_1]^T. \quad (31)$$

Similarly, the components of the initial member generalized stress  $\sigma^0$  are determined as

$$\sigma^0 = \mathbf{P}\beta^0, \quad (32)$$

where

$$\beta^0 = [n^0 \quad {}^1m_3^0 \quad {}^2m_3^0 \quad {}^1m_2^0 \quad {}^2m_2^0 \quad m_1^0]^T. \quad (33)$$

Note that  ${}^i m_2 ({}^i m_2^0)$  and  ${}^i m_3 ({}^i m_3^0)$  are, respectively, bending moments (initial ones) around the  $x_2$ - and  $x_3$ -axes at the  $i$ -th node. Here,  $n (n^0)$  and  $m_1 (m_1^0)$  are the (initial) axial force and the (initial) twisting moment along the element, respectively. Therefore, the incremental internal nodal force vector  $\mathcal{B}$  for the element shown in Figure 1, with nodes 1 and 2 at the ends, can be expressed as

$$\mathcal{B} = [{}^1N \quad {}^1m_1 \quad {}^1m_2 \quad {}^1m_3 \quad {}^2N \quad {}^2m_1 \quad {}^2m_2 \quad {}^2m_3]^T, \quad (34)$$

which can be written as

$$\mathcal{B} = \mathfrak{R}\beta, \quad (35)$$

with

$$\mathfrak{R} = \begin{bmatrix} 1 & 0 & 0 & 0 & 0 & 0 \\ 0 & 0 & 0 & 0 & 0 & 1 \\ 0 & 1 & 0 & 0 & 0 & 0 \\ 1 & 0 & 0 & 0 & 0 & 0 \\ 0 & 0 & 0 & 0 & 0 & 1 \\ 0 & 0 & 0 & 0 & 1 & 0 \\ 0 & 0 & 1 & 0 & 0 & 0 \end{bmatrix}. \quad (36)$$

From (26), it is seen that only the squares of  $u_{20,1}$  and  $u_{30,1}$  appear within each member. Therefore, we assume the trial functions for the displacement field in such a way that  $u_{20,1}$  and  $u_{30,1}$  become linear for each member. Moreover, we suppose that the bend angles around the  $x_2$ - and  $x_3$ -axes along the member



shown in [Figure 1](#) change with respect to the nodal rotations  ${}^i\theta_{20}$  and  ${}^i\theta_{30}$  ( $i = 1, 2$ ) via the following relation:

$$\mathbf{u}_\theta = \mathbf{N}_\theta \mathbf{a}_\theta = \begin{bmatrix} 1 - x_1/l & 0 & x_1/l & 0 \\ 0 & 1 - x_1/l & 0 & x_1/l \end{bmatrix} \begin{bmatrix} {}^1\theta_{20} \\ {}^1\theta_{30} \\ {}^2\theta_{20} \\ {}^2\theta_{30} \end{bmatrix}. \quad (37)$$

Therefore, the nodal generalized displacement vector of the member can be expressed in the updated Lagrangian corotational frame  $\mathbf{e}_i$  as

$$\mathbf{a} = [{}^1\mathbf{a} \quad {}^2\mathbf{a}]^T, \quad (38)$$

where  ${}^i\mathbf{a}$  ( $i = 1, 2$ ) is the displacement vector of the  $i$ -th node:

$${}^i\mathbf{a} = [{}^i u_{10} \quad {}^i u_{20} \quad {}^i u_{30} \quad {}^i \hat{\theta} \quad {}^i \theta_{20} \quad {}^i \theta_{30}]^T. \quad (39)$$

The nodal generalized displacement vector of the member  $\mathbf{a}$  is related to the vector  $\mathbf{a}_\theta$  by

$$\mathbf{a}_\theta = \mathbf{T}_\theta \mathbf{a}, \quad (40)$$

in which

$$\mathbf{T}_\theta = \begin{bmatrix} 0 & 0 & 0 & 0 & 1 & 0 & 0 & 0 & 0 & 0 & 0 & 0 \\ 0 & 0 & 0 & 0 & 0 & 1 & 0 & 0 & 0 & 0 & 0 & 0 \\ 0 & 0 & 0 & 0 & 0 & 0 & 0 & 0 & 0 & 0 & 1 & 0 \\ 0 & 0 & 0 & 0 & 0 & 0 & 0 & 0 & 0 & 0 & 0 & 1 \end{bmatrix}. \quad (41)$$

Applying the trial functions of the stresses, (29) into the (26), the functional of the mixed variational principle in the corotational updated Lagrangian reference frame can be rewritten as

$$\mathcal{H}_R = -\mathcal{H}_{R1} + \mathcal{H}_{R2} + \mathcal{H}_{R3} - \mathcal{H}_{R4}. \quad (42)$$

Here,

$$\mathcal{H}_{R1} = \sum_{m=1}^N \int_l (\frac{1}{2} \boldsymbol{\sigma}^T \mathbf{D}^{-1} \boldsymbol{\sigma}) dl = \sum_{m=1}^N \int_l (\frac{1}{2} \boldsymbol{\beta}^T \mathbf{P}^T \mathbf{C} \mathbf{P} \boldsymbol{\beta}) dl, \quad (43)$$

$$\begin{aligned} \mathcal{H}_{R2} &= \sum_{m=1}^N \left\{ {}^2 N^2 u_{10} - {}^1 N^1 u_{10} + \frac{1}{l} ({}^1 m_3 - {}^2 m_3) ({}^2 u_{20} - {}^1 u_{20}) + {}^2 m_3^2 \theta_{30} - {}^1 m_3^1 \theta_{30} \right. \\ &\quad \left. + \frac{1}{l} ({}^2 m_2 - {}^1 m_2) ({}^2 u_{30} - {}^1 u_{30}) + {}^2 m_2^2 \theta_{20} - {}^1 m_2^1 \theta_{20} + {}^2 m_1^2 \hat{\theta} - {}^1 m_1^1 \hat{\theta} \right\} \\ &= \sum_{m=1}^N \{ \mathbf{B}^T \boldsymbol{\mathfrak{A}} \mathbf{a} \} = \sum_{m=1}^N \{ \boldsymbol{\beta}^T \boldsymbol{\mathfrak{R}}^T \boldsymbol{\mathfrak{A}} \mathbf{a} \}, \end{aligned} \quad (44)$$

$$\begin{aligned} \mathcal{H}_{R3} &= \sum_{m=1}^N \int_l N_{11}^0 \left[ \frac{1}{2} (u_{20,1})^2 + \frac{1}{2} (u_{30,1})^2 \right] dl = \sum_{m=1}^N \int_l \sigma_1^0 \left[ \frac{1}{2} (\theta_{20})^2 + \frac{1}{2} (\theta_{30})^2 \right] dl \\ &= \sum_{m=1}^N \int_l \frac{1}{2} \sigma_1^0 \mathbf{u}_\theta^T \mathbf{u}_\theta dl = \sum_{m=1}^N \int_l \frac{1}{2} \sigma_1^0 \mathbf{a}^T \mathbf{A}_{nm} \mathbf{a} dl, \end{aligned} \quad (45)$$

$$\mathcal{H}_{R4} = \sum_{m=1}^N (\mathbf{a}^T \mathbf{F} - \mathbf{a}^T \mathfrak{T}^T \mathfrak{R} \boldsymbol{\beta}^0), \tag{46}$$

where

$$\mathbf{C} = \mathbf{D}^{-1}, \tag{47}$$

$$\mathfrak{T} = \begin{bmatrix} -1 & 0 & 0 & 0 & 0 & 0 & 0 & 0 & 0 & 0 & 0 & 0 \\ 0 & 0 & 0 & -1 & 0 & 0 & 0 & 0 & 0 & 0 & 0 & 0 \\ 0 & 0 & 1/l & 0 & -1 & 0 & 0 & 0 & -1/l & 0 & 0 & 0 \\ 0 & -1/l & 0 & 0 & 0 & -1 & 0 & 1/l & 0 & 0 & 0 & 0 \\ 0 & 0 & 0 & 0 & 0 & 0 & 1 & 0 & 0 & 0 & 0 & 0 \\ 0 & 0 & 0 & 0 & 0 & 0 & 0 & 0 & 0 & 1 & 0 & 0 \\ 0 & 0 & -1/l & 0 & 0 & 0 & 0 & 0 & 1/l & 0 & 1 & 0 \\ 0 & 1/l & 0 & 0 & 0 & 0 & 0 & -1/l & 0 & 0 & 0 & 1 \end{bmatrix}, \tag{48}$$

$$\mathbf{A}_{nn} = \mathbf{T}_\theta^T \mathbf{N}_\theta^T \mathbf{N}_\theta \mathbf{T}_\theta. \tag{49}$$

Invoking the variational form for the functional of the mixed variational principle results in the following equation:

$$\sum_{m=1}^N \delta \boldsymbol{\beta}^T \left( - \int_l (\mathbf{P}^T \mathbf{C} \mathbf{P} \boldsymbol{\beta}) dl + \mathfrak{R}^T \mathfrak{T} \mathbf{a} \right) + \sum_{m=1}^N \delta \mathbf{a}^T \left( \mathfrak{T}^T \mathfrak{R} \boldsymbol{\beta} + \sigma_1^0 \int_l \mathbf{A}_{nn} \mathbf{a} dl - \mathbf{F} + \mathfrak{T}^T \mathfrak{R} \boldsymbol{\beta}^0 \right) = 0. \tag{50}$$

By letting  $\mathbf{H} = \int_l \mathbf{P}^T \mathbf{C} \mathbf{P} dl$ ,  $\mathbf{G} = \mathfrak{R}^T \mathfrak{T}$ ,  $\mathbf{K}_N = \sigma_1^0 \int_l \mathbf{A}_{nn} dl$ ,  $\mathbf{F}^0 = \mathbf{G}^T \boldsymbol{\beta}^0$ , (50) can be rewritten as

$$\sum_{m=1}^N \delta \boldsymbol{\beta}^T (-\mathbf{H} \boldsymbol{\beta} + \mathbf{G} \mathbf{a}) + \sum_{m=1}^N \delta \mathbf{a}^T (\mathbf{G}^T \boldsymbol{\beta} + \mathbf{K}_N \mathbf{a} - \mathbf{F} + \mathbf{F}^0) = 0. \tag{51}$$

**2.2.2. Plasticity effects in the large deformation analysis of members of a cellular microstructure.** For an elastic-perfectly plastic material, the incremental work done on the material per unit volume is  $dw = \sigma_{ij} (d\varepsilon_{ij}^p + d\varepsilon_{ij}^e)$  in which  $\varepsilon_{ij}^e$  and  $\varepsilon_{ij}^p$  are elastic and plastic components of strain, respectively, and  $\sigma_{ij}$  are the stress components. Using the plastic hinge method, the plastic deformation is developed along the member wherever the plasticity condition is satisfied. Therefore, the total work expended in deforming the material of the body is

$$W = \int_V \sigma_{ij} (d\varepsilon_{ij}^p + d\varepsilon_{ij}^e) dv = \int_V U(\varepsilon_{ij}^e) dV + \sum_i dW_i^p, \tag{52}$$

where  $U(\varepsilon_{ij}^e)$  is the elastic strain energy density function, and  $dW_i^p$  is the increment of plastic work at the  $i$ -th plastic hinge. When the theory of plastic potential is applied, the plasticity condition in terms of the stress components at the  $i$ -th node is expressed as

$$f_i(\sigma_{xi}, \sigma_{yi}, \dots, \tau_{xyi}, \dots, \sigma_Y) = 0, \tag{53}$$

the increment of plastic work at the  $i$ -th node can be expressed as

$$dW_i^P = d\mathbf{u}^{pT} \mathbf{x}, \quad (54)$$

in which  $d\mathbf{u}^P$ , the increment of plastic nodal displacement at the  $i$ -th node, is explained in terms of the function  $f_i(\mathbf{x}, \sigma_Y)$ :

$$d\mathbf{u}^P = d\lambda_i \boldsymbol{\phi}_i, \quad (55)$$

$$\boldsymbol{\phi}_i = \left[ \frac{\partial f_i(\mathbf{x}, \sigma_Y)}{\partial \mathbf{x}} \right], \quad (56)$$

where  $\mathbf{x}$  is the nodal force, and  $\delta\lambda_i$  is a positive scalar. Therefore, (52) can be rewritten as

$$W = \int_V U(\varepsilon_{ij}^e) dV + \sum d\lambda_i \boldsymbol{\phi}_i^T|_{l_p} \mathbf{x}, \quad (57)$$

where  $\hat{x}_i = l_p$  is the location of the plastic hinge. A variational form for the plastic work can be written as

$$\begin{aligned} \delta \left\{ \sum_{m=1}^N \left( \sum d\lambda_i \boldsymbol{\phi}_i^T|_{l_p} \right) (\mathbf{P}\boldsymbol{\beta}^0 + \mathbf{P}\boldsymbol{\beta}) \right\} &= \sum_{m=1}^N \delta \left( \sum d\lambda_i \boldsymbol{\phi}_i^T|_{l_p} \right) (\mathbf{P}\boldsymbol{\beta}^0 + \mathbf{P}\boldsymbol{\beta}) + \left( \sum d\lambda_i \boldsymbol{\phi}_i^T|_{l_p} \right) \mathbf{P} \delta \boldsymbol{\beta} \\ &= \sum_{m=1}^N \sum \delta d\lambda_i \boldsymbol{\phi}_i^T|_{l_p} (\mathbf{P}\boldsymbol{\beta}^0 + \mathbf{P}\boldsymbol{\beta}) + \left( \sum d\lambda_i \boldsymbol{\phi}_i^T|_{l_p} \right) \mathbf{P} \delta \boldsymbol{\beta} \\ &= \sum_{m=1}^N \sum \delta d\lambda_i \boldsymbol{\phi}_i^T|_{l_p} (\mathbf{P}\boldsymbol{\beta}^0 + \mathbf{P}\boldsymbol{\beta}) + \delta \boldsymbol{\beta}^T \mathbf{P}^T \left( \sum d\lambda_i \boldsymbol{\phi}_i^T|_{l_p} \right)^T. \end{aligned} \quad (58)$$

**2.2.3. Explicit derivation of tangent stiffness accompanying plasticity effects.** Using the functional of the mixed variational principle given in Section 2.2.1, (42)–(46), (57) is expressed as

$$\begin{aligned} W = \sum_{m=1}^N \left\{ - \int_l \left( \frac{1}{2} \boldsymbol{\beta}^T \mathbf{P}^T \mathbf{C} \mathbf{P} \boldsymbol{\beta} \right) dl + (\boldsymbol{\beta}^T \boldsymbol{\mathfrak{R}}^T \boldsymbol{\mathfrak{Z}} \mathbf{a}) + \int_l \frac{1}{2} \sigma_1^0 \mathbf{a}^T \mathbf{T}_\theta^T \mathbf{N}_\theta^T \mathbf{N}_\theta \mathbf{T}_\theta \mathbf{a} dl - (\mathbf{a}^T \mathbf{F} - \mathbf{a}^T \boldsymbol{\mathfrak{Z}}^T \boldsymbol{\mathfrak{R}} \boldsymbol{\beta}^0) \right. \\ \left. + \left( \sum d\lambda_i \boldsymbol{\phi}_i^T|_{l_p} \right) (\mathbf{P}\boldsymbol{\beta}^0 + \mathbf{P}\boldsymbol{\beta}) \right\}. \end{aligned} \quad (59)$$

Then, invoking  $\delta W = 0$  and using (51) and (58), (51) can be modified to include the effect of plasticity by introducing new determined matrices  $\hat{\boldsymbol{\beta}}$ ,  $\hat{\mathbf{H}}$ , and  $\hat{\mathbf{G}}$  by means of

$$\sum_{m=1}^N \delta \hat{\boldsymbol{\beta}}^T (-\hat{\mathbf{H}} \hat{\boldsymbol{\beta}} + \hat{\mathbf{G}} \mathbf{a}) + \sum_{m=1}^N \delta \mathbf{a}^T (\hat{\mathbf{G}}^T \hat{\boldsymbol{\beta}} + \mathbf{K}_N \mathbf{a} - \mathbf{F} + \mathbf{F}^0) = 0, \quad (60)$$

with

$$\hat{\boldsymbol{\beta}}^T = [\boldsymbol{\beta}^T \quad d\lambda], \quad \hat{\mathbf{H}} = \begin{bmatrix} \mathbf{H} & \mathbf{A}_{12} \\ \mathbf{A}_{12}^T & 0 \end{bmatrix}, \quad \hat{\mathbf{G}}^T = [\mathbf{G}^T \quad 0], \quad (61)–(63)$$

in which

$$\mathbf{A}_{12}^T = \left[ \frac{\partial f}{\partial N} \quad \frac{\partial f}{\partial \hat{M}_3} \left( -1 + \frac{l_p}{l} \right) \quad \frac{\partial f}{\partial \hat{M}_3} \left( -\frac{l_p}{l} \right) \quad \frac{\partial f}{\partial \hat{M}_2} \left( 1 - \frac{l_p}{l} \right) \quad \frac{\partial f}{\partial \hat{M}_2} \frac{l_p}{l} \quad \frac{\partial f}{\partial \hat{M}_1} \right]. \quad (64)$$

Since  $\delta \hat{\boldsymbol{\beta}}^T$  in (60) are independent and arbitrary in each element, we have

$$\hat{\mathbf{H}} \hat{\boldsymbol{\beta}} = \hat{\mathbf{G}} \mathbf{a}, \quad (65)$$

$$\hat{\boldsymbol{\beta}} = \hat{\mathbf{H}}^{-1} \hat{\mathbf{G}} \mathbf{a}. \quad (66)$$

By letting  $\sum_{m=1}^N \delta \mathbf{a}^T (\hat{\mathbf{G}}^T \hat{\boldsymbol{\beta}} + \mathbf{K}_N \mathbf{a} - \mathbf{F} + \mathbf{F}^0) = 0$  and substituting  $\hat{\boldsymbol{\beta}}$  from (66), we obtain

$$(\hat{\mathbf{G}}^T \hat{\mathbf{H}}^{-1} \hat{\mathbf{G}} + \mathbf{K}_N) \mathbf{a} - \mathbf{F} + \mathbf{F}^0 = 0, \quad (67)$$

Therefore, the stiffness matrix  $\mathcal{K}$  in the presence of plasticity is derived explicitly as

$$\mathcal{K} = \hat{\mathbf{G}}^T \hat{\mathbf{H}}^{-1} \hat{\mathbf{G}} + \mathbf{K}_N = \mathbf{G}^T \mathbf{H}^{-1} \mathbf{G} + \mathbf{K}_N - \mathbf{G}^T \mathbf{H}^{-1} \mathbf{A}_{12} \mathbf{C}^T \mathbf{G} = \mathbf{K} - \mathbf{G}^T \mathbf{H}^{-1} \mathbf{A}_{12} \mathbf{C}^T \mathbf{G} = \mathbf{K} - \mathbf{K}_P, \quad (68)$$

where

$$\mathbf{K} = \mathbf{G}^T \mathbf{H}^{-1} \mathbf{G} + \mathbf{K}_N = \mathbf{K}_L + \mathbf{K}_N, \quad (69)$$

$$\mathbf{K}_P = \mathbf{G}^T \mathbf{H}^{-1} \mathbf{A}_{12} \mathbf{C}^T \mathbf{G}, \quad (70)$$

$$\mathbf{C}^T = (\mathbf{A}_{12}^T \mathbf{H}^{-1} \mathbf{A}_{12})^{-1} \mathbf{A}_{12}^T \mathbf{H}^{-1}. \quad (71)$$

Since we are studying the nonlinear coupling of axial, torsional, and bidirectional-bending deformations for each element, the plasticity condition is introduced by  $f_i(N, \hat{M}_1, \hat{M}_2, \hat{M}_3) = 0$  at the location of the  $i$ -th plastic hinge; then

$$\boldsymbol{\phi}_i = \left[ \frac{\partial f_i}{\partial N} \quad \frac{\partial f_i}{\partial \hat{M}_1} \quad \frac{\partial f_i}{\partial \hat{M}_2} \quad \frac{\partial f_i}{\partial \hat{M}_3} \right]^T \quad (72)$$

and

$$\begin{aligned} \sum d\lambda_i \boldsymbol{\phi}_i^T |_{l_p} &= \left[ \sum d\lambda_i \frac{\partial f_i}{\partial N} |_{l_p} \quad \sum d\lambda_i \frac{\partial f_i}{\partial \hat{M}_1} |_{l_p} \quad \sum d\lambda_i \frac{\partial f_i}{\partial \hat{M}_2} |_{l_p} \quad \sum d\lambda_i \frac{\partial f_i}{\partial \hat{M}_3} |_{l_p} \right] \\ &= [H_P \quad \theta_{P1}^* \quad \theta_{P2}^* \quad \theta_{P3}^*], \end{aligned} \quad (73)$$

in which  $H_P$  is the plastic elongation and  $\theta_{P_i}^*$ ,  $i = (1, 2, 3)$  are the plastic rotations at the location of plastic hinges. Components of the element tangent stiffness matrices,  $\mathbf{K}_N$ ,  $\mathbf{K}_L$ , and  $\mathbf{K}_P$ , are presented in [Appendix B](#). Transformation matrices relating coordinate systems corresponding to the deformed and undeformed states to the global coordinates system ([Figure 1](#)) are given in [Appendix C](#).

**2.3. Solution algorithm.** To solve the incremental tangent stiffness equations, we employ a Newton homotopy method [[Liu et al. 2009](#); [Dai et al. 2014](#)]. One of the most important reasons that we use the newly developed scalar homotopy method is that this approach does not need to invert the Jacobian matrix (the tangent stiffness matrix) to solve NAEs. In the case of complex problems (such as elastic-plastic analyses of large deformations and near the limit-load points in post-buckling analyses of geometrically nonlinear frames) where the Jacobian matrix may be singular, the iterative Newton's methods become problematic and necessitate the use of arc-length methods found in software such as ABAQUS.

One of the other advantages of the recently developed homotopy methods is the improved performance over the Newton–Raphson method when the Jacobian matrix is nearly singular or is severely ill-conditioned. For instance, when we considered the problem discussed in [Section 3.1](#) (three-member rigid-knee frame) using the Newton–Raphson algorithm, the provided code couldn’t converge to capture the critical load, while it converged rapidly after switching to the homotopy algorithm. Moreover, we discovered that while the Newton-type algorithm fails to converge, the Newton homotopy method provides convergent solutions in the presence of plasticity and buckling in a large number of members of the microlattice. As another benefit of the employed algorithm, our developed CELLS/LIDS code is not sensitive to the initial guess of the solution vector, unlike the Newton–Raphson method.

The homotopy method was first introduced by Davidenko [1953] to enhance the convergence rate from a local convergence to a global one for the solution of the NAEs of  $\mathbf{F}(\mathbf{X}) = \mathbf{0}$ ; where  $\mathbf{X} \in \mathbb{R}^n$  is the solution vector. This methodology was based on the employment of a vector homotopy function  $\mathbf{H}(\mathbf{X}, t)$  to continuously transform a function  $\mathbf{G}(\mathbf{X})$  into  $\mathbf{F}(\mathbf{X})$ . The variable  $t$  ( $0 \leq t \leq 1$ ) was the homotopy parameter, treated as a time-like fictitious variable, and the homotopy function was any continuous function such that  $\mathbf{H}(\mathbf{X}, 0) = \mathbf{0} \Leftrightarrow \mathbf{G}(\mathbf{X}) = \mathbf{0}$  and  $\mathbf{H}(\mathbf{X}, 1) = \mathbf{0} \Leftrightarrow \mathbf{F}(\mathbf{X}) = \mathbf{0}$ . More details on the vector homotopy functions are given in [Appendix D](#). To improve the vector homotopy method, Liu et al. [2009] proposed a scalar homotopy function  $h(\mathbf{X}, t)$  such that  $h(\mathbf{X}, 0) = 0 \Leftrightarrow \|\mathbf{G}(\mathbf{X})\| = 0$  and  $h(\mathbf{X}, 1) = 0 \Leftrightarrow \|\mathbf{F}(\mathbf{X})\| = 0$ . They introduced the following scalar fixed-point homotopy function:

$$h(\mathbf{X}, t) = \frac{1}{2}(t\|\mathbf{F}(\mathbf{X})\|^2 - (1-t)\|\mathbf{X} - \mathbf{X}_0\|^2), \quad 0 \leq t \leq 1. \quad (74)$$

Later, Dai et al. [2014] suggested more convenient scalar homotopy functions which hold for  $t \in [0, \infty)$  instead of  $t \in [0, 1]$ . We consider the following scalar Newton homotopy function to solve the system of equations  $\mathbf{F}(\mathbf{X}) = \mathbf{0}$ :

$$h_n(\mathbf{X}, t) = \frac{1}{2}\|\mathbf{F}(\mathbf{X})\|^2 + \frac{1}{2Q(t)}\|\mathbf{F}(\mathbf{X}_0)\|^2, \quad t \geq 0, \quad (75)$$

resulting in

$$\dot{\mathbf{X}} = -\frac{1}{2} \frac{\dot{Q}\|\mathbf{F}\|^2}{Q\|\mathbf{B}^T \mathbf{F}\|^2} \mathbf{B}^T \mathbf{F}, \quad t \geq 0, \quad (76)$$

where  $\mathbf{B}$  is the Jacobian (tangent stiffness) matrix evaluated with  $\mathbf{B} = \partial \mathbf{F} / \partial \mathbf{X}$  and  $Q(t)$  is a positive and monotonically increasing function to enhance the convergence speed. Various possible choices of  $Q(t)$  can be found in [Dai et al. 2014]. Finally, the solution vector  $\mathbf{X}$  can be obtained by numerically integrating (76) or using iterative Newton homotopy methods discussed in [Appendix D](#).

### 3. Representative approach and its validation

This section is devoted to considering the validity of our proposed methodology. To this end, three different problems are analyzed and compared with results from other methods given in the literature. The critical load of the three-member rigid-knee frame is computed in [Section 3.1](#). [Section 3.2](#) examines the classical Williams toggle problem. [Section 3.3](#) is devoted to considering the accuracy and efficiency of the calculated stiffness matrix in the presence of plasticity by solving the problem of the right-angle bent.

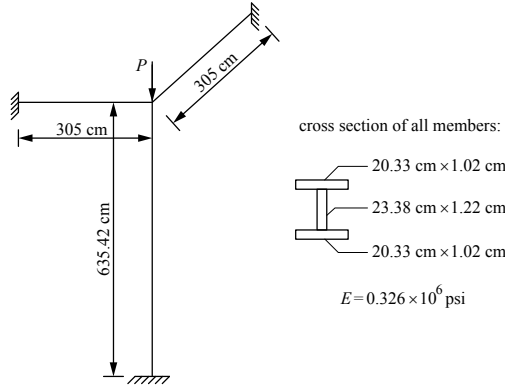


**Figure 2.** The geometry of three-member rigid-knee frame and the cross section of elements.

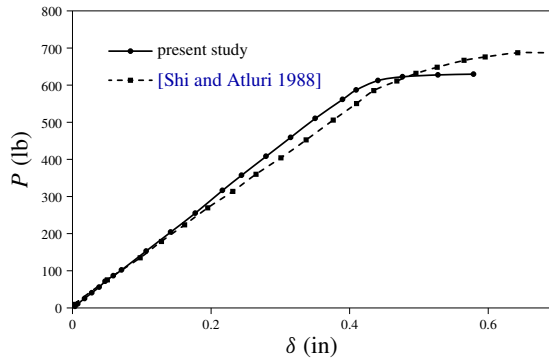


**Figure 3.** Load versus displacement at the location of point load.

**3.1. Three-member rigid-knee frame.** The geometry of the three-member rigid-knee frame and the cross section of elements are shown in Figure 2. Using the CELLS/LIDS (CELLular Structures/Large Inelastic DeformationS) code, the longer element is divided into 6 elements and shorter elements are divided into 3 elements. A transverse perturbation loading  $0.001P$  is also applied at the midpoint of the longer member. Load versus displacement at the location of point load is plotted in Figure 3 and is compared with the corresponding results presented by Shi and Atluri [1988]. As it is observed, there is a good agreement between present calculated results and those obtained in [Shi and Atluri 1988]. Please note that Shi and Atluri [1988] have also mentioned that their computed critical load is a little higher than that obtained by Mallett and Berke [1966].

**3.2. Classical Williams toggle problem.** Williams [1964] developed a theory to study the behavior of the members of a rigid jointed plane framework and applied it to the case of the rigid jointed toggle. The classical toggle problem is exhibited in Figure 4, consisting of two rigidly jointed elements with equal lengths  $L$  and anchored at their remote ends. The angle between the element and the horizontal axis  $b$  is related to the length of the elements via the relation  $L \sin(b) = 0.32$ . The characteristics of the cross section of elements are also included in Figure 4. The structure is subjected to an external load  $W$  along the  $z$ -direction at the apex, as illustrated in Figure 4. The deflection of the apex versus the applied

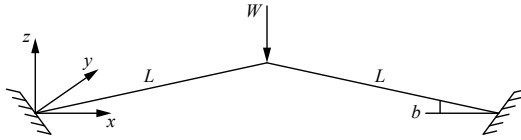


**Figure 4.** Classical toggle problem.

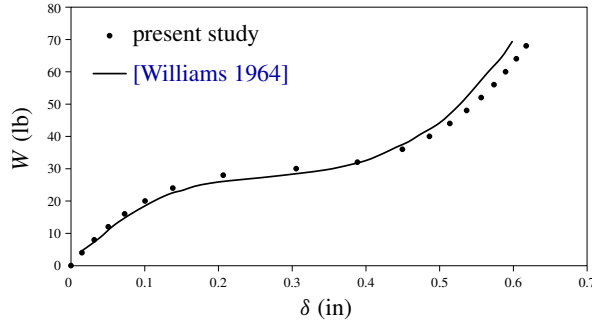


**Figure 5.** Displacement at the apex of toggle versus the applied load.

load is calculated and compared with results given by Williams [1964] in Figure 5. As it is seen, good correspondence is obtained.

**3.3. Elastic-plastic right-angle bent.** Throughout this section, the accuracy and efficiency of our methodology to consider the effect of plasticity is investigated. To this end, the problem of right-angle bent is calculated and compared with the results from other works. Two equal members of length  $l$  with square cross sections are located in the  $xy$ -plane and are subjected to an external load  $F$  along the  $z$ -direction at the midpoint of one element, as shown in Figure 6. Both members are anchored at their remote ends. Therefore, they are under both bending  $M$  and twisting  $T$ . The yielding condition for such a perfectly plastic material subjected to bending and twisting is  $(M/M_0)^2 + (T/T_0)^2 = 1$ , in which  $M_0$  and  $T_0$  are, respectively, fully plastic bending and twisting moments. Employing our CELLS/LIDS code, each member is simulated by four elements. The formation of plastic hinges via the increase of external load is presented in Figure 6 and the calculated amounts of  $F l / M_0$  at the onset of plastic hinges are compared with the results given by Shi and Atluri [1988]. The variation of  $\delta \times EI / (M_0 l^2)$  with respect to  $F l / M_0$  is also plotted in Figure 7. Here,  $\delta$  is the displacement of the tip of the right-angle bent along the  $z$ -direction, and  $E$  is the Young’s modulus. The results also show good agreement with those in [Hodge 1959].

#### 4. Low-mass metallic systems with architected cellular microstructures

This section is devoted to the computational study of large elastic-plastic deformations of the nickel-based cellular microlattices fabricated at HRL Laboratories [Schaedler et al. 2011; Torrents et al. 2012]. To mimic the fabricated cellular microstructures, we model repetitive RVEs constructed by the strut members with the same geometry and dimension as the experiment. Each member of the actual cellular microstructure undergoing large elastic-plastic deformations is modeled by a single spatial beam finite element with 12 DOF, providing the capability to decrease considerably the number of DOF in comparison with the same simulation using commercial FE software. The strut members are connected in such



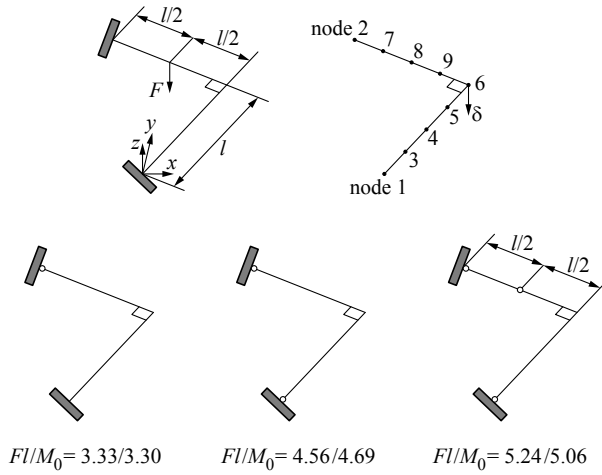


**Figure 6.** Progressive development of plastic hinges in the right-angle bent. The first number in the  $FI/M_0$  sets is from the present study, and the second is from [Shi and Atluri 1988].

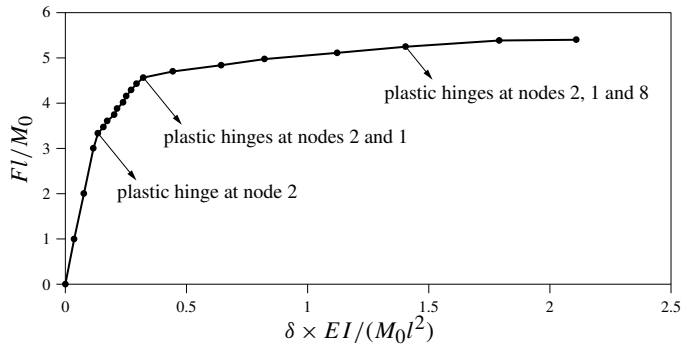


**Figure 7.** The variation of normalized load with respect to the normalized displacement at the tip of right-angle bent.

a way that the topology of the fabricated cellular material is achieved. In the following, more details on the formation of RVE mimicking the actual microstructural samples are given. The properties of nickel as the parent material of the architected material is introduced within the CELLS/LIDS code by the Young’s modulus  $E^s = 200$  GPa and the yield stress  $\sigma_y^s = 450$  MPa. The considered RVE is a Bravais lattice formed by repeating octahedral unit cells without any lattice members in the basal plane, as shown in Figure 8. The lattice constant parameter of the unit cell is  $a$ ; see Figure 8. The RVE is constructed by a node-strut representation and includes the nodes coordinate and the nodes connectivity, which determines the length of the members as well as the topology of the microlattice. Furthermore, the present RVE approach accurately captures the microstructural length scale by introducing the area, the first and the second moments of inertia, and the polar moment of inertia of the symmetrical/unsymmetrical cross section of the hollow tube member within the formulation. Periodic boundary conditions (PBCs) are considered along the  $x$ - and  $y$ -directions of the RVE, which are the directions perpendicular to the depth

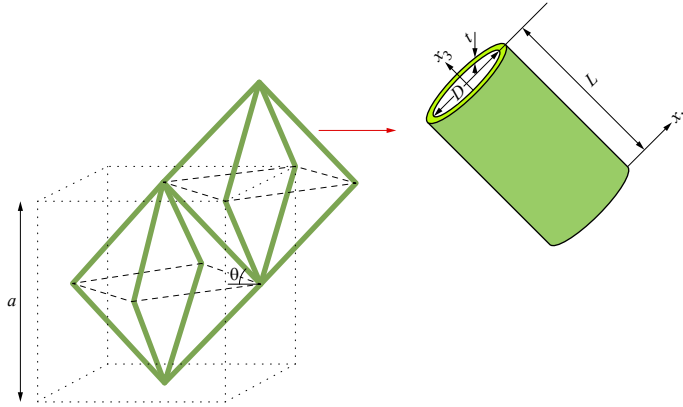


**Figure 8.** The unit cell of RVE consisting of an octahedron as well as the geometry of strut members.

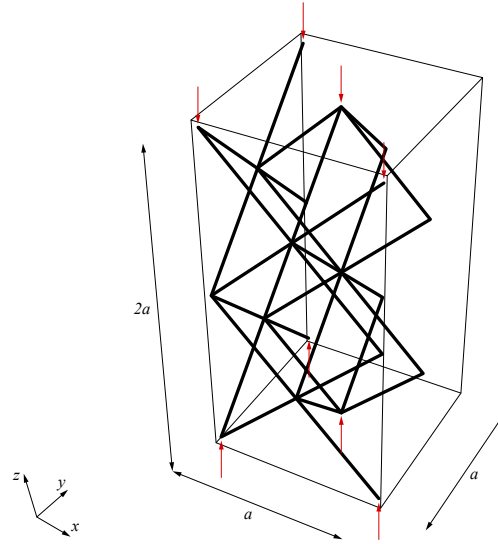
of the thin film microlattice. PBCs are involved by  ${}^i\mathbf{a}|_{x=0} = {}^j\mathbf{a}|_{x=na}$  along the  $x$ -direction and by  ${}^k\mathbf{a}|_{y=0} = {}^l\mathbf{a}|_{y=ma}$  along the  $y$ -direction, in which  ${}^\alpha\mathbf{a}$  ( $\alpha = i, j, k, l$ ) is the displacement vector of the  $\alpha$ -th node (39) on the boundary of the RVE, and  $n$  or  $m$  is determined based on the size of the RVE along the  $x$ - or  $y$ -direction, respectively. For example, for the  $Na \times Ma \times Ka$  RVE,  $n = N$  and  $m = M$ . The depth of the RVE is modeled to be equal to the thickness of the thin film. Section 4.1 studies the  $1a \times 1a \times 2a$  RVE including 20 nodes and 32 strut members, and Section 4.2 examines both the  $2a \times 2a \times 2a$  RVE with 60 nodes and 128 strut members and the  $1a \times 1a \times 4a$  RVE with 36 nodes and 64 members. We study the mechanical behavior of the thin film cellular microlattice under tension, compression, and shear loadings. To this end, nodes on both the top and bottom faces of the RVE are loaded accordingly. Microlattice members are cylindrical hollow tubes, the dimensions of which are also included in Figure 8. Torrents et al. [2012] tested samples with the strut member length of  $L = 1\text{--}4$  mm, strut member diameter of  $D = 100\text{--}500 \mu\text{m}$ , wall thickness of  $t = 100\text{--}500 \mu\text{m}$ , and inclination angle of  $\theta = 60^\circ$ . In Sections 4.1 and 4.2, we analyze the mechanical behavior of two different fabricated cellular microlattices in which the geometry of their strut members ( $L$ ,  $D$ ,  $t$ , and  $\theta$ ) are explained, respectively. Since nonlinear coupling of axial, torsional, and bidirectional-bending deformations is considered for each member, the plasticity condition is determined by the following relation:

$$f(N_{11}, M_{22}, M_{33}, T) = \frac{1}{M_0} \{M_{22}^2 + M_{33}^2 + T^2\}^{1/2} + \frac{N_{11}^2}{N_0^2} - 1 = 0, \tag{77}$$

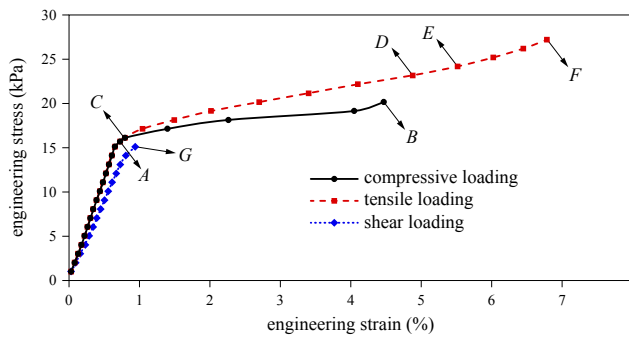
where  $M_0$  and  $N_0$  are the fully plastic bending moment and fully plastic axial force, respectively.

**4.1. Architected material with more flexibility as compared to parent material.** An RVE including 20 nodes and 32 members with PBCs along the  $x$ - and  $y$ -directions is employed to model a cellular thin film with the thickness of  $2a$ ; see Figure 9. This figure shows the application of the external compressive loading, which changes according to tensile as well as shear loads. The dimensions of each member in the microlattice is as follows:  $L = 1050 \mu\text{m}$ ,  $D = 150 \mu\text{m}$ , and  $t = 500 \text{ nm}$ .

The engineering stress as a function of the engineering strain is presented in Figure 10 for the nickel cellular microlattice under compressive, tensile, and shear loads. The stress-strain curves corresponding



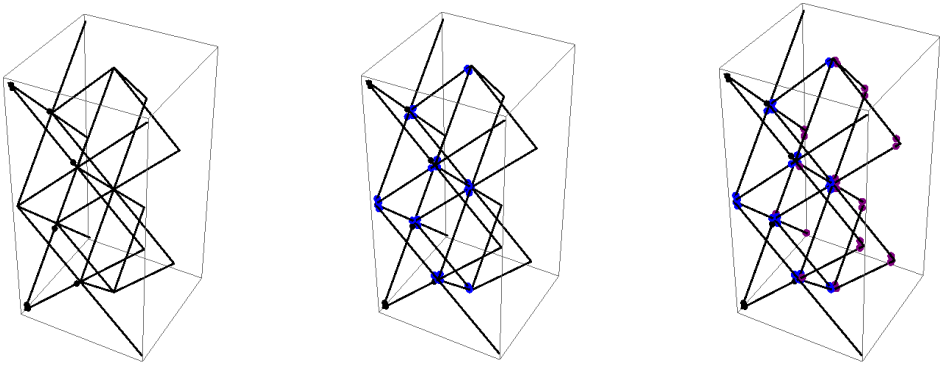
**Figure 9.**  $1a \times 1a \times 2a$  RVE including 20 nodes and 32 strut members.



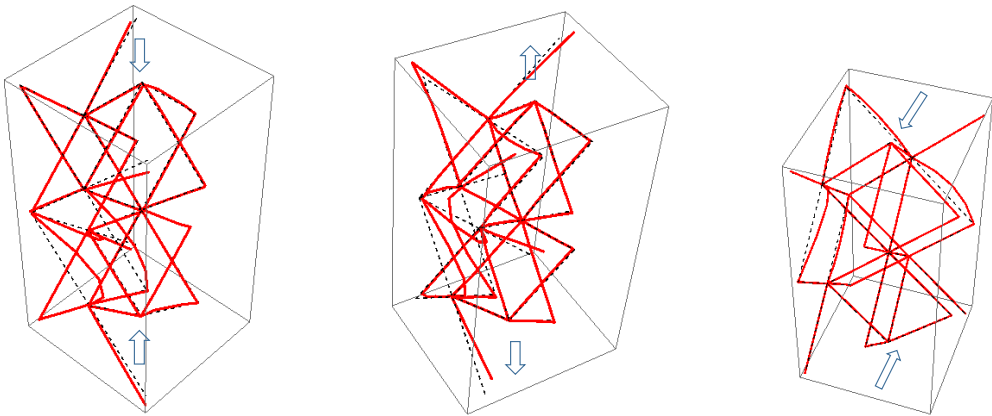
**Figure 10.** Stress-strain curve of the cellular microlattice subjected to tension, compression, and shear.

to the tensile and compressive loads result in the overall yield stress of the RVE  $\sigma_y = 15.117$  kPa and the Young's modulus  $E = 2.291$  MPa. Torrents et al. [2012] measured the respective values  $\sigma_y = 14.2 \pm 2.5$  kPa and  $E = 1.0 \pm 0.15$  MPa for their tested microlattice labeled with  $G$  ( $L = 1050 \pm 32 \mu\text{m}$ ,  $D = 160 \pm 24 \mu\text{m}$ ,  $t = 0.55 \pm 0.06 \mu\text{m}$ ). The results calculated from our computational methodology agree excellently with those obtained from experiment by Torrents et al. [2012]. It is found that this architected material shows a yield stress much smaller than the parent material, which offers more flexibility in tailoring the response to impulsive loads. In addition, we are able to calculate the shear modulus of the cellular microlattice from our obtained stress-strain curve corresponding to the shear load, resulting in  $G = 1.773$  MPa.

The progressive development of plastic hinges as the tensile and compressive loads increase is shown in Figure 11. The total deformation of the RVE considering the effect of plasticity corresponding to the step  $B$  of compressive loading, step  $F$  of tensile loading, and step  $G$  of shear loading is also given in



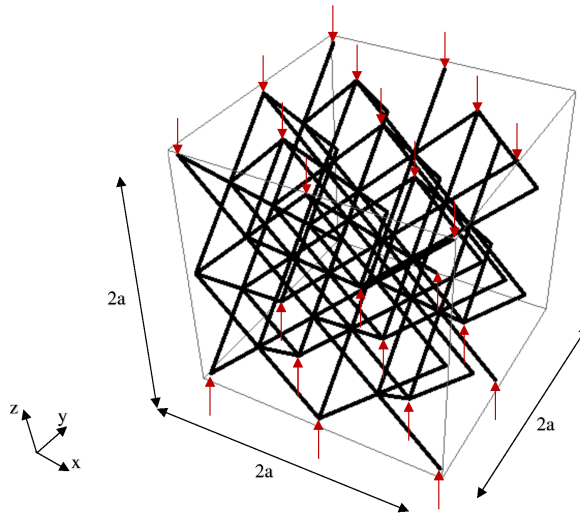
**Figure 11.** Progressive development of plastic hinges in cellular microlattice under tension and compression at different steps of loading shown in Figure 10. Left: plastic hinges formed at steps *A* and *C*. Middle: plastic hinges formed at steps *B* and *D*. Right: plastic hinges formed at step *E*.



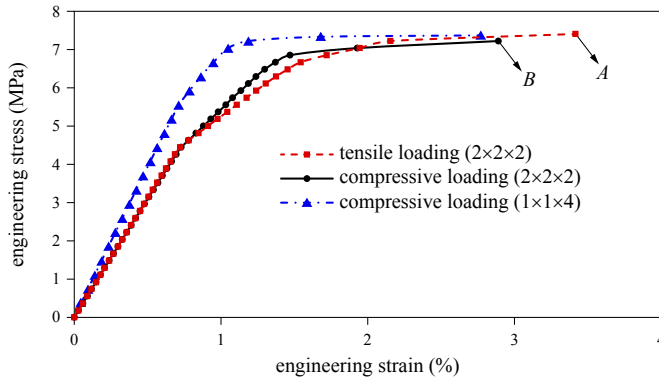
**Figure 12.** Total elastic-plastic deformation of the cellular microstructure in red color at different steps of loading shown in Figure 10. Left: at step *B* of the compressive loading. Middle: at step *F* of the tensile loading. Right: at the step *G* of shear loading. The initial unloaded state is also shown (dashed lines).

Figure 12. Since plastic deformation can absorb energy, this architected material will be appropriate for protection from impacts and shockwaves in applications varying from helmets to vehicles and sporting gear [Schaedler and Carter 2016].

**4.2. Architected material with further increased relative density.** In this case, the fabricated sample is computationally modeled using an RVE consisting of 60 nodes and 128 members with PBCs along the  $x$ - and  $y$ -directions; see Figure 13. The strut member dimensions are  $L = 1200 \mu\text{m}$ ,  $D = 175 \mu\text{m}$  and  $t = 26 \mu\text{m}$ . The wall thickness of the member in this case is 52 times greater than that of the previous case in Section 4.1. The RVE is subjected to both tensile and compressive loading in order to study the mechanical properties of the architected material. The engineering stress-engineering strain



**Figure 13.**  $2a \times 2a \times 2a$  RVE including 60 nodes and 128 strut members.



**Figure 14.** Stress-strain curve of the cellular microlattice subjected to tension and compression.

curve is plotted in [Figure 14](#). Stress analysis shows bilinear elastic moduli for this cellular microlattice subjected to both tension and compression. Elastic modulus for the first phase is calculated as 0.619 GPa under both tensile and compressive loading. For the second phase it is calculated to be 0.284 GPa under tension and 0.364 GPa under compression. The yield stress is obtained as 7.2222 MPa and 6.8519 MPa subjected to tensile and compressive loading, respectively. Plastic hinges emanate at the stress level 6.6667 MPa when the microlattice is under tension and originate at the stress level 6.8519 MPa when the microlattice is subjected to compression. It is found that both Young's modulus and the yield stress of the cellular microlattice increase significantly by increasing the strut thickness. It is well-known that the elastic modulus and the yield strength of the cellular materials increase with the increase of their relative density [[Gibson and Ashby 1988](#)]. Relative density is calculated as  $\rho/\rho_s$ , where  $\rho$  is the mass of the lattice divided by the total bounding volume  $v$  and  $\rho_s$  is the mass of the lattice divided by only the volume of the constituent solid material  $v_s$ . Therefore,  $\rho/\rho_s = (m/v)/(m/v_s) = v_s/v$  in which  $v_s = \# \text{ of members} \times \pi [(\frac{1}{2}D + t)^2 - (\frac{1}{2}D)^2] \times L$  and  $v = 8a^3$  or  $2a^3$  for a  $2a \times 2a \times 2a$  RVE or a  $1a \times 1a \times 2a$  RVE,

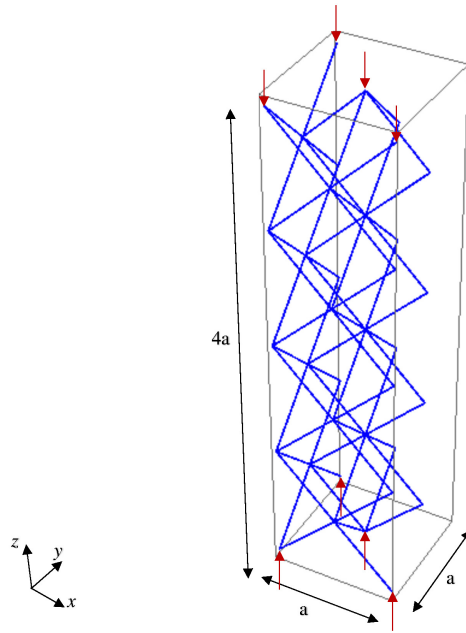


**Figure 15.**  $1a \times 1a \times 4a$  RVE consisting of 36 nodes and 64 strut members.

respectively. We calculate the relative densities of the cellular microlattices examined through this section and Section 4.1 as 0.03511 and 0.00066, respectively. Torrents et al. [2012] extracted experimentally the strain-stress curve of this microlattice (labeled A) under compression. They measured the Young's modulus  $E = 0.58 \pm 0.003$  GPa and the yield stress  $\sigma_y = 8.510 \pm 0.025$  MPa for the tested microlattice with strut diameter  $D = 175 \pm 26 \mu\text{m}$ , strut length  $L = 1200 \pm 36 \mu\text{m}$ , and wall thickness  $t = 26.00 \pm 2.6 \mu\text{m}$ . We see that there is a very good correspondence between our calculated mechanical properties of the sample under compressive loading and those measured experimentally by Torrents et al. [2012].

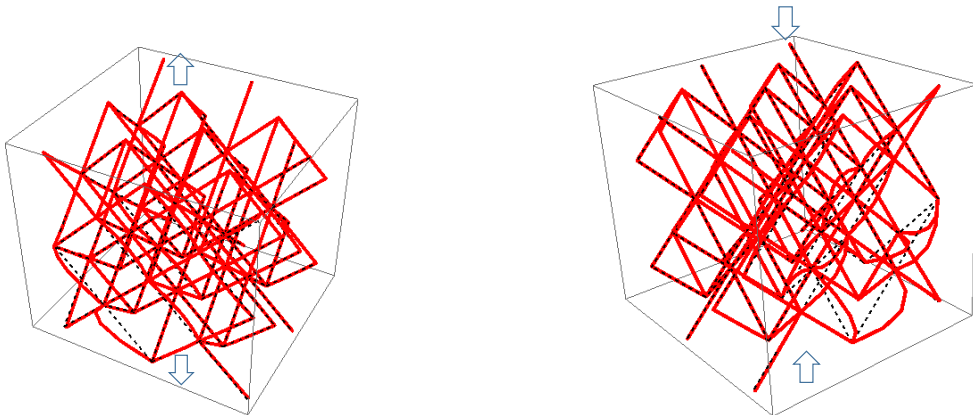


**Figure 16.** Elastic-plastic deformation of the cellular microstructure in red color at different steps of loading shown in Figure 14. Left: at step A of tensile loading. Right: at step B of compressive loading. The initial unloaded state is also shown (dashed lines).

To investigate the effect of the size of the RVE on the macroscale response of the cellular microlattice, the depth of the  $2a \times 2a \times 2a$  RVE (Figure 13) is increased by a factor of two. Due to the PBCs along the  $x$ - and  $y$ -directions, the size of the RVE along these directions is considered to be  $1a$ . Therefore, a  $1a \times 1a \times 4a$  RVE consisting of 36 nodes and 64 strut members is modeled (see Figure 15), and the corresponding stress-strain curve under compression is included in Figure 14. The stress analysis of this  $1a \times 1a \times 4a$  RVE also exhibits bilinear elastic behavior with the elastic moduli of 0.7841 GPa for the first linear phase and 0.4721 GPa for the second linear phase. The yield stress is calculated to be 7.3704 MPa, which comes closer to the corresponding experimental value,  $\sigma_y = 8.510 \pm 0.025$  MPa, in comparison with 6.8519 MPa calculated for a  $2a \times 2a \times 2a$  RVE. Figure 16 shows the elastic-plastic deformation of the  $2a \times 2a \times 2a$  RVE under tension and compression.

## 5. Conclusion

We presented a computational approach for the large elastic-plastic deformation analysis of low-mass metallic systems with architected cellular microstructures. Studies on this class of materials are of interest since they can be optimized for specific loading conditions by changing the base material as well as the topology of the architecture. The repetitive RVE approach is utilized to mimic the fabricated cellular microlattices. The RVE is generated by a node-strut representation consisting of the coordinate of nodes and the connectivity of nodes. Therefore, we can easily study the effect of the change of topology on the overall mechanical response of the cellular material by changing both the coordinates and connectivity of nodes. Moreover, the microstructural length scale of the cellular material is accurately captured by introducing the area, the first and the second moments of inertia, and the polar moment of inertia of the symmetrical/unsymmetrical cross section of the strut member within the formulation.

In the current methodology, each member of the actual microlattice undergoing large elastic-plastic deformations is modeled by a single FE with 12 DOF, which enables the study of the static and dynamic behavior of the macrostructure directly and efficiently by using an arbitrarily large number of members. We study the nonlinear coupling of axial, torsional, and bidirectional-bending deformations for each 3D spatial beam element. The effect of plasticity is included by employing the plastic hinge method, and the tangent stiffness matrix is explicitly derived for each member, utilizing the mixed variational principle in the updated Lagrangian corotational reference frame. To avoid inverting the Jacobian matrix, we employ homotopy methods to solve the incremental tangent stiffness equations.

The proposed methodology is validated by comparing the results of the elastic and elastic-plastic large deformation analyses of some problems with the corresponding results given in the literature. Moreover, two fabricated cellular microlattices with different dimensional parameters including the unit cell size and the strut thickness are modeled using different RVEs. We study their mechanical behaviors under all tensile, compressive, and shear loading. The comparison of the calculated mechanical properties utilizing the present methodology with the corresponding experimental measurements available in the literature reveals a very good agreement. Using this developed computational approach, we can homogenize any cellular structure easily, and we can design the topology of microstructure for any designated properties.

**Appendix A. Toward the simplification of (26)**

$$\int_l \hat{N}_{11} \varepsilon_{11}^{0L} dl = \int_l \hat{N}_{11} u_{10,1} dl = - \int_l \hat{N}_{11,1} u_{10} dl + \hat{N}_{11} u_{10} \Big|_0^l, \quad (\text{A.1})$$

$$\int_l \hat{M}_{22} \mathfrak{N}_{22} dl = - \int_l \hat{M}_{22} u_{20,11} dl = - \int_l \hat{M}_{22,11} u_{20} dl + \hat{M}_{22,1} u_{20} \Big|_0^l - \hat{M}_{22} u_{20,1} \Big|_0^l, \quad (\text{A.2})$$

$$\int_l \hat{M}_{33} \mathfrak{N}_{33} dl = - \int_l \hat{M}_{33} u_{30,11} dl = - \int_l \hat{M}_{33,11} u_{30} dl + \hat{M}_{33,1} u_{30} \Big|_0^l - \hat{M}_{33} u_{30,1} \Big|_0^l, \quad (\text{A.3})$$

$$\int_l \hat{T} \Theta dl = \int_l \hat{T} \hat{\theta}_{,1} dl = - \int_l \hat{T}_{,1} \hat{\theta} dl + \hat{T} \hat{\theta} \Big|_0^l. \quad (\text{A.4})$$

**Appendix B. Expressions for  $K_N$ ,  $K_L$  and  $K_P$** 

$$\mathbf{K}_N = \frac{l}{6} \sigma_1^0 \begin{bmatrix} 0 & 0 & 0 & 0 & 0 & 0 & 0 & 0 & 0 & 0 & 0 & 0 \\ 0 & 0 & 0 & 0 & 0 & 0 & 0 & 0 & 0 & 0 & 0 & 0 \\ & 0 & 0 & 0 & 0 & 0 & 0 & 0 & 0 & 0 & 0 & 0 \\ & & 0 & 0 & 0 & 0 & 0 & 0 & 0 & 0 & 0 & 0 \\ & & & 0 & 0 & 0 & 0 & 0 & 0 & 0 & 0 & 0 \\ & & & & 2 & 0 & 0 & 0 & 0 & 1 & 0 & 0 \\ & & & & & 2 & 0 & 0 & 0 & 0 & 0 & 1 \\ & & & & & & 0 & 0 & 0 & 0 & 0 & 0 \\ & & & & & & & 0 & 0 & 0 & 0 & 0 \\ & & & & & & & & 0 & 0 & 0 & 0 \\ & & & & & & & & & 0 & 0 & 0 \\ & & & & & & & & & & 2 & 0 \\ & & & & & & & & & & & 2 \end{bmatrix}. \quad (\text{B.1})$$

To write  $K_L$  and  $K_P$  we split them into blocks:

$$\mathbf{K}_L = \begin{bmatrix} \mathbf{K}_L^{11} & \mathbf{K}_L^{12} \\ \mathbf{K}_L^{12} & \mathbf{K}_L^{22} \end{bmatrix}, \quad (\text{B.2})$$

with

$$\mathbf{K}_L^{11} = \frac{E}{lA} \begin{bmatrix} A^2 & 0 & 0 & 0 & AI_3 & -AI_2 \\ \frac{12(-I_2^2 + AI_{22})}{l^2} & \frac{12(-I_2 I_3 + AI_{23})}{l^2} & 0 & \frac{6(I_2 I_3 - AI_{23})}{l} & \frac{6(-I_2^2 + AI_{22})}{l} \\ & \frac{12(-I_3^2 + AI_{33})}{l^2} & 0 & \frac{6(I_3^2 - AI_{33})}{l} & \frac{6(-I_2 I_3 + AI_{23})}{l} \\ & & \frac{A\mu I_{rr}}{E} & 0 & 0 \\ & & & (-3I_3^2 + 4AI_{33}) & (3I_2 I_3 - 4AI_{23}) \\ & & & & (-3I_2^2 + 4AI_{22}) \end{bmatrix}, \quad (\text{B.3})$$



$$\mathbf{K}_L^{12} = \frac{E}{lA} \begin{bmatrix} -A^2 & 0 & 0 & 0 & -AI_3 & AI_2 \\ \frac{12(I_2^2 - AI_{22})}{l^2} & \frac{12(I_2I_3 - AI_{23})}{l^2} & 0 & \frac{6(I_2I_3 - AI_{23})}{l} & \frac{6(-I_2^2 + AI_{22})}{l} \\ & \frac{12(I_3^2 - AI_{33})}{l^2} & 0 & \frac{6(I_3^2 - AI_{33})}{l} & \frac{6(-I_2I_3 + AI_{23})}{l} \\ \text{symm.} & & -\frac{A\mu I_{rr}}{E} & 0 & 0 \\ & & & (-3I_3^2 + 2AI_{33}) & (3I_2I_3 - 2AI_{23}) \\ & & & & (-3I_2^2 + 2AI_{22}) \end{bmatrix}, \quad (\text{B.4})$$

$$\mathbf{K}_L^{22} = \frac{E}{lA} \begin{bmatrix} A^2 & 0 & 0 & 0 & AI_3 & -AI_2 \\ \frac{12(-I_2^2 + AI_{22})}{l^2} & \frac{12(-I_2I_3 + AI_{23})}{l^2} & 0 & \frac{6(-I_2I_3 + AI_{23})}{l} & \frac{6(I_2^2 - AI_{22})}{l} \\ & \frac{12(-I_3^2 + AI_{33})}{l^2} & 0 & \frac{6(-I_3^2 + AI_{33})}{l} & \frac{6(I_2I_3 - AI_{23})}{l} \\ \text{symm.} & & \frac{A\mu I_{rr}}{E} & 0 & 0 \\ & & & (-3I_3^2 + 4AI_{33}) & (3I_2I_3 - 4AI_{23}) \\ & & & & (-3I_2^2 + 4AI_{22}) \end{bmatrix}. \quad (\text{B.5})$$

To express  $\mathbf{K}_P$  we first define

$$S = M_0\{M_1^2 + M_2^2 + M_3^2\}^{1/2}, \quad (\text{B.6})$$

$$\begin{aligned} \mathcal{D}_1 = E \left( -3I_3^2(l - 2l_p)^2 M_2^2 N_0^4 - 6I_2I_3(l - 2l_p)^2 M_2M_3N_0^4 \right. \\ \left. + (-3I_2^2(l - 2l_p)^2 M_3^2 + 4A(l^2 - 3ll_p + 3l_p^2)(I_{33}M_2^2 + 2I_{23}M_2M_3 + I_{22}M_3^2))N_0^4 \right. \\ \left. + 4AI_3l^2M_2NN_0^2S + 4AI_2l^2M_3NN_0^2S + 4A^2l^2N^2S^2 \right) + AI_{rr}l^2M_1^2N_0^4v, \end{aligned} \quad (\text{B.7})$$

$$\mathcal{N}_1 = I_3M_2N_0^2 + I_2M_3N_0^2 + 2ANS, \quad (\text{B.8})$$

$$\mathcal{N}_2 = -AI_{23}M_2 + I_2I_3M_2 + I_2^2M_3 - AI_{22}M_3, \quad (\text{B.9})$$

$$\mathcal{N}_3 = I_3^2M_2 - AI_{33}M_2 - AI_{23}M_3 + I_2I_3M_3, \quad (\text{B.10})$$

$$\mathcal{N}_4 = (-3I_3^2(l - 2l_p)M_2 - 3I_2I_3(l - 2l_p)M_3 + 2A(2l - 3l_p)(I_{33}M_2 + I_{23}M_3))N_0^2 + 2AI_3lNS, \quad (\text{B.11})$$

$$\mathcal{N}_5 = (-3I_2(l - 2l_p)(I_3M_2 + I_2M_3) + 2A(2l - 3l_p)(I_{23}M_2 + I_{22}M_3))N_0^2 + 2AI_2lNS, \quad (\text{B.12})$$

$$\mathcal{N}_6 = (-3I_2(l - 2l_p)(I_3M_2 + I_2M_3) + 2A(l - 3l_p)(I_{23}M_2 + I_{22}M_3))N_0^2 - 2AI_2lNS, \quad (\text{B.13})$$

$$\mathcal{N}_7 = (3I_3^2(l - 2l_p)M_2 + 3I_2I_3(l - 2l_p)M_3 - 2A(l - 3l_p)(I_{33}M_2 + I_{23}M_3))N_0^2 + 2AI_3lNS. \quad (\text{B.14})$$

Here  $N_0$  and  $M_0$  are the fully plastic axial force and the fully plastic bending moment, respectively.

Then write

$$\mathbf{K}_P = \begin{bmatrix} {}^{11}\mathbf{K}_P^{11} & {}^{12}\mathbf{K}_P^{11} & {}^{11}\mathbf{K}_P^{12} & {}^{12}\mathbf{K}_P^{12} \\ & {}^{22}\mathbf{K}_P^{11} & {}^{12}\mathbf{K}_P^{12} & {}^{22}\mathbf{K}_P^{12} \\ & & {}^{11}\mathbf{K}_P^{22} & {}^{12}\mathbf{K}_P^{22} \\ \text{symm.} & & & {}^{22}\mathbf{K}_P^{22} \end{bmatrix}, \quad (\text{B.15})$$

with

$${}^{11}\mathbf{K}_P^{11} = \frac{E(l-2l_p)}{lAD_1} \begin{bmatrix} \frac{A^2 E l^2 \mathcal{N}_1^2}{(l-2l_p)} & 6AEN_2 N_0^2 \mathcal{N}_1 & 6AEN_3 N_0^2 \mathcal{N}_1 \\ & \frac{36E(l-2l_p)\mathcal{N}_2^2 N_0^4}{l^2} & \frac{36E(l-2l_p)\mathcal{N}_2 \mathcal{N}_3 N_0^4}{l^2} \\ \text{symm.} & & \frac{36E(l-2l_p)\mathcal{N}_3^2 N_0^4}{l^2} \end{bmatrix}, \quad (\text{B.16})$$

$${}^{12}\mathbf{K}_P^{11} = \frac{E(l-2l_p)}{lAD_1} \begin{bmatrix} \frac{A^2 I_{rr} l^2 M_1 N_0^2 \mathcal{N}_1 v}{(l-2l_p)} & \frac{AEI \mathcal{N}_1 \mathcal{N}_4}{(l-2l_p)} & -\frac{lAE \mathcal{N}_1 \mathcal{N}_5}{(l-2l_p)} \\ 6AI_{rr} M_1 \mathcal{N}_2 N_0^4 v & \frac{6E \mathcal{N}_2 N_0^2 \mathcal{N}_4}{l} & -\frac{6E \mathcal{N}_2 N_0^2 \mathcal{N}_5}{l} \\ 6AI_{rr} M_1 \mathcal{N}_3 N_0^4 v & \frac{6E \mathcal{N}_3 N_0^2 \mathcal{N}_4}{l} & -\frac{6E \mathcal{N}_3 N_0^2 \mathcal{N}_5}{l} \end{bmatrix}, \quad (\text{B.17})$$

$${}^{22}\mathbf{K}_P^{11} = \frac{E(l-2l_p)}{lAD_1} \begin{bmatrix} \frac{A^2 I_{rr}^2 l^2 M_1^2 N_0^4 v^2}{(l-2l_p)} & \frac{EAI I_{rr} M_1 N_0^2 \mathcal{N}_4 v}{(l-2l_p)} & -\frac{lAI_{rr} M_1 N_0^2 \mathcal{N}_5 v}{(l-2l_p)} \\ & \frac{E \mathcal{N}_4^2}{(l-2l_p)} & -\frac{E \mathcal{N}_5 \mathcal{N}_4}{(l-2l_p)} \\ \text{symm.} & & \frac{E \mathcal{N}_5^2}{(l-2l_p)} \end{bmatrix}, \quad (\text{B.18})$$

$${}^{11}\mathbf{K}_P^{12} = \begin{bmatrix} -\frac{Al(E\mathcal{N}_1)^2}{\mathcal{D}_1} & -\frac{6E^2(l-2l_p)\mathcal{N}_2 N_0^2 \mathcal{N}_1}{l\mathcal{D}_1} & -\frac{6E^2(l-2l_p)\mathcal{N}_3 N_0^2 \mathcal{N}_1}{l\mathcal{D}_1} \\ & -\frac{36E^2(l-2l_p)^2 \mathcal{N}_2^2 N_0^4}{Al^3 \mathcal{D}_1} & -\frac{36E^2(l-2l_p)^2 \mathcal{N}_3 \mathcal{N}_2 N_0^4}{Al^3 \mathcal{D}_1} \\ \text{symm.} & & -\frac{36E^2(l-2l_p)^2 \mathcal{N}_3^2 N_0^4}{Al^3 \mathcal{D}_1} \end{bmatrix}, \quad (\text{B.19})$$

$${}^{12}\mathbf{K}_P^{12} = \begin{bmatrix} -\frac{AEI_{rr} l M_1 N_0^2 \mathcal{N}_1 v}{\mathcal{D}_1} & -\frac{E^2 \mathcal{N}_1 \mathcal{N}_7}{\mathcal{D}_1} & -\frac{E^2 \mathcal{N}_1 \mathcal{N}_6}{\mathcal{D}_1} \\ \frac{6EI_{rr}(l-2l_p)M_1 \mathcal{N}_2 N_0^4 v}{l\mathcal{D}_1} & -\frac{6E^2(l-2l_p)\mathcal{N}_2 N_0^2 \mathcal{N}_7}{Al^2 \mathcal{D}_1} & -\frac{6E^2(l-2l_p)\mathcal{N}_2 N_0^2 \mathcal{N}_6}{Al^2 \mathcal{D}_1} \\ \frac{6EI_{rr}(l-2l_p)M_1 \mathcal{N}_3 N_0^4 v}{l\mathcal{D}_1} & -\frac{6E^2(l-2l_p)\mathcal{N}_3 N_0^2 \mathcal{N}_7}{Al^2 \mathcal{D}_1} & -\frac{6E^2(l-2l_p)\mathcal{N}_3 N_0^2 \mathcal{N}_6}{Al^2 \mathcal{D}_1} \end{bmatrix}, \quad (\text{B.20})$$

$${}^{22}\mathbf{K}_P^{12} = \begin{bmatrix} \frac{AI_{rr}^2 l M_1^2 N_0^4 v^2}{\mathcal{D}_1} & -\frac{EI_{rr} M_1 N_0^2 \mathcal{N}_7 v}{\mathcal{D}_1} & -\frac{EI_{rr} M_1 N_0^2 \mathcal{N}_6 v}{\mathcal{D}_1} \\ & -\frac{E^2 \mathcal{N}_4 \mathcal{N}_7}{AI\mathcal{D}_1} & -\frac{E^2 \mathcal{N}_{10} \mathcal{N}_4}{AI\mathcal{D}_1} \\ \text{symm.} & & \frac{E^2 \mathcal{N}_{10} \mathcal{N}_5}{AI\mathcal{D}_1} \end{bmatrix}, \tag{B.21}$$

$${}^{11}\mathbf{K}_P^{22} = \begin{bmatrix} \frac{AIEN_1^2}{\mathcal{D}_1} & \frac{6E^2(l-2l_p)\mathcal{N}_2 N_0^2 \mathcal{N}_1}{l\mathcal{D}_1} & \frac{6E^2(l-2l_p)\mathcal{N}_3 N_0^2 \mathcal{N}_1}{l\mathcal{D}_1} \\ & \frac{36E^2(l-2l_p)^2 \mathcal{N}_2^2 N_0^4}{AI^3 \mathcal{D}_1} & \frac{36E^2(l-2l_p)^2 \mathcal{N}_3 \mathcal{N}_2 N_0^4}{AI^3 \mathcal{D}_1} \\ \text{symm.} & & \frac{36E^2(l-2l_p)^2 \mathcal{N}_3^2 N_0^4}{AI^3 \mathcal{D}_1} \end{bmatrix}, \tag{B.22}$$

$${}^{12}\mathbf{K}_P^{22} = \begin{bmatrix} \frac{AEI_{rr} l M_1 N_0^2 \mathcal{N}_1 v}{\mathcal{D}_1} & \frac{E^2 \mathcal{N}_1 \mathcal{N}_7}{\mathcal{D}_1} & \frac{E^2 \mathcal{N}_1 \mathcal{N}_6}{\mathcal{D}_1} \\ \frac{6EI_{rr}(l-2l_p)M_1 \mathcal{N}_2 N_0^2 v}{l\mathcal{D}_1} & \frac{6E^2(l-2l_p)\mathcal{N}_2 N_0^2 \mathcal{N}_7}{AI^2 \mathcal{D}_1} & \frac{6E^2(l-2l_p)\mathcal{N}_2 N_0^2 \mathcal{N}_6}{AI^2 \mathcal{D}_1} \\ \frac{6EI_{rr}(l-2l_p)M_1 \mathcal{N}_3 N_0^4 v}{l\mathcal{D}_1} & \frac{6E^2(l-2l_p)\mathcal{N}_3 N_0^2 \mathcal{N}_7}{AI^2 \mathcal{D}_1} & \frac{6E^2(l-2l_p)\mathcal{N}_3 N_0^2 \mathcal{N}_6}{AI^2 \mathcal{D}_1} \end{bmatrix}, \tag{B.23}$$

$${}^{22}\mathbf{K}_P^{22} = \begin{bmatrix} \frac{AI_{rr}^2 l M_1^2 N_0^4 v^2}{\mathcal{D}_1} & \frac{EI_{rr} M_1 N_0^2 \mathcal{N}_7 v}{\mathcal{D}_1} & \frac{EI_{rr} M_1 N_0^2 \mathcal{N}_6 v}{\mathcal{D}_1} \\ & \frac{(E\mathcal{N}_7)^2}{AI\mathcal{D}_1} & \frac{E^2 \mathcal{N}_6 \mathcal{N}_7}{AI\mathcal{D}_1} \\ \text{symm.} & & \frac{(E\mathcal{N}_6)^2}{AI\mathcal{D}_1} \end{bmatrix}, \tag{B.24}$$

**Appendix C. Transformation matrices between coordinate systems**

Referring to Figure 1,  $\bar{x}_i$  are the global coordinates and  $\bar{e}_i$  are the corresponding orthonormal basis vectors. Similarly,  $\tilde{x}_i$  and  $\tilde{e}_i$  are respectively the local coordinates and the corresponding basis vectors of the undeformed state and  $x_i$  and  $e_i$  are those of the deformed state. Herein, transformation matrices relating local coordinates corresponding to the deformed and undeformed states to the global coordinates are discussed. If  ${}^\alpha X_i$  denote the global coordinates of the  $\alpha$ -th node of the element in the undeformed state, then the local orthonormal basis vectors of the undeformed state can be described with respect to those of the global coordinates as

$$\tilde{e}_1 = (\Delta \tilde{X}_1 \bar{e}_1 + \Delta \tilde{X}_2 \bar{e}_2 + \Delta \tilde{X}_3 \bar{e}_3) / \tilde{L}, \tag{C.1}$$

$$\tilde{e}_2 = (\bar{e}_3 \times \tilde{e}_1) / |\bar{e}_3 \times \tilde{e}_1|, \tag{C.2}$$

$$\tilde{e}_3 = \tilde{e}_1 \times \tilde{e}_2, \tag{C.3}$$

in which

$$\Delta \tilde{X}_i = {}^2 X_i - {}^1 X_i \quad i = 1, 2, 3, \tag{C.4}$$

$$\tilde{L} = \{(\Delta \tilde{X}_1)^2 + (\Delta \tilde{X}_2)^2 + (\Delta \tilde{X}_3)^2\}^{1/2}. \tag{C.5}$$

Thus,  $\tilde{\mathbf{e}}_i$  and  $\bar{\mathbf{e}}_i$  ( $i = 1, 2, 3$ ) are related via the following equation [Simo 1985]:

$$\begin{bmatrix} \tilde{\mathbf{e}}_1 \\ \tilde{\mathbf{e}}_2 \\ \tilde{\mathbf{e}}_3 \end{bmatrix} = \begin{bmatrix} \Delta\tilde{X}_1/\tilde{L} & \Delta\tilde{X}_2/\tilde{L} & \Delta\tilde{X}_3/\tilde{L} \\ -\Delta\tilde{X}_2/\tilde{S} & \Delta\tilde{X}_1/\tilde{S} & 0 \\ -\Delta\tilde{X}_1\Delta\tilde{X}_3/(\tilde{L}\tilde{S}) & -\Delta\tilde{X}_2\Delta\tilde{X}_3/(\tilde{L}\tilde{S}) & \tilde{S}/\tilde{L} \end{bmatrix} \begin{bmatrix} \bar{\mathbf{e}}_1 \\ \bar{\mathbf{e}}_2 \\ \bar{\mathbf{e}}_3 \end{bmatrix}, \quad (\text{C.6})$$

where

$$\tilde{S} = \{(\Delta\tilde{X}_1)^2 + (\Delta\tilde{X}_2)^2\}^{1/2}. \quad (\text{C.7})$$

Therefore, the matrix transforming global coordinates to the local coordinates of the undeformed state is obtained as

$$\tilde{T} = \begin{bmatrix} \Delta\tilde{X}_1/\tilde{L} & \Delta\tilde{X}_2/\tilde{L} & \Delta\tilde{X}_3/\tilde{L} \\ -\Delta\tilde{X}_2/\tilde{S} & \Delta\tilde{X}_1/\tilde{S} & 0 \\ -\Delta\tilde{X}_1\Delta\tilde{X}_3/(\tilde{L}\tilde{S}) & -\Delta\tilde{X}_2\Delta\tilde{X}_3/(\tilde{L}\tilde{S}) & \tilde{S}/\tilde{L} \end{bmatrix}. \quad (\text{C.8})$$

Note that, for the case when the element is parallel to the  $\bar{x}_3$ -axis, the local coordinates for the undeformed state are determined by

$$\tilde{\mathbf{e}}_1 = \bar{\mathbf{e}}_3, \quad \tilde{\mathbf{e}}_2 = \bar{\mathbf{e}}_2, \quad \tilde{\mathbf{e}}_3 = -\bar{\mathbf{e}}_1. \quad (\text{C.9})$$

Similarly, the transformation matrix relating local coordinates of the deformed state to the global coordinates can be obtained. For this case,  ${}^\alpha X'_i$  is introduced to describe the global coordinates of the  $\alpha$ -th node of the element in the deformed state. Therefore, orthonormal basis vectors in the corotational reference coordinate system  $\mathbf{e}_i$  can be chosen as

$$\mathbf{e}_1 = (\Delta X_1 \bar{\mathbf{e}}_1 + \Delta X_2 \bar{\mathbf{e}}_2 + \Delta X_3 \bar{\mathbf{e}}_3)/L, \quad (\text{C.10})$$

$$\mathbf{e}_2 = (\tilde{\mathbf{e}}_3 \times \mathbf{e}_1)/|\tilde{\mathbf{e}}_3 \times \mathbf{e}_1|, \quad (\text{C.11})$$

$$\mathbf{e}_3 = \mathbf{e}_1 \times \mathbf{e}_2, \quad (\text{C.12})$$

where  $\Delta X_i = {}^2 X'_i - {}^1 X'_i$  and  $L = \{(\Delta X_1)^2 + (\Delta X_2)^2 + (\Delta X_3)^2\}^{1/2}$ .

By replacing  $\tilde{\mathbf{e}}_3$  from (C.6) into (C.11), we obtain

$$\begin{bmatrix} \mathbf{e}_1 \\ \mathbf{e}_2 \\ \mathbf{e}_3 \end{bmatrix} = \begin{bmatrix} \Delta X_1/L & \Delta X_2/L & \Delta X_3/L \\ -\frac{\Delta\tilde{X}_2\Delta\tilde{X}_3\Delta X_3}{\tilde{L}\tilde{S}L} - \frac{\Delta X_2\tilde{S}}{LL} & \frac{\Delta\tilde{X}_1\Delta\tilde{X}_3\Delta X_3}{\tilde{L}\tilde{S}L} - \frac{\Delta X_1\tilde{S}}{LL} & -\frac{\Delta\tilde{X}_1\Delta\tilde{X}_3\Delta X_2}{\tilde{L}\tilde{S}L} + \frac{\Delta X_1\Delta\tilde{X}_2\Delta\tilde{X}_3}{LL\tilde{S}C} \\ A_{31} & A_{32} & A_{33} \end{bmatrix} \begin{bmatrix} \bar{\mathbf{e}}_1 \\ \bar{\mathbf{e}}_2 \\ \bar{\mathbf{e}}_3 \end{bmatrix} \quad (\text{C.13})$$

where

$$A_{31} = \frac{\Delta\tilde{X}_1\Delta\tilde{X}_3\Delta X_1\Delta X_3}{\tilde{L}\tilde{S}L^2\mathcal{L}} + \frac{\Delta X_1^2\tilde{S}}{L^2\tilde{L}\mathcal{L}} + \frac{\Delta\tilde{X}_2\Delta\tilde{X}_3\Delta X_2\Delta X_3}{\tilde{L}\tilde{S}L^2\mathcal{L}} + \frac{\Delta X_2^2\tilde{S}}{L^2\tilde{L}\mathcal{L}},$$

$$\begin{aligned}
 A_{32} &= \frac{\Delta \tilde{X}_1 \Delta \tilde{X}_3 \Delta X_1 \Delta X_2}{\tilde{L} \tilde{S} L^2 \mathcal{L}} - \frac{\Delta X_1^2 \Delta \tilde{X}_2 \Delta \tilde{X}_3}{L^2 \tilde{L} \tilde{S} \mathcal{L}} - \frac{\Delta \tilde{X}_2 \Delta \tilde{X}_3 \Delta X_3^2}{\tilde{L} \tilde{S} L^2 \mathcal{L}} - \frac{\Delta X_2 \Delta X_3 \tilde{S}}{L^2 \tilde{L} \mathcal{L}}, \\
 A_{33} &= \frac{\Delta \tilde{X}_1 \Delta \tilde{X}_3 \Delta X_1 \Delta X_3}{\tilde{L} \tilde{S} L^2 \mathcal{L}} + \frac{\Delta X_1^2 \tilde{S}}{L^2 \tilde{L} \mathcal{L}} + \frac{\Delta \tilde{X}_2 \Delta \tilde{X}_3 \Delta X_2 \Delta X_3}{\tilde{L} \tilde{S} L^2 \mathcal{L}} + \frac{\Delta X_2^2 \tilde{S}}{L^2 \tilde{L} \mathcal{L}}, \\
 \mathcal{L} &= \left\{ \left( -\frac{\Delta \tilde{X}_2 \Delta \tilde{X}_3 \Delta X_3}{\tilde{L} \tilde{S} L} - \frac{\Delta X_2 \tilde{S}}{L \tilde{L}} \right)^2 + \left( \frac{\Delta \tilde{X}_1 \Delta \tilde{X}_3 \Delta X_3}{\tilde{L} \tilde{S} L} + \frac{\Delta X_1 \tilde{S}}{L \tilde{L}} \right)^2 \right. \\
 &\quad \left. + \left( -\frac{\Delta \tilde{X}_1 \Delta \tilde{X}_3 \Delta X_2}{\tilde{L} \tilde{S} L} + \frac{\Delta X_1 \Delta \tilde{X}_2 \Delta \tilde{X}_3}{L \tilde{L} \tilde{S}} \right)^2 \right\}^{1/2}. \tag{C.14}
 \end{aligned}$$

Thus, the transformation matrix is obtained as

$$\mathcal{T} = \begin{bmatrix} \Delta X_1/L & \Delta X_2/L & \Delta X_3/L \\ -\frac{\Delta \tilde{X}_2 \Delta \tilde{X}_3 \Delta X_3}{\tilde{L} \tilde{S} L \mathcal{L}} - \frac{\Delta X_2 \tilde{S}}{L \tilde{L} \mathcal{L}} & \frac{\Delta \tilde{X}_1 \Delta \tilde{X}_3 \Delta X_3}{\tilde{L} \tilde{S} L \mathcal{L}} + \frac{\Delta X_1 \tilde{S}}{L \tilde{L} \mathcal{L}} & -\frac{\Delta \tilde{X}_1 \Delta \tilde{X}_3 \Delta X_2}{\tilde{L} \tilde{S} L \mathcal{L}} + \frac{\Delta X_1 \Delta \tilde{X}_2 \Delta \tilde{X}_3}{L \tilde{L} \tilde{S} \mathcal{L}} \\ B_{31} & B_{32} & B_{33} \end{bmatrix}, \tag{C.15}$$

where

$$\begin{aligned}
 B_{31} &= \frac{\Delta \tilde{X}_1 \Delta \tilde{X}_3 \Delta X_1 \Delta X_3}{\tilde{L} \tilde{S} L^2 \mathcal{L}} + \frac{\Delta X_1^2 \tilde{S}}{L^2 \tilde{L} \mathcal{L}} + \frac{\Delta \tilde{X}_2 \Delta \tilde{X}_3 \Delta X_2 \Delta X_3}{\tilde{L} \tilde{S} L^2 \mathcal{L}} + \frac{\Delta X_2^2 \tilde{S}}{L^2 \tilde{L} \mathcal{L}}, \\
 B_{32} &= \frac{\Delta \tilde{X}_1 \Delta \tilde{X}_3 \Delta X_1 \Delta X_2}{\tilde{L} \tilde{S} L^2 \mathcal{L}} - \frac{\Delta X_1^2 \Delta \tilde{X}_2 \Delta \tilde{X}_3}{L^2 \tilde{L} \tilde{S} \mathcal{L}} - \frac{\Delta \tilde{X}_2 \Delta \tilde{X}_3 \Delta X_3^2}{\tilde{L} \tilde{S} L^2 \mathcal{L}} - \frac{\Delta X_2 \Delta X_3 \tilde{S}}{L^2 \tilde{L} \mathcal{L}}, \\
 B_{33} &= \frac{\Delta \tilde{X}_1 \Delta \tilde{X}_3 \Delta X_1 \Delta X_3}{\tilde{L} \tilde{S} L^2 \mathcal{L}} + \frac{\Delta X_1^2 \tilde{S}}{L^2 \tilde{L} \mathcal{L}} + \frac{\Delta \tilde{X}_2 \Delta \tilde{X}_3 \Delta X_2 \Delta X_3}{\tilde{L} \tilde{S} L^2 \mathcal{L}} + \frac{\Delta X_2^2 \tilde{S}}{L^2 \tilde{L} \mathcal{L}}.
 \end{aligned}$$

Finally, the transformation matrix for changing the generalized element coordinates consisting of 12 components in the global reference frame to the corresponding coordinates in the corotational reference frame is given by

$$\mathcal{Q} = \begin{bmatrix} \mathcal{T} & & 0 \\ & \mathcal{T} & \\ 0 & & \mathcal{T} \end{bmatrix}. \tag{C.16}$$

Then, components of the second-order tensors, such as the tangent stiffness matrix, as well as first-order tensors, like the generalized nodal displacements and the generalized nodal forces, are transformed to the global coordinates system based on quotient rule using the presented transformation matrices.

### Appendix D.

Two of the extensively used vector homotopy functions are the fixed-point homotopy function and the Newton homotopy function, defined respectively as

$$\mathbf{H}_F(\mathbf{X}, t) = t\mathbf{F}(\mathbf{X}) + (1-t)(\mathbf{X} - \mathbf{X}_0) = 0, \quad 0 \leq t \leq 1, \tag{D.1}$$

$$\mathbf{H}_N(\mathbf{X}, t) = t\mathbf{F}(\mathbf{X}) + (1-t)(\mathbf{F}(\mathbf{X}) - \mathbf{F}(\mathbf{X}_0)) = 0, \quad 0 \leq t \leq 1. \quad (\text{D.2})$$

Here,  $\mathbf{X}_0$  represents the initial guess of the solution. Using the vector homotopy method, the solution of  $\mathbf{F}(\mathbf{X}) = 0$  can be obtained by numerically integrating the following relation:

$$\dot{\mathbf{X}} = -\left(\frac{\partial \mathbf{H}}{\partial \mathbf{X}}\right)^{-1} \frac{\partial \mathbf{H}}{\partial t}, \quad 0 \leq t \leq 1, \quad (\text{D.3})$$

which requires the inversion of the matrix  $\partial \mathbf{H} / \partial \mathbf{X}$  at each iteration.

A series of iterative Newton homotopy methods has also been developed, where  $Q(t)$  does not need to be determined [Dai et al. 2014]. Considering  $\dot{\mathbf{X}} = \lambda \mathbf{u}$ , the general form of the scalar Newton homotopy function becomes

$$\dot{\mathbf{X}} = -\frac{\dot{Q}(t)}{2Q(t)} \frac{\|\mathbf{F}(\mathbf{X})\|^2}{\mathbf{F}^T \mathbf{B} \mathbf{u}} \mathbf{u}. \quad (\text{D.4})$$

Using the forward Euler method, (D.4) is discretized and the general form of the iterative Newton homotopy method is obtained as

$$\mathbf{X}(t + \Delta t) = \mathbf{X}(t) - (1 - \gamma) \frac{\mathbf{F}^T \mathbf{B} \mathbf{u}}{\|\mathbf{B} \mathbf{u}\|^2} \mathbf{u}, \quad (\text{D.5})$$

where  $-1 < \gamma < 1$ .

The reason homotopy methods converge with the required accuracy in the case of complex problems (in the presence of the plasticity and buckling in a large number of members of the microlattice) is thanks to raising the position of the driving vector  $\mathbf{u}$  in  $\dot{\mathbf{X}} = \lambda \mathbf{u}$  to introduce the best descent direction in searching the solution vector  $\mathbf{X}$ . In the so-called continuous Newton method we have  $\mathbf{u} = \mathbf{B}^{-1} \mathbf{F}$ , resulting in loss of accuracy from inverting the Jacobian matrix when it is singular or severely ill-conditioned, leading to oscillatory, nonconvergent behavior. Whereas in (76), we have  $\mathbf{u} = \mathbf{B}^T \mathbf{F}$  with  $\lambda = -\frac{1}{2} \dot{Q} \|\mathbf{F}\|^2 / (Q \|\mathbf{B}^T \mathbf{F}\|^2)$ , and it can also be expressed by two vectors such as  $\mathbf{F}$  and  $\mathbf{B}^T \mathbf{F}$ . The hypersurface formulated in (75) defines a future cone in the Minkowski space  $\mathbb{M}^{n+1}$  in terms of the residual vector  $\mathbf{F}$  and a positive and monotonically increasing function  $Q(t)$  as

$$\mathcal{X}^T \mathbf{g} \mathcal{X} = 0, \quad (\text{D.6})$$

where

$$\mathcal{X} = \begin{bmatrix} \mathbf{F}(\mathbf{X}) / \|\mathbf{F}(\mathbf{X}_0)\| \\ 1 / \sqrt{Q(t)} \end{bmatrix}, \quad (\text{D.7})$$

$$\mathbf{g} = \begin{bmatrix} \mathbf{I}_n & \mathbf{0}_{n \times 1} \\ \mathbf{0}_{1 \times n} & -1 \end{bmatrix}, \quad (\text{D.8})$$

and  $\mathbf{I}_n$  is the  $n \times n$  identity matrix. Then the solution vector  $\mathbf{X}$  is searched along the path kept on the manifold defined by the following equation:

$$\|\mathbf{F}(\mathbf{X})\|^2 = \frac{\|\mathbf{F}(\mathbf{X}_0)\|^2}{Q(t)}. \quad (\text{D.9})$$

Therefore, an absolutely convergent property is achieved by guaranteeing  $Q(t)$  as a monotonically increasing function of  $t$ . In fact, (D.9) enforces the residual error  $\|\mathbf{F}(\mathbf{X})\|$  to vanish when  $t$  is large.

## References

- [Ashby et al. 2000] M. F. Ashby, A. G. Evans, N. A. Fleck, L. J. Gibson, J. W. Hutchinson, and H. N. G. Wadley, *Metal foams: a design guide*, Butterworth-Heinemann, Waltham, MA, 2000.
- [Bathe and Bolourchi 1979] K.-J. Bathe and S. Bolourchi, “Large displacement analysis of three-dimensional beam structures”, *Int. J. Numer. Methods Eng.* **14**:7 (1979), 961–986.
- [Besseling 1986] J. F. Besseling, “Large rotations in problems of structural mechanics”, pp. 25–39 in *Finite element methods for nonlinear problems* (Trondheim, Norway, 1985), edited by P. G. Bergan et al., Springer, 1986.
- [Cai et al. 2009a] Y. Cai, J. K. Paik, and S. N. Atluri, “Large deformation analyses of space-frame structures, using explicit tangent stiffness matrices, based on the Reissner variational principle and a von Karman type nonlinear theory in rotated reference frames”, *Comput. Model. Eng. Sci.* **54**:3 (2009), 335–368.
- [Cai et al. 2009b] Y. Cai, J. K. Paik, and S. N. Atluri, “Large deformation analyses of space-frame structures, with members of arbitrary cross-section, using explicit tangent stiffness matrices, based on a von Karman type nonlinear theory in rotated reference frames”, *Comput. Model. Eng. Sci.* **53**:2 (2009), 117–145.
- [Dai et al. 2014] H. Dai, X. Yue, and S. N. Atluri, “Solutions of the von Kármán plate equations by a Galerkin method, without inverting the tangent stiffness matrix”, *J. Mech. Mater. Struct.* **9**:2 (2014), 195–226.
- [Davidenko 1953] D. F. Davidenko, “On a new method of numerical solution of systems of nonlinear equations”, *Dokl. Akad. Nauk SSSR* **88** (1953), 601–602. In Russian.
- [Evans et al. 2010] A. G. Evans, M. Y. He, V. S. Deshpande, J. W. Hutchinson, A. J. Jacobsen, and W. Carter, “Concepts for enhanced energy absorption using hollow micro-lattices”, *Int. J. Impact Eng.* **37**:9 (2010), 947–959.
- [Geradin and Cardona 1988] M. Geradin and A. Cardona, “Kinematics and dynamics of rigid and flexible mechanisms using finite elements and quaternion algebra”, *Comput. Mech.* **4**:2 (1988), 115–135.
- [Gibson and Ashby 1988] L. J. Gibson and M. F. Ashby, *Cellular solids: structure and properties*, Pergamon, Oxford, 1988.
- [Han and Gouma 2006] D. Han and P.-I. Gouma, “Electrospun bioscaffolds that mimic the topology of extracellular matrix”, *Nanomedicine* **2**:1 (2006), 37–41.
- [Hodge 1959] P. G. Hodge, Jr., *Plastic analysis of structures*, McGraw-Hill, New York, 1959.
- [Hutmacher 2000] D. W. Hutmacher, “Scaffolds in tissue engineering bone and cartilage”, *Biomater.* **21**:24 (2000), 2529–2543.
- [Izzuddin 2001] B. A. Izzuddin, “Conceptual issues in geometrically nonlinear analysis of 3D framed structures”, *Comput. Methods Appl. Mech. Eng.* **191**:8-10 (2001), 1029–1053.
- [Kondoh and Atluri 1987] K. Kondoh and S. N. Atluri, “Large-deformation, elasto-plastic analysis of frames under nonconservative loading, using explicitly derived tangent stiffnesses based on assumed stresses”, *Comput. Mech.* **2**:1 (1987), 1–25.
- [Kondoh et al. 1986] K. Kondoh, K. Tanaka, and S. N. Atluri, “An explicit expression for tangent-stiffness of a finitely deformed 3-D beam and its use in the analysis of space frames”, *Comput. Struct.* **24**:2 (1986), 253–271.
- [Liu et al. 2009] C.-S. Liu, W. Yeih, C.-L. Kuo, and S. N. Atluri, “A scalar homotopy method for solving an over/under-determined system of non-linear algebraic equations”, *Comput. Model. Eng. Sci.* **53**:1 (2009), 47–71.
- [Lo 1992] S. H. Lo, “Geometrically nonlinear formulation of 3D finite strain beam element with large rotations”, *Comput. Struct.* **44**:1-2 (1992), 147–157.
- [Lu et al. 2005] T. J. Lu, L. Valdevit, and A. G. Evans, “Active cooling by metallic sandwich structures with periodic cores”, *Prog. Mater. Sci.* **50**:7 (2005), 789–815.
- [Mallett and Berke 1966] R. H. Mallett and L. Berke, “Automated method for the large deflection and instability analysis of three-dimensional truss and frame assemblies”, technical report AFFDL-TR-66-102, Air Force Flight Dynamics Lab., 1966.
- [Mota et al. 2015] C. Mota, D. Puppi, F. Chiellini, and E. Chiellini, “Additive manufacturing techniques for the production of tissue engineering”, *J. Tissue Eng. Regen. Med.* **9**:3 (2015), 174–190.
- [Punch and Atluri 1984] E. F. Punch and S. N. Atluri, “Development and testing of stable, invariant, isoparametric curvilinear 2- and 3-D hybrid-stress elements”, *Comput. Methods Appl. Mech. Eng.* **47**:3 (1984), 331–356.
- [Reissner 1953] E. Reissner, “On a variational theorem for finite elastic deformations”, *J. Math. Phys.* **32**:1-4 (1953), 129–135.

- [Salari-Sharif and Valdevit 2014] L. Salari-Sharif and L. Valdevit, “Accurate stiffness measurement of ultralight hollow metallic microlattices by laser vibrometry”, *Exp. Mech.* **54**:8 (2014), 1491–1495.
- [Schaedler and Carter 2016] T. A. Schaedler and W. B. Carter, “Architected cellular materials”, *Annu. Rev. Mater. Res.* **46** (2016), 187–210.
- [Schaedler et al. 2011] T. A. Schaedler, A. J. Jacobsen, A. Torrents, A. E. Sorensen, J. Lian, J. R. Greer, L. Valdevit, and W. B. Carter, “Ultralight metallic microlattices”, *Science* **334**:6058 (2011), 962–965.
- [Schaedler et al. 2014] T. A. Schaedler, C. J. Ro, A. E. Sorensen, Z. Eckel, S. S. Yang, W. B. Carter, and A. J. Jacobsen, “Designing metallic microlattices for energy absorber applications”, *Adv. Eng. Mater.* **16**:3 (2014), 276–283.
- [Shi and Atluri 1988] G. Shi and S. N. Atluri, “Elasto-plastic large deformation analysis of space-frames: a plastic-hinge and stress-based explicit derivation of tangent stiffnesses”, *Int. J. Numer. Methods Eng.* **26**:3 (1988), 589–615.
- [Simo 1985] J. C. Simo, “A finite strain beam formulation: the three-dimensional dynamic problem, I”, *Comput. Methods Appl. Mech. Eng.* **49**:1 (1985), 55–70.
- [Torrents et al. 2012] A. Torrents, T. A. Schaedler, A. J. Jacobsen, W. B. Carter, and L. Valdevit, “Characterization of nickel-based microlattice materials with structural hierarchy from the nanometer to the millimeter scale”, *Acta Mater.* **60**:8 (2012), 3511–3523.
- [Ueda and Yao 1982] Y. Ueda and T. Yao, “The plastic node method: a new method of plastic analysis”, *Comput. Methods Appl. Mech. Eng.* **34**:1-3 (1982), 1089–1104.
- [Ueda et al. 1968] Y. Ueda, M. Matsuishi, T. Yamakawa, and Y. Akamatsu, “Elastic-plastic analysis of framed structures using the matrix method”, *J. Soc. Naval Arch. Japan* **1968**:124 (1968), 183–191. In Japanese.
- [Valdevit et al. 2011] L. Valdevit, A. J. Jacobsen, J. R. Greer, and W. B. Carter, “Protocol for the optimal design of multifunctional structures: from hypersonics to micro-architected materials”, *J. Am. Ceram. Soc.* **94**:s1 (2011), S15–S34.
- [Valentin et al. 2006] J. E. Valentin, J. S. Badylak, G. P. McCabe, and S. F. Badylak, “Extracellular matrix bioscaffolds for orthopaedic applications: a comparative histologic study”, *J. Bone Jt. Surg. Am.* **88**:12 (2006), 2673–2686.
- [Wadley 2002] H. N. G. Wadley, “Cellular metals manufacturing”, *Adv. Eng. Mater.* **4**:10 (2002), 726–733.
- [Williams 1964] F. W. Williams, “An approach to the nonlinear behaviour of the members of a rigid jointed plane framework with finite deflections”, *Quart. J. Mech. Appl. Math.* **17** (1964), 451–469.

Received 22 Jan 2017. Revised 14 Jul 2017. Accepted 28 Jul 2017.

MARYAM TABATABAEI: [maryam.tabatabaei@ttu.edu](mailto:maryam.tabatabaei@ttu.edu)

Center for Advanced Research in the Engineering Sciences, Institute for Materials, Manufacturing, and Sustainment, Texas Tech University, Lubbock, TX, United States

DY LE: [dy.d.le@ttu.edu](mailto:dy.d.le@ttu.edu)

Center for Advanced Research in the Engineering Sciences, Institute for Materials, Manufacturing, and Sustainment, Texas Tech University, Lubbock, TX, United States

SATYA N. ATLURI: [snatluri.ttu@gmail.com](mailto:snatluri.ttu@gmail.com)

Center for Advanced Research in the Engineering Sciences, Institute for Materials, Manufacturing, and Sustainment, Texas Tech University, Lubbock, TX, United States





## TRANSIENT ANALYSIS OF FRACTURE INITIATION IN A COUPLED THERMOELASTIC SOLID

LOUIS M. BROCK

An isotropic, thermoelastic solid is initially at rest at uniform (absolute) temperature, and contains a semi-infinite, plane crack. Application of in-plane and normal point forces to each face of the crack causes transient 3D growth. The related problem of discontinuities in temperature and displacement that exist on regions that exhibit dynamic similarity is first considered. Asymptotic expressions, whose inverses are valid near the crack edges for short times, are obtained in integral transform space. These lead to equations of the Wiener–Hopf type for the fracture problem. Analytical solutions are obtained and, upon inversion, subjected to a dynamic energy release rate criterion that accounts for kinetic energy. A particular form of rapid growth in time of the forces is found to cause crack initiation growth rates that indeed vary with position, but not with time. The influence of particular types of mixed-mode loading upon crack edge contour and thermal response near the edge is also examined.

### 1. Introduction

Crack edge location in a transient 3D study is defined by a (possibly nonrectilinear) contour in the crack plane. The semi-infinite, planar crack in an unbounded isothermal solid is treated in [Brock 2017a]. Fracture is driven by mixed-mode, point force loading on the crack faces. The dynamic energy release rate criterion [Freund 1972; 1990] is imposed, but with kinetic energy taken into account [Gdoutos 1993]. It is found that a particular time history for the loading can generate a crack edge contour that varies with position, but not with time. The solution process begins by considering the related problem of displacement discontinuity generation on a portion of a planar surface in the solid. A set of three equations is generated that involve six integral transform functions (three components of discontinuity, three components of planar surface traction). However, the set can be rewritten as three equations of the Wiener–Hopf type [Morse and Feshbach 1953]. Exact solutions are possible, and upon inversion they lead to a nonlinear differential equation for the crack edge contour.

The corresponding problem for the coupled thermoelastic solid is treated in [Brock 2017b]. Crack initiation is the focus, so that:

- (a) thermal relaxation [Ignaczak and Ostoja-Starzewski 2010] can be important, and
- (b) asymptotic forms of the governing equations for thermal relaxation are viable.

The results are similar in nature to those in [Brock 2017a], with the proviso that response is valid for short times.

---

*Keywords:* thermoelastic, relaxation, transient, fracture, kinetic energy, crack contour.

However, as a first step the possibility of discontinuity in temperature across the crack gap is ignored in [Brock 2017b]. A consequence is that the solution process again involves three equations of the Wiener-Hopf type in transform space. In the present article, the possibility of temperature discontinuity is treated. It will be seen that the solution process must now deal with a set of four equations, with integral transforms for the temperature discontinuity and heat flux across the planar surface involved. Two of the Wiener-Hopf equations now yield analytical expressions whose inverses are valid only near the crack edge. However, imposition of the energy release rate criterion [Freund 1972; 1990] in [Brock 2017a; 2017b], and subsequent analysis of crack edge contour, actually involve the use of such asymptotic expressions. Therefore several key results of the present article can be compared with those of [Brock 2017b].

### 2. Problem statement

A closed crack  $A_C(x_3^0 = 0, x_1^0 < 0)$  with boundary  $C(x_1^0, x_3^0) = 0$  exists in an unbounded, coupled thermoelastic, solid. Cartesian coordinates  $\mathbf{x}_0 = x_0(x_k^0), k = (1, 2, 3)$  are used. The solid is at rest for time  $t \leq 0$  at (absolute) uniform temperature  $T_0$ . For  $t > 0$  point forces (both shear and compressive) appear on both crack faces at  $(x_1^0 = 0-, x_2^0 = 0, x_3^0 = 0\pm)$ . Brittle fracture is instantaneous, and the crack extends outward from  $x_0 = 0$ . The crack now occupies region  $A_C + \delta A$ . Boundary  $C$  now includes a concave bulge:

$$\sqrt{(x_1^0)^2 + (x_2^0)^2} = l(\psi, t), \quad l(\psi, t) = V(\psi)t, \tag{1a}$$

$$0 < V < V_R, \quad \psi = \tan^{-1} \frac{x_2^0}{x_1^0} (|\psi| < \pi/2). \tag{1b}$$

Equation (1) implies a dynamically similar fracture process, and requires that (speed parameter)  $V$  not exceed Rayleigh value  $V_R$ . Displacement  $\mathbf{u}(u_k)$ , traction  $\mathbf{T}(\sigma_{ik})$  and  $\theta$ , the change in temperature from  $T_0$ , are field variables. For the Lord and Shulman thermal relaxation model [Lord and Shulman 1967; Brock 2009; Ignaczak and Ostoja-Starzewski 2010]:

$$\nabla \cdot \mathbf{T} - \rho D^2 \mathbf{u} = 0, \tag{2a}$$

$$(k_T \nabla^2 - \rho C_E P D) \theta + \mu \alpha_D T_0 P D (\nabla \cdot \mathbf{u}) = 0, \tag{2b}$$

$$\frac{1}{\mu} \mathbf{T} = \left[ \frac{2\nu}{1-2\nu} (\nabla \cdot \mathbf{u}) \mathbf{1} - \alpha_D \theta \right] + \nabla \mathbf{u} + \mathbf{u} \nabla = 0. \tag{2c}$$

In (2)  $\theta$  and components  $(u_k, \sigma_{ik})$  are functions of  $(\mathbf{x}_0, t)$ , and  $(\nabla, \nabla^2, \mathbf{1})$  respectively are gradient and Laplacian operators and identity tensor. Symbols  $(Df, \dot{f})$  represent time differentiation in basis  $\mathbf{x}_0$  and

$$P = 1 + t_0 D. \tag{3}$$

Here constants  $(\mu, \rho, \nu)$  are shear modulus, mass density and Poisson's ratio, and  $(k_T, C_E, \alpha_D)$  are thermal conductivity, specific heat at constant strain, and coefficient of (volumetric) thermal expansion. Constant  $t_0$  is the thermal relaxation time. Equation (1) reflects assumptions that body forces can be ignored, and heat is neither added to, nor extracted from, the solid. Partial uncoupling of (2a) and (2b) gives

$$\mathbf{u} = \mathbf{u}_S + \mathbf{u}_D, \tag{4a}$$

$$(\nabla^2 - D_S^2)\mathbf{u}_S = 0, \quad \nabla \cdot \mathbf{u}_S = 0, \tag{4b}$$

$$(c_D^2 \nabla^2 - D_S^2)\mathbf{u}_D - \alpha_D \nabla \theta = 0, \quad \nabla \times \mathbf{u}_D = 0, \tag{4c}$$

$$[(c_D^2 \nabla^2 - D_S^2)(h \nabla^2 - D_S P) - \varepsilon D_S P \nabla^2](\mathbf{u}_D, \theta) = 0. \tag{4d}$$

In (4)  $D = V_S D_S$ , and a modification of (3) was used:

$$P = 1 + h_0 D_S. \tag{5}$$

Equation (4) also introduces parameters

$$V_S = \sqrt{\frac{\mu}{\rho}}, \quad V_D = c_D V_S, \quad c_D = \sqrt{2 \frac{1-\nu}{1-2\nu}}, \quad \varepsilon = \frac{\mu T_0}{\rho C_E} \alpha_D, \tag{6a}$$

$$h = \frac{k_T}{C_E \sqrt{\mu \rho}}, \quad h_0 = V_S t_0. \tag{6b}$$

In (6)  $\varepsilon$  is the dimensionless thermal coupling constant, and  $(h, h_0)$  are thermoelastic characteristic lengths. Symbols  $(V_S, V_D)$  are, respectively, shear speed and isothermal dilatational speed. In light of restriction (1b), it is noted that  $V_R < V_S$  and that  $V_R$  will be shown to depend both on material properties and the nature of the point forces.

For  $x_3^0 = 0 \pm, (x_1^0, x_2^0) \in A_C + \delta A$  ( $t > 0$ ):

$$\sigma_{3k} = -P_k \delta(x_1^0) \delta(x_2^0), \quad \frac{\partial \theta}{\partial x_3^0} = 0. \tag{7a}$$

For  $x_3^0 = 0, (x_1^0, x_2^0) \notin A_C + \delta A$  ( $t > 0$ ),

$$[u_k] = [\theta] = 0. \tag{7b}$$

In (7) force  $P_k$  is a positive constant,  $\delta(f)$  denotes Dirac function, and  $[f] = f^{(+)} - f^{(-)}$  where  $f^{(\pm)} = f(x_1^0, x_2^0, 0 \pm, t)$ . Equation (7a) reflects the assumption that thermal convection on the crack faces is negligible. In addition  $[u_k]$  and  $[\theta]$  must vanish continuously on  $C$ , but  $\sigma_{3k}$  can exhibit (integrable) singular behavior on  $C$ . For  $t \leq 0, (\mathbf{u}, \mathbf{T}, \theta) \equiv 0$  and for finite  $t > 0, (\mathbf{u}, \mathbf{T}, \theta)$  must be bounded as  $|\mathbf{x}_0| \rightarrow \infty$ .

### 3. Discontinuity problem

A common practice for solving crack problems is to represent the relative motion of crack faces as unknown discontinuities in displacement, e.g., [Barber 1992]. To implement that procedure, the related problem of discontinuities in  $(u_k, \sigma_{3k}, \theta, \partial \theta / \partial x_3^0)$  is now considered: The unbounded solid is again at rest at uniform (absolute) temperature  $T_0$  when for time  $t > 0$  the discontinuities are imposed in the same region  $A_C + \delta A$  of the  $x_1^0 x_2^0$ - plane. In place of (7) we have for  $x_3^0 = 0, (x_1^0, x_2^0) \in A_C + \delta A$  ( $t > 0$ ):

$$[u_k] = \Delta_k, \quad [\sigma_{3k}] = \Sigma_k, \quad [\theta] = \Theta, \quad [\partial \theta / \partial x_3^0] = d\Theta. \tag{8a}$$

For  $x_3^0 = 0, (x_1^0, x_2^0) \notin A_C + \delta A$  ( $t > 0$ ),

$$[u_k] = [\sigma_{3k}] = [\theta] = [\partial \theta / \partial x_3^0] = 0. \tag{8b}$$

Here  $(\Delta_k, \Sigma_k, \Theta, d\Theta)$  are continuous functions of  $(x_1^0, x_2^0, t)$ . They vanish on  $C$  and for  $t \leq 0$  are bounded in  $A_C + \delta A$  for  $\sqrt{(x_1^0)^2 + (x_2^0)^2} \rightarrow \infty$ . Therefore, as in the crack problem,  $(\mathbf{u}, \mathbf{T}, \theta) \equiv 0$  for  $t \leq 0$  and are bounded as  $|\mathbf{x}_0|$  for finite  $t > 0$ .

#### 4. Transform solution

An effective procedure, e.g., [Brock and Achenbach 1973], for 2D transient study of semi-infinite crack extension at constant speed employs

- (a) coordinates that translate with the crack edge, and
- (b) unilateral temporal and bilateral spatial integral transform [Sneddon 1972].

In view of (1) a translating basis  $\mathbf{x}$  is defined for  $|\psi| < \frac{1}{2}\pi$  as

$$x_1 = x_1^0 - [c(\psi) \cos \psi]s, \quad x_2 = x_2^0 - [c(\psi) \sin \psi]s, \quad x_3 = x_3^0, \quad (9a)$$

$$s = V_S t, \quad c(\psi) = \frac{V(\psi)}{V_S}, \quad (9b)$$

$$Df = \dot{f} = V_S[\partial_S f - c(\psi)(\partial_1 f \cos \psi + \partial_2 f \sin \psi)], \quad (9c)$$

$$\partial_S f = \frac{\partial f}{\partial s}, \quad \partial_k f = \frac{\partial f}{\partial x_k}, \quad k = (1, 2, 3). \quad (9d)$$

The temporal Laplace transform operation is

$$L(f) = \hat{f} = \int f(s) \exp(-ps) ds. \quad (10a)$$

Integration is over positive real  $s$  and  $\text{Re}(p) > 0$ . A double spatial integral transform and inversion, respectively, can be defined [Sneddon 1972] by

$$\tilde{f}(p, q_1, q_2) = \iint \hat{f}(p, x_1, x_2) \exp[-p(q_1 x_1 + q_2 x_2)] dx_1 dx_2, \quad (10b)$$

$$\hat{f}(p, x_1, x_2) = \left(\frac{p}{2\pi i}\right)^2 \iint \tilde{f}(p, q_1, q_2) \exp[p(q_1 x_1 + q_2 x_2)] dq_1 dq_2. \quad (10c)$$

Integration in (10b) is over real  $(x_1, x_2)$ ; integration in (10c) is along the imaginary  $(q_1, q_2)$ -axes. It is noted that  $(\mathbf{x}, s)$  have dimensions of length,  $p$  has dimensions of inverse length, and  $(q_1, q_2)$  are dimensionless. Because (1) involves a speed that varies with direction, application of (9) and (10b) to (2)–(5) and (7) is complicated. Despite use of  $\psi$  the discontinuity problem is not axially symmetric. However, 3D studies of sliding and rolling contact [Brock 2012] and crack growth [Brock 2017a; 2017b] suggest transformations

$$\text{Im}(q_1) = \text{Im}(q) \cos \psi, \quad \text{Im}(q_2) = \text{Im}(q) \sin \psi, \quad (11a)$$

$$x_1 = x \cos \psi, \quad x_2 = x \sin \psi. \quad (11b)$$

Here  $\text{Re}(q) = 0+$ ,  $|\text{Im}(q)|, |x| < \infty$  and  $|\psi| < \frac{1}{2}\pi$ . Parameters  $(x, \psi)$  and  $(q, \psi)$  resemble quasipolar coordinates, i.e.,

$$dx_1 dx_2 = |x| dx d\psi, \quad dq_1 dq_2 = |q| dq d\psi. \quad (11c)$$

The uncoupling effect of (11) leads to the combination

$$\tilde{f}(p, q_1, q_2) \rightarrow \bar{f}(p, q, \psi), \tag{12a}$$

$$\hat{f}(p, x, \psi) = -\frac{p^2}{2\pi} \int \frac{|q|}{q} \bar{f}(p, q, \psi) \exp(pqx) dq. \tag{12b}$$

Integration is along the positive ( $\text{Re}(q) = 0+$ ) side of the  $\text{Im}(q)$ -axis.

In view of (9)–(11) and (12a), (4) and (5) give a corresponding set in transform space by making formal substitutions

$$\nabla \rightarrow (pq \cos \psi, pq \sin \psi, \partial_3), \quad D_S \rightarrow p\beta, \quad \nabla^2 \rightarrow \partial_3^2 + p^2q^2, \tag{13a}$$

$$P \rightarrow 1 + h_0p\beta, \tag{13b}$$

$$\beta = 1 - cq. \tag{13c}$$

Set elements that correspond to (4b)–(4d) are homogeneous, ordinary differential equations in  $x_3$ , with characteristic functions  $pB(q)$  and  $A_{\pm}(p, q)$ :

$$B(q) = \sqrt{\beta^2 - q^2}, \tag{14a}$$

$$A_{\pm}(p, q) = p\sqrt{\left(\frac{2\beta}{\Gamma_{+} \pm \Gamma_{-}}\right)^2 - q^2}, \tag{14b}$$

$$\Gamma_{\pm} = \sqrt{\left[\sqrt{\frac{hp\beta}{1+h_0p\beta}} \pm c_D\right]^2 + \varepsilon}. \tag{14c}$$

Focus of this transient study is on the initiation phase of fracture, i.e., small  $t$  (and therefore small  $s$ ). The Lord and Shulman [1967] model is quite robust for this purpose. Indeed [Brock 2009; Ignaczak and Ostojca-Starzewski 2010] indicate that  $h \approx O(10^{-9})$  m,  $h_0 \approx O(10^{-10})$  m so that, in view of (10a), transform expressions valid for  $|h_0p| \gg 1$  are sufficient. Result (14b) assumes the form  $pA_{\pm}(q)$  defined below, and the set corresponding to (4b)–(4d) gives general solutions:

$$\bar{u}_s \left[ U_1^{(\pm)}, U_2^{(\pm)}, (\pm) \frac{q}{B} (U_1^{(\pm)} \cos \psi + U_2^{(\pm)}) \right] \exp(-pB|x_3|), \tag{15a}$$

$$\bar{u}_D = \bar{u}_+ + \bar{u}_-, \quad \bar{\theta} = \bar{\theta}_+ + \bar{\theta}_-, \tag{15b}$$

$$\bar{u}_{\pm} = [q \cos \psi, q \sin \psi, (\mp) A_{\pm}] U_{\pm}^{(\pm)} \exp(-pA_{\pm}|x_3|), \tag{15c}$$

$$\bar{\theta}_{\pm} = -C_{\pm} \frac{\beta^2}{\alpha_D} p U_{\pm}^{(\pm)} \exp(-pA_{\pm}|x_3|). \tag{15d}$$

Here  $(U_{\pm}^{(\pm)}, U_1^{(\pm)}, U_2^{(\pm)})$  are unknown functions of  $(p, q, \psi)$  and  $(\pm)$  signifies  $x_3 > 0$  (+),  $x_3 < 0$  (–). In addition,

$$A_{\pm} = \sqrt{\beta^2/c_{\pm}^2 - q^2}, \tag{16a}$$

$$C_{\pm} = 1 - c_D^2/c_{\pm}^2, \quad c_{\pm} = \frac{1}{2}(\Gamma_{+} \pm \Gamma_{-}), \tag{16b}$$

$$\Gamma_{\pm} = \sqrt{(\sqrt{\lambda} \pm c_D)^2 + \varepsilon}, \quad \lambda = h/h_0. \tag{16c}$$

Combinations of terms in (16) also prove useful:

$$C_+ - C_- = \Omega = \frac{\Gamma_+ \Gamma_-}{\lambda}, \quad C_+ C_- = -\frac{\varepsilon}{\lambda}, \tag{17a}$$

$$c_+^2 - c_-^2 = \Gamma_+ \Gamma_-, \quad c_+ c_- = c_D \sqrt{\lambda}. \tag{17b}$$

The dimensionless terms  $c_{\pm}$  in (16) show that solution behavior is governed by the three wave speeds ( $V_S, V_{\pm} = c_{\pm} V_S$ ) where  $1 < c_- < c_+$ . Data, e.g., [Brock 2009; Ignaczak and Ostoja-Starzewski 2010], suggest moreover that  $c_+ > c_D, c_- \approx c_D$ — so that  $V_+$  is larger than isothermal dilatational wave speed  $V_D = c_D V_S$  while  $V_-$  is approximately the same. Bounded behavior for  $(\hat{u}_k, \hat{\theta})$  as  $|x_3| \rightarrow \infty$  requires in light of (15) that  $\text{Re}(A_{\pm}) > 0$  and  $\text{Re}(B) > 0$  in the  $q$ -plane with, respectively, branch cuts

$$\text{Im}(q) = 0, \quad \frac{-1}{c_{\pm} - c} < \text{Re}(q) < \frac{1}{c_{\pm} + c}, \tag{18a}$$

$$\text{Im}(q) = 0, \quad \frac{-1}{1 - c} < \text{Re}(q) < \frac{1}{1 + c}. \tag{18b}$$

It is noted that (18) is valid only so long as  $c < 1$ ; i.e.,  $V(\psi) < V_S(|\psi| < \frac{1}{2}\pi)$ .

### 5. Application to fracture problem: equations for solution

In order that (15) and results in Appendix A represent the transform solution for the fracture problem, the transforms of (7) must be satisfied. Because (7) does not involve  $(\Sigma_k, d\Theta)$ , their transforms can be dropped. Use of (2c), (9), (10a), (10b), (11) and (12b) then give five equations for transforms of  $(\sigma_{3k}, \theta^{(\pm)}, \partial_3 \theta)$  along  $x_3 = 0$  in terms of transforms of  $(\Delta_k, \Theta)$ . It is noted that for  $(s > 0, x_3 = 0)$ ,

$$\sigma_{3k} = \sigma_{3k}^C - P_k \delta(x_1^0) \delta(x_2^0), \tag{19a}$$

$$\partial_3 \theta = \partial_3 \theta^C. \tag{19b}$$

Here  $(\sigma_{3k}^C, \partial_3 \theta^C)$  exists for  $x > 0$  in a region generated behind wave front  $c_+ s - x - cs > 0$ . Thus the corresponding transform exists for  $\text{Re}(q) > -1/(c_+ - c)$ . The Dirac function term has transform

$$-\frac{P_k}{p\beta} (\text{Re}(q) < 1/c). \tag{20}$$

Function  $(\Delta_k, \Theta)$  occurs for  $x < 0$  in a region generated behind wave front  $c_+ s + x + cs > 0$ . Thus the corresponding transform exists for  $\text{Re}(q) < 1/(c_+ + c)$ . Four transform equations can be written and are given in Appendix B. There it is noted that

$$M_{12}(q_{12}) = 0, \quad M_{12} \approx R_{12} q^4 (|q| \rightarrow \infty), \quad q_{12} = \frac{\pm 1}{c_{12} \pm c}, \tag{21a}$$

$$M_3(q_3) = 0, \quad M_3 \approx R_3 q^4 (|q| \rightarrow \infty), \quad q_3 = \frac{\pm 1}{c_3 \pm c}, \tag{21b}$$

$$M_{\pm}(q_R^{\pm}) = 0, \quad M_{\pm} q^4 (|q| \rightarrow \infty), \quad q_R^{\pm} = \frac{1}{c_R^{\pm} + c}, \frac{-1}{c_R^{\pm} - c}. \tag{21c}$$

In (21),  $(R_{12}, R_3, R_{\pm})$  are functions of  $c$ :

$$R_{12} = C_+ R_- - C_- R_+, \quad R_{12}(c_{12}^2) = 0 \quad (0 < c_{12} < 1), \tag{22a}$$

$$R_3 = C_+ a_+ \frac{R_-}{b} - C_- a_- \frac{R_+}{b}, \quad R_3(c_3^2) = 0 \quad (0 < c_3 < 1), \tag{22b}$$

$$R_{\pm} = 4a_{\pm} b - k^2, \quad R_{\pm}(0) = R_{\pm}((c_R^{\pm})^2) = 0 \quad (0 < c_R^{\pm} < 1), \tag{22c}$$

$$a_{\pm}(c) = \frac{1}{c_{\pm}} \sqrt{c_{\pm}^2 - c^2}, \quad b(c) = \sqrt{1 - c^2}, \quad k(c) = c^2 - 2. \tag{22d}$$

Terms  $(R_{\pm}, M_{\pm})$  have the form of the Rayleigh function [Achenbach 1976]. Thus  $(R_{12}, R_3)$  and  $(M_{12}, M_3)$  are thermoelastic Rayleigh functions of respectively, variables  $c$  and  $q$ . Data, e.g., [Brock 2009; Ignaczak and Ostoja-Starzewski 2010] indicate that in general,

$$0 < c_3 < c_{12} < 1 < c_- < c_+, \quad c_- \approx c_D -. \tag{23}$$

In view of (6) and (9) the fracture problem solution is governed by both  $(V_S, V_{\pm} = c_{\pm} V_S)$  and Rayleigh speeds  $V_{12} = c_{12} V_S$  and  $V_3 = c_3 V_S$ . Moreover, subcritical speed is defined as  $V(\psi) < V_3 (|\psi| < \frac{1}{2}\pi)$ .

### 6. Solution: Wiener–Hopf equation

The four equations, (B.1) and (B.2), involve eight unknown transforms  $(\bar{\sigma}_{3k}^C, \partial_3 \bar{\theta}^C)$  and  $(\bar{\Delta}_k, \bar{\Theta})$ . The regions of analyticity in the  $q$ -plane of the two transform sets differ but can also overlap. Thus (B.1) and (B.2) can be viewed as a set of coupled equations of the Wiener–Hopf type [Morse and Feshbach 1953; Achenbach 1976].

**Equation (B.1c).** It is noted that  $(A_{\pm}, B)$  form products  $(A_+^+ A_+^-, A_-^+ A_-^-, B^+ B^-)$  where

$$A_{\pm}^{\pm} = \frac{1}{\sqrt{c_{\pm}}} \sqrt{1 \pm q(c_{\pm} \mp c)}, \quad A_{\pm}^{\mp} = \frac{1}{\sqrt{c_{\mp}}} \sqrt{1 \pm q(c_{\mp} \mp c)}, \tag{24a}$$

$$B^{\mp} = \sqrt{1 \pm q(1 \mp c)}. \tag{24b}$$

In (24a)  $(A_{\pm}^+, A_{\pm}^-)$  are analytic in, respectively, overlapping half-planes  $\text{Re}(q) > -1/(c_{\pm} - c)$  and  $\text{Re}(q) < 1/(c_{\pm} + c)$ . Terms  $(B^+, B^-)$  in (24b) are analytic in overlapping half-planes  $\text{Re}(q) > -1/(1 - c)$  and  $\text{Re}(q) < 1/(1 + c)$ . Study of  $M_3$  in (B.3b) leads to construction of function

$$G_3 = -\frac{M_3}{\beta^2} \frac{c^2}{R_3} \frac{c_3^2 - c^2}{[1 + q(c_3 - c)][1 - q(c_3 + c)]}. \tag{25}$$

Here  $G_3 \rightarrow 1 (|q| \rightarrow \infty)$ , and has no zeros in the  $q$ -plane with branch cut  $\text{Im}(q) = 0, -1/(1 - c) < \text{Re}(q) < -1/(c_+ - c), 1/(c_+ + c) < \text{Re}(q) < 1/(1 + c)$ . Therefore  $G_3$  forms  $G_3^+ G_3^-$ , where  $(G_3^+, G_3^-)$  are defined by (C.1a) and are analytic in overlapping half-planes  $\text{Re}(q) > -1/(c_+ - c)$  and  $\text{Re}(q) < 1/(c_+ + c)$ .

Equation (B.1c) can then be written as

$$\begin{aligned} \frac{F^+}{G_3^+} \bar{\sigma}_{33}^C \frac{c_3 - c}{1 + q(c_3 - c)} - \frac{P_3}{p\beta} \left[ \frac{F^+}{G_3^+} \frac{c_3 - c}{1 + q(c_3 - c)} - \frac{\sqrt{c}}{g_3^+} \left(1 - \frac{c}{c_3}\right) \right] \\ = -\mu \frac{\Omega R_3}{2c^2} \frac{G_3^-}{F^-} \left( \frac{1}{c_3 + c} - 1 \right) p \bar{\Delta}_3 + \frac{P_3}{p\beta} \frac{\sqrt{c}}{g_3^+} \left(1 - \frac{c}{c_3}\right), \end{aligned} \tag{26a}$$



$$F^+ = \frac{A_+^+ A_-^+}{B^+}, \quad F^- = \frac{A_+^- A_-^-}{B^-}, \tag{26b}$$

$$A_\pm^+ \left(\frac{1}{c}\right) = B^+ \left(\frac{1}{c}\right) = F^+ \left(\frac{1}{c}\right) = \frac{1}{\sqrt{c}}, \quad g_3^+ = G_3^+ \left(\frac{1}{c}\right). \tag{26c}$$

The left-hand and right-hand sides of (26a) are analytic for respectively the overlapping half-planes  $\text{Re}(q) > -1/(c_+ - c)$  and  $\text{Re}(q) < 1/(c_+ + c)$  so that each side is an analytic continuation of the same entire function. In connection with (7),  $\Delta_k$  must vanish continuously on  $C$  for  $x \rightarrow 0-$ . Equation (10a) and (12b) therefore require that  $pq\bar{\Delta}_k$ , and also the right-hand side of (26a), vanish for  $|q| \rightarrow \infty$ . The entire function itself must then in light of Liouville’s theorem [Morse and Feshbach 1953] vanish, and (26a) leads to

$$\bar{\Delta}_3 = \frac{2\sqrt{c}\beta}{\mu p^2 g_3^+} \frac{F^- G_3^+}{c_3 \Omega M_3} [1 + q(c_3 - c)] P_3, \tag{27a}$$

$$\bar{\sigma}_{33}^C = -\frac{\sqrt{c} P_3}{c_3 p g_3^+} \frac{G_3^+}{\beta F^+} [1 + q(c_3 - c)]. \tag{27b}$$

Examination of the fracture problem solution requires knowledge of  $(\bar{\sigma}_{33}^C, \bar{\Delta}_3)$  for  $x \rightarrow 0-$  and  $x \rightarrow 0+$ , respectively. In view of (9)–(11),

$$\dot{f} = V_S(\partial_S - c\partial)f, \quad \partial f = \frac{\partial f}{\partial x}. \tag{28}$$

Therefore (13a) shows that expressions for transforms  $(\bar{\sigma}_{33}^C, p\beta\bar{\Delta}_3)$  that are valid for  $|q| \rightarrow \infty$  suffice in this regard, and are given by (D.2c) and (D.5c).

**Equation (B.1a) and (B.1b).** Algebraic manipulation of (B.1a) and (B.1b) leads to a partial uncoupling:

$$\left(\bar{\sigma}_{31}^C - \frac{P_1}{p\beta}\right) \cos \psi + \left(\bar{\sigma}_{32}^C - \frac{P_2}{p\beta}\right) \sin \psi = \frac{\mu}{\Omega\beta^2} \left(\frac{M_{12}}{2B} p\bar{\Delta}_P + qM_A\alpha_D\bar{\Theta}\right), \tag{29a}$$

$$\left(\bar{\sigma}_{31}^C - \frac{P_1}{p\beta}\right) \sin \psi - \left(\bar{\sigma}_{32}^C - \frac{P_2}{p\beta}\right) \cos \psi = \mu B p \bar{\Delta}_M. \tag{29b}$$

In view of (24b), (29b) can be written in Wiener–Hopf form (compare (26a)):

$$\frac{2}{B^+} \bar{\sigma}_M - \frac{2}{p\beta} \left(\frac{1}{B^+} - \sqrt{c}\right) (P_1 \sin \psi - P_2 \cos \psi) = \mu p B^- \bar{\Delta}_M + \frac{2\sqrt{c}}{p\beta} (P_1 \sin \psi - P_2 \cos \psi), \tag{30a}$$

$$\bar{\sigma}_M = \bar{\sigma}_{31}^C \sin \psi - \bar{\sigma}_{32}^C \cos \psi. \tag{30b}$$

Behavior of  $\Delta_k$  for  $x \rightarrow 0-$  dictates that both sides of (30a) vanish. Therefore,

$$\bar{\sigma}_M = \frac{1}{p\beta} (1 - \sqrt{c}B^+) (P_1 \sin \psi - P_2 \cos \psi), \tag{31a}$$

$$\bar{\Delta}_M = \frac{-2\sqrt{c}}{\mu p^2 \beta B^-} (P_1 \sin \psi - P_2 \cos \psi). \tag{31b}$$

**Equation (B.2) and (29a).** Equations (29a) and (B.2) are treated as linear equations for  $(\bar{\Theta}, \bar{\Delta}_P)$ , and are solved simultaneously to yield

$$\alpha_D \bar{\Theta} = \frac{M_{12}}{BM_3} \left( \frac{2}{p} \alpha_D \partial_3 \bar{\theta}^C \right) + 4q \frac{M_A}{M_3} \frac{\varepsilon}{\lambda} \frac{\beta^2}{\mu} [\bar{\sigma}_P - (P_1 \cos \psi + P_2 \sin \psi)], \quad (32a)$$

$$p \bar{\Delta}_P = -4q \frac{M_A}{M_3} \left( \frac{2}{p} \alpha_D \partial_3 \bar{\theta}^C \right) + \frac{2M_C}{M_3} \frac{\beta^2}{\mu} [\bar{\sigma}_P - (P_1 \cos \psi + P_2 \sin \psi)], \quad (32b)$$

$$\bar{\sigma}_P = \bar{\sigma}_{31}^C \cos \psi + \bar{\sigma}_{32}^C \sin \psi. \quad (32c)$$

As in the case of  $M_3$  functions related to  $(M_{12}, M_A, M_C)$  can be defined as

$$G_{12} = -\frac{M_{12}}{\beta^2} \frac{c^2}{R_{12}} \frac{c_{12}^2 - c^2}{[1 + q(c_{12} - c)][1 - q(c_{12} + c)]} = G_{12}^+ G_{12}^-, \quad (33a)$$

$$G_A = \frac{M_A a_+(c)}{A + m_A(c)} = G_A^+ G_A^-, \quad m_A(c) = a_+(c) - a_-(c), \quad (33b)$$

$$G_C = \frac{M_C a_+(c)}{A + m_C(c)} = G_C^+ G_C^-, \quad m_C(c) = C_+ a_+(c) - C_- a_-(c). \quad (33c)$$

Functions  $(G_{12}^+, G_A^+, G_C^+)$  and  $(G_{12}^-, G_A^-, G_C^-)$  are analytic in overlapping halves of the cut  $q$ -plane, and are given by (C.2) and (C.4), respectively. Factorization based on these results does not in general put (32a) and (32b) in standard Wiener–Hopf form [Achenbach 1976]. Equation (24a) and (24b) show for  $|q| \rightarrow \infty$  however that

$$A_{\pm}^+ \approx \sqrt{q} \sqrt{1 + c/c_{\pm}}, \quad B^+ \approx \sqrt{q} \sqrt{1 + c} \quad (\text{Re}(q) > 0-), \quad (34a)$$

$$A_{\pm}^- \approx \sqrt{-q} \sqrt{1 - c/c_{\pm}}, \quad B^- \approx \sqrt{-q} \sqrt{1 - c} \quad (\text{Re}(q) < 0+). \quad (34b)$$

Equations (21), (B.3) and (34) show that (32) for  $|q| \rightarrow \infty$  depends on  $(\beta, \sqrt{\pm q})$ , and that  $\sqrt{\pm q}$  define overlapping half-planes  $\text{Re}(q) > 0-$  and  $\text{Re}(q) < 0+$  as regions of analyticity. As exemplified by (D.1), (D.2c) and (D.5c), functions of  $\sqrt{\pm q}$  are sufficient for study of solution behavior when  $|x| \approx 0$ . Equation (32a) and (32b) then yield Wiener–Hopf equations whose solutions are combined with asymptotic forms for (31). This process leads to (D.2a) and (D.2b) valid for  $x \rightarrow 0+$ , and (D.4) and (D.5) valid for  $x \rightarrow 0-$ .

### 7. Transform inversions valid on crack plane near C

For  $(1/\sqrt{q}, \sqrt{q})$  and  $1/\sqrt{-q}$  respectively inverse operation (12b) yields

$$-\frac{p^2}{\pi \sqrt{x}} \int_+ \frac{du}{\sqrt{u}} \exp(-pu), \quad \frac{p}{2\pi} \frac{1}{x^{3/2}} \int_+ \frac{du}{\sqrt{u}} \exp(-pu) \quad (x > 0), \quad (35a)$$

$$-\frac{p^2}{\pi \sqrt{-x}} \int_+ \frac{du}{\sqrt{u}} \exp(-pu) \quad (x < 0). \quad (35b)$$

The “+” signifies integration over the entire positive real  $u$ -axis. In view of (37) functions in Appendix D involve  $p \exp(-pu)$ , and its inverse is recognized as  $\partial_S \delta(s - u)$  [Abramowitz and Stegun 1972]. The

point force represents a step-function in time, so for generality we now consider the case

$$P_k = P_k(V_S t), \quad P_k(0) = 0. \tag{36}$$

Clarity of solution is enhanced if points in the  $x_1^0 x_2^0$ -plane are located with respect to fixed point  $\mathbf{x}_0 = 0$ . Therefore the inverses from (D.1)–(D.3) are, by convolution, written as functions of  $(x_0, \psi, s)$ , where  $x_0 = x + cs$ , and for  $(s > 0, x_0 \rightarrow cs+, |\psi| < \frac{1}{2}\pi)$ ,

$$\alpha_D \partial_3 \theta^C \approx -\frac{2\varepsilon}{\mu \Gamma_+ \Gamma_-} \frac{m_A m_C K_{II}}{\sqrt{c}(x_0 - cs)^{3/2}}, \tag{37}$$

$$\sigma_{31}^C \approx \frac{1}{\sqrt{c}\sqrt{x_0 - cs}} \left[ \sin \psi \sqrt{1 - c} K_{III} + \cos \psi \frac{R_3}{c^2} N_{12} K_{II} \right], \tag{38a}$$

$$\sigma_{32}^C \approx \frac{1}{\sqrt{c}\sqrt{x_0 - cs}} \left[ -\cos \psi \sqrt{1 - c} K_{III} + \sin \psi \frac{R_3}{c^2} N_{12} K_{II} \right], \tag{38b}$$

$$\sigma_{33}^C \approx \frac{K_1}{\sqrt{c}\sqrt{x_0 - cs}} \frac{c^2}{R_3} \frac{\sqrt{c_+ c_-} \sqrt{1 - c}}{\sqrt{c_+ - c} \sqrt{c_- - c}}. \tag{38c}$$

In similar fashion (D.4) and (D.5) yield for  $(s > 0, x_0 \rightarrow cs-, |\psi| < \frac{1}{2}\pi)$ ,

$$\alpha_D \Theta \approx \frac{4m_A}{\mu \sqrt{cs - x_0}} \frac{\varepsilon}{\lambda} K_{II}, \tag{39}$$

$$\dot{\Delta}_1 \approx \frac{2V_S \sqrt{c}}{\mu \sqrt{cs - x_0}} \left[ \frac{\sin \psi}{\sqrt{1 + c}} K_{III} + m_C \cos \psi K_{II} \right], \tag{40a}$$

$$\dot{\Delta}_2 \approx \frac{2V_S \sqrt{c}}{\mu \sqrt{cs - x_0}} \left[ \frac{\cos \psi}{\sqrt{1 + c}} K_{III} + m_C \sin \psi K_{II} \right], \tag{40b}$$

$$\dot{\Delta}_3 \approx \frac{2V_S \sqrt{c} \Omega}{\mu \sqrt{cs - x_0}} \frac{\sqrt{c_+ + c} \sqrt{c_- + c}}{\sqrt{c_+ c_-} \sqrt{1 + c}} K_I. \tag{40c}$$

In (37)–(40),

$$K_I = \frac{c^2}{\pi g_3^+ R_3} \left(1 - \frac{c}{c_3}\right) \partial_S \int_0^s \frac{du}{\sqrt{s-u}} \frac{d}{du} P_3, \tag{41a}$$

$$K_{II} = \frac{c^2}{\pi g_3^+ R_3} \left(1 - \frac{c}{c_3}\right) \partial_S \int_0^s \frac{du}{\sqrt{s-u}} \frac{d}{du} (P_1 \cos \psi + P_2 \sin \psi), \tag{41b}$$

$$K_{III} = \frac{1}{\pi} \partial_S \int_0^s \frac{du}{\sqrt{s-u}} \frac{d}{du} (P_1 \sin \psi + P_2 \cos \psi). \tag{41c}$$

The roman numeral subscripts reflect the observation that, in a 2D study ( $\psi = 0$ ) terms (41a), (41b) and (41c) would be associated with, respectively, the opening, in-plane shear and antiplane shear modes of fracture [Freund 1990].

### 8. Transform inversions valid near C

Expressions for  $(\dot{u}_k, \theta)$  near C for  $(x_3^0, x_3) \neq 0$  are also required. In view of (9c) and (28),  $L(\dot{u}_k) = \beta p \bar{u}_k$  and  $(\bar{u}_k, \bar{\theta})$  can be generated from (15) and Appendix A by setting  $(d\bar{\Theta}, \bar{\Sigma}_k) = 0$  and substituting results from Appendix D. For  $x_3 \neq 0$ , a more explicit version of inversion formula (12) is useful:

$$\tilde{f}(p, q_1, q_2, x_3) \rightarrow f_\Psi(p, q, \psi) \exp(-pA|x_3|), \quad A = (A_\pm, B), \quad (42a)$$

$$\hat{f}(p, x, \psi, x_3) = -\frac{p^2}{2\pi} \int \frac{|q|}{q} f_\Psi(p, q, \psi) \exp[p(qx - A|x_3|)] dq. \quad (42b)$$

Result (37) follows from use of Cauchy theory to change the integration path in (12b) to the  $\text{Re}(q)$ -axis. For (42b) the path is changed to a contour  $q(A)$  in the complex  $q$ -plane along which the exponential term assumes the form  $\exp(-pu)$ , where  $u$  is real and positive. Because inversions valid near C are sufficient, local coordinates  $(r, \psi, \phi)$  centered on the portion of C that borders  $\delta A$  are introduced:

$$r = \sqrt{x^2 + x_3^2}, \quad \phi = \tan^{-1} \frac{x_3}{x} \quad (|\phi| < \pi). \quad (43)$$

In (42b)  $q(A_\pm)$  and  $q(B)$  for  $r \approx 0$  have, respectively, asymptotic forms

$$-\frac{u}{4Q_\pm}, \quad Q_\pm = \cos \phi \mp ia_\pm \sin \phi, \quad (44a)$$

$$-\frac{u}{rQ_B}, \quad Q_B = \cos \phi \mp ib \sin \phi. \quad (44b)$$

It is noted that (D.4) and (D.5), which depend on  $1/\sqrt{-q}$ , are associated in Appendix with operator  $(\pm)$ . In the case of contour  $q(B)$  therefore, (35a) and (35b) respectively are replaced by

$$-\frac{p}{\pi c} \frac{B^{(+)}}{\sqrt{2r}} \int_+ \frac{du}{\sqrt{u}} \exp(-pu), \quad (\mp) \frac{p}{\pi c} \frac{B^{(-)}}{\sqrt{2r}} \int_+ \frac{du}{\sqrt{u}} \exp(-pu). \quad (45a)$$

In the case of contour  $q(A_\pm)$  replacements are

$$-\frac{p}{\pi c} \frac{A_\pm^{(+)}}{\sqrt{2r}} \int_+ \frac{du}{\sqrt{u}} \exp(-pu), \quad (\mp) \frac{p}{\pi c} \frac{A_\pm^{(-)}}{\sqrt{2r}} \int_+ \frac{du}{\sqrt{u}} \exp(-pu). \quad (45b)$$

In (45),  $(B^{(\pm)}, A_\pm^{(\pm)})$  are factors of the real (+) and imaginary (-) parts of  $(\sqrt{Q_1}, \sqrt{Q_\pm})$ :

$$B^{(\pm)} = \sqrt{1(\pm)(\cos \phi)/B_\Phi}, \quad B_\Phi = \sqrt{1 - c^2 \sin^2 \phi}, \quad (46a)$$

$$A_\pm^{(\pm)} = \sqrt{1(\pm)(\cos \phi)/A_\Phi^\pm}, \quad A_\Phi^\pm = \sqrt{1 - c^2/c_\pm^2 \sin^2 \phi}. \quad (46b)$$

Convolution involving (38) is again introduced, and results for  $\dot{u}_k(r \rightarrow 0)$  follow:

$$\begin{aligned} \dot{u}_1 \approx & \frac{\sqrt{2c}}{\mu\sqrt{r}} \left[ \frac{\sqrt{c_+ + c}\sqrt{c_- + c}}{c^2\sqrt{1+c}\sqrt{c_+c_-}} P_3^{(+)} K_I - \frac{P_{12}^{(-)}}{c^2} K_{II} \text{sgn}(\phi) \right] \cos \psi \\ & - \frac{\sqrt{c}}{\mu\sqrt{2r}} \frac{B^{(-)} K_{III}}{\sqrt{1+c}} \text{sgn}(\phi) \sin \psi, \end{aligned} \quad (47a)$$

$$\dot{u}_2 \approx \frac{\sqrt{2c}}{\mu\sqrt{r}} \left[ \frac{\sqrt{c_+ + c}\sqrt{c_- + c}}{c^2\sqrt{1+c}\sqrt{c_+c_-}} P_3^{(+)} K_I - \frac{P_{12}^{(-)}}{c^2} K_{II} \operatorname{sgn}(\phi) \right] \sin \psi + \frac{\sqrt{c}}{\mu\sqrt{2r}} \frac{B^{(-)} K_{III}}{\sqrt{1+c}} \operatorname{sgn}(\phi) \cos \psi, \quad (47b)$$

$$\dot{u}_3 \approx \frac{\sqrt{2c}}{\mu\sqrt{r}} \left[ \frac{\sqrt{c_+ + c}\sqrt{c_- + c}}{c^2\sqrt{1+c}\sqrt{c_+c_-}} P_3^{(-)} K_I \operatorname{sgn}(\phi) - \frac{P_{12}^{(+)}}{c^2} K_{II} \right]. \quad (47c)$$

In (47), ( $|\psi| < \frac{1}{2}\pi$ ,  $|\phi| < \pi$ ) and

$$P_3^{(+)} = \frac{k}{2} \left( \frac{C_+}{a_-} A_-^{(+)} - \frac{C_-}{a_+} A_+^{(+)} \right) + b\Omega B^{(+)}, \quad (48a)$$

$$P_3^{(-)} = \frac{k}{2} (C_+ A_-^{(-)} - C_- A_+^{(-)}) + \Omega B^{(-)}, \quad (48b)$$

$$P_{12}^{(+)} = C_+ a_+ A_-^{(+)} - C_- a_- A_+^{(+)} + \frac{kmC}{2b} B^{(+)}, \quad (48c)$$

$$P_{12}^{(-)} = C_+ a_+ A_-^{(-)} - C_- a_- A_+^{(-)} + \frac{k}{2} mC B^{(-)}. \quad (48d)$$

For ( $r \rightarrow 0$ ,  $|\psi| < \frac{1}{2}\pi$ ,  $|\phi| < \pi$ ) temperature change takes the form

$$\theta \approx \frac{\varepsilon}{\mu\lambda} \frac{\sqrt{2c}}{\alpha_D \sqrt{r}} \left[ T_{12}^{(-)} \frac{K_{II}}{c^2} \operatorname{sgn}(\phi) - T_3^{(+)} \frac{\sqrt{c_+ + c}\sqrt{c_- + c}}{c^2\sqrt{c_+c_-}\sqrt{1+c}} K_I \right], \quad (49a)$$

$$T_{12}^{(-)} = a_- A_+^{(-)} - a_+ A_-^{(-)}, \quad T_3^{(+)} = \frac{k}{2} \left( \frac{A_+^{(+)}}{a_+} - \frac{A_-^{(+)}}{a_-} \right). \quad (49b)$$

### 9. Criterion: dynamic energy release rate

A standard criterion for brittle fracture, e.g., [Freund 1972], equates the rate at which surface energy is released to the rate of work associated with traction and relative displacements in the fracture zone  $\mathfrak{I}$ . In this study heat is neither added to, nor extracted from, the solid. Therefore, if kinetic energy is included [Gdoutos 1993] the equation takes the form

$$D \iint_{\delta A} e_F dx_1^0 dx_2^0 = \iint_{\mathfrak{I}} \sigma_{3k}^C \dot{\Delta}_k dx_1^0 dx_2^0 + D \iiint_{123} \frac{1}{2} \rho \dot{u}_k \dot{u}_k dx_1^0 dx_2^0 dx_3^0. \quad (50)$$

Here  $e_F$  is the surface energy per unit area, and is generally assumed to be constant [de Boer et al. 1988; Skriver and Rosengard 1992]. Fracture zone  $\mathfrak{I}$  is a strip of infinitesimal thickness in the  $x_1^0 x_2^0$ -plane that straddles the portion of  $C$  that borders  $\delta A$ . Subscript 123 signifies integration over the solid. Use of transport theory [Malvern 1969] and translating basis  $\mathbf{x}$  expressed in terms of  $(x, \psi, x_3 = 0)$  gives for the first term in (47)

$$V e_{FS} \int_{\Psi} d\psi c \sqrt{c^2 + (c')^2}, \quad f' = \frac{df}{d\psi}. \quad (51)$$

Here  $\Psi$  signifies integration over  $|\psi| < \frac{1}{2}\pi$ . Use of  $\mathbf{x}$  for the integration over  $\mathfrak{T}$  gives

$$\int_{\Psi} d\psi \int_{cs-}^{cs+} |x_0| \sigma_{3k}^C \dot{\Delta}_k dx_0. \tag{52a}$$

In light of (38) and (40) it can be shown [Freund 1972] that the integrand of (52a) features Dirac function  $\delta(x_0 - cs)$ . Moreover, linear behavior in  $s$  displayed in (50) places a restriction on  $\partial_S P_k$ , e.g., [Achenbach and Brock 1973]. That is,  $V$  must in general vary with time. One case, however, for which time-invariance is valid is

$$\partial_S P_k = p_k \sqrt{s}. \tag{52b}$$

Equation (41) and (52a) then give

$$\pi \frac{s}{\mu} \int_{\Psi} V d\psi \left[ \frac{R_3}{c^2} N_{12} m_C K_{II}^2 + \sqrt{\frac{1-c}{1+c}} \left( K_{III}^2 + \Omega \frac{R_3}{c^2} \frac{\sqrt{c_+ + c} \sqrt{c_- + c}}{\sqrt{c_+ - c} \sqrt{c_- - c}} K_I^2 \right) \right], \tag{52c}$$

$$K_I = \frac{c^2}{g_3^+ R_3} \left( 1 - \frac{c}{c_3} \right) p_3, \tag{53a}$$

$$K_{II} = \frac{c^2}{g_3^+ R_3} \left( 1 - \frac{c}{c_3} \right) (p_1 \cos \psi + p_2 \sin \psi), \tag{53b}$$

$$K_{III} = p_1 \sin \psi - p_2 \cos \psi. \tag{53c}$$

Equation (47) is singular near  $C$ . The last integration in (50) can then be, via transport theory [Malvern 1969], taken over the surface of a tube of radius  $r_C \rightarrow 0$  that encloses the portion of  $C$  that borders  $\delta A$ . Integration can be performed with coordinates (43) and expressions (47) and (53), so that the last term in (50) becomes

$$-\frac{s}{\mu} \int_{\Psi} V d\psi \sqrt{c^2 + (c')^2} \left[ \left( 1 + \frac{c}{c_+} \right) \left( 1 + \frac{c}{c_-} \right) \frac{K_I^2 E_I}{c^3 (1+c)} + \frac{K_{II}^2}{c^3} E_{II} + \frac{K_{III}^2 E_{III}}{c(1+c)} \right]. \tag{54}$$

Coefficients ( $E_I, E_{II}, E_{III}$ ) are defined, in light of (48), as

$$E_I = \int_{\Psi} \cos \phi [(P_3^{(+)})^2 + (P_3^{(-)})^2] d\phi, \tag{55a}$$

$$E_{II} = \int_{\Psi} \cos \phi [(P_{12}^{(+)})^2 + (P_{12}^{(-)})^2] d\phi, \tag{55b}$$

$$E_{III} = \int_{\Psi} \cos \phi (B^{(-)})^2 d\phi. \tag{55c}$$

Here  $\Phi$  signifies integration over range  $|\phi| < \pi$ . Equations (51), (52c) and (54) all involve integration with respect to  $\psi$ , so that (50) gives for  $|\psi| < \frac{1}{2}\pi$ ,

$$\begin{aligned} \mu e_F \sqrt{c^2 + (c')^2} = & \frac{K_I^2}{1+c} \left( 1 + \frac{c}{c_+} \right) \left( 1 + \frac{c}{c_-} \right) \left[ \frac{\pi b \Omega R_3}{c^2 a_+ a_-} - \frac{E_I}{c^3} \sqrt{c^2 + (c')^2} \right] \\ & + K_{II}^2 \left[ \frac{\pi R_3}{c^2} N_{12} m_C - \frac{E_{II}}{c^3} \sqrt{c^2 + (c')^2} \right] + \frac{K_{III}^2}{1+c} \left[ \pi b - \frac{E_{III}}{c} \sqrt{c^2 + (c')^2} \right]. \end{aligned} \tag{56}$$

### 10. Aspects of solution behavior

Formula (56) is a nonlinear differential equation for  $c(\psi)$ . Asymptotic expressions preserved the singular behavior of  $(\sigma_{3k}^C, \dot{\Delta}_k, \dot{u}_k)$  and were therefore sufficient for derivation of (56). The singular behavior seen in asymptotic expression (49) for  $\theta$  is also useful in generating a finite measure of thermal response near  $C$ . Norm  $\|\theta\|$  is defined as

$$\|\theta\| = \sqrt{\oint \theta^2 dl}. \tag{57}$$

Equation (57) involves (49a) in a line integral for given  $\psi$  taken counterclockwise about the circumference of the circle of radius  $r = r_C \rightarrow 0$ . Because  $dl = r d\phi$  integration is over range  $|\phi| < \pi$ , so that (57) gives for  $|\psi| < \frac{1}{2}\pi$  the finite result

$$\|\theta\| = \frac{\sqrt{2c}}{\mu c^2} \frac{\varepsilon}{\lambda \alpha_D} \sqrt{\left(1 + \frac{c}{c_+}\right) \left(1 + \frac{c}{c_-}\right) \frac{K_I^2}{1+c} T_I + K_{II}^2 T_{II}}, \tag{58a}$$

$$T_I = \int_{\phi} (T_3^{(+)})^2 d\phi, \quad T_{II} = \int_{\phi} (T_{12}^{(-)})^2 d\phi. \tag{58b}$$

Equations (56) and (58) are somewhat complicated and opaque. Insight concerning  $c(\psi)$  and  $\|\theta\|$ , based partly on analytical expressions, is possible by considering values of parameter  $V(\psi)$  that are not negligible, but well below critical, i.e.,  $c/c_3 \approx O(10^{-1})$ . To this end first-order expansions in  $c^2$  for  $(P_{12}^{(\pm)}, P_3^{(\pm)}, B^{(-)})$  and  $(T_3^{(+)}, T_{12}^{(-)})$  are developed and given by (E.1)–(E.3). Integration in (55) is performed on the basis of (E.1) and (E.2), and (56) gives for  $|\psi| < \frac{1}{2}\pi$  asymptotic form

$$\begin{aligned} \frac{\mu e_F}{\pi} \sqrt{c^2 + (c')^2} &\approx \frac{p_3^2}{k_C} [1 + E_I^0 c \sqrt{c^2 + (c')^2}] \\ &+ \frac{1}{k_C} (p_1 \cos \psi + p_2 \sin \psi)^2 [1/\Omega + E_{II}^0 c \sqrt{c^2 + (c')^2}] \\ &+ (p_1 \sin \psi - p_2 \cos \psi)^2 [1 + E_{III}^0 c \sqrt{c^2 + (c')^2}], \end{aligned} \tag{59a}$$

$$E_I^0 = \frac{5}{32} \left(1 + \frac{1}{c_D^2}\right), \quad E_{II}^0 = \frac{1}{32} \frac{4 + 3c_D^2}{c_D^2 - 1}, \quad E_{III}^0 = \frac{1}{4}, \tag{59b}$$

$$k_C = 2 \left(1 - \frac{1}{c_D^2}\right). \tag{59c}$$

Use of (E.1), (E.3) and (58b) leads to an asymptotic form of (58a) for  $|\psi| < \frac{1}{2}\pi$ :

$$\|\theta\| \approx \frac{\varepsilon}{\lambda \alpha_D} \frac{\sqrt{33\pi c}}{8\mu(c_D^2 - 1)} \sqrt{p_3^2 + (p_1 \cos \psi + p_2 \sin \psi)^2}. \tag{60}$$

Equation (59a) differs from its counterpart in [Brock 2017b] in that it does depend on thermal properties, i.e.,  $\Omega$ . In the previous work, thermal properties have a second-order, i.e.,  $O(c^4)$  effect. Equation (60) differs from its counterpart in that the relative influence of compression and shear loading depends only on  $\psi$  and the values of  $p_k$ . Equation (59) and (60) are now used to study two cases.

### 11. Case A: pure compression

Here  $p_1 = p_2 = 0$ ,  $p_3 = p_A > 0$ . Problem symmetry exists with respect to the  $x_1^0 x_3^0$ -plane, and (59) reduces to

$$(1 - c_A^2 E_I^0 z)z = 1, \quad (61a)$$

$$z = \frac{c}{c_A}, \quad c_A = \frac{\pi p_A^2}{\mu e_F k_C}. \quad (61b)$$

When kinetic energy is, respectively, neglected ( $E_I^0 = 0$ ) and included, (61a) gives

$$c(\psi) = c_A, \quad (62a)$$

$$c(\psi) = c_A^E = \frac{1}{2E_I^0 c_A} (1 - \sqrt{1 - 4E_I^0 c_A^2}). \quad (62b)$$

Equation (62) describes circular crack edge extension zone contours. Equation (60) gives for (62a) and (62b) respectively the constant values

$$\|\theta\| \approx \frac{\varepsilon}{\lambda \alpha_D} \frac{\sqrt{33\pi} p_A}{8\mu(c_D^2 - 1)} (\sqrt{c_A}, \sqrt{c_A^E}). \quad (63)$$

For illustration consider a generic metal with properties [de Boer et al. 1988; Skriver and Rosengaard 1992; Brock 2009; Ignaczak and Ostoja-Starzewski 2010]

$$\begin{aligned} \mu &= 79 \text{ GPa}, & e_F &= 2.2 \text{ J/m}^2, & V_S &= 3094 \text{ m/s}, & c_D &= 2, \\ c_+ &= 4.5452, & c_- &= 1.997, & c_3 &= 0.9332, & T_0 &= 294 \text{ K}, \\ \alpha_D &= 89.6(10^{-6}) \text{ K}^{-1}, & \varepsilon &= 0.05044, & h &= 3.1862(10^{-9}) \text{ m}, & h_0 &= 1.547(10^{-10}) \text{ m}. \end{aligned}$$

Calculations for  $c_A$ ,  $c_A^E$  and  $\|\theta\|$  are given in Table 1 for different values of  $p_A$ . There  $c_A^E > c_A$ , thus showing that neglect of kinetic energy leads to under-prediction of crack extension speed  $V \cos \psi$ . This effect decreases with increasing  $p_A$  however. Entries for  $\|\theta\|$  that correspond to  $(c_A, c_A^E)$  behave in the same manner, but the under-prediction effect is more pronounced. It is noted that the same behavior is exhibited in [Brock 2017b]. However, there the effect of increasing  $p_A$  on the under-prediction of  $\|\theta\|$  is less pronounced.

### 12. Case B: mixed-mode loading

Here ( $p_1 = f_B p_3$ ,  $p_2 = 0$ ,  $p_3 = p_B$ ) with ( $0 < f_B < 1$ ,  $p_B > 0$ ). Problem symmetry again exists with respect to the  $x_1^0 x_3^0$ -plane, and (59) can now reduce for  $|\psi| < \frac{1}{2}\pi$  to

$$\sqrt{z^2 + (z')^2} [1 - z(\Omega_0 + \Omega_1 \cos^2 \psi)] = 1 + f_B^2 k_C + f_B^2 (1/\Omega - k_C) \cos^2 \psi, \quad (64a)$$

$$\|\theta\| = \frac{\varepsilon p_B}{\lambda \alpha_D} \frac{\sqrt{33\pi c(\psi)}}{8\mu(c_D^2 - 1)} \sqrt{1 + f_B^2 \cos^2 \psi}, \quad (64b)$$

$$z = \frac{c(\psi)}{c_B}, \quad c_B = \frac{\pi p_B^2}{\mu e_F k_C}. \quad (64c)$$



kinetic energy neglected

$f_A$	1	3	5	10	15
$c_A$	0.00127	0.01143	0.03174	0.12694	0.28562
$f_N$	0.05509	0.49578	1.37714	5.50834	12.3934

kinetic energy included

$f_A$	1	3	5	10	15
$c_A^E$	0.02017	0.01143	0.31741	0.12734	0.29032
$f_N$	0.21957	0.49578	1.37727	5.51726	12.4959

**Table 1.** Case A:  $c_A, c_A^F, \|\theta\| = f_N(10^{-1}) \text{ Km}^{1/2}$  for  $p_A = f_A(10^4) \text{ N/m}^{3/2}$ .

When kinetic energy is neglected we have  $\Omega_0 = \Omega_1 = 0$ ; when it is included,

$$\Omega_0 = c_B^2(E_I^0 + k_C f_B^2 E_{III}^0), \quad \Omega_1 = c_B^2 f_B^2 (E_{II}^0 - k_C E_{III}^0). \quad (65)$$

Explicit  $\psi$ -dependence of (64a) implies that the crack extension zone contour is not a circular arc, and that obtaining an analytical solution for  $c(\psi)$  may not be simple. Analysis in [Brock 2017b] suggests use of series representation:

$$c(\psi) = c_B \left[ g_0 + \sum_1^N \frac{g_{2j}}{2j} \cos^{2j} \psi \right]. \quad (66)$$

Substitution of (66) into (64a) and equating coefficients of terms  $\cos^{2j} \psi$  gives recursive equations for  $(g_0, g_{2j})$ . Equations for  $(g_0, g_2)$  are quadratic, and solutions are given in Appendix F. Equations for  $(g_4, g_6, \dots)$  are linear.

Calculations for  $c$  and  $\|\theta\|$  are listed in Table 2 (kinetic energy neglected) and Table 3 (kinetic energy included) for various values of  $\psi$  and loading ratio  $f_B$ . Compression load  $p_3 = p_B = 5(10^4) \text{ N/m}^{1/2}$  is used, and the same generic metal featured in Table 1. Entries for  $c$  show that increasing  $f_B$  (i.e., relative importance of shear loading) produces crack contours that are somewhat elliptical. That is the maximum rate of crack extension into the solid is less than the rate at which new crack surface spreads along the original, semi-infinite crack contour. Inclusion of kinetic energy appears to enhance the deviation from a circular arc. It is also noted that the relation between the two rates is the reverse of that found in [Brock 2017b], where discontinuity in temperature across the crack plane is not allowed.

Entries in Table 2 and Table 3 indicate that increasing  $f_B$  also enhances  $\|\theta\|$ . When kinetic energy is neglected the maximum value occurs directly ahead of the translating point forces. When kinetic energy is included however,  $\|\theta\|$  can achieve maximum values for  $|\psi| \neq 0$  when  $f_B$  is large enough. A maximum for  $|\psi| \neq 0$  is also seen in [Brock 2017b], which however only considered the case  $p_1 = p_3$ .

### 13. Some observations

This paper extends the range of [Brock 2017a; 2017b] for 3D dynamic fracture by considering a transient problem with mixed-mode loading in a thermoelastic solid with relaxation. The solid is initially at rest

## kinetic energy neglected

	$f_B = \frac{1}{4}$	$f_B = \frac{1}{3}$	$f_B = \frac{1}{2}$	$f_B = \frac{2}{3}$	$f_B = 1.0$
$\psi = 0^\circ : c$	0.03417	0.03605	0.04136	0.04881	0.06522
$f_N$	1.47304	1.54726	1.7578	2.0526	2.79198
$\psi = 15^\circ : c$	0.03421	0.03612	0.0415	0.04906	0.0663
$f_N$	1.47091	1.54344	1.74908	2.03649	2.76738
$\psi = 30^\circ : c$	0.03431	0.03629	0.04191	0.04975	0.06914
$f_N$	1.46503	1.53287	1.72458	1.99105	2.689
$\psi = 45^\circ : c$	0.03444	0.03654	0.04248	0.05075	0.07279
$f_N$	1.45689	1.51811	1.68996	1.92525	2.5544
$\psi = 60^\circ : c$	0.03458	0.03678	0.04305	0.05179	0.07619
$f_N$	1.44862	1.05301	1.65333	1.8545	2.38568
$\psi = 75^\circ : c$	0.34674	0.03696	0.04348	0.05259	0.07852
$f_N$	1.4425	1.49167	1.62539	1.79905	2.23758
$\psi = 90^\circ : c$	0.03471	0.03702	0.04364	0.05209	0.07934
$f_N$	1.44024	1.48747	1.61492	1.77788	2.17748

**Table 2.** Case B:  $c, \|\theta\| = f_N(10^{-6}) \text{ Km}^{1/2}$  for  $p_B = 5(10^4) \text{ N/m}^{3/2}$ , various  $f_B = p_1/p_B$  and  $\psi$ .

at uniform (absolute) temperature, and contains a semi-infinite, closed slit. Shearing and compressive point forces are applied just behind the crack edge, and initiate brittle fracture. Dynamic similarity is assumed, i.e., extension rate of points on the crack edge is constant in time, but can vary with location.

Unilateral temporal and spatial transforms are employed. In the latter case however, use is made of variable transformations based on quasipolar coordinates. Focus upon fracture initiation, moreover, justifies use of asymptotic expressions that, in integral transform space, give four equations that relate discontinuity in crack surface temperature, crack opening, crack plane heat flux and traction. The equations can be rewritten in Wiener–Hopf [Morse and Feshbach 1953; Achenbach 1976] form. Analytical solutions for transforms with inverse valid near the crack edge are obtained. Such inverses are sufficient to derive the nonlinear differential equation for the crack edge contour and an exact formula for the norm of the change in crack edge temperature.

As is predictable [Achenbach and Brock 1973], assumption of dynamic similarity restricts the type of time variation of the point forces. A suitable type is identified, however, and used to study an example of pure compression (Case A) and one of mixed-mode loading (Case B). For Case A, the extending portion of the crack edge is circular, and the norm of temperature near the edge is constant. In Case B, extending portion of the crack edge is elliptical, with the maximum rate of extension into the solid being less than the expansion rate of new crack surface along the original rectilinear crack contour. The temperature norm is also not constant. In both cases, inclusion of kinetic energy gives larger extension rates and temperature norms. However, this effect decreases as the force magnitudes are increased.

kinetic energy included

	$f_B = \frac{1}{4}$	$f_B = \frac{1}{3}$	$f_B = \frac{1}{2}$	$f_B = \frac{2}{3}$	$f_B = 1.0$
$\psi = 0^\circ : c$	0.03414	0.0361	0.04172	0.04843	0.05253
$f_N$	1.47228	1.54833	1.76545	2.04463	2.5057
$\psi = 15^\circ : c$	0.03422	0.03616	0.04183	0.05063	0.05526
$f_N$	1.47116	1.5444	1.75575	2.06896	2.5266
$\psi = 30^\circ : c$	0.03432	0.03632	0.04213	0.05078	0.06204
$f_N$	1.4652	1.53346	1.72904	2.01157	2.5473
$\psi = 45^\circ : c$	0.03444	0.03648	0.04258	0.05122	0.0697
$f_N$	1.45696	1.51838	1.69195	1.9342	2.4996
$\psi = 60^\circ : c$	0.03458	0.03678	0.04309	0.05194	0.07551
$f_N$	1.44864	1.50301	1.65411	1.85707	2.37501
$\psi = 75^\circ : c$	0.03467	0.03696	0.0435	0.05263	0.07858
$f_N$	1.4425	1.49169	1.62577	1.79968	2.23839
$\psi = 90^\circ : c$	0.03471	0.03702	0.04365	0.05293	0.07945
$f_N$	1.44024	1.48747	1.61516	1.77844	2.17899

**Table 3.** Case B:  $c, \|\theta\| = f_N(10^{-6}) \text{ Km}^{1/2}$  for  $p_B = 5(10^4) \text{ N/m}^{3/2}$ , various  $f_B = p_1/p_B$  and  $\psi$ .

Analysis considers the Lord and Shulman [1967] thermal relaxation model. Sub-Rayleigh crack extension rates are treated and, in contrast to [Brock 2017b], thermoelastic properties affect both the rates and crack edge temperature norm. The difference represents the inclusion of temperature discontinuity. Another difference with [Brock 2017b] is that the role of compression/shear ratio in mixed-mode loading is examined here.

Appendix A

$$U_1^{(\pm)} = \frac{qB}{\beta^2} \bar{\Delta}_3 \cos \psi - \frac{1}{2B\beta^2} \left( B^2 \frac{\bar{\Sigma}_1}{\mu p} + q^2 \frac{\bar{\Sigma}_M}{\mu p} \sin \psi \right) (\mp) \frac{q}{2\beta^2} \frac{\bar{\Sigma}_3}{\mu p} \cos \psi (\pm) \frac{1}{2\beta^2} (T \bar{\Delta}_1 + 2q^2 \bar{\Delta}_M \sin \psi), \quad (\text{A.1a})$$

$$U_2^{(\pm)} = \frac{qB}{\beta^2} \bar{\Delta}_3 \sin \psi - \frac{1}{2B\beta^2} \left( B^2 \frac{\bar{\Sigma}_2}{\mu p} - q^2 \frac{\bar{\Sigma}_M}{\mu p} \cos \psi \right) (\mp) \frac{q}{2\beta^2} \frac{\bar{\Sigma}_3}{\mu p} \sin \psi (\pm) \frac{1}{2\beta^2} (T \bar{\Delta}_2 - 2q^2 \bar{\Delta}_M \cos \psi). \quad (\text{A.1b})$$

$$U_+^{(\pm)} = \frac{1}{2\Omega\beta^2 A_+} \left[ \frac{\alpha_D}{p^2} d\bar{\Theta} + C_- (T \bar{\Delta}_3 + q \bar{\Sigma}_P) \right] (\mp) \frac{1}{2\Omega\beta^2} \left[ \frac{\alpha_D}{p} \bar{\Theta} + C_- \left( \frac{\bar{\Sigma}_3}{\mu p} + 2q \bar{\Delta}_P \right) \right], \quad (\text{A.1c})$$

$$U_{-}^{(\pm)} = \frac{-1}{2\Omega\beta^2 A_{-}} \left[ \frac{\alpha_D}{p^2} d\bar{\Theta} + C_{+}(T\bar{\Delta}_3 + q\bar{\Sigma}_P) \right] (\pm) \frac{1}{2\Omega\beta^2} \left[ \frac{\alpha_D}{p} \bar{\Theta} + C_{+} \left( \frac{\bar{\Sigma}_3}{\mu p} + 2q\bar{\Delta}_P \right) \right], \quad (\text{A.1d})$$

$$T = \beta^2 - 2q^2. \quad (\text{A.2})$$

$$\bar{\Delta}_P = \bar{\Delta}_1 \cos \psi + \bar{\Delta}_2 \sin \psi, \quad \bar{\Delta}_M = \bar{\Delta}_1 \sin \psi - \bar{\Delta}_2 \cos \psi, \quad (\text{A.3a})$$

$$\bar{\Sigma}_P = \bar{\Sigma}_1 \cos \psi + \bar{\Sigma}_2 \sin \psi, \quad \bar{\Sigma}_M = \bar{\Sigma}_1 \sin \psi - \bar{\Sigma}_2 \cos \psi. \quad (\text{A.3b})$$

**Appendix B**

$$\frac{1}{\mu} \left( \bar{\sigma}_{31}^C - \frac{P_1}{p\beta} \right) = \frac{\cos \psi}{\Omega\beta^2} \left( \frac{pM_{12}}{2B} \bar{\Delta}_P + qM_A \alpha_D \bar{\Theta} \right) + pB \bar{\Delta}_M \sin \psi, \quad (\text{B.1a})$$

$$\frac{1}{\mu} \left( \bar{\sigma}_{32}^C - \frac{P_2}{p\beta} \right) = \frac{\sin \psi}{\Omega\beta^2} \left( \frac{pM_{12}}{2B} \bar{\Delta}_P + qM_A \alpha_D \bar{\Theta} \right) - pB \bar{\Delta}_M \cos \psi, \quad (\text{B.1b})$$

$$\frac{1}{\mu} \left( \bar{\sigma}_{33}^C - \frac{P_3}{p\beta} \right) = \frac{pB}{2A_{+}A_{-}} \frac{M_3 \bar{\Delta}_3}{\Omega\beta^2}. \quad (\text{B.1c})$$

$$\partial_3 \bar{\theta}^C = \frac{\varepsilon}{\alpha_D \Gamma_{+} \Gamma_{-}} p^2 q M_A \bar{\Delta}_P - \frac{P}{2\Omega} M_C \bar{\Theta}. \quad (\text{B.2})$$

$$M_{12} = C_{-} M_{+} - C_{+} M_{-}, \quad (\text{B.3a})$$

$$M_3 = C_{-} \frac{A_{-}}{B} M_{+} - C_{+} \frac{A_{+}}{B} M_{-}, \quad (\text{B.3b})$$

$$M_A = A_{+} - A_{-}, \quad M_C = C_{+} A_{+} - C_{-} A_{-}, \quad (\text{B.3c})$$

$$M_{\pm} = T^2 + 4q^2 A_{\pm} B. \quad (\text{B.3d})$$

**Appendix C**

$$G_3^{\pm}(q) = \exp \left[ \frac{1}{\pi} \int \frac{du}{u \mp c} \frac{S_3(u)}{q(u \mp c) \pm 1} \right] \quad (1 < u < c_{+}), \quad (\text{C.1a})$$

$$S_3(u) = -\tan^{-1} \frac{1}{4\Omega} \frac{k^2(u) m_C(u)}{a_{+}(u) a_{-}(u) \sqrt{u^2 - 1}} \quad (1 < u < c_{-}), \quad (\text{C.1b})$$

$$S_3(u) = \tan^{-1} \frac{a_{+}(u)}{C_{-}} \left[ 4\Omega \frac{\sqrt{u^2 - 1}}{k^2(u)} - \frac{c_{-} C_{+}}{\sqrt{u^2 - c_{-}^2}} \right] \quad (c_{-} < c < c_{+}). \quad (\text{C.1c})$$

$$G_{12}^{\pm}(q) = \exp \left[ \frac{1}{\pi} \int \frac{du}{u \mp c} \frac{S_{12}(u)}{q(u \mp c) \pm 1} \right] \quad (1 < u < c_{+}), \quad (\text{C.2a})$$

$$S_{12}(u) = \tan^{-1} \frac{4}{\Omega} \frac{n_C(u)}{k^2(u)} \sqrt{u^2 - 1} \quad (1 < u < c_{-}), \quad (\text{C.2b})$$

$$n_C(u) = C_{-} a_{+}(u) - C_{+} a_{-}(u) \quad (\text{C.2c})$$

$$S_{12}(u) = \tan^{-1} \frac{C_{-a_+}(u)}{\frac{\Omega}{4} \frac{k^2(u)}{\sqrt{u^2-1}} - \frac{C_+}{c_-} \sqrt{u^2-c_-^2}} \quad (c_- < u < c_+). \quad (\text{C.2d})$$

$$G_A^\pm(q) = \exp \left[ \frac{1}{\pi} \int \frac{1}{u \mp c} \tan^{-1} \frac{\sqrt{u^2-c_-^2}}{c_{-a_+}(u)} \frac{du}{q(u \mp c) \pm 1} \right] \quad (c_- < u < c_+). \quad (\text{C.3})$$

$$G_C^\pm(q) = \exp \left[ \frac{1}{\pi} \int \frac{1}{u \mp c} \tan^{-1} \frac{C_{-} \sqrt{u^2-c_-^2}}{c_{-C_+a_+}(u)} \frac{du}{q(u \mp c) \pm 1} \right] \quad (c_- < u < c_+). \quad (\text{C.4})$$

### Appendix D

Asymptotic ( $|q| \rightarrow \infty$ ) expressions with inverses valid for  $x_3 = 0, x \rightarrow 0+$ :

$$\alpha_D \partial_3 \bar{\theta}^C \approx -\frac{\varepsilon \sqrt{q}}{\mu \Gamma_+ \Gamma_-} \frac{4c^2 m_A m_C}{g_3^+ R_3 \sqrt{c}} \left(1 - \frac{c}{c_3}\right) (P_1 \cos \psi + P_2 \sin \psi). \quad (\text{D.1})$$

$$\bar{\sigma}_{31}^C \approx -\frac{\sin \psi}{p \sqrt{q}} \frac{\sqrt{1-c}}{\sqrt{c}} (P_1 \sin \psi - P_2 \cos \psi) - \frac{\cos \psi}{p \sqrt{q}} \frac{N_{12}}{g_3^+ \sqrt{c}} \left(1 - \frac{c}{c_3}\right) (P_1 \cos \psi + P_2 \sin \psi), \quad (\text{D.2a})$$

$$\bar{\sigma}_{32}^C \approx -\frac{\cos \psi}{p \sqrt{q}} \frac{\sqrt{1-c}}{\sqrt{c}} (P_1 \sin \psi - P_2 \cos \psi) - \frac{\sin \psi}{p \sqrt{q}} \frac{N_{12}}{g_3^+ \sqrt{c}} \left(1 - \frac{c}{c_3}\right) (P_1 \cos \psi + P_2 \sin \psi), \quad (\text{D.2b})$$

$$\bar{\sigma}_{33}^C \approx \frac{P_3}{p \sqrt{q}} \frac{1}{g_3^+} \left(1 - \frac{c}{c_3}\right) \frac{\sqrt{c_+ c_-} \sqrt{1-c}}{\sqrt{c} \sqrt{c_+ - c_-} \sqrt{c_- - c}}. \quad (\text{D.2c})$$

$$N_{12} = 1 + \frac{8\varepsilon m_A^2}{\lambda R_3} \quad (\text{D.3})$$

Asymptotic ( $|q| \rightarrow \infty$ ) expressions with inverses valid for  $x_3 = 0, x \rightarrow 0-$ :

$$\alpha_D \bar{\Theta} \approx -\frac{4\varepsilon}{\Gamma_+ \Gamma_-} \frac{m_A}{\mu p \sqrt{-q}} \frac{c^2}{\sqrt{c} g_3^+ R_3} \left(1 - \frac{c}{c_3}\right) (P_1 \cos \psi + P_2 \sin \psi) \quad (\text{D.4})$$

$$p\beta \bar{\Delta}_1 \approx -\frac{2 \sin \psi}{\mu p \sqrt{-q}} \frac{\sqrt{c}}{\sqrt{1+c}} (P_1 \sin \psi - P_2 \cos \psi) - \frac{2 \cos \psi}{\mu p \sqrt{-q}} \frac{c^2 \sqrt{c}}{g_3^+ R_3} \left(1 - \frac{c}{c_3}\right) (P_1 \cos \psi + P_2 \sin \psi), \quad (\text{D.5a})$$

$$p\beta \bar{\Delta}_2 \approx -\frac{2 \cos \psi}{\mu p \sqrt{-q}} \frac{\sqrt{c}}{\sqrt{1+c}} (P_1 \sin \psi - P_2 \cos \psi) - \frac{2 \sin \psi}{\mu p \sqrt{-q}} \frac{c^2 \sqrt{c}}{g_3^+ R_3} \left(1 - \frac{c}{c_3}\right) (P_1 \cos \psi + P_2 \sin \psi), \quad (\text{D.5b})$$

$$p\beta \bar{\Delta}_3 \approx \frac{2P_3}{\mu p \sqrt{-q}} \frac{\Omega c^2}{g_3^+ R_3} \left(1 - \frac{c}{c_3}\right) \frac{\sqrt{c}}{\sqrt{c_+ c_-} \sqrt{1+c}} \sqrt{c_+ + c} \sqrt{c_- + c}. \quad (\text{D.5c})$$

**Appendix E**

$$A_{\pm}^{(+)} \approx \sqrt{1 + \cos \phi} \left[ 1 + \frac{c^2}{4c_{\pm}^2} (1 - \cos \phi) \cos \phi \right], \quad (\text{E.1a})$$

$$A_{\pm}^{(-)} \approx \sqrt{1 - \cos \phi} \left[ 1 - \frac{c^2}{4c_{\pm}^2} (1 + \cos \phi) \cos \phi \right], \quad (\text{E.1b})$$

$$B^{(+)} \approx \sqrt{1 + \cos \phi} \left[ 1 + \frac{1}{4} c^2 (1 - \cos \phi) \cos \phi \right], \quad (\text{E.1c})$$

$$B^{(-)} \approx \sqrt{1 - \cos \phi} \left[ 1 - \frac{1}{4} c^2 (1 + \cos \phi) \cos \phi \right]. \quad (\text{E.1d})$$

$$P_3^{(+)} \approx -\frac{\Omega c^2}{2c_D^2} \sqrt{1 + \cos \phi} \left[ 1 - \frac{1}{2} \cos \phi (c_D^2 - 1) (1 - \cos \phi) \right], \quad (\text{E.2a})$$

$$P_3^{(-)} \approx \frac{\Omega c^2}{2c_D^2} \sqrt{1 - \cos \phi} \left[ c_D^2 + \frac{1}{2} \cos \phi (1 - c_D^2) (1 + \cos \phi) \right], \quad (\text{E.2b})$$

$$P_{12}^{(+)} \approx \frac{\Omega c^2}{4c_D^2} \sqrt{1 + \cos \phi} \cos \phi (1 - \cos \phi) (c_D^2 - 1), \quad (\text{E.2c})$$

$$P_{12}^{(-)} \approx -\frac{\Omega c^2}{2c_D^2} \sqrt{1 - \cos \phi} \left[ c_D^2 + \frac{1}{2} \cos \phi (1 + \cos \phi) (c_D^2 - 1) \right]. \quad (\text{E.2d})$$

$$T_3^{(+)} \approx \frac{\Omega c^2}{2c_D^2} \sqrt{1 + \cos \phi} \left[ 1 + \frac{1}{2} \cos \phi (1 - \cos \phi) \right], \quad (\text{E.3a})$$

$$T_{12}^{(-)} \approx -\frac{\Omega c^2}{2\lambda_D^2} \sqrt{1 - \cos \phi} \left[ 1 - \frac{1}{2} \cos \phi (1 + \cos \phi) \right]. \quad (\text{E.3b})$$

**Appendix F**

Kinetic energy neglected:

$$g_0 = 1 + f_B^2 k_C, \quad (\text{F.1a})$$

$$g_2 = -\frac{1}{2} g_0 \left[ 1 - \sqrt{1 + 2/g_0 (2f_B)^2 (1/\Omega - k_C)} \right]. \quad (\text{F.1b})$$

Kinetic energy included:

$$g_0 = \frac{1}{2\Omega_0} (1 - C_B), \quad C_B = \sqrt{1 - 4\Omega_0 (1 + f_B^2 k_C)}, \quad (\text{F.2a})$$

$$g_2 = -2F_1/F_2^2 \left[ 1 - \sqrt{1 - F_0 (F_2/F_1)^2} \right]. \quad (\text{F.2b})$$

$$F_0 = \Omega_1 g_0^3 (2 - C_B) - 2f_B^2 (1/\Omega - k_C) (1 + f_B^2 k_C), \quad (\text{F.3a})$$

$$F_1 = (1 + f_B^2 k_C) C_B, \quad F_2 = 1 + C_B. \quad (\text{F.3b})$$

## References

- [Abramowitz and Stegun 1972] M. Abramowitz and I. A. Stegun (editors), *Handbook of mathematical functions*, Dover, New York, 1972.
- [Achenbach 1976] J. D. Achenbach, *Wave propagation in elastic solids*, 1st ed., North-Holland Series in Applied Mathematics and Mechanics **16**, North-Holland Publishing Co., Amsterdam, 1976.
- [Achenbach and Brock 1973] J. D. Achenbach and L. M. Brock, “On quasistatic and dynamic fracture”, pp. 529–541 in *Proceedings of an international conference on dynamic crack propagation*, edited by G. C. Sih, Springer, Dordrecht, 1973.
- [Barber 1992] J. R. Barber, *Elasticity*, Solid Mechanics and its Applications **12**, Kluwer Academic Publishers Group, Dordrecht, The Netherlands, 1992.
- [de Boer et al. 1988] F. R. de Boer, W. C. M. Mattens, R. Boom, A. R. Miedema, and A. K. Niessen, *Cohesion in metals*, North-Holland, Amsterdam, 1988.
- [Brock 2009] L. M. Brock, “Basic problems of coupled thermoelasticity with thermal relaxation and pre-stress: aspects observed in exact and asymptotic solutions”, *J. Therm. Stresses* **32**:6-7 (2009), 593–622.
- [Brock 2012] L. M. Brock, “Two cases of rapid contact on an elastic half-plane: the sliding ellipsoid, rolling sphere”, *J. Mech. Mater. Struct.* **7**:5 (2012), 469–483.
- [Brock 2017a] L. Brock, “Transient growth of a planar crack in three dimensions: mixed mode”, *J. Mech. Mater. Struct.* **12**:3 (2017), 313–328.
- [Brock 2017b] L. M. Brock, “Fracture initiation in a thermoelastic solid with relaxation: transient three-dimensional analysis”, *J. Therm. Stresses* **40**:8 (2017), 995–1014.
- [Brock and Achenbach 1973] L. Brock and J. Achenbach, “Extension of an interface flaw under the influence of transient waves”, *Int. J. Solids Struct.* **9** (1973), 53–68.
- [Freund 1972] L. B. Freund, “Energy flux into the tip of an extending crack in an elastic solid”, *J. Elasticity* **2**:4 (1972), 341–349.
- [Freund 1990] L. B. Freund, *Dynamic fracture mechanics*, Cambridge University Press, 1990.
- [Gdoutos 1993] E. E. Gdoutos, *Fracture mechanics: an introduction*, Solid Mechanics and its Applications **14**, Kluwer Academic Publishers Group, Dordrecht, The Netherlands, 1993.
- [Ignaczak and Ostoja-Starzewski 2010] J. Ignaczak and M. Ostoja-Starzewski, *Thermoelasticity with finite wave speeds*, Oxford University Press, 2010.
- [Lord and Shulman 1967] H. W. Lord and Y. Shulman, “A generalized dynamical theory of thermoelasticity”, *J. Mech. Phys. Solids* **15**:5 (1967), 299–309.
- [Malvern 1969] L. S. Malvern, *Introduction to the mechanics of continuous media*, Prentice-Hall, Englewood Cliffs, NJ, 1969.
- [Morse and Feshbach 1953] P. M. Morse and H. Feshbach, *Methods of theoretical physics*, McGraw-Hill, New York, 1953.
- [Skriver and Rosengaard 1992] H. L. Skriver and N. M. Rosengaard, “Surface energy and work function of elemental metals”, *Phys. Rev. B* **46** (1992), 7157–7168.
- [Sneddon 1972] I. N. Sneddon, *The use of integral transforms*, McGraw-Hill, New York, 1972.

Received 28 Apr 2017. Accepted 17 May 2017.

LOUIS M. BROCK: [louis.brock@uky.edu](mailto:louis.brock@uky.edu)

Department of Mechanical Engineering, University of Kentucky, Lexington, KY, United States

# GEOMETRICALLY NONLINEAR COSSERAT ELASTICITY IN THE PLANE: APPLICATIONS TO CHIRALITY

SEBASTIAN BAHAMONDE, CHRISTIAN G. BÖHMER AND PATRIZIO NEFF

Modeling two-dimensional chiral materials is a challenging problem in continuum mechanics because three-dimensional theories reduced to isotropic two-dimensional problems become nonchiral. Various approaches have been suggested to overcome this problem. We propose a new approach to this problem by formulating an intrinsically two-dimensional model which does not require references to a higher dimensional one. We are able to model planar chiral materials starting from a geometrically nonlinear Cosserat-type elasticity theory. Our results are in agreement with previously derived equations of motion but can contain additional terms due to our nonlinear approach. Plane wave solutions are briefly discussed within this model.

*A list of symbols can be found on page 707.*

## 1. Introduction

Classical elasticity theory assumes structureless material points. These points are not allowed to possess an additional so-called microstructure which could take into account properties like orientation or volume of the material points. It is possible to extend the theory of classical elasticity to take into account this additional structure; this is known as the Cosserat [1909] model. In the Cosserat continuum, material points can, for instance, experience rotations without stretches. Therefore, in addition to the standard deformation field  $\varphi$  there is an independent rotation field  $\bar{R}$ , which means that  $\bar{R}$  is an orthogonal matrix. Many models in continuum mechanics were motivated by this idea, which has resulted in many interesting research lines, sometimes with varying names [Ericksen and Truesdell 1957; Toupin 1962; 1964; Ericksen 1962a; 1962b; 1967; Mindlin 1964; Eringen and Suhubi 1964; Suhubi and Eringen 1964; Green and Rivlin 1964; Schaefer 1967; Eringen 1999]

The three-dimensional static nonlinear Cosserat model has seen a tremendous increase of interest in recent years [Neff 2006b; Neff and Münch 2009; Münch et al. 2011; Neff et al. 2008; Fischle et al. 2017; Borisov et al. 2016; Fischle and Neff 2017c]. This is connected to its potential to model uncommon effects like lattice rotations. Working with the manifold  $SO(3)$  of proper rotations requires, however, many new tools from the mathematical and implementational side. Expositions regarding the mathematical treatment can be found in [Neff 2004a; 2006a; Neff and Münch 2008; Neff et al. 2015; Lankeit et al. 2017]; similarly for computational results in [Fischle and Neff 2017a; 2017b]. The Cosserat approach is maybe best known for its ability to model thin shell structures. Here, the additional orthogonal frame provided by the Cosserat theory fits well into the theory of deformable surfaces [Neff 2004b; 2007; Neff

---

MSC2000: 74J35, 74A35, 74J30, 74A30.

Keywords: Cosserat continuum, geometrically nonlinear micropolar elasticity, chiral materials, planar models.



et al. 2010; Bîrsan and Neff 2013; 2014; Sander et al. 2016]. Not much is known, regrettably, in the case of general nonlinear dynamics. Our contribution [Böhmer et al. 2016] sheds some light in this direction.

One of the major unresolved issues of the theory is the precise matter in which elastic deformations (macroscopic) and Cosserat microrotations are coupled. If we consider a quadratic ansatz in the stretch tensor, it usually comes down to writing a coupling term of the form  $\mu_c \|\text{skew}(\bar{U} - \mathbb{1})\|^2$ , in which  $\mu_c \geq 0$  is known as the Cosserat couple modulus. The effect of this coupling term is clear by increasing  $\mu_c \rightarrow \infty$ . Then the Cosserat rotations become the continuum rotations  $R = \text{polar } F$ . A similar effect can be obtained by instead considering the coupling  $\mu_c \|\bar{R}^T \text{polar } F - \mathbb{1}\|^2$ . Both terms induce the same linear response. It is important to note that the geometrically nonlinear Cosserat model can be used also with  $\mu_c \equiv 0$ , a possibility which is meaningless in the linear Cosserat model. In the case  $\mu_c = 0$  one has a Cosserat model with symmetric stresses, whereas stretches may be nonsymmetric.

Cosserat elasticity is generally formulated as a three-dimensional continuum mechanics theory and planar problems are usually considered by restricting either displacements or microrotations to the plane. One sometimes speaks of the first planar problem when  $\mathbf{u} = (u_1, u_2, 0)$  and rotations are constrained to be about the  $z$ -direction. The second planar problem deals with the opposite situation where  $\mathbf{u} = (0, 0, u_3)$  while the rotations are constrained about the  $x$ -axis and  $y$ -axis; see for instance [Ostoja-Starzewski and Jasiuk 1995; Joumaa and Ostoja-Starzewski 2011].

Chirality<sup>1</sup> or handedness is a common feature in various fields of science. It refers to the possibility of an object or system to be distinguishable from its mirror image. Many molecules in chemistry are chiral, most often due to the presence of an asymmetric carbon atom. Chiral materials have been of interest in continuum mechanics since the 1980s. When one is interested in studying chiral materials [Lakes and Benedict 1982; Lakes 2001], it turns out that a three-dimensional theory when reduced to an isotropic two-dimensional problem becomes nonchiral [Lakes 2001; Rosi and Auffray 2016; Liu et al. 2012b].

Typically, a chiral term in a three-dimensional elasticity model would be of the form

$$(\bar{R}^T F)_{ij} C_{ijmn} (\bar{R}^T \text{Curl } \bar{R})_{mn}, \quad (1-1)$$

where  $C_{ijmn}$  is a material tensor; see also Appendix A. If one considers an isotropic material tensor of the form  $c_1 \delta_{ij} \delta_{mn} + c_2 \delta_{im} \delta_{jn} + c_3 \delta_{in} \delta_{jm}$ , then the above term yields three contributions. It turns out that these three terms identically vanish when the first Cosserat planar problem is considered<sup>2</sup>. For instance, based on representation theorems [Cheverton and Beatty 1981], a total of 20 invariants were discussed, five of which are chiral according to our formulation in Appendix A. However, a direct calculation verifies that all chiral terms vanish when the deformation gradient is confined to the plane; see (2-1).

Hence, studying two-dimensional chiral materials requires a new approach. One such approach is the use of strain gradient theories; see [Rosi and Auffray 2016], for instance. Another approach goes back to [Liu et al. 2012b] where chirality was introduced in the two-dimensional setting by revisiting isotropic fourth-order tensors and identifying an extra piece in the constitutive relation. It was subsequently shown that this additional part of the elastic tensor can indeed give a meaningful model with chirality. The model

<sup>1</sup>“I call any geometrical figure, or group of points, chiral, and say that it has chirality if its image in a plane mirror, ideally realized, cannot be brought to coincide with itself” (Lord Kelvin 1894).

<sup>2</sup>It might be possible to construct chiral terms using nonlinear functionals beyond the usual quadratic terms which yield a nontrivial planar theory.

considered in [Liu et al. 2012b] is based on linear Cosserat elasticity; see also [Liu et al. 2012a; Liu and Hu 2016].

In the present paper, we approach this problem from a very different point of view. We begin by carefully studying the basic formulation of geometrically nonlinear Cosserat elasticity in the plane by following three different routes. First, we will follow the standard approach of formulating three-dimensional Cosserat elasticity and restricting it to the plane, thereby recalling the first and second Cosserat problems, respectively. Next we will formulate an intrinsically two dimensional model. After stating the energy functional of our model, the equations of motion are rigorously derived using the calculus of variations. Our intrinsically two-dimensional formulation requires no reference to a theory in three dimensions. Within this setting we are able to introduce a new displacement vector which allows us to model planar chiral materials without the use of new constitutive relations. Our model, which is geometrically nonlinear, yields equations very similar to those reported in [Liu et al. 2012b] when we assume small rotations and small displacements. However, due to our nonlinear theory as a starting point, we find an additional contribution which naturally appears in the equations of motion.

## 2. The Cosserat problem in the plane

We are interested in studying the dynamical geometrically nonlinear Cosserat problem in the plane and this immediately poses the rather interesting question of how to formulate such a theory. On the one hand, one could simply start with three-dimensional Cosserat elasticity and consider an ansatz which reduces the equations to the planar case. This approach yields two different types of models, often called the first and second Cosserat planar model; see for instance [Joumaa and Ostoja-Starzewski 2011]. However, as Cosserat elasticity takes into account the possible microrotations of matter points, we must recall that rotations in the plane are very different from those in three dimensions, since the latter need not commute. An intrinsically two-dimensional model of Cosserat elasticity could thus be formulated, which would differ from the three-dimensional case restricted to the plane.

**2.1. The first Cosserat planar problem.** The first Cosserat planar problem is defined by  $\mathbf{u} = (u_1, u_2, 0)$  and  $\mathbf{a} = (0, 0, a_3)$ , where the vector  $\mathbf{a}$  defines the axis of the Cosserat rotation. This means we can begin with a three-dimensional setup confined to the  $xy$ -plane, with rotations about the  $z$ -axis only. In this case the deformation is given by  $\varphi = (\varphi_1(x, y), \varphi_2(x, y), z)$  so that the deformation gradient  $F$  reads

$$F = \nabla\varphi = \begin{pmatrix} \varphi_{1,x} & \varphi_{1,y} & 0 \\ \varphi_{2,x} & \varphi_{2,y} & 0 \\ 0 & 0 & 1 \end{pmatrix}. \quad (2-1)$$

Next we consider the rotations in the  $xy$ -plane. We call the angle of rotation  $\phi = \phi(x, y)$ , which yields

$$\bar{R} = \begin{pmatrix} \cos \phi & -\sin \phi & 0 \\ \sin \phi & \cos \phi & 0 \\ 0 & 0 & 1 \end{pmatrix}. \quad (2-2)$$

Now we can compute  $\bar{R}^T \text{Curl } \bar{R}$ , a useful curvature measure of the Cosserat theory [Neff and Münch 2008]. Using the index notation, it can be written as

$$(\text{Curl } \bar{R})_{ij} = \varepsilon_{jmn} \partial_m \bar{R}_{in}, \quad (2-3)$$

where  $\varepsilon_{jmn}$  is the Levi-Civita symbol. For the given orthogonal matrix (2-2) this is given by

$$\bar{R}^T \text{Curl } \bar{R} = \left( \begin{array}{cc|c} 0 & 0 & -\phi_x \\ 0 & 0 & -\phi_y \\ \hline 0 & 0 & 0 \end{array} \right). \quad (2-4)$$

At this point we already see the root cause of the problem when trying to formulate the desired theory. All the components of  $\bar{R}^T \text{Curl } \bar{R}$  restricted to the plane are zero. We also note that the components of this matrix are determined by the object  $\text{grad } \phi$ ; this means effectively a vector with two components which already points towards an intrinsically two-dimensional model.

A direct calculation establishes

$$\begin{aligned} \text{dev}(\bar{R}^T \text{Curl } \bar{R}) &= \frac{1}{2} \begin{pmatrix} 0 & 0 & -\phi_x \\ 0 & 0 & -\phi_y \\ -\phi_x & -\phi_y & 0 \end{pmatrix}, \\ \text{skew}(\bar{R}^T \text{Curl } \bar{R}) &= \frac{1}{2} \begin{pmatrix} 0 & 0 & -\phi_x \\ 0 & 0 & -\phi_y \\ \phi_x & \phi_y & 0 \end{pmatrix}, \\ \text{tr}(\bar{R}^T \text{Curl } \bar{R}) &= 0. \end{aligned} \quad (2-5)$$

The important issue at this point is that there are no planar contributions in any of the irreducible parts of  $\bar{R}^T \text{Curl } \bar{R}$  in (2-5).

Also, we can compute the nonsymmetric stretch tensor, which gives

$$\bar{U} = \bar{R}^T F = \begin{pmatrix} \varphi_{1,x} \cos \phi + \varphi_{2,x} \sin \phi & \varphi_{1,y} \cos \phi + \varphi_{2,y} \sin \phi & 0 \\ \varphi_{2,x} \cos \phi - \varphi_{1,x} \sin \phi & \varphi_{2,y} \cos \phi - \varphi_{1,y} \sin \phi & 0 \\ 0 & 0 & 1 \end{pmatrix}. \quad (2-6)$$

This implies that the irreducible parts of  $\bar{U} = \bar{R}^T F$  and  $\bar{R}^T \text{Curl } \bar{R}$  are orthogonal in the sense that

$$\begin{aligned} \text{tr}(\bar{R}^T \text{Curl } \bar{R}) \text{tr}(\bar{R}^T F) &= 0, \\ \langle \text{dev}(\bar{R}^T \text{Curl } \bar{R}), \text{dev}(\bar{R}^T F) \rangle &= 0, \\ \langle \text{skew}(\bar{R}^T \text{Curl } \bar{R}), \text{skew}(\bar{R}^T F) \rangle &= 0. \end{aligned} \quad (2-7)$$

This implies that we cannot construct interaction terms between the displacements and the microrotations. Interaction terms of the above form were considered in [Böhmer and Tamanini 2015; Böhmer et al. 2016]. These terms allow for a natural coupling between elastic deformations and the microrotations which, for instance, gives rise to soliton solutions; see [Böhmer et al. 2016].

Let us also remark that in case of the finite theory one may as well consider the irreducible components of  $F^T F$  rather than  $\bar{R}^T F$ . The form of  $F$  given in (2-1) implies that  $F^T F$  will be the same form as  $\bar{U}$  given by (2-6). Hence, all inner product considered in (2-7) would also vanish which implies that it is also not possible to construct interaction terms in the finite theory.

However, one can still construct interaction terms, albeit less natural ones. Consider the Frobenius norm of the dislocation density tensor

$$\|(\bar{R}^T \text{Curl } \bar{R})\|^2 = \phi_x^2 + \phi_y^2, \quad (2-8)$$

which agrees with the vector norm of  $\text{grad } \phi$ . Hence, the only option to construct an interaction term would be to consider an expression of the form

$$V_{\text{interaction}} \propto \|(\bar{R}^T \text{Curl } \bar{R})\| \text{tr}(\bar{R}^T F). \quad (2-9)$$

An interaction of this type is quite unnatural since we are not considering the inner products of objects in the same irreducible spaces, which is what led to (2-7). From a more mathematical point of view, the presence of the square root in (2-9) might cause differentiability issues when the orthogonal matrix  $\bar{R}$  approaches a constant rotation.

It is also clear from (2-6) that the polar part of any deformation tensor restricted to the plane will be of the same form as the rotation matrix (2-2) which means we could, in principle, construct the Cosserat couple term which contains the term  $\bar{R}^T \text{polar } F$ .

**2.2. The second Cosserat planar problem.** The second Cosserat planar problem is defined by  $\mathbf{u} = (0, 0, u_3)$  and  $\mathbf{a} = (a_1, a_2, 0)$ . This means  $\varphi = (x, y, \varphi_3(t, x, y))$ , so that elastic displacements are only allowed along the direction perpendicular to the plane. The rotations can be about the  $x$ -axis and the  $y$ -axis in this case. While this is mathematically well-defined, this is less well motivated than the first Cosserat problem from a practical point of view.

The deformation gradient of the second Cosserat planar model is given by

$$F = \nabla \varphi = \begin{pmatrix} 1 & 0 & 0 \\ 0 & 1 & 0 \\ \varphi_{3,x} & \varphi_{3,y} & 1 \end{pmatrix}. \quad (2-10)$$

Next we consider the rotations about the  $x$  and about the  $y$  axes. We call the respective angles of rotation  $\alpha = \alpha(t, x, y)$  and  $\beta = \beta(t, x, y)$  so that

$$\bar{R} = \begin{pmatrix} \alpha^2/\ell^2 + \cos \ell \beta^2/\ell^2 & (1 - \cos \ell)\alpha\beta/\ell^2 & \sin \ell \beta/\ell \\ (1 - \cos \ell)\alpha\beta/\ell^2 & \cos \ell \alpha^2/\ell^2 + \beta^2/\ell^2 & -\sin \ell \alpha/\ell \\ -\sin \ell \beta/\ell & \sin \ell \alpha/\ell & \cos \ell \end{pmatrix}, \quad (2-11)$$

where  $\ell = \sqrt{\alpha^2 + \beta^2}$ . Due to the more complicated structure of the rotation matrix, the second Cosserat planar problem differs from the first problem substantially. This is due to our geometrically nonlinear setup which allows for large rotations. The explicit form of  $\bar{R}^T \text{Curl } \bar{R}$  is rather involved and therefore we will not state it explicitly. It suffices to mention that the only vanishing components are  $(\bar{R}^T \text{Curl } \bar{R})_{31} = (\bar{R}^T \text{Curl } \bar{R})_{32} = 0$ . It is instructive, however, to consider this quantity assuming small rotations  $\alpha, \beta \ll 1$ , in which case one finds

$$\bar{R}^T \text{Curl } \bar{R} \simeq \begin{pmatrix} \beta_y & -\beta_x & 0 \\ -\alpha_y & \alpha_x & 0 \\ 0 & 0 & \alpha_x + \beta_y \end{pmatrix}. \quad (2-12)$$

One interesting aspect of this equation is the presence of the  $(zz)$  components. When linear Cosserat elasticity is considered, as in [Joumaa and Ostoja-Starzewski 2011], then the curvature tensor does not have this component and is indeed restricted to the plane. In the nonlinear setting this is no longer the case which also motivates a different approach to the planar case.

It is clear that the stretch tensor  $\bar{U} = \bar{R}^T F$  is not orthogonal to any of the components of  $\bar{R}^T \text{Curl } \bar{R}$ . Therefore the aforementioned coupling terms could in principle be constructed. However, this construction appears to be quite unnatural when compared to the first Cosserat problem.

The conceptual problem of using either the first or the second Cosserat planar model is simply that both theories differ considerably, and also differ from the nonlinear theory. This motivates us to formulate an intrinsically two-dimensional model which does not refer to the three-dimensional setting altogether.

### 3. Intrinsic planar model

**3.1. Basic quantities.** In order to formulate an intrinsically two-dimensional model we simply begin with the two-dimensional deformation vector  $\varphi = (\varphi_1, \varphi_2)$  so that the deformation gradient reads

$$F = \nabla \varphi = \begin{pmatrix} \varphi_{1,x} & \varphi_{1,y} \\ \varphi_{2,x} & \varphi_{2,y} \end{pmatrix}. \tag{3-1}$$

Similar to rotations about the  $z$ -axis in the first Cosserat planar model, we consider a two-dimensional rotation matrix where, as before, we call the angle  $\vartheta = \vartheta(x, y)$  so that

$$\bar{R} = \begin{pmatrix} \cos \vartheta & -\sin \vartheta \\ \sin \vartheta & \cos \vartheta \end{pmatrix}. \tag{3-2}$$

These definitions are purely two-dimensional and do not require the higher dimensional setting. However, as expected, the components of the intrinsic deformation gradient are identical to the planar components of the corresponding three-dimensional one; see (2-1). Likewise, the intrinsic rotation matrix has the planar components of the three-dimensional rotation matrix (2-2) of the first Cosserat planar problem.

The first object which requires a more careful approach is the matrix curl of the curvature measure. In three dimensions the matrix curl requires the object  $\varepsilon_{jmn}$ , see (2-3). However, the Levi-Civita tensor  $\varepsilon_{jmn}$  is a three-dimensional object which has no geometrical meaning in any dimension other than three. Therefore, one has to change this definition and adopt it to the planar case.

Let us begin by recalling the lesser-known fact that the vector curl is sometimes introduced in two dimensions to give a scalar quantity. Consequently, one would expect the two-dimensional matrix curl to give a vector. It turns out that this follows quite naturally when the Levi-Civita symbol in two dimensions is considered. Namely, it has two indices  $\epsilon_{ij}$ , instead of  $\varepsilon_{ijk}$  in three dimensions. Hence, the contraction of the partial derivative of a matrix with the Levi-Civita gives a vector. This leads us to define the two-dimensional matrix curl  $\bar{R}^T \text{Curl } \bar{R}$  in the following way:

$$(\text{Curl } \bar{R})_i := \epsilon_{rs} \partial_r \bar{R}_{is}. \tag{3-3}$$

This matrix curl maps matrices to vectors, as expected.

This definition is quite natural in the present context as can be seen by computing the quantity  $\bar{R}^T \text{Curl } \bar{R}$ , which then becomes

$$\bar{R}^T \text{Curl } \bar{R} = \begin{pmatrix} \vartheta_x \\ \vartheta_y \end{pmatrix} = \text{grad } \vartheta. \tag{3-4}$$

This result contains the two nonvanishing components of the three-dimensional object  $\bar{R}^T \text{Curl } \bar{R}$ ; compare with (2-4).

Now, we are faced with a similar problem as before: we cannot simply couple the two-dimensional vector (the two-dimensional Cosserat curvature measure) to the deformation gradient which is, of course, a  $2 \times 2$  matrix. However, we can proceed as follows. Let us write any vector  $\mathbf{v}$  as  $\mathbf{v} = |\mathbf{v}|\hat{\mathbf{v}}$ , which we can view as the irreducible decomposition of the vector into a scalar  $|\mathbf{v}|$  and a direction  $\hat{\mathbf{v}}$  with  $|\hat{\mathbf{v}}| = 1$ . Applied to the vector  $\bar{\mathbf{R}}^T \text{Curl } \bar{\mathbf{R}}$ , we can consider the scalar quantity  $\|\bar{\mathbf{R}}^T \text{Curl } \bar{\mathbf{R}}\|$  which can be coupled to the trace part of the deformation gradient. Hence, we can consider the term

$$V_{\text{interaction}} \propto \text{tr}(\bar{\mathbf{R}}^T F) \|\bar{\mathbf{R}}^T \text{Curl } \bar{\mathbf{R}}\|, \quad (3-5)$$

which in the two-dimensional setting is a natural choice. We recall that in the three-dimensional case we could write a very similar term, namely (2-9), however, it was not well justified in that setting.

The main point to note is that modeling planar material requires, independently of the approach, two geometrically different quantities: Matrix-valued objects (which describe the elastic deformations) and vectors (which describe the rotations about the axis perpendicular to the material). Any model which attempts at introducing interactions between these two quantities needs to address the principal issue of how such couplings can be achieved.

Since  $\bar{\mathbf{R}}$  is still an orthogonal matrix, it appears best to consider the coupling based on  $\bar{\mathbf{R}}^T$  polar  $F$ , which does not involve conceptual problems in either dimensions two or three.

The Cosserat model is cast in a variational framework on the reference configuration. The dynamical equations follow from a generalized Hamiltonian principle. A replacement of the first Piola–Kirchhoff tensor of classical nonlinear elasticity is easily seen to be  $\partial V / \partial F_{ij}$  with  $V$  being the energy function of the model considered.

**3.2. Elastic energy and curvature energy.** We write the energy functional for the elastic deformation as

$$V_{\text{elastic}}(F, \bar{\mathbf{R}}) = \mu \|\text{sym } \bar{\mathbf{R}}^T F - \mathbb{1}\|^2 + \frac{1}{2} \lambda (\text{tr}(\text{sym}(\bar{\mathbf{R}}^T F) - \mathbb{1}))^2, \quad (3-6)$$

where  $\lambda$  and  $\mu$  are the standard elastic Lamé parameters in two dimensions. For the dynamical treatment, we will need to subtract kinetic energy, which we assume to be of the form  $\frac{1}{2} \rho \|\dot{\boldsymbol{\varphi}}\|^2$ .

The three-dimensional energy functional of the microrotations  $V_{\text{rotational}}$  is based on the energy functional containing  $\|\bar{\mathbf{R}}^T \text{Curl } \bar{\mathbf{R}}\|_{\mathbb{R}^{3 \times 3}}^2$ . It is natural to consider the same functional form in two dimensions using the matrix curl defined in  $\mathbb{R}^2$ , as in (3-3).

Using the previously stated (3-4), we write the two-dimensional curvature energy as

$$V_{\text{curvature}}(\nabla \vartheta) = \mu L_c^2 \|\bar{\mathbf{R}}^T \text{Curl } \bar{\mathbf{R}}\|_{\mathbb{R}^2}^2 = \mu L_c^2 \|\text{grad } \vartheta\|_{\mathbb{R}^2}^2, \quad (3-7)$$

where  $L_c$  is the characteristic length and  $\mu$  is the shear modulus from above. We emphasize that this (vector) norm is computed in two dimensions by using the subscript  $\mathbb{R}^2$ ; this is to avoid confusion with the 3D (matrix) norm in  $\mathbb{R}^{3 \times 3}$ . The simple form of the energy when expressed in vector form is in fact expected as rotations in the plane are characterized by only one angle  $\vartheta$ .

In order to study the dynamical problem, we will need to subtract kinetic energy, which we assume to be of the form  $\rho_{\text{rot}} \|\dot{\vartheta}\|^2$  where  $\rho_{\text{rot}}$  is the scalar rotational density. One could also choose the kinetic energy as  $\text{tr}(\dot{\bar{\mathbf{R}}}^T \dot{\bar{\mathbf{R}}})$  as this is somewhat more natural; however, a direct calculation gives that  $\text{tr}(\dot{\bar{\mathbf{R}}}^T \dot{\bar{\mathbf{R}}}) = 2\|\dot{\vartheta}\|^2$ , which means that they only differ by a factor of 2.

**3.3. Interaction and coupling terms.** Next, we wish to introduce a coupling between the elastic displacements and the microrotations. To do so, we will “couple” the irreducible parts of the elastic deformation with the microrotations. This gives

$$V_{\text{interaction}}(F, \bar{R}) = \mu L_c \chi \|\bar{R}^T \text{Curl } \bar{R}\| \text{tr}(\bar{R}^T F), \quad (3-8)$$

where  $\chi$  is the coupling constant which was first introduced in [Böhmer and Tamanini 2015; Böhmer et al. 2016].

Finally, we will consider the Cosserat couple term we assume to be given by

$$V_{\text{coupling}}(F, \bar{R}) = \mu_c \|\bar{R}^T \text{polar } F - \mathbb{1}\|^2, \quad (3-9)$$

where  $\mu_c \geq 0$  is the Cosserat couple modulus. Alternatively, one can consider the coupling

$$V_{\text{coupling}(2)}(F, \bar{R}) = \mu_c \|\text{skew}(\bar{R}^T F - \mathbb{1})\|^2, \quad (3-10)$$

which induces the same linear response as the coupling containing the polar part.

The complete static model is therefore given by

$$\begin{aligned} V &= V_{\text{elastic}} + V_{\text{curvature}} + V_{\text{interaction}} + V_{\text{coupling}} \\ &= \mu \|\text{sym}(\bar{R}^T F - \mathbb{1})\|_{\mathbb{R}^{2 \times 2}}^2 + \frac{1}{2} \lambda (\text{tr}(\text{sym}(\bar{R}^T F - \mathbb{1})))^2 + \mu L_c^2 \|\bar{R}^T \text{Curl } \bar{R}\|_{\mathbb{R}^2}^2 \\ &\quad + \mu L_c \chi \|\bar{R}^T \text{Curl } \bar{R}\|_{\mathbb{R}^2} \text{tr}(\bar{R}^T F) + \mu_c \|\bar{R}^T \text{polar } F - \mathbb{1}\|_{\mathbb{R}^{2 \times 2}}^2. \end{aligned} \quad (3-11)$$

Where necessary, we indicated the space over which the norm has to be computed. This is only to clarify this expression as it should be clear from the context which is the appropriate space.

**3.4. Modeling to chiral lattices.** The proposed intrinsic model can be applied to chiral lattices. It turns out that considering small elastic displacements and small microrotations leads to a model very similar to the one studied in [Liu et al. 2012b] with an additional term contributing to the dynamics of the microrotations. In order to allow for chirality to be incorporated into our approach we define the quantity

$$u_i^* = \varepsilon_{ij} u_j. \quad (3-12)$$

In the three-dimensional setting one could not construct a term like this as the object  $\varepsilon_{ij}$  is intrinsically two-dimensional. The corresponding term in three dimensions is  $\varepsilon_{ijk}$  which would map the vector  $u_k$  to a matrix. The two-dimensional Levi-Civita symbol  $\varepsilon_{ij}$  is identical to our rotation matrix  $\bar{R}$  for  $\vartheta = -\pi/2$ . This means we can write

$$\varepsilon = \begin{pmatrix} 0 & 1 \\ -1 & 0 \end{pmatrix}. \quad (3-13)$$

Thus, the vector  $\mathbf{u}^*$  is the vector  $\mathbf{u}$  rotated by  $90^\circ$  in the counterclockwise direction and is given by

$$\mathbf{u}^* = \varepsilon \mathbf{u} = \begin{pmatrix} 0 & 1 \\ -1 & 0 \end{pmatrix} \begin{pmatrix} u_1 \\ u_2 \end{pmatrix} = \begin{pmatrix} u_2 \\ -u_1 \end{pmatrix}. \quad (3-14)$$

Now we define the corresponding deformation gradient of the rotated vector

$$F^* = \mathbb{1} + \nabla \mathbf{u}^*, \quad (3-15)$$



so that we can define a corresponding elastic energy

$$V_{\text{elastic}}^*(F^*, \bar{R}) = \mu^* \|\text{sym } \bar{R}^T F^* - \mathbb{1}\|^2 + \frac{1}{2} \lambda^* (\text{tr}(\text{sym}(\bar{R}^T F^*) - \mathbb{1}))^2 + \mu_c^* \|\text{skew}(\bar{R}^T F^* - \mathbb{1})\|^2. \quad (3-16)$$

The use of  $F^*$  in this new elastic energy is the only difference to (3-6). This means we are introducing a new elastic energy which depends on the rotated vector  $\mathbf{u}^*$ . Let us emphasize again that an analogous construction in three dimensions cannot be achieved.

Due to these new terms based on  $\mathbf{u}^*$ , we can also define the following mixing terms

$$V_{\text{mixing}} = m_1 \text{tr}[(\text{sym}(\bar{R}^T F^*) - \mathbb{1})^T (\text{sym}(\bar{R}^T F) - \mathbb{1})] + m_2 \text{tr}(\bar{R}^T F^* - \mathbb{1}) \text{tr}(\bar{R}^T F - \mathbb{1}), \quad (3-17)$$

where we note that we could also introduce a third mixing term of the form

$$m_3 \text{tr}[(\text{skew}(\bar{R}^T F^* - \mathbb{1}))^T (\text{skew}(\bar{R}^T F - \mathbb{1}))].$$

As this term will not be required in what follows, we will neglect this contribution henceforth.

Putting together everything that is needed to model chiral effects leads to the energy functional

$$V_{\text{chiral}}(F, F^*, \bar{R}) = V_{\text{curvature}} + V_{\text{elastic}} + V_{\text{elastic}}^* + V_{\text{mixing}} + V_{\text{coupling}(2)}. \quad (3-18)$$

#### 4. Equations of motion

In the following subsections we will state the equations of motion of our model which are derived using the calculus of variations. While most of this is fairly standard from a mathematical point of view, it is instructive to provide enough detail of this derivation, most of which can be found in [Appendix B](#). We work predominantly in the matrix notation and we also need to consider variations with respect to the polar part of the deformation gradient, which is a nonstandard result. Also our use of matrix curls and matrix divergences requires a careful treatment, which is shown.

**4.1. Field equations without chiral terms.** The complete variational energy functional of the nonlinear Cosserat micropolar theory in 2D will be the sum of each variational term, so we have

$$\delta V = \delta V_{\text{curvature}} + \delta V_{\text{elastic}} + \delta V_{\text{interaction}} + \delta V_{\text{coupling}}. \quad (4-1)$$

Rotations in two dimensions depend only on one angle and one can verify that

$$\delta \bar{R} = -(\cos \vartheta \epsilon + \sin \vartheta I) \delta \vartheta = -\epsilon \bar{R} \delta \vartheta, \quad (4-2)$$

where  $\epsilon$  is the 2D Levi-Civita matrix. While we computed the variations with respect to  $\delta F$ , we are in fact interested in the variations with respect to the displacements  $\delta u$ . So, let  $M$  be an arbitrary matrix; then we can easily find the relation between  $\delta F$  and  $\delta u$  which is given by

$$\langle A, \delta F \rangle = A : \delta F = -(\text{Div } M) \delta u, \quad (4-3)$$

or in other words, we need to integrate by parts once more to arrive at the equations of motions in the displacements.



We can now use (4-2) and (4-3) to rewrite the variations of Appendix B as follows:

$$\begin{aligned} \delta V_{\text{elastic}} = & -(\mu F \bar{R}^T F - 2(\mu + \lambda) F + \lambda \operatorname{tr}(\bar{R}^T F) F) : (\epsilon \bar{R}) \delta \vartheta \\ & - \operatorname{Div}[\mu(\bar{R} F^T \bar{R} + F) - 2(\mu + \lambda) \bar{R} + \lambda \operatorname{tr}(\bar{R}^T F) \bar{R}] \delta u, \end{aligned} \quad (4-4)$$

$$\delta V_{\text{curvature}} = -2\mu L_c^2 \operatorname{div}(\operatorname{grad} \vartheta) \delta \vartheta, \quad (4-5)$$

$$\begin{aligned} \delta V_{\text{interaction}} = & -\mu L_c \chi \left( \operatorname{div} \left[ \operatorname{tr}(\bar{R}^T F) \frac{\operatorname{grad} \vartheta}{\|\operatorname{grad} \vartheta\|} \right] + \|\operatorname{grad} \vartheta\| F \right) : (\epsilon \bar{R}) \delta \vartheta \\ & - \mu L_c \chi \operatorname{Div}[\|\operatorname{grad} \vartheta\| \bar{R}] \delta u, \end{aligned} \quad (4-6)$$

$$\delta V_{\text{coupling}} = 2\mu_c \operatorname{polar} F : (\epsilon \bar{R}) \delta \vartheta + 2\mu_c \operatorname{Div} \left[ \frac{1}{\operatorname{tr}(U)} (\bar{R} - \operatorname{polar} F \bar{R}^T \operatorname{polar} F) \right] \delta u. \quad (4-7)$$

**4.2. Fully nonlinear equations without chiral terms.** The variations with respect to our two dynamical variables, the vector  $u$  and the scalar  $\vartheta$ , give two Euler–Lagrange equations. The equations of motion including kinetic energy for the displacement vector  $u$  are now written in their final form, which is

$$\begin{aligned} \rho u_{tt} = & \operatorname{Div} \left[ 2\mu \bar{R} \operatorname{sym}(\bar{R}^T F) + \lambda \operatorname{tr}(\bar{R}^T F) \bar{R} - 2(\mu + \lambda) \bar{R} \right. \\ & \left. + \frac{4\mu_c}{\operatorname{tr}(\sqrt{F^T F})} \operatorname{polar} F \operatorname{skew}(\bar{R}^T \operatorname{polar} F) + \mu L_c \chi \|\bar{R}^T \operatorname{Curl} \bar{R}\| \bar{R} \right]. \end{aligned} \quad (4-8)$$

Here we used the useful identities  $2 \operatorname{polar} F \operatorname{skew}(\bar{R}^T \operatorname{polar} F) = -\bar{R} + \operatorname{polar} F \bar{R}^T \operatorname{polar} F$ , and moreover,  $2\bar{R} \operatorname{sym}(\bar{R}^T F) = \bar{R} F^T \bar{R} + F$ .

Before stating the equation of motion for the rotation, let us have a closer look at the various terms. The first line corresponds to the equations of nonlinear elasticity and the second line contains the interaction term and the Cosserat couple term.

Variations with respect to the rotation yield the following equation of motion:

$$\begin{aligned} \rho_{\text{rot}} \vartheta_{tt} = & \mu L_c^2 \operatorname{div}(\bar{R}^T \operatorname{Curl} \bar{R}) - (\mu + \lambda) \operatorname{tr}(\epsilon \bar{R}^T F) + \frac{1}{2} \mu \operatorname{tr}(\epsilon (\bar{R}^T F)^2) + \frac{1}{2} \lambda \operatorname{tr}(\bar{R}^T F) \operatorname{tr}(\epsilon \bar{R}^T F) \\ & + \frac{1}{2} \mu L_c \chi \left\{ \operatorname{div} \left[ \frac{\bar{R}^T \operatorname{Curl} \bar{R}}{\|\bar{R}^T \operatorname{Curl} \bar{R}\|} \operatorname{tr}(\bar{R}^T F) \right] + \|\bar{R}^T \operatorname{Curl} \bar{R}\| \operatorname{tr}(\epsilon \bar{R}^T F) \right\} - \mu_c \operatorname{tr}(\epsilon \bar{R}^T \operatorname{polar} F). \end{aligned} \quad (4-9)$$

The most complicated term comes from the interaction term and, in particular, the presence of the square-root when we work with the norm of  $\bar{R}^T \operatorname{Curl} \bar{R}$ . One has to be careful with this term as the square root is not differentiable at the origin. Due to the nonlinear nature of these equations it is very difficult to find explicit solutions or make generic statements about such solutions.

**4.3. Fully nonlinear equations of the chiral model.** The complete variational energy functional of the nonlinear Cosserat micropolar theory with chiral terms is given by

$$\delta V = \delta V_{\text{curvature}} + \delta V_{\text{elastic}} + \delta V_{\text{elastic}}^* + \delta V_{\text{mixing}} + \delta V_{\text{coupling}(2)}. \quad (4-10)$$

The equations of motion of the chiral model for the displacement  $\mathbf{u}$  are given by

$$\begin{aligned} \rho \mathbf{u}_{tt} = & \text{Div} [2\mu \bar{\mathbf{R}} \text{sym}(\bar{\mathbf{R}}^T F) + \lambda \text{tr}(\bar{\mathbf{R}}^T F) \bar{\mathbf{R}} - 2(\mu + \lambda) \bar{\mathbf{R}} + \mu_c (F - \bar{\mathbf{R}} F^T \bar{\mathbf{R}})] \\ & - \text{Div} [\mu^* (\bar{\mathbf{R}} (F^*)^T \bar{\mathbf{R}} + F^*) - 2(\mu^* + \lambda^*) \bar{\mathbf{R}} + \lambda^* \text{tr}(\bar{\mathbf{R}}^T F^*) \bar{\mathbf{R}} + \mu_c^* (\bar{\mathbf{R}} (F^*)^T \bar{\mathbf{R}} - F^*)] : \epsilon \\ & - \text{Div} [\frac{1}{2} m_1 (\epsilon^T \bar{\mathbf{R}} F^T \bar{\mathbf{R}} + \bar{\mathbf{R}} (F^*)^T \bar{\mathbf{R}} + F : \epsilon + F^* - 2(\bar{\mathbf{R}} : \epsilon + \bar{\mathbf{R}})) \\ & \quad + m_2 (\text{tr}(\bar{\mathbf{R}}^T F^*) R + \text{tr}(\bar{\mathbf{R}}^T F) (R : \epsilon) - (\bar{\mathbf{R}} : \epsilon + \bar{\mathbf{R}})) \\ & \quad + \frac{1}{2} m_3 (F : \epsilon + F^* - (F \bar{\mathbf{R}}^T \epsilon^T F + \epsilon^T F \bar{\mathbf{R}} F))]. \end{aligned} \quad (4-11)$$

Additionally, the equation of motion for  $\vartheta_{tt}$  is given by

$$\begin{aligned} \rho_{\text{rot}} \vartheta_{tt} = & \mu L_c^2 \text{div}(\bar{\mathbf{R}}^T \text{Curl} \bar{\mathbf{R}}) - (\mu + \lambda) \text{tr}(\epsilon \bar{\mathbf{R}}^T F) + \frac{1}{2} \mu \text{tr}(\epsilon (\bar{\mathbf{R}}^T F)^2) \\ & + \frac{1}{2} \lambda \text{tr}(\bar{\mathbf{R}}^T F) \text{tr}(\epsilon \bar{\mathbf{R}}^T F) + \mu_c \text{tr}(\epsilon \bar{\mathbf{R}}^T F \bar{\mathbf{R}}^T) \\ & + [\mu^* F^* \bar{\mathbf{R}}^T F^* - 2(\mu^* + \lambda^*) F^* + \lambda^* \text{tr}(\bar{\mathbf{R}}^T F^*) F^* + \mu_c^* F^* \bar{\mathbf{R}}^T F^* \\ & \quad + \frac{1}{2} m_1 (F \bar{\mathbf{R}}^T \epsilon^T F + \epsilon^T F \bar{\mathbf{R}} F - 2(F + F^*)) \\ & \quad + m_2 (\text{tr}(\bar{\mathbf{R}}^T F^*) F + \text{tr}(\bar{\mathbf{R}}^T F) F^* - (F + F^*)) \\ & \quad - \frac{1}{2} m_3 (F \bar{\mathbf{R}}^T \epsilon^T F + \epsilon^T F \bar{\mathbf{R}} F)] : (-\epsilon \bar{\mathbf{R}}). \end{aligned} \quad (4-12)$$

Before having a closer look at these equations and discussing applications to chiral lattices, we will briefly state two special solutions to the equations without chiral terms.

**4.4. Special solution — no displacements, static and homogeneous microrotations.** One of the simplest possible solutions can be sought in the form  $\mathbf{u} \equiv 0$  and  $\vartheta = \vartheta_0$ , where  $\vartheta_0$  is a constant angle. Using this ansatz, the equations for the displacements (4-8) are identically satisfied. Equation (4-9) for the microrotations reduces to the simple equation

$$(\lambda + \mu + \mu_c - (\lambda + \mu) \cos \vartheta_0) \sin \vartheta_0 = 0. \quad (4-13)$$

This equation has two somewhat trivial solutions when  $\vartheta_0 = 0$  or  $\vartheta_0 = \pi$ . These correspond to all the oriented material points to be aligned horizontally. Interestingly, there are more solutions, and their properties depend on the value of the Cosserat couple modulus  $\mu_c$ . If  $\mu_c = 0$ , then (4-13) is also satisfied by  $\vartheta_0 = \frac{1}{2}\pi$  or  $\vartheta_0 = \frac{3}{2}\pi$  which corresponds to all the oriented material points to be aligned vertically.

On the other hand, if  $\mu_c > 0$ , then we find

$$\cos \vartheta_0 = 1 + \frac{\mu_c}{\lambda + \mu}, \quad (4-14)$$

for which a solution exists provided that  $\lambda + \mu \leq 0$ . This, however, contradicts the standard assumptions of linear elasticity. These results appear to be consistent with our expectations of the theory.

**4.5. Special solution — no displacements, static and homogeneous microrotations with chiral terms.**

Next, let us consider  $\mathbf{u} \equiv 0$  and  $\vartheta = \vartheta_0$  in the equations with chiral terms. The equations for the displacements (4-8) are again identically satisfied. Equation (4-9) for the microrotations reduces to

$$\begin{aligned} [-m_1 - 2m_2 - \lambda + \lambda^* - \mu - \mu_{c1} + \mu^* \\ + (m_1 + 2m_2 - m_3 - \mu_c - \mu_c^* + \lambda + \lambda^* + \mu + \mu^*) \cos \phi_0] \sin \phi_0 = 0, \end{aligned} \quad (4-15)$$

where we also include the chiral and the mixing terms. As before, this equation has two trivial solutions when  $\vartheta_0 = 0$  or  $\vartheta = \pi$ . Lastly,

$$\cos \vartheta_0 = 1 + \frac{\mu_{c1} + \mu_c + \mu_c^* - 2\lambda^* - 2\mu^* + m_3}{\lambda + \lambda^* + \mu + \mu^* - \mu_c - \mu_c^* + m_1 + 2m_2 - m_3}, \quad (4-16)$$

for which a solution exists provided that the fraction is between 0 and  $-2$ . Due to the extra parameters present in this theory there is no *a priori* reason for this equation to have no solutions.

## 5. Applications to chiral lattices

Finally, we are able to demonstrate that our intrinsic two-dimensional model is applicable to chiral lattices. In doing so it is shown that it may not be necessary to begin with a three-dimensional theory and reduce it to the plane.

**5.1. Equations of motion.** By assuming small microrotations and small elastic displacements, we arrive at the following set of equations where we rescaled  $\rho_{\text{rot}} = \frac{1}{4}\varrho_{\text{rot}}$  to match the factors used in [Liu et al. 2012b] and also introduce  $\vartheta = -\phi$ . This gives

$$\begin{aligned} \rho \frac{\partial^2 u_1}{\partial t^2} = & (\lambda + 2\mu + \mu^* + \mu_c^*)u_{1,xx} + (\mu + \mu_c + \lambda^* + 2\mu^*)u_{1,yy} + (\lambda + \mu - \mu_c - \lambda^* - \mu^* + \mu_c^*)u_{2,xy} \\ & + \left(\frac{1}{2}m_1 + m_2\right)(-2u_{1,xy} + u_{2,xx} - u_{2,yy}) - 2(2\lambda^* + 2\mu^* - \mu_c^*)\phi_x + 2\mu_c\phi_y, \end{aligned} \quad (5-1)$$

and the second equation

$$\begin{aligned} \rho \frac{\partial^2 u_2}{\partial t^2} = & (\mu + \mu_c + \lambda^* + 2\mu^*)u_{2,xx} + (\lambda + 2\mu + \mu^* + \mu_c^*)u_{2,yy} + (\lambda + \mu - \mu_c - \lambda^* - \mu^* + \mu_c^*)u_{1,xy} \\ & + \left(\frac{1}{2}m_1 + m_2\right)(u_{1,xx} - u_{1,yy} + 2u_{2,xy}) - 2\mu_c\phi_x - 2(2\lambda^* + 2\mu^* - \mu_c^*)\phi_y. \end{aligned} \quad (5-2)$$

Lastly, the equation for the microrotations is given by

$$\begin{aligned} \varrho_{\text{rot}} \frac{\partial^2 \phi}{\partial t^2} = & 2d_1(\phi_{xx} + \phi_{yy}) + 4(2\lambda^* + 2\mu^* - \mu_c^* - \mu_c)\phi + 2\mu_c(u_{2,x} - u_{1,y}) \\ & - 2(\mu_c^* - 2\lambda^* - 2\mu^*)(u_{1,x} + u_{2,y}). \end{aligned} \quad (5-3)$$

Setting  $2d_1 = \gamma$ ,  $\mu^* = -\mu_c^* = A$ ,  $\lambda^* = -2A$ , and  $\frac{1}{2}m_1 + m_2 = -A$ , we recover the equations reported in [Liu et al. 2012b, (17)]. The only difference is an additional term in the rotational equation; namely this becomes

$$\varrho_{\text{rot}} \frac{\partial^2 \phi}{\partial t^2} = \gamma(\phi_{xx} + \phi_{yy}) - 4(\mu_c + A)\phi + 2\mu_c(u_{2,x} - u_{1,y}) - 2A(u_{1,x} + u_{2,y}), \quad (5-4)$$

where the term  $-4A\phi$  is the additional contribution. We believe that this term is present due to our starting point being the fully nonlinear model. Consequently, when studying plane wave solutions of this modified model, we expect some changes with respect to the wave speeds and the ratio of the amplitudes of the elastic waves, as will be discussed henceforth. It appears that our model can also be used in the context of tetrachiral lattices; see the equations of motion reported in [Chen et al. 2014].

**5.2. Plane wave solutions for the chiral model.** Along the lines of [Böhmer et al. 2011; 2016; Liu et al. 2012b; Böhmer and Obukhov 2012; Böhmer and Tamanini 2015], for instance, we can now study plane wave solutions of our more general model. For concreteness, let us consider a plane wave in the  $x$ -direction only. Then our ansatz for the displacements and microrotations is taken to be

$$\begin{pmatrix} u \\ v \\ \phi \end{pmatrix} = \begin{pmatrix} \hat{u} \\ \hat{v} \\ \hat{\phi} \end{pmatrix} e^{ikx - i\omega t}, \quad (5-5)$$

where  $k$  is the wave number and  $\omega$  is the angular frequency. The quantities  $\hat{u}$ ,  $\hat{v}$ ,  $\hat{\phi}$  denote the corresponding amplitudes. Substituting (5-5) into the equations of motion by replacing this form in (5-1)–(5-3) and using the above renaming of constants  $2d_1 = \gamma$ ,  $\mu^* = -\mu_c^* = A$ ,  $\lambda^* = -2A$ ,  $\frac{1}{2}m_1 + m_2 = -A$ , we can rewrite the equations in the following form:

$$\begin{pmatrix} k^2(\lambda + 2\mu) - \rho\omega^2 & -Ak^2 & 2iAk \\ -Ak^2 & k^2(\mu_c + \mu) - \rho\omega^2 & -2ik\mu_c \\ -2iAk & 2ik\mu_c & (\gamma k^2 + 4\mu_c + 4A) - \varrho_{\text{rot}}\omega^2 \end{pmatrix} \begin{pmatrix} \hat{u} \\ \hat{v} \\ \hat{\phi} \end{pmatrix} = 0. \quad (5-6)$$

As one would expect, the above equation is very similar to the one reported in [Liu et al. 2012b] with the difference of the additional term  $4A$  in the final component of the matrix. It is straightforward to show that the ratio of the amplitudes of the displacements is given by

$$\frac{\hat{u}}{\hat{v}} = \frac{A(k^2\mu - \rho\omega^2)}{A^2k^2 - \mu_c(k^2(\lambda + 2\mu) - \rho\omega^2)}. \quad (5-7)$$

Next, let us find the dispersion relation using this ratio, which gives

$$v = \frac{\omega}{k} = \sqrt{\frac{\hat{u}/\hat{v}(\mu_c(\lambda + 2\mu) - A^2) + A\mu}{\rho(\mu_c\hat{u}/\hat{v} + A)}}. \quad (5-8)$$

The two interesting limits of this relation are when the ratio of the amplitudes is either very small or very large. In these cases we find

$$v_t := v_{\hat{u}/\hat{v} \rightarrow 0} = \sqrt{\mu/\rho}, \quad (5-9)$$

which is the well-known speed for the transversal elastic wave. Likewise,

$$v_l := v_{\hat{u}/\hat{v} \rightarrow \infty} = \sqrt{\frac{\lambda + 2\mu}{\rho} - \frac{A^2}{\rho\mu_c}}, \quad (5-10)$$

so that we note that the longitudinal wave's speed is decreased by the chiral term  $A$ . The dispersion relation is shown in Figure 1. For this wave speed to be positive requires that the constant  $A$  satisfies the inequality

$$A^2 > \mu_c(\lambda + 2\mu). \quad (5-11)$$

Finally, we can consider the specific case where we only have displacements for the horizontal direction  $u$ , so that  $v = 0$ . In this case we use the ansatz  $u = \hat{u} \cos(kx - \omega t + \delta_u)$  and  $\phi = \hat{\phi} \cos(kx - \omega t + \delta_\phi)$ .

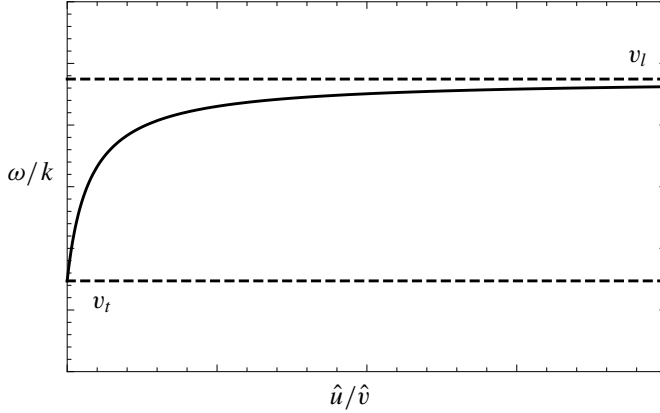


**Figure 1.** Visualization of the dispersion relation (5-8) as a function of the ratio of amplitudes  $\hat{u}/\hat{v}$ . The dashed lines indicate the limiting cases when  $\hat{u}/\hat{v} \rightarrow 0$  (bottom) and  $\hat{u}/\hat{v} \rightarrow \infty$  (top), respectively.

Provided the phase difference between the two waves is  $\frac{1}{2}\pi$ , this means  $\delta_\phi - \delta_u = \frac{1}{2}\pi$ , one can find a special solution to the linearised equations given by

$$\hat{u} = -\frac{2\mu_c}{Ak}\hat{\phi}, \quad \rho = \frac{k^2(\mu_c(\lambda + 2\mu) - A^2)}{\mu_c\omega^2}, \quad \varrho_{\text{rot}} = \frac{\gamma k^2 + 4A}{\omega^2}. \quad (5-12)$$

This is an interesting result as solutions of this type imply conditions that have to be satisfied regarding the parameters of the theory. There does not exist a nontrivial solution when  $\mu_c = 0$ ; in this case one finds  $u = v = \phi = 0$ . This is consistent with theoretical considerations since the choice  $\mu_c = 0$  is not admitted in the linearised context.

**5.3. Other possible applications.** Our intrinsic two-dimensional model might be particularly suited to describe materials like graphene and carbon nanotubes. These materials have unusual properties which make them valuable for applications in nanotechnology. The mathematical description of electrons propagating in graphene, for example, requires the use of the two-dimensional massless Dirac equation. The microstructure of Cosserat elasticity lends itself naturally to consider applications in this area, and some research along those lines is ongoing. In [Caillerie et al. 2006] a homogenization was applied to model a graphene sheet, while applications of Cosserat elasticity were considered in [De Cicco and Ieşan 2013] and also [Yang et al. 2016]. Elastic properties of graphene were studied in [Cadelano et al. 2010]. Carbon nanotubes, on the other hand, were studied in the context of Cosserat elasticity in [Selmi et al. 2014]. It will be interesting to apply our approach to some of these models in the future.

## 6. Conclusions

The primary motivation of this paper was the formulation of an intrinsic two-dimensional, geometrically nonlinear Cosserat theory of elasticity that could be used to model, amongst other features, chiral lattices. Our construction circumvents the problems one faces when reducing a three-dimensional isotropic and chiral theory to the plane. It is well known that the resulting two-dimensional theory is no longer chiral.

Our model is intrinsically two-dimensional and does not refer to a three-dimensional model for its construction. Chirality is introduced into this model by defining a new rotated deformation gradient  $F^*$ , see (3-15), which is constructed from the deformation vector rotated by  $\frac{1}{2}\pi$  in the counterclockwise direction. This deformation gradient is then used to define a new elastic energy and also new interaction terms between the deformation gradient  $F$  and the new quantity  $F^*$ . This approach is different to other approaches as we are directly modeling the planar chiral material.

Due to our intrinsic approach, our model displays a certain flexibility in the sense that it depends on up to 10 different elastic constants and the characteristic length  $L_c$ . These are the two-dimensional elastic (Lamé) constants  $\mu, \lambda$ , the Cosserat couple modulus  $\mu_c$ , and the interaction term  $\chi$ . Moreover, we have the corresponding constants  $\mu^*, \lambda^*, \mu_c^*$  and finally the three constants  $m_1, m_2, m_3$ . This allows us to formulate previously studied models using our intrinsic approach. It would also be interesting to apply our approach to other two-dimensional materials like graphene.

Finally, let us draw the attention back to the question of how to obtain a chiral two-dimensional model. We have seen that using a quadratic ansatz in the three-dimensional Cosserat model necessarily cannot give a two-dimensional chiral model, no matter our effort. However, it is not clear whether this problematic issue can be avoided by using some higher order (nonquadratic) model in the first place. If this were possible, the chiral effect would be absent under linearization. Therefore, more experimental evidence is needed to decide whether chirality can and should appear already as a discernible effect in an infinitesimal neighborhood of the identity.

### Acknowledgement

Bahamonde is supported by the Comisión Nacional de Investigación Científica y Tecnológica (Becas Chile Grant No. 72150066).

### Appendix A: Chirality and the matrix curl

Let us define the new deformation vector  $\varphi^\#$  by

$$\varphi^\#(x, y, z) := \varphi(-x, -y, -z). \quad (\text{A-1})$$

This means we evaluate the function  $\varphi$  at the inverted coordinate  $(-x, -y, -z)$ . However, we will work in the original Cartesian coordinate system and will not make the coordinate transformation of the previous appendix. Then, one verifies that

$$F^\# = \nabla \varphi^\# = -\nabla \varphi(-x, -y, -z) = -F(-x, -y, -z), \quad (\text{A-2})$$

because of the chain rule. Under this “inversion” the deformation gradient picks up a sign, making it noninvariant. On the other hand,  $F^T F$  is invariant.

Next, let us define the new orthogonal matrix  $R^\#$  which we define by

$$R^\# := -R(-x, -y, -z), \quad (\text{A-3})$$

where an additional minus sign was included in the definition. Then one immediately finds  $(R^\#)^T = -R(-x, -y, -z)^T = -(R^T)(-x, -y, -z)$  and

$$\text{Curl } R^\# = \begin{pmatrix} \partial_y R^\#_{xz} - \partial_z R^\#_{xy} & \partial_z R^\#_{xx} - \partial_x R^\#_{xz} & \partial_x R^\#_{xy} - \partial_y R^\#_{xx} \\ \partial_y R^\#_{yz} - \partial_z R^\#_{yy} & \partial_z R^\#_{yx} - \partial_x R^\#_{yz} & \partial_x R^\#_{yy} - \partial_y R^\#_{yx} \\ \partial_y R^\#_{zz} - \partial_z R^\#_{zy} & \partial_z R^\#_{zx} - \partial_x R^\#_{zz} & \partial_x R^\#_{zy} - \partial_y R^\#_{zx} \end{pmatrix}. \quad (\text{A-4})$$

Each single derivative will yield a minus sign by virtue of the chain rule. For instance,

$$\partial_y R^\# := -\partial_y R(-x, -y, -z) = \partial_{-y} R(-x, -y, -z) = (\partial_y R)(-x, -y, -z). \quad (\text{A-5})$$

Hence, applying this through all terms in the matrix curl of  $R^\#$ , one arrives at

$$\text{Curl } R^\# = (\text{Curl } R)(-x, -y, -z). \quad (\text{A-6})$$

Finally, one can study the curvature measure  $(R^\#)^T \text{Curl } R^\#$  which satisfies

$$(R^\#)^T \text{Curl } R^\# = -(R^T)(-x, -y, -z)(\text{Curl } R)(-x, -y, -z) = -(R^T \text{Curl } R)(-x, -y, -z). \quad (\text{A-7})$$

This result shows the desired chiral properties. Consequently, we showed that the term  $\langle F^T F, R^T \text{Curl } R \rangle$  is chiral.

## Appendix B: Variations and equations of motion

Each of the four parts of our energy functional (3-11) and (3-18) are considered separately. The various matrix derivatives that occur in this calculation are computed using standard formulae, all of which can be found nicely presented in [Petersen and Pedersen 2012].

**B.1. Elastic energy  $V_{\text{elastic}}$ .** We can rewrite the elastic energy functional as

$$\begin{aligned} V_{\text{elastic}} &= \mu \|\text{sym } \bar{R}^T F - \mathbb{1}\|^2 + \frac{1}{2} \lambda (\text{tr}(\text{sym}(\bar{R}^T F) - \mathbb{1}))^2 \\ &= 2\mu - 2\mu \text{tr}(F \bar{R}^T) + \frac{1}{2} \mu (\text{tr}(\bar{R}^T F \bar{R}^T F) + \text{tr}(F F^T)) \\ &\quad + 2\lambda - 2\lambda \text{tr}(\bar{R}^T F) + \frac{1}{2} \lambda (\text{tr}(\bar{R}^T F))^2. \end{aligned} \quad (\text{B-1})$$

Now we can compute the variations of this energy functional:

$$\begin{aligned} \delta V_{\text{elastic}}(F, \bar{R}) &= \frac{1}{2} \mu \left( \frac{d}{d\bar{R}} [\text{tr}(\bar{R}^T F \bar{R}^T F)] : \delta \bar{R} + \frac{d}{dF} \left[ \text{tr}(\bar{R}^T F \bar{R}^T F) + \frac{d}{dF} (\text{tr}(F F^T)) \right] : \delta F \right) \\ &\quad - 2(\mu + \lambda) \left( \frac{d}{d\bar{R}} (\text{tr}(\bar{R}^T F)) : \delta \bar{R} + \frac{d}{dF} (\text{tr}(\bar{R}^T F)) : \delta F \right) \\ &\quad + \frac{1}{2} \lambda \left( \frac{d}{d\bar{R}} [\text{tr}(\bar{R}^T F)]^2 : \delta \bar{R} + \frac{d}{dF} [\text{tr}(\bar{R}^T F)]^2 : \delta F \right). \end{aligned} \quad (\text{B-2})$$

Now, computing the various matrix derivatives yields

$$\begin{aligned} \delta V_{\text{elastic}}(F, \bar{R}) &= \langle \mu (\bar{R} F^T \bar{R} + F) - 2(\mu + \lambda) \bar{R} + \lambda \text{tr}(\bar{R}^T F) \bar{R}, \delta F \rangle \\ &\quad + \langle \mu F \bar{R}^T F - 2(\mu + \lambda) F + \lambda \text{tr}(\bar{R}^T F) F, \delta \bar{R} \rangle. \end{aligned} \quad (\text{B-3})$$

If we want to study the dynamical problem, we will need to subtract the kinetic energy term

$$V_{\text{elastic,kinetic}} = \frac{1}{2}\rho\|\dot{\varphi}\|^2. \quad (\text{B-4})$$

Here  $\rho$  is the density. If we vary this term we will obtain  $\delta V_{\text{elastic,kinetic}} = -\rho\ddot{\varphi}\delta\varphi$ , where we neglected a boundary term when integrating by parts once. Next, using that  $\nabla\varphi = \mathbb{1} + \nabla u$  implies  $\delta\varphi = \delta u$ . Hence, the elastic kinetic term can finally be written as

$$\delta V_{\text{elastic,kinetic}} = -\rho\ddot{u}\delta u. \quad (\text{B-5})$$

**B.2. Curvature energy  $V_{\text{curvature}}$ .** The curvature energy functional depends only on the rotation angle  $\vartheta$  so that

$$V_{\text{curvature}}(\vartheta) = \mu L_c^2 \|\text{grad } \vartheta\|^2. \quad (\text{B-6})$$

Variations with respect to  $\delta\vartheta$  are well known (we are dealing with a standard vector), and one finds

$$\delta V_{\text{curvature}} = -2\mu L_c^2 \text{div}(\text{grad } \vartheta)\delta\vartheta = -2\mu L_c^2 \Delta\vartheta\delta\vartheta, \quad (\text{B-7})$$

where, as before, we have neglected a boundary term. Recall that  $\text{div grad } \vartheta$  is the scalar Laplacian  $\Delta\vartheta$ . If we want to study the dynamical problem, we will need to subtract the kinetic energy term

$$V_{\text{curvature,kinetic}} = \rho_{\text{rot}}\|\dot{\vartheta}\|^2. \quad (\text{B-8})$$

Variations with respect to  $\delta\vartheta$  lead to

$$\delta V_{\text{curvature,kinetic}} = -2\rho_{\text{rot}}\ddot{\vartheta}\delta\vartheta, \quad (\text{B-9})$$

up to a boundary term.

**B.3. Interaction energy  $V_{\text{interaction}}$ .** The interaction term is

$$V_{\text{interaction}}(F, \bar{R}) = \mu L_c \chi \|\bar{R}^T \text{Curl } \bar{R}\| \text{tr}(\bar{R}^T F) = \mu L_c \chi \|\text{grad } \vartheta\| \text{tr}(\bar{R}^T F). \quad (\text{B-10})$$

Computing the variations with respect to  $\bar{R}$  and  $F$  yields

$$\begin{aligned} \delta V_{\text{interaction}}(F, \vartheta) &= \mu L_c \chi \text{tr}(\bar{R}^T F) \frac{\text{grad } \vartheta}{\|\text{grad } \vartheta\|} \delta(\text{grad } \vartheta) \\ &\quad + \mu L_c \chi \|\text{grad } \vartheta\| \left( \frac{d}{dF} [\text{tr}(\bar{R}^T F)] : \delta F + \frac{d}{d\bar{R}} [\text{tr}(\bar{R} F^T)] : \delta \bar{R} \right) \\ &= -\mu L_c \chi \frac{\text{grad } \vartheta}{\|\text{grad } \vartheta\|} \text{grad}[\text{tr}(\bar{R}^T F)]\delta\vartheta - \mu L_c \chi \text{tr}(\bar{R}^T F) \text{div} \left[ \frac{\text{grad } \vartheta}{\|\text{grad } \vartheta\|} \right] \delta\vartheta \\ &\quad + \mu L_c \chi \langle \|\text{grad } \vartheta\| F, \delta \bar{R} \rangle + \mu L_c \chi \langle \|\text{grad } \vartheta\| \bar{R}, \delta F \rangle, \end{aligned} \quad (\text{B-11})$$

which is probably the most complicated of all terms.

**B.4. Cosserat couplings  $V_{\text{coupl}}$ .** We have the energy functional of the coupling as follows

$$V_{\text{coupling}}(F, \bar{R}) = \mu_c \|\bar{R}^T \text{polar } F - \mathbb{1}\|^2 = 4\mu_c - 2\mu_c \text{tr}(\bar{R}^T \text{polar } F). \quad (\text{B-12})$$

The variations of  $\text{polar } F$  with respect to  $F$  are somewhat nonstandard; however, the result is well-known and has been reported for instance in [Chen and Wheeler 1993; Rosati 1999]. In particular, in



two dimensions, the result is straightforward to verify directly. We briefly recall that the polar part of  $F$  can be written as polar  $F = F(F^T F)^{-1/2}$ . Then

$$\delta V_{\text{coupling}}(F, \bar{R}) = -2\mu_c \text{polar } F : \delta \bar{R} - 2\mu_c \left[ \frac{d}{dF} (\text{tr}(\bar{R}^T \text{polar } F)) \right] : \delta F. \quad (\text{B-13})$$

Using the chain rule for matrix differentiation we find

$$\begin{aligned} \frac{d}{dF_{ml}} (\text{tr}(\bar{R}^T \text{polar } F)) &= \text{tr} \left[ \left( \frac{d}{d \text{polar } F} \text{tr}(\bar{R}^T \text{polar } F) \right)^T \frac{d \text{polar } F}{dF_{ml}} \right] \\ &= \text{tr} \left[ \bar{R}^T \frac{d \text{polar } F}{dF_{ml}} \right]. \end{aligned} \quad (\text{B-14})$$

Following [Chen and Wheeler 1993; Rosati 1999] we have

$$\frac{d \text{polar } F}{dF} = \frac{1}{\text{tr}(U)} (\mathbb{I} - \text{polar}(F) \hat{\boxtimes} \text{polar}(F)^T), \quad (\text{B-15})$$

where we followed the notation used in [Rosati 1999]. Recall that  $U$  is the positive definite symmetric part of the polar decomposition  $F = \text{polar}(F)U$ . The symbol  $\hat{\boxtimes}$  denotes the operation  $(A \hat{\boxtimes} B)_{ijkl} = A_{il}B_{jk}$  for any two matrices  $A$  and  $B$ . In addition we use the notation  $\mathbb{I} = \mathbb{1} \hat{\boxtimes} \mathbb{1}$ . Putting this together yields

$$\text{tr} \left[ \bar{R}^T \frac{d \text{polar } F}{dF_{ml}} \right] = \frac{1}{\text{tr}(U)} [\bar{R} - R \bar{R}^T R]. \quad (\text{B-16})$$

Finally, we will obtain the variations  $\delta V_{\text{coupling}}$ , which are given by

$$\delta V_{\text{coupling}}(F, \bar{R}) = -2\mu_c \langle R, \delta \bar{R} \rangle - \frac{2\mu_c}{\text{tr}(U)} \langle \bar{R} - R \bar{R}^T R, \delta F \rangle. \quad (\text{B-17})$$

Now we will focus on the second coupling term (3-10) that can be rewritten as follows

$$V_{\text{coupling}(2)}(F, \bar{R}) = 3\mu_c + \frac{1}{2}\mu_c \text{tr}[F^T F - \bar{R}^T F \bar{R}^T F], \quad (\text{B-18})$$

which yields

$$\delta V_{\text{coupling}(2)}(F, \bar{R}) = \mu_c \langle F - \bar{R} F^T \bar{R}, \delta F \rangle - \mu_c \langle \bar{R}^T F, \delta \bar{R} \rangle. \quad (\text{B-19})$$

**B.5. Chiral terms.** Let us begin by computing the term  $\delta V_{\text{elastic}}^*$ . A direct calculation yields

$$\begin{aligned} \delta V_{\text{elastic}}^* &= -\text{Div} \left[ \mu^* (\bar{R} (F^*)^T \bar{R} + F^*) - 2(\mu^* + \lambda^*) \bar{R} + \lambda^* \text{tr}(\bar{R}^T F^*) \bar{R} + \mu_c^* (\bar{R} (F^*)^T \bar{R} - F^*) \right] : \epsilon \delta u \\ &\quad + \left[ \mu^* F^* \bar{R}^T F^* - 2(\mu^* + \lambda^*) F^* + \lambda^* \text{tr}(\bar{R}^T F^*) F^* + \mu_c^* F^* \bar{R}^T F^* \right] : (-\epsilon \bar{R}) \delta \vartheta. \end{aligned} \quad (\text{B-20})$$

Next, we consider the mixing terms

$$\begin{aligned} \delta V_{\text{mixing}} &= \frac{1}{2} m_1 (\delta [\text{tr}(\bar{R}^T F^* \bar{R}^T F)] + \delta [\text{tr}(F (F^*)^T)] - 2\delta [\text{tr}(\bar{R}^T F^*) + \text{tr}(\bar{R}^T F)]) \\ &\quad + m_2 (\delta [\text{tr}(\bar{R}^T F^*) \text{tr}(\bar{R}^T F)] - \delta [\text{tr}(\bar{R}^T F^*) + \text{tr}(\bar{R}^T F)]) \\ &\quad + \frac{1}{2} m_3 (\delta [\text{tr}(F (F^*)^T)] - \delta [\text{tr}(\bar{R}^T F^* \bar{R}^T F)]). \end{aligned} \quad (\text{B-21})$$

These variations are slightly more involved than the previous ones, so some additional details are given in the following. The first three respective terms are given by

$$\delta[\text{tr}(\bar{R}^T F^* \bar{R}^T F)] = (F \bar{R}^T \epsilon^T F + \epsilon^T F \bar{R} F) : \delta \bar{R} + (\epsilon^T \bar{R} F^T \bar{R} + \bar{R} F^T \epsilon^T \bar{R}) : \delta F, \quad (\text{B-22})$$

$$\delta[\text{tr}(F(F^*)^T)] = F : \delta F^* + F^* : \delta F = [(F : \epsilon) + F^*] : \delta F, \quad (\text{B-23})$$

$$\delta[\text{tr}(\bar{R}^T F^*) + \text{tr}(\bar{R}^T F)] = (\bar{R} : \epsilon + \bar{R}) : \delta F + (F + F^*) : \delta \bar{R}. \quad (\text{B-24})$$

The fourth and final term is given by

$$\delta[\text{tr}(\bar{R}^T F^*) \text{tr}(\bar{R}^T F)] = (\text{tr}(\bar{R}^T F^*) F + \text{tr}(\bar{R}^T F) F^*) : \delta R + (\text{tr}(\bar{R}^T F^*) R + \text{tr}(\bar{R}^T F) (R : \epsilon)) : \delta F. \quad (\text{B-25})$$

Therefore, the complete variations are given by

$$\begin{aligned} \delta V_{\text{mixing}} = & \left[ \frac{1}{2} m_1 (F \bar{R}^T \epsilon^T F + \epsilon^T F \bar{R} F - 2(F + F^*)) \right. \\ & + m_2 (\text{tr}(\bar{R}^T F^*) F + \text{tr}(\bar{R}^T F) F^* - (F + F^*)) - \frac{1}{2} m_3 (F \bar{R}^T \epsilon^T F + \epsilon^T F \bar{R} F) \left. \right] : \delta \bar{R} \\ & + \left[ \frac{1}{2} m_1 (\epsilon^T \bar{R} F^T \bar{R} + \bar{R} (F^*)^T \bar{R} + F : \epsilon + F^* - 2(\bar{R} : \epsilon + \bar{R})) \right. \\ & + m_2 (\text{tr}(\bar{R}^T F^*) R + \text{tr}(\bar{R}^T F) (R : \epsilon) - (\bar{R} : \epsilon + \bar{R})) \\ & \left. + \frac{1}{2} m_3 (F : \epsilon + F^* - (F \bar{R}^T \epsilon^T F + \epsilon^T F \bar{R} F)) \right] : \delta F. \quad (\text{B-26}) \end{aligned}$$

### List of Symbols

$\mathbb{1}$	identity matrix
$\varphi$	deformation vector in 3D and 2D
$\phi$	rotation angle in 3D
$\mathbf{u}$	displacement vector
$\mathbf{a}$	rotation vector
$F = \nabla \varphi = I + \nabla \mathbf{u}$	deformation gradient
$F_{ij} = \delta_{ij} + \mathbf{u}_{i,j} = \delta_{ij} + \partial_j \mathbf{u}_i$	deformation gradient in index notation
$\bar{R} = \exp(\bar{A})$	rotation matrix
$\bar{A}$	skew-symmetric matrix generating $\bar{R}$
$\epsilon$	2D Levi-Civita symbol, $\epsilon_{12} = 1 = -\epsilon_{21}$ , $\epsilon_{11} = \epsilon_{22} = 0$
$\bar{U} = \bar{R}^T F$	nonsymmetric stretch tensor, first Cosserat deformation tensor
$F = RU = \text{polar}(F)U$	classical polar decomposition
$(\text{Curl } M)_i = \epsilon_{rs} \partial_r M_{is}$	matrix curl in 2D
$(\text{Div } M)_i = \partial_s M_{is}$	matrix divergence in 2D
$\text{sym } M = \frac{1}{2}(M + M^T)$	symmetric part of matrix $M$
$\text{skew } M = \frac{1}{2}(M - M^T)$	skew-symmetric part of $M$
$\text{dev } M = M - \frac{1}{3} \text{tr}(M) \mathbb{1}$	deviatoric or trace-free part of $M$
$\vartheta$	rotation angle in 2D
$\bar{R} = (\cos \vartheta) \mathbb{1} - (\sin \vartheta) \epsilon$	rotation in 2D

**Remark.** We write the above tensors  $\bar{R}$  and  $\bar{U}$  with superposed bars in order to distinguish them from the factors  $R$  and  $U$  of the classical polar decomposition  $F = RU$ , in which  $R = \text{polar } F$  is orthogonal and  $U$  is positive definite, symmetric, and is a standard notation in elasticity. We also note the standard relation  $F^T F = (RU)^T (RU) = U^T R^T T U = U^T U = U^2$  so that  $U = \sqrt{F^T F}$ .

We will use the Frobenius scalar product defined as

$$\langle A, B \rangle = A : B = A_{ij} B_{ij} = \text{tr}(AB^T). \quad (\text{B-27})$$

## References

- [Bîrsan and Neff 2013] M. Bîrsan and P. Neff, “Existence theorems in the geometrically non-linear 6-parameter theory of elastic plates”, *J. Elasticity* **112**:2 (2013), 185–198.
- [Bîrsan and Neff 2014] M. Bîrsan and P. Neff, “Existence of minimizers in the geometrically non-linear 6-parameter resultant shell theory with drilling rotations”, *Math. Mech. Solids* **19**:4 (2014), 376–397.
- [Böhmer and Obukhov 2012] C. G. Böhmer and Y. N. Obukhov, “A gauge-theoretical approach to elasticity with microrotations”, *Proc. R. Soc. Lond. A* **468**:2141 (2012), 1391–1407.
- [Böhmer and Tamanini 2015] C. G. Böhmer and N. Tamanini, “Rotational elasticity and couplings to linear elasticity”, *Math. Mech. Solids* **20**:8 (2015), 959–974.
- [Böhmer et al. 2011] C. G. Böhmer, R. J. Downes, and D. Vassiliev, “Rotational elasticity”, *Quart. J. Mech. Appl. Math.* **64**:4 (2011), 415–439.
- [Böhmer et al. 2016] C. G. Böhmer, P. Neff, and B. Seymenoğlu, “Soliton-like solutions based on geometrically nonlinear Cosserat micropolar elasticity”, *Wave Motion* **60** (2016), 158–165.
- [Borisov et al. 2016] L. Borisov, A. Fischle, and P. Neff, “Optimality of the relaxed polar factors by a characterization of the set of real square roots of real symmetric matrices”, preprint, 2016.
- [Cadelano et al. 2010] E. Cadelano, P. L. Palla, S. Giordano, and L. Colombo, “Elastic properties of hydrogenated graphene”, *Phys. Rev. B* **82** (2010), art. id. 235414.
- [Caillerie et al. 2006] D. Caillerie, A. Mourad, and A. Raoult, “Discrete homogenization in graphene sheet modeling”, *J. Elasticity* **84**:1 (2006), 33–68.
- [Chen and Wheeler 1993] Y.-C. Chen and L. Wheeler, “Derivatives of the stretch and rotation tensors”, *J. Elasticity* **32**:3 (1993), 175–182.
- [Chen et al. 2014] Y. Chen, X. N. Liu, G. K. Hu, Q. P. Sun, and Q. S. Zheng, “Micropolar continuum modeling of bi-dimensional tetrachiral lattices”, *Proc. R. Soc. Lond. A* **470**:2165 (2014), art. id. 20130734.
- [Cheverton and Beatty 1981] K. J. Cheverton and M. F. Beatty, “Extension, torsion and expansion of an incompressible, hemitropic Cosserat circular cylinder”, *J. Elasticity* **11**:2 (1981), 207–227.
- [Cosserat and Cosserat 1909] E. Cosserat and F. Cosserat, *Théorie des corps déformables*, Hermann, Paris, 1909.
- [De Cicco and Ieşan 2013] S. De Cicco and D. Ieşan, “A theory of chiral Cosserat elastic plates”, *J. Elasticity* **111**:2 (2013), 245–263.
- [Ericksen 1962a] J. L. Ericksen, “Hydrostatic theory of liquid crystals”, *Arch. Ration. Mech. Anal.* **9** (1962), 371–378.
- [Ericksen 1962b] J. L. Ericksen, “Kinematics of macromolecules”, *Arch. Ration. Mech. Anal.* **9** (1962), 1–8.
- [Ericksen 1967] J. L. Ericksen, “Twisting of liquid crystals”, *J. Fluid Mech.* **27**:1 (1967), 59–64.
- [Ericksen and Truesdell 1957] J. L. Ericksen and C. Truesdell, “Exact theory of stress and strain in rods and shells”, *Arch. Ration. Mech. Anal.* **1** (1957), 295–323.
- [Eringen 1999] A. C. Eringen, *Microcontinuum field theories, I: Foundations and solids*, Springer, 1999.
- [Eringen and Suhubi 1964] A. C. Eringen and E. S. Suhubi, “Nonlinear theory of simple micro-elastic solids, I”, *Int. J. Eng. Sci.* **2** (1964), 189–203.

- [Fischle and Neff 2017a] A. Fischle and P. Neff, “The geometrically nonlinear Cosserat micropolar shear-stretch energy, I: A general parameter reduction formula and energy-minimizing microrotations in 2D”, *Z. Angew. Math. Mech.* **97**:7 (2017), 828–842.
- [Fischle and Neff 2017b] A. Fischle and P. Neff, “The geometrically nonlinear Cosserat micropolar shear-stretch energy, II: Non-classical energy-minimizing microrotations in 3D and their computational validation”, *Z. Angew. Math. Mech.* **97**:7 (2017), 843–871.
- [Fischle and Neff 2017c] A. Fischle and P. Neff, “Grioli’s theorem with weights and the relaxed-polar mechanism of optimal Cosserat rotations”, *Rend. Accad. Naz. Lincei* **28**:3 (2017), 573–600.
- [Fischle et al. 2017] A. Fischle, P. Neff, and D. Raabe, “The relaxed-polar mechanism of locally optimal Cosserat rotations for an idealized nanoindentation and comparison with 3D-EBSD experiments”, *Z. Angew. Math. Phys.* **68**:4 (2017), art. id. 90.
- [Green and Rivlin 1964] A. E. Green and R. S. Rivlin, “Multipolar continuum mechanics”, *Arch. Ration. Mech. Anal.* **17** (1964), 113–147.
- [Joumaa and Ostoja-Starzewski 2011] H. Joumaa and M. Ostoja-Starzewski, “Stress and couple-stress invariance in non-centrosymmetric micropolar planar elasticity”, *Proc. R. Soc. Lond. A* **467**:2134 (2011), 2896–2911.
- [Lakes 2001] R. S. Lakes, “Elastic and viscoelastic behavior of chiral materials”, *Int. J. Mech. Sci.* **43**:7 (2001), 1579–1589.
- [Lakes and Benedict 1982] R. S. Lakes and R. L. Benedict, “Noncentrosymmetry in micropolar elasticity”, *Int. J. Eng. Sci.* **20**:10 (1982), 1161–1167.
- [Lankeit et al. 2017] J. Lankeit, P. Neff, and F. Osterbrink, “Integrability conditions between the first and second Cosserat deformation tensor in geometrically nonlinear micropolar models and existence of minimizers”, *Z. Angew. Math. Phys.* **68**:1 (2017), art. id. 11.
- [Liu and Hu 2016] X. N. Liu and G. K. Hu, “Elastic metamaterials making use of chirality: a review”, *J. Mech. Eng.* **62**:7-8 (2016), 403–418.
- [Liu et al. 2012a] X. N. Liu, G. L. Huang, and G. K. Hu, “Analytical formation of a discrete chiral elastic metamaterial model”, art. id. 834823 in *Health monitoring of surgical and biological systems* (San Diego, 2012), edited by T. Kundu, SPIE Proceedings **8348**, SPIE, Bellingham, WA, 2012.
- [Liu et al. 2012b] X. N. Liu, G. L. Huang, and G. K. Hu, “Chiral effect in plane isotropic micropolar elasticity and its application to chiral lattices”, *J. Mech. Phys. Solids* **60**:11 (2012), 1907–1921.
- [Mindlin 1964] R. D. Mindlin, “Micro-structure in linear elasticity”, *Arch. Ration. Mech. Anal.* **16**:1 (1964), 51–78.
- [Münch et al. 2011] I. Münch, P. Neff, and W. Wagner, “Transversely isotropic material: nonlinear Cosserat versus classical approach”, *Contin. Mech. Therm.* **23**:1 (2011), 27–34.
- [Neff 2004a] P. Neff, “Existence of minimizers for a geometrically exact Cosserat solid”, *Proc. Appl. Math. Mech.* **4**:1 (2004), 548–549.
- [Neff 2004b] P. Neff, “A geometrically exact Cosserat shell-model including size effects, avoiding degeneracy in the thin shell limit, I: Formal dimensional reduction for elastic plates and existence of minimizers for positive Cosserat couple modulus”, *Contin. Mech. Therm.* **16**:6 (2004), 577–628.
- [Neff 2006a] P. Neff, “Existence of minimizers for a finite-strain micromorphic elastic solid”, *Proc. Roy. Soc. Edinburgh A* **136**:5 (2006), 997–1012.
- [Neff 2006b] P. Neff, “A finite-strain elastic-plastic Cosserat theory for polycrystals with grain rotations”, *Int. J. Eng. Sci.* **44**:8-9 (2006), 574–594.
- [Neff 2007] P. Neff, “A geometrically exact planar Cosserat shell-model with microstructure: existence of minimizers for zero Cosserat couple modulus”, *Math. Models Methods Appl. Sci.* **17**:3 (2007), 363–392.
- [Neff and Münch 2008] P. Neff and I. Münch, “Curl bounds grad on  $SO(3)$ ”, *ESAIM Control Optim. Calc. Var.* **14**:1 (2008), 148–159.
- [Neff and Münch 2009] P. Neff and I. Münch, “Simple shear in nonlinear Cosserat elasticity: bifurcation and induced microstructure”, *Contin. Mech. Therm.* **21**:3 (2009), 195–221.
- [Neff et al. 2008] P. Neff, A. Fischle, and I. Münch, “Symmetric Cauchy stresses do not imply symmetric Biot strains in weak formations of isotropic hyperelasticity with rotational degrees of freedom”, *Acta Mech.* **197**:1-2 (2008), 19–30.

- [Neff et al. 2010] P. Neff, K.-I. Hong, and J. Jeong, “The Reissner–Mindlin plate is the  $\Gamma$ -limit of Cosserat elasticity”, *Math. Models Methods Appl. Sci.* **20**:9 (2010), 1553–1590.
- [Neff et al. 2015] P. Neff, M. Bîrsan, and F. Osterbrink, “Existence theorem for geometrically nonlinear Cosserat micropolar model under uniform convexity requirements”, *J. Elasticity* **121**:1 (2015), 119–141.
- [Ostoja-Starzewski and Jasiuk 1995] M. Ostoja-Starzewski and I. Jasiuk, “Stress invariance in planar Cosserat elasticity”, *Proc. R. Soc. Lond. A* **451**:1942 (1995), 453–470.
- [Petersen and Pedersen 2012] K. B. Petersen and M. S. Pedersen, “The matrix cookbook”, preprint, Technical Univ. Denmark, 2012, available at [www2.imm.dtu.dk/pubdb/p.php?3274](http://www2.imm.dtu.dk/pubdb/p.php?3274).
- [Rosati 1999] L. Rosati, “Derivatives and rates of the stretch and rotation tensors”, *J. Elasticity* **56**:3 (1999), 213–230.
- [Rosi and Auffray 2016] G. Rosi and N. Auffray, “Anisotropic and dispersive wave propagation within strain-gradient framework”, *Wave Motion* **63** (2016), 120–134.
- [Sander et al. 2016] O. Sander, P. Neff, and M. Bîrsan, “Numerical treatment of a geometrically nonlinear planar Cosserat shell model”, *Comput. Mech.* **57**:5 (2016), 817–841.
- [Schaefer 1967] H. Schaefer, “Das Cosserat Kontinuum”, *Z. Angew. Math. Mech.* **47**:8 (1967), 485–498.
- [Selmi et al. 2014] A. Selmi, H. Hassis, I. Doghri, and H. Zenzri, “A Cosserat-type plate theory and its application to carbon nanotube microstructure”, *Amer. J. Appl. Sci.* **11**:8 (2014), 1255–1273.
- [Suhubi and Eringen 1964] E. S. Suhubi and A. C. Eringen, “Nonlinear theory of micro-elastic solids, II”, *Int. J. Eng. Sci.* **2** (1964), 389–404.
- [Toupin 1962] R. A. Toupin, “Elastic materials with couple-stresses”, *Arch. Ration. Mech. Anal.* **11** (1962), 385–414.
- [Toupin 1964] R. A. Toupin, “Theories of elasticity with couple-stress”, *Arch. Ration. Mech. Anal.* **17** (1964), 85–112.
- [Yang et al. 2016] G. Yang, Z. Huang, C.-F. Gao, and B. Zhang, “Theoretical consideration of a microcontinuum model of graphene”, *AIP Adv.* **6**:5 (2016), art. id. 055115.

Received 13 May 2017. Revised 9 Aug 2017. Accepted 14 Aug 2017.

SEBASTIAN BAHAMONDE: [sebastian.beltran.14@ucl.ac.uk](mailto:sebastian.beltran.14@ucl.ac.uk)  
 Department of Mathematics, University College London, London, United Kingdom

CHRISTIAN G. BÖHMER: [c.boehmer@ucl.ac.uk](mailto:c.boehmer@ucl.ac.uk)  
 Department of Mathematics, University College London, London, United Kingdom

PATRIZIO NEFF: [patrizio.neff@uni-due.de](mailto:patrizio.neff@uni-due.de)  
 Lehrstuhl für Nichtlineare Analysis und Modellierung, Fakultät für Mathematik, Universität Duisburg-Essen, Essen, Germany

## TRANSIENT RESPONSE OF MULTILAYERED ORTHOTROPIC STRIPS WITH INTERFACIAL DIFFUSION AND SLIDING

XU WANG AND PETER SCHIAVONE

We use transfer matrix and state-space methods to derive exact solutions for the time-dependent and plane strain deformations of simply supported multilayered orthotropic elastic strips with simultaneous interfacial diffusion and rate-dependent sliding. Our analysis considers the corresponding interfacial tractions as the fundamental state variables. As a result, a homogeneous state-space equation can be obtained by enforcing the interfacial diffusion and sliding conditions. The relaxation times of the multilayered orthotropic strip and the evolution of the interfacial tractions can then be determined from the derived state-space equation. Once the transient interfacial tractions are known, all of the field variables at any time and at any position of the multilayered strip can be conveniently obtained.

### 1. Introduction

Interfacial diffusion and sliding are responsible for many phenomena at high temperatures [Sofronis and McMeeking 1994; Mori et al. 1997; He and Hu 2003] and are also closely related to room temperature plastic deformations in nanocrystalline materials [Wei et al. 2008]. The combined effect of interfacial diffusion and sliding in particulate, fibrous, laminated composites and in polycrystalline solids has been investigated in [Sofronis and McMeeking 1994; Kim and McMeeking 1995; Onaka et al. 1998; 1999; He and Hu 2003; Wang and Pan 2010; Wang et al. 2016; Wang and Wang 2016; Wei et al. 2008].

Most of the early discussions on laminated plates with rate-dependent imperfect interfaces are confined to short range diffusion-induced rate-dependent sliding (or viscous) interfaces in which the diffusion-induced long range mass transport at the interface is absent (see, for example, [He and Jiang 2003; Chen and Lee 2004]). Chen and Lee [2004] adopted power series expansions to approximate the variations of field variables with time. Very recently, Wang and Wang [2016] studied the time-dependent deformations of multilayered isotropic elastic strips with interfacial diffusion and sliding under cylindrical bending.

In this research, we endeavor to study the plane strain deformations of multilayered orthotropic elastic strips with simultaneous interfacial diffusion and sliding. First, we derive a general solution for displacements and stresses in a homogeneous orthotropic layer following Suo's method [1990]. Secondly, we use this general solution to obtain a transfer matrix relating the displacements and tractions on the upper interface of an orthotropic layer to those on its lower interface. Next, we derive a homogeneous state-space equation with interfacial tractions as state variables by imposing the interfacial diffusion and sliding conditions and by utilizing the transfer matrix method. It is noted that the construction of the state-space equation differs from that in [Wang and Wang 2016] in that here, the state vector is composed of the traction components on all of the existing interfaces whereas in that paper, the state vector is composed

---

*Keywords:* multilayered orthotropic strip, interfacial diffusion and sliding, transfer matrix, state-space equation, relaxation time.

of functions of time appearing in the expressions of displacements and stresses in all of the isotropic layers. Finally, the relaxation times and the transient elastic field in the multilayered strip can then be obtained by solving the corresponding state-space equation.

### 2. Analysis of a multilayered orthotropic strip

In a Cartesian coordinate system  $x_i$  ( $i = 1, 2, 3$ ), let  $u_i$  and  $\sigma_{ij}$  represent the displacements and stresses. As shown in **Figure 1**, we consider the plane strain deformations of a strip composed of  $N$  orthotropic elastic layers, labeled  $1, 2, \dots, N$  from the bottom up. The  $x_2 = 0$  plane coincides with the bottom surface of the strip and the  $x_2$ -axis is perpendicular to the strip. The strip of width  $l$  is simply supported at  $x_1 = 0$  and  $x_1 = l$ . The thickness of layer  $j$  is  $h_j$  and the total thickness of the strip is  $h = \sum_{j=1}^N h_j$ . The subscript  $j$  or the superscript  $(j)$  will be used to denote the associated quantities in layer  $j$ . The strip is subjected only to a sinusoidal pressure loading  $p = p_0 \sin kx_1$  with  $k = \pi/l$  applied on its top surface. The boundary and interface conditions for the problem are specified as follows:

$$\sigma_{22}^{(N)} = -p_0 \sin kx_1, \quad \sigma_{12}^{(N)} = 0, \quad \text{at } x_2 = h; \tag{1a}$$

$$\sigma_{22}^{(1)} = \sigma_{12}^{(1)} = 0 \quad \text{at } x_2 = 0; \tag{1b}$$

$$\sigma_{22}^{(j+1)} = \sigma_{22}^{(j)}, \quad \sigma_{12}^{(j+1)} = \sigma_{12}^{(j)}, \quad \dot{u}_2^{(j)} - \dot{u}_2^{(j+1)} = D_j \frac{\partial^2 \sigma_{22}^{(j)}}{\partial x_1^2},$$

$$\vartheta_j [\dot{u}_1^{(j+1)} - \dot{u}_1^{(j)}] = \sigma_{12}^{(j)}, \quad \text{at } x_2 = \sum_{n=1}^j h_n, \quad j = 1, 2, \dots, N-1; \tag{1c}$$

$$\sigma_{11}^{(1)} = \sigma_{11}^{(2)} = \dots = \sigma_{11}^{(N)} = 0, \quad \text{and } x_1 = 0 \quad \text{and } x_1 = l; \tag{1d}$$

where the overdot denotes differentiation with respect to the time  $t$ , and  $D_j$  and  $\vartheta_j$  are, respectively, the interface diffusion constant and viscosity for the interface between layer  $j$  and layer  $j + 1$ .

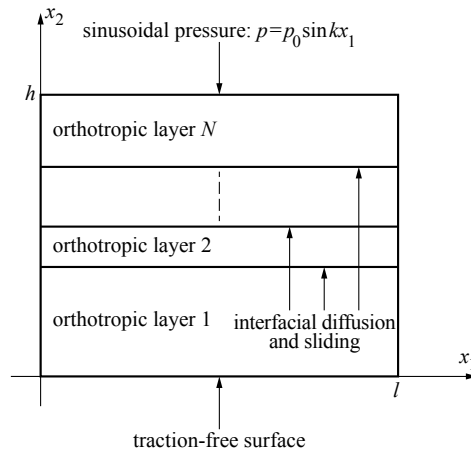


**Figure 1.** A multilayered orthotropic elastic strip with interfacial diffusion and rate-dependent sliding.

Let  $s_{ij}$  be the reduced elastic compliances in a certain layer. The general solution for displacements and stresses in this layer can be derived using the method proposed in [Suo 1990] as

$$\begin{bmatrix} \frac{u_1}{\cos kx_1} \\ \frac{u_2}{\sin kx_1} \end{bmatrix} = \frac{s_{11}\lambda^2}{k} \begin{bmatrix} (n+m)^2-\delta & (n-m)^2-\delta & (n+m)^2-\delta & (n-m)^2-\delta \\ \frac{\lambda}{n+m}-\delta\lambda(n+m) & \frac{\lambda}{n-m}-\delta\lambda(n-m) & \delta\lambda(n+m)-\frac{\lambda}{n+m} & \delta\lambda(n-m)-\frac{\lambda}{n-m} \end{bmatrix} \begin{bmatrix} C_1 e^{k\lambda(n+m)x_2} \\ C_2 e^{k\lambda(n-m)x_2} \\ C_3 e^{-k\lambda(n+m)x_2} \\ C_4 e^{-k\lambda(n-m)x_2} \end{bmatrix},$$

$$\begin{bmatrix} \frac{\sigma_{12}}{\cos kx_1} \\ \frac{\sigma_{22}}{\sin kx_1} \end{bmatrix} = \begin{bmatrix} \lambda(n+m) & \lambda(n-m) & -\lambda(n+m) & -\lambda(n-m) \\ 1 & 1 & 1 & 1 \end{bmatrix} \begin{bmatrix} C_1 e^{k\lambda(n+m)x_2} \\ C_2 e^{k\lambda(n-m)x_2} \\ C_3 e^{-k\lambda(n+m)x_2} \\ C_4 e^{-k\lambda(n-m)x_2} \end{bmatrix}, \tag{2}$$

where  $C_1, C_2, C_3, C_4$  are coefficients to be determined, and  $\lambda, \rho, \delta, n, m$  are dimensionless parameters defined by

$$\lambda = \left(\frac{s_{22}}{s_{11}}\right)^{1/4}, \quad \rho = \frac{2s_{12} + s_{66}}{2\sqrt{s_{11}s_{22}}} (\rho > -1), \quad \delta = \frac{s_{12}}{\sqrt{s_{12}s_{22}}} \quad (-1 \leq \delta < \min\{\rho, 1\}),$$

$$n = [\frac{1}{2}(\rho + 1)]^{1/2}, \quad m = [\frac{1}{2}(\rho - 1)]^{1/2}.$$

The general solution in (2) is valid only for the nondegenerate case of  $\rho \neq 1$ . For the degenerate case  $\rho = 1$  [Suo 1990], the displacements and stresses can be derived as

$$u_1 = [e^{kx_2^\lambda} (C_1 + x_2^\lambda C_2) + e^{-kx_2^\lambda} (C_3 + x_2^\lambda C_4)] \cos kx_1,$$

$$u_2 = \lambda \left\{ e^{kx_2^\lambda} \left[ C_1 + \left( x_2^\lambda - \frac{3-4\tilde{v}}{k} \right) C_2 \right] - e^{-kx_2^\lambda} \left[ C_3 + \left( x_2^\lambda + \frac{3-4\tilde{v}}{k} \right) C_4 \right] \right\} \sin kx_1, \tag{4}$$

$$\sigma_{12} = 2\lambda\tilde{\mu} \left\{ e^{kx_2^\lambda} [kC_1 + (kx_2^\lambda - 1 + 2\tilde{v})C_2] - e^{-kx_2^\lambda} [kC_3 + (kx_2^\lambda + 1 - 2\tilde{v})C_4] \right\} \cos kx_1,$$

$$\sigma_{22} = 2\tilde{\mu} \left\{ e^{kx_2^\lambda} [kC_1 + (kx_2^\lambda - 2 + 2\tilde{v})C_2] + e^{-kx_2^\lambda} [kC_3 + (kx_2^\lambda + 2 - 2\tilde{v})C_4] \right\} \sin kx_1, \tag{5}$$

where  $x_2^\lambda = \lambda x_2$ ;  $C_1, C_2, C_3, C_4$  are coefficients to be determined and

$$\tilde{\mu} = \frac{1}{s_{66}} = \frac{1}{2(\sqrt{s_{11}s_{22}} - s_{12})} = \frac{\lambda^2}{2s_{22}(1 - \delta)},$$

$$\tilde{v} = 1 - \frac{\sqrt{s_{11}s_{22}}}{\sqrt{s_{11}s_{22}} - s_{12}} = 1 - \frac{2\sqrt{s_{11}s_{22}}}{s_{66}} = \frac{\delta}{\delta - 1} \leq \frac{1}{2}.$$

**Remark.** Note that  $\rho = 1$  is degenerate in the sense that we have  $k\lambda(n + m) = k\lambda(n - m) = k\lambda$  and  $-k\lambda(n + m) = -k\lambda(n - m) = -k\lambda$  in (2).

When  $\rho = \lambda = 1$  for a transversely isotropic layer [Suo 1990], with isotropy being a special case, (4) and (5) simply reduce to those in [He and Jiang 2003]. It is interesting to note that the general solutions (2), (4) and (5) can be adapted to study the surface instability of orthotropic films due to surface van der



Waals forces [Wang and Li 2017]. From (2), (4) and (5) it follows that the displacements and tractions on the lower interface of layer  $j$  can be expressed in terms of those on its upper interface as

$$\begin{bmatrix} \tilde{\mathbf{u}}_0^{(j)} \\ \tilde{\boldsymbol{\sigma}}_0^{(j)} \end{bmatrix} = \mathbf{Q}(K_j, \delta_j, \rho_j) \begin{bmatrix} \tilde{\mathbf{u}}_1^{(j)} \\ \tilde{\boldsymbol{\sigma}}_1^{(j)} \end{bmatrix}, \quad (7)$$

where the subscripts 0 and 1 denote, respectively, the values on the lower and upper interfaces of layer  $j$ ,

$$\tilde{\mathbf{u}}^{(j)} = [u_1^{(j)} \ u_2^{(j)}/\lambda_j]^T, \quad \tilde{\boldsymbol{\sigma}}^{(j)} = [\lambda_j s_{11}^{(j)} \sigma_{12}^{(j)}/k \ \lambda_j^2 s_{11}^{(j)} \sigma_{22}^{(j)}/k]^T, \quad K_j = kh_j \lambda_j; \quad (8)$$

$$\begin{aligned} \mathbf{Q}(K, \delta, \rho) = & \frac{\cosh[K(n+m)]}{4nm} \\ & \times \begin{bmatrix} (n+m)^2 - \delta & 0 & 0 & [\delta(n-m)^2 - 1][1 - \delta(n+m)^2] \\ 0 & \delta - (n-m)^2 & [1 - \delta(n-m)^2][1 - \delta(n+m)^2] & 0 \\ 0 & -1 & (n+m)^2 - \delta & 0 \\ 1 & 0 & 0 & \delta - (n-m)^2 \end{bmatrix} \\ & + \frac{\cosh[K(n-m)]}{4nm} \\ & \times \begin{bmatrix} \delta - (n-m)^2 & 0 & 0 & [1 - \delta(n-m)^2][1 - \delta(n+m)^2] \\ 0 & (n+m)^2 - \delta & [\delta(n-m)^2 - 1][1 - \delta(n+m)^2] & 0 \\ 0 & 1 & \delta - (n-m)^2 & 0 \\ -1 & 0 & 0 & (n+m)^2 - \delta \end{bmatrix} \\ & + \frac{\sinh[K(n+m)]}{4nm(n+m)} \begin{bmatrix} 0 & (n+m)^2 - \delta & -[(n+m)^2 - \delta]^2 & 0 \\ \delta(n+m)^2 - 1 & 0 & 0 & [n-m - \delta(n+m)]^2 \\ -(n+m)^2 & 0 & 0 & 1 - \delta(n+m)^2 \\ 0 & 1 & \delta - (n+m)^2 & 0 \end{bmatrix} \\ & + \frac{\sinh[K(n-m)]}{4nm(n+m)} \begin{bmatrix} 0 & \delta(n+m)^2 - 1 & [n-m - \delta(n+m)]^2 & 0 \\ (n+m)^2 - \delta & 0 & 0 & -[(n+m)^2 - \delta]^2 \\ 1 & 0 & 0 & \delta - (n+m)^2 \\ 0 & -(n+m)^2 & 1 - \delta(n+m)^2 & 0 \end{bmatrix} \end{aligned}$$

for  $\rho \neq 1$ ; (9a)

and

$$\begin{aligned} \mathbf{Q}(K, \delta, \rho) = & \cosh(K) \left[ \mathbf{I} + \frac{K}{2} \begin{bmatrix} 0 & 1/(1-\tilde{\nu}) & -1/(1-\tilde{\nu})^2 & 0 \\ -1/(1-\tilde{\nu}) & 0 & 0 & 1/(1-\tilde{\nu})^2 \\ -1 & 0 & 0 & 1/(1-\tilde{\nu}) \\ 0 & 1 & -1/(1-\tilde{\nu}) & 0 \end{bmatrix} \right] \\ & + \frac{\sinh(K)}{2} \begin{bmatrix} K/(1-\tilde{\nu}) & (1-2\tilde{\nu})/(1-\tilde{\nu}) & -(3-4\tilde{\nu})/(1-\tilde{\nu})^2 & -K/(1-\tilde{\nu})^2 \\ (1-2\tilde{\nu})/(1-\tilde{\nu}) & -K/(1-\tilde{\nu}) & K/(1-\tilde{\nu})^2 & -(3-4\tilde{\nu})/(1-\tilde{\nu})^2 \\ -1 & -K & K/(1-\tilde{\nu}) & -(1-2\tilde{\nu})/(1-\tilde{\nu}) \\ K & -1 & -(1-2\tilde{\nu})/(1-\tilde{\nu}) & -K/(1-\tilde{\nu}) \end{bmatrix} \end{aligned}$$

for  $\rho = 1$ . (9b)

In writing (8), the factors  $\cos kx_1$  and  $\sin kx_1$  in the displacements and stresses have been excluded. Here  $\mathbf{Q}(K, \delta, \rho)$  is a  $4 \times 4$  transfer matrix. For convenience in the subsequent analysis, the transfer matrix is written in the following partitioned form

$$\mathbf{Q}(K_j, \delta_j, \rho_j) = \begin{bmatrix} \mathbf{Q}_1^{(j)} & \mathbf{Q}_2^{(j)} \\ \mathbf{Q}_3^{(j)} & \mathbf{Q}_4^{(j)} \end{bmatrix}, \tag{10}$$

where  $\mathbf{Q}_1^{(j)}$ ,  $\mathbf{Q}_2^{(j)}$ ,  $\mathbf{Q}_3^{(j)}$  and  $\mathbf{Q}_4^{(j)}$  are four  $2 \times 2$  submatrices.

It follows from (7) that the displacements on the two interfaces of layer  $j$  can be expressed in terms of the tractions on the two interfaces of the layer as follows:

$$\begin{aligned} \tilde{\mathbf{u}}_1^{(j)} &= [\mathbf{Q}_3^{(j)}]^{-1} \tilde{\boldsymbol{\sigma}}_0^{(j)} - [\mathbf{Q}_3^{(j)}]^{-1} \mathbf{Q}_4^{(j)} \tilde{\boldsymbol{\sigma}}_1^{(j)}, \\ \tilde{\mathbf{u}}_0^{(j)} &= \mathbf{Q}_1^{(j)} [\mathbf{Q}_3^{(j)}]^{-1} \tilde{\boldsymbol{\sigma}}_0^{(j)} + [\mathbf{Q}_2^{(j)} - \mathbf{Q}_1^{(j)} [\mathbf{Q}_3^{(j)}]^{-1} \mathbf{Q}_4^{(j)}] \tilde{\boldsymbol{\sigma}}_1^{(j)}. \end{aligned} \tag{11}$$

In view of the fact the tractions are *continuous* across all of the interfaces, we have from the above that

$$\tilde{\mathbf{u}}_1^{(j)} = \frac{1}{\alpha_{j-1} \beta_{j-1}} [\mathbf{Q}_3^{(j)}]^{-1} \mathbf{L}_{j-1} \tilde{\boldsymbol{\sigma}}_1^{(j-1)} - [\mathbf{Q}_3^{(j)}]^{-1} \mathbf{Q}_4^{(j)} \tilde{\boldsymbol{\sigma}}_1^{(j)}, \tag{12a}$$

$$\tilde{\mathbf{u}}_0^{(j+1)} = \frac{1}{\alpha_j \beta_j} \mathbf{Q}_1^{(j+1)} [\mathbf{Q}_3^{(j+1)}]^{-1} \mathbf{L}_j \tilde{\boldsymbol{\sigma}}_1^{(j)} + [\mathbf{Q}_2^{(j+1)} - \mathbf{Q}_1^{(j+1)} [\mathbf{Q}_3^{(j+1)}]^{-1} \mathbf{Q}_4^{(j+1)}] \tilde{\boldsymbol{\sigma}}_1^{(j+1)}, \tag{12b}$$

where

$$\alpha_j = \frac{\lambda_{j+1}}{\lambda_j}, \quad \beta_j = \sqrt{\frac{s_{11}^{(j)} s_{22}^{(j)}}{s_{11}^{(j+1)} s_{22}^{(j+1)}}}, \quad \mathbf{L}_j = \begin{bmatrix} 1 & 0 \\ 0 & \alpha_j \end{bmatrix}. \tag{13}$$

The interfacial diffusion and sliding conditions on the interface between layer  $j$  and layer  $j + 1$  in (1c) can be equivalently expressed as

$$\mathbf{L}_j \dot{\tilde{\mathbf{u}}}_0^{(j+1)} - \dot{\tilde{\mathbf{u}}}_1^{(j)} = \boldsymbol{\Lambda}_j \tilde{\boldsymbol{\sigma}}_1^{(j)}, \quad j = 1, 2, \dots, N - 1, \tag{14}$$

where

$$\boldsymbol{\Lambda}_j = \begin{bmatrix} \frac{k}{\lambda_j s_{11}^{(j)} \vartheta_j} & 0 \\ 0 & \frac{k^3 D_j}{\lambda_j^3 s_{11}^{(j)}} \end{bmatrix}. \tag{15}$$

Substituting (12) into (14), we arrive at

$$\mathbf{R}_1^{(j)} \dot{\tilde{\boldsymbol{\sigma}}}_1^{(j-1)} + \mathbf{R}_2^{(j)} \dot{\tilde{\boldsymbol{\sigma}}}_1^{(j)} + \mathbf{R}_3^{(j)} \dot{\tilde{\boldsymbol{\sigma}}}_1^{(j+1)} = \boldsymbol{\Lambda}_j \tilde{\boldsymbol{\sigma}}_1^{(j)}, \quad j = 1, 2, \dots, N - 1, \tag{16}$$

where

$$\begin{aligned} \mathbf{R}_1^{(j)} &= -\frac{1}{\alpha_{j-1} \beta_{j-1}} [\mathbf{Q}_3^{(j)}]^{-1} \mathbf{L}_{j-1}, \\ \mathbf{R}_2^{(j)} &= [\mathbf{Q}_3^{(j)}]^{-1} \mathbf{Q}_4^{(j)} + \frac{1}{\alpha_j \beta_j} \mathbf{L}_j \mathbf{Q}_1^{(j+1)} [\mathbf{Q}_3^{(j+1)}]^{-1} \mathbf{L}_j, \\ \mathbf{R}_3^{(j)} &= \mathbf{L}_j [\mathbf{Q}_2^{(j+1)} - \mathbf{Q}_1^{(j+1)} [\mathbf{Q}_3^{(j+1)}]^{-1} \mathbf{Q}_4^{(j+1)}]. \end{aligned} \tag{17}$$

By considering the fact that the pressure prescribed on the top surface of the multilayered strip is static and that the bottom surface of the strip is traction-free (i.e.,  $\dot{\tilde{\sigma}}_1^{(0)} = \dot{\tilde{\sigma}}_0^{(1)} = \dot{\tilde{\sigma}}_1^{(N)} = 0$ ), (16) can be recast into the following standard homogeneous state-space equation:

$$A\dot{\xi} = B\xi, \tag{18}$$

where

$$\xi = \begin{bmatrix} \tilde{\sigma}_1^{(1)} \\ \tilde{\sigma}_1^{(2)} \\ \vdots \\ \tilde{\sigma}_1^{(N-1)} \end{bmatrix}, \tag{19}$$

$$A = \begin{bmatrix} R_2^{(1)} & R_3^{(1)} & \mathbf{0} & \mathbf{0} & \cdots & \mathbf{0} \\ R_1^{(2)} & R_2^{(2)} & R_3^{(2)} & \mathbf{0} & \cdots & \mathbf{0} \\ \vdots & \vdots & \vdots & \vdots & \ddots & \vdots \\ \mathbf{0} & \cdots & \mathbf{0} & R_1^{(N-2)} & R_2^{(N-2)} & R_3^{(N-2)} \\ \mathbf{0} & \cdots & \mathbf{0} & \mathbf{0} & R_1^{(N-1)} & R_2^{(N-1)} \end{bmatrix}, \tag{20}$$

$$B = \text{diag}[\Lambda_1 \ \Lambda_2 \ \cdots \ \Lambda_{N-1}]. \tag{21}$$

It is observed that

- (i) the state vector  $\xi$  is composed of the  $2(N - 1)$  traction components on all of the existing  $N - 1$  interfaces;
- (ii) the dimensionless matrix  $A$  can be completely determined by the following dimensionless parameters of the  $N$  layers:  $\delta_j, \rho_j, K_j$  ( $j = 1, 2, \dots, N$ ) and  $\alpha_j, \beta_j$  ( $j = 1, 2, \dots, N - 1$ ); and
- (iii) the matrix  $B$  having the dimension of 1/time depends on the diffusion and sliding properties of the  $N - 1$  interfaces and is independent of the thicknesses of all the layers.

The general solution to the homogeneous state-space equation in (18) is simply given by

$$\xi(t) = \exp(A^{-1}Bt)\xi(0), \quad t \geq 0, \tag{22}$$

where  $\exp(A^{-1}Bt)$  is the state transition matrix, and the initial state  $\xi(0)$  can be simply determined by assuming that all of the interfaces are initially perfectly bonded. Indeed, by assuming that all of the interfaces are initially perfectly bonded, we can derive the relationship

$$\begin{bmatrix} \tilde{u}_0^{(1)} \\ \tilde{\sigma}_0^{(1)} \end{bmatrix} = \begin{bmatrix} M_{11} & M_{12} \\ M_{21} & M_{22} \end{bmatrix} \begin{bmatrix} \tilde{u}_1^{(N)} \\ \tilde{\sigma}_1^{(N)} \end{bmatrix} \quad \text{at } t = 0, \tag{23}$$

where the four  $2 \times 2$  sub-matrices  $M_{11}, M_{12}, M_{21}$  and  $M_{22}$  are given by

$$\begin{bmatrix} M_{11} & M_{12} \\ M_{21} & M_{22} \end{bmatrix} = Q(K_1, \delta_1, \rho_1) \times T(\alpha_1, \beta_1) \times Q(K_2, \delta_2, \rho_2) \times T(\alpha_2, \beta_2) \times \cdots \tag{24}$$

with

$$T(\alpha, \beta) = \text{diag}[1 \ \alpha \ \alpha\beta \ \beta]. \tag{25}$$

In view of the fact that  $\tilde{\sigma}_0^{(1)} = \mathbf{0}$  and  $\tilde{\sigma}_1^{(N)} = -(p_0\sqrt{s_{11}^{(N)}s_{22}^{(N)}}/k)[0 \ 1]^T$  at any time, we find from (23) that

$$\tilde{\mathbf{u}}_1^{(N)} = \frac{p_0\sqrt{s_{11}^{(N)}s_{22}^{(N)}}}{k} \mathbf{M}_{21}^{-1} \mathbf{M}_{22} \begin{bmatrix} 0 \\ 1 \end{bmatrix} \quad \text{at } t = 0. \tag{26}$$

Consequently, the initial displacements and tractions on the upper interface of layer  $j$  at can be arrived at by using the recursion relation

$$\begin{bmatrix} \tilde{\mathbf{u}}_1^{(j)} \\ \tilde{\sigma}_1^{(j)} \end{bmatrix} = \mathbf{T}(\alpha_j, \beta_j) \times \mathbf{Q}(K_{j+1}, \delta_{j+1}, \rho_{j+1}) \begin{bmatrix} \tilde{\mathbf{u}}_1^{(j+1)} \\ \tilde{\sigma}_1^{(j+1)} \end{bmatrix}, \quad j = N - 1, N - 2, \dots, 1 \quad \text{at } t = 0. \tag{27}$$

The initial state  $\xi(0)$  can then be extracted from the above expression. It is seen from (22) that as time  $t$  approaches infinity, all of the interfacial tractions will be relaxed to zero. The evolution of the displacements on the upper interfaces of the  $N$  layers can then be obtained from (12a). Consequently, the field variables at any position within layer  $j$  and at any time can be determined from (7) with  $h_j$  reinterpreted as the distance to the upper interface of layer  $j$ . In addition, the relaxation times of the multilayered strip can be obtained by solving the following generalized eigenvalue problem:

$$(\mathbf{A} + \eta\mathbf{B})\mathbf{v} = \mathbf{0}, \tag{28}$$

where  $\eta$  is the eigenvalue and  $\mathbf{v}$  the associated eigenvector. Equation (28) follows immediately from (18) by assuming the solution to be of the form  $\xi = \mathbf{v}e^{-t/\eta}$ . The  $2(N - 1)$  positive real eigenvalues  $\eta_1, \eta_2, \dots, \eta_{2(N-1)}$  are just the  $2(N - 1)$  relaxation times of the laminated plate.

### 3. Illustrative examples and discussion

In this section, we demonstrate the exact solution derived in the previous section via

- (i) a bilayered strip,
- (ii) a trilayered strip, and
- (iii) a 1001-layered strip.

Remember that the factors  $\cos kx_1$  and  $\sin kx_1$  have been excluded in the illustrations of displacements and stresses.

**3.1. A bilayered strip.** We first consider a bilayered orthotropic strip. For a bilayered strip with  $N = 2$ , both  $\mathbf{A}$  and  $\mathbf{B}$  are  $2 \times 2$  matrices and are given by

$$\begin{aligned} \mathbf{A} &= \mathbf{R}_2^{(1)}[\mathbf{Q}_3^{(1)}]^{-1} \mathbf{Q}_4^{(1)} + \frac{1}{\alpha_1\beta_1} \mathbf{L}_1 \mathbf{Q}_1^{(2)}[\mathbf{Q}_3^{(2)}]^{-1} \mathbf{L}_1, \\ \mathbf{B} &= \mathbf{\Lambda}_1. \end{aligned} \tag{29}$$

In this case, analytical expressions of the two relaxation times of the bilayered strip are given by

$$\eta_{1,2} = -(A_{11}\chi + A_{22}\gamma) \pm \sqrt{(A_{11}\chi - A_{22}\gamma)^2 + 4A_{12}A_{21}\chi\gamma} > 0, \tag{30}$$

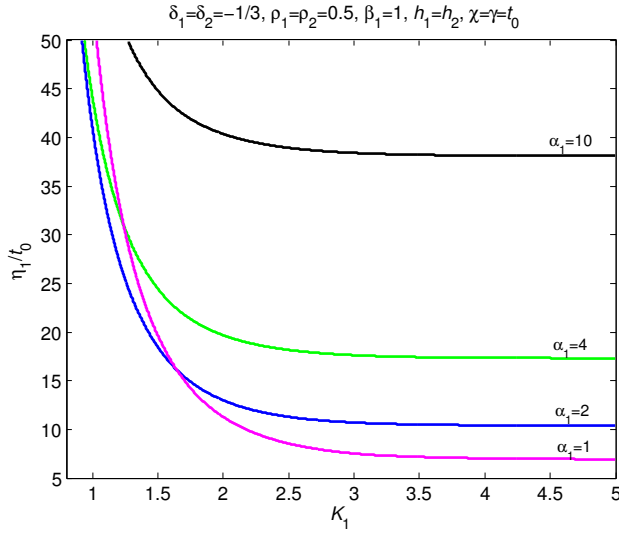


**Figure 2.** The larger relaxation time  $\eta_1$  of a bilayered strip as a function of  $K_1$  for different values of  $\alpha_1$  with  $\delta_1 = \delta_2 = -\frac{1}{3}, \rho_1 = \rho_2 = 0.5, \beta_1 = 1, h_1 = h_2, \chi = \gamma = t_0$ .

where

$$\chi = \frac{\lambda_1 s_{11}^{(1)} \vartheta_1}{2k}, \quad \gamma = \frac{\lambda_1^3 s_{11}^{(1)}}{2k^3 D_1}. \tag{31}$$

We illustrate in Figures 2 and 3 the two relaxation times  $\eta_1$  and  $\eta_2$  as functions of  $K_1$  for different values of  $\alpha_1$  with  $\delta_1 = \delta_2 = -\frac{1}{3}, \rho_1 = \rho_2 = 0.5, \beta_1 = 1, h_1 = h_2, \chi = \gamma = t_0$ . The elastic constants for layer 2 are obtained after an in-plane coordinate rotation of the angle  $\pi/2$  for layer 1. It is seen from

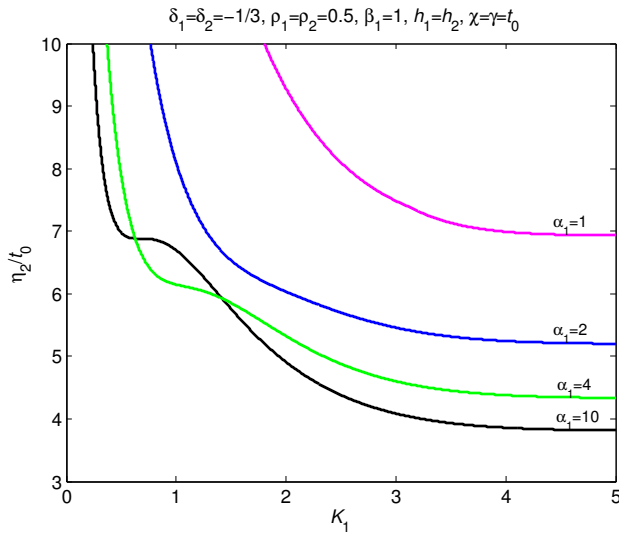


**Figure 3.** The smaller relaxation time  $\eta_2$  of a bilayered strip as a function of  $K_1$  for different values of  $\alpha_1$  with  $\delta_1 = \delta_2 = -\frac{1}{3}, \rho_1 = \rho_2 = 0.5, \beta_1 = 1, h_1 = h_2, \chi = \gamma = t_0$ .

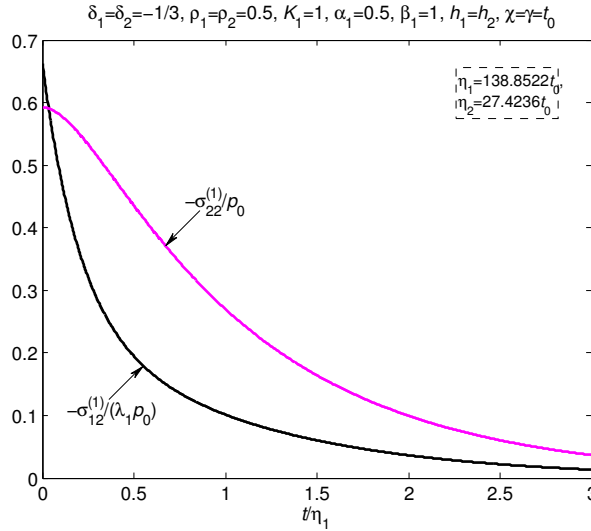


**Figure 4.** The evolution of the normal and shear tractions on the interface with  $\delta_1 = \delta_2 = -\frac{1}{3}$ ,  $\rho_1 = \rho_2 = 0.5$ ,  $K_1 = 1$ ,  $\alpha_1 = 0.5$ ,  $\beta_1 = 1$ ,  $h_1 = h_2$ ,  $\chi = \gamma = t_0$ .

the two figures that as the thickness of the strip increases (or equivalently  $K_1$  increases), the relaxation times decrease. **Figure 4** shows the evolution of the normal and shear tractions on the interface with  $\delta_1 = \delta_2 = -\frac{1}{3}$ ,  $\rho_1 = \rho_2 = 0.5$ ,  $K_1 = 1$ ,  $\alpha_1 = 0.5$ ,  $\beta_1 = 1$ ,  $h_1 = h_2$ ,  $\chi = \gamma = t_0$ . It is observed from **Figure 4** that

- (i) the shear traction decays faster than the normal traction;
- (ii) the interfacial tractions evolve on the time scale of the larger relaxation time  $\eta_1 = 138.8522t_0$  and their magnitudes are minimal when  $t > 3\eta_1$ .

When  $h_1, h_2 \rightarrow \infty$ , the two relaxation times of a bilayered strip are given explicitly by

$$\eta_{1,2} = 2\chi(n_1 + \alpha_1^{-1}\beta_1^{-1}n_2) + 2\gamma(n_1 + \alpha_1\beta_1^{-1}n_2) \pm 2\sqrt{[\chi(n_1 + \alpha_1^{-1}\beta_1^{-1}n_2) - \gamma(n_1 + \alpha_1\beta_1^{-1}n_2)]^2 + \chi\gamma[1 + \delta_1 - \beta_1^{-1}(1 + \delta_2)]^2}, \quad (32)$$

where  $\chi$  and  $\gamma$  have been defined by (31). The above analytical result is derived using analytic continuation and the positive definite Hermitian matrix for an orthotropic material in [Suo 1990, (9.6)]. If the two half-planes of the bimaterial are elastically isotropic, we have

$$\alpha_1 = \lambda_1 = \lambda_2 = n_1 = n_2 = 1, \quad \beta_1 = \frac{\mu_2(1 - \nu_1)}{\mu_1(1 - \nu_2)}; \quad s_{11}^{(j)} = \frac{1 - \nu_j}{2\mu_j}, \quad \delta_j = \frac{\nu_j}{\nu_j - 1}, \quad j = 1, 2, \quad (33)$$

where  $\mu$  and  $\nu$  are the shear modulus and Poisson’s ratio. In this case, (32) simply reduces to [Wang and Wang 2016, (38)].

Furthermore, we note that the relaxation times in Figures 2 and 3 for  $K_1 = 5$  are very close to the result in (32).

**3.2. A trilayered strip.** Next we consider a trilayered orthotropic strip. For a trilayered strip with  $N = 3$ , both  $\mathbf{A}$  and  $\mathbf{B}$  are  $4 \times 4$  matrices and are given by

$$\mathbf{A} = \begin{bmatrix} \mathbf{R}_2^{(1)} & \mathbf{R}_3^{(1)} \\ \mathbf{R}_1^{(2)} & \mathbf{R}_2^{(2)} \end{bmatrix}, \quad \mathbf{B} = \text{diag}[\Lambda_1 \ \Lambda_2]. \quad (34)$$

It is convenient to numerically determine the four relaxation times in the trilayered strip. For example, if the parameters of the trilayered strip are chosen as

$$\begin{aligned} \delta_1 = \delta_2 = \delta_3 = -\frac{1}{3}, \quad \rho_1 = \rho_2 = \rho_3 = 0.5, \quad h_1 = h_2 = h_3, \quad K_1 = 1, \\ \alpha_1 = \frac{1}{\alpha_2} = 0.5, \quad \beta_1 = \beta_2 = 1, \quad \vartheta_1 = \vartheta_2, \quad D_1 = D_2, \quad \chi = \gamma = t_0, \end{aligned} \quad (35)$$

where  $\chi$  and  $\gamma$  have been defined by (31); the four relaxation times of the trilayered strip are determined as

$$\eta_1 = 258.9914t_0, \quad \eta_2 = 38.3432t_0, \quad \eta_3 = 21.5497t_0, \quad \eta_4 = 13.6673t_0. \quad (36)$$

In this example, the top and bottom layers have identical elastic constants, whilst the elastic constants for the middle layer are obtained after an in-plane coordinate rotation of the angle  $\pi/2$  for the top or bottom layer. We illustrate in Figure 5 the evolution of the normal and shear tractions on the two interfaces. It is observed from Figure 5 that

- (1) the tractions on the lower interface and the shear stress on the upper interface will eventually change sign with time whilst the normal traction on the upper interface will always maintain its sign;
- (2) on each interface, the shear traction decays faster than the normal traction;
- (3) at any instant, the magnitude of the normal traction on the upper interface is always higher than that on the lower interface.

**3.3. A 1001-layered strip.** Finally, we consider a strip composed of 1001 identical orthotropic layers of equal thickness. The diffusional and sliding properties on all of the interfaces are identical (i.e.,  $\vartheta_1 = \vartheta_2 = \dots = \vartheta_{1000}$  and  $D_1 = D_2 = \dots = D_{1000}$ ). Our results indicate that the relaxation times are independent of the specific value of  $\delta$ . We further set  $K_1 = 1$  and  $\chi = \gamma = t_0$ , where  $\chi$  and  $\gamma$  have been defined by (31). The variation of all the  $2(N - 1) = 2000$  relaxation times  $\eta_j$  as a decreasing function of  $j$  for different values of  $\rho$  is illustrated in Figure 6. It is observed from Figure 6 that

- (i) the relaxation times are increasing functions of  $\rho$ , which implies that a decrement in  $\rho$  will expedite the relaxation process;
- (ii) the curve for  $\rho \rightarrow -1$  forms the lower bound of the relaxation times;
- (iii) there is a large jump between  $\eta_{1001}$  and  $\eta_{1002}$ , there is a small jump between  $\eta_{999}$  and  $\eta_{1000}$ .

## 4. Conclusions

Based on the rigorous theory of elasticity, we derive an exact solution to the plane strain problem associated with a multilayered orthotropic elastic strip with simultaneous interfacial diffusion and rate-dependent sliding. By using the transfer matrix method and by enforcing the diffusion and sliding

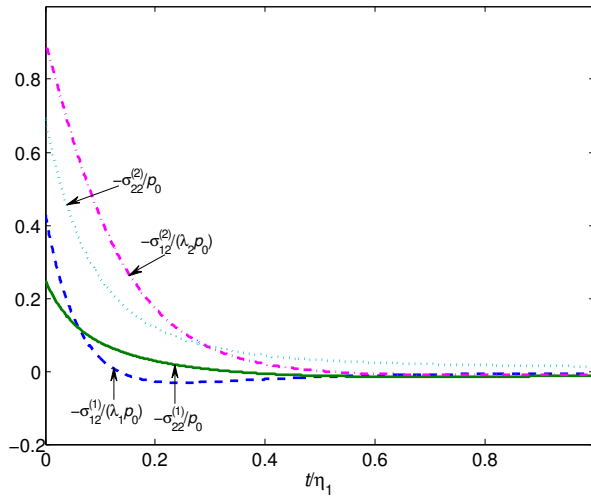


**Figure 5.** The evolution of the normal and shear tractions on the two interfaces in the trilayered strip described by (35).

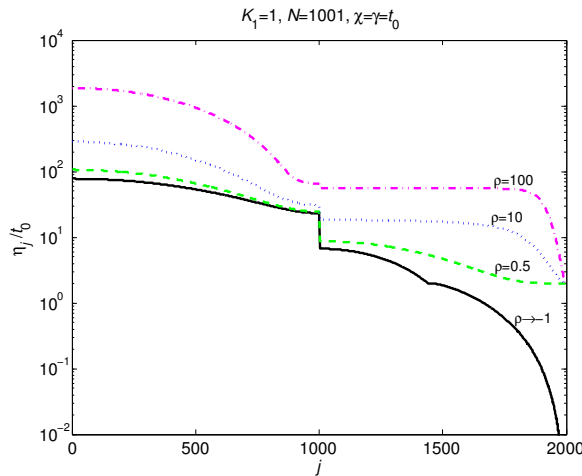


**Figure 6.** Variation of all the 2000 relaxation times  $\eta_j$  as a decreasing function of  $j$  for different values of the anisotropic parameter  $\rho$  with  $K_1 = 1$  and  $\chi = \gamma = t_0$  in a 1001-layered orthotropic strip.

conditions on all of the existing interfaces, we obtain a homogeneous state-space equation with state variables identified as the traction components on the interfaces. Once the initial values of the interfacial tractions are known by assuming that initially all interfaces are perfectly bonded, the evolution of the state variables can be uniquely determined. It is seen that the transfer matrix  $\mathbf{Q}(K, \delta, \rho)$  and the state transition matrix  $\exp(\mathbf{A}^{-1} \mathbf{B}t)$  are the key components of our solution. Using Matlab, numerical results for relaxation times and evolution of interfacial tractions for bilayered, trilayered and 1001-layered orthotropic strips are presented to demonstrate the exact solution. The solution strategy adopted in this



research can also be employed to study the case in which the orthotropic elastic coefficients of each layer vary continuously along the thickness direction.

### Acknowledgements

This work is supported by the National Natural Science Foundation of China (Grant No. 11272121) and through a Discovery Grant from the Natural Sciences and Engineering Research Council of Canada (RGPIN 2017-03716115112).

### References

- [Chen and Lee 2004] W. Q. Chen and K. Y. Lee, “Time-dependent behaviors of angle-ply laminates with viscous interfaces in cylindrical bending”, *Eur. J. Mech. A Solids* **23**:2 (2004), 235–245.
- [He and Hu 2003] L. H. He and X. F. Hu, “Transient stress relaxation around a spherical inclusion: the role of the combination of interfacial diffusion and sliding”, *Mater. Chem. Phys.* **77**:1 (2003), 147–152.
- [He and Jiang 2003] L. H. He and J. Jiang, “Transient mechanical response of laminated elastic strips with viscous interfaces in cylindrical bending”, *Compos. Sci. Technol.* **63**:6 (2003), 821–828.
- [Kim and McMeeking 1995] K. T. Kim and R. M. McMeeking, “Power law creep with interface slip and diffusion in a composite material”, *Mech. Mater.* **20**:2 (1995), 153–164.
- [Mori et al. 1997] T. Mori, J. H. Huang, and M. Taya, “Stress relaxation by plastic flow, interfacial sliding and diffusion in an inclusion bearing material”, *Acta Mater.* **45**:2 (1997), 429–438.
- [Onaka et al. 1998] S. Onaka, J. H. Huang, K. Wakashima, and T. Mori, “Kinetics of stress relaxation caused by the combination of interfacial sliding and diffusion: two-dimensional analysis”, *Acta Mater.* **46**:11 (1998), 3821–3828.
- [Onaka et al. 1999] S. Onaka, J. H. Huang, K. Wakashima, and T. Mori, “Stress relaxation caused by the combination of interfacial sliding and diffusion around spherical inclusions”, *Mech. Mater.* **31**:11 (1999), 717–727.
- [Sofronis and McMeeking 1994] P. Sofronis and R. M. McMeeking, “The effect of interface diffusion and slip on the creep resistance of particulate composite materials”, *Mech. Mater.* **18**:1 (1994), 55–68.
- [Suo 1990] Z. Suo, “Singularities, interfaces and cracks in dissimilar anisotropic media”, *Proc. R. Soc. Lond. A* **427**:1873 (1990), 331–358.
- [Wang and Li 2017] X. Wang and S. Li, “Surface instability of orthotropic films under surface van der Waals forces”, *Z. Angew. Math. Phys.* **68**:4 (2017), art. id. 85.
- [Wang and Pan 2010] X. Wang and E. Pan, “A circular inhomogeneity with interface slip and diffusion under in-plane deformation”, *Int. J. Eng. Sci.* **48**:12 (2010), 1733–1748.
- [Wang and Wang 2016] X. Wang and C. Wang, “Transient response of bilayered elastic strips with interfacial diffusion and sliding in cylindrical bending”, *Math. Mech. Solids* (online publication February 2016).
- [Wang et al. 2016] X. Wang, C. Wang, and P. Schiavone, “In-plane deformations of a nano-sized circular inhomogeneity with interface slip and diffusion”, *Int. J. Eng. Sci.* **108** (2016), 9–15.
- [Wei et al. 2008] Y. Wei, A. F. Bower, and H. Gao, “Recoverable creep deformation and transient local stress concentration due to heterogeneous grain-boundary diffusion and sliding in polycrystalline solids”, *J. Mech. Phys. Solids* **56**:4 (2008), 1460–1483.

Received 30 May 2017. Revised 27 Jul 2017. Accepted 5 Aug 2017.

XU WANG: [xuwang@ecust.edu.cn](mailto:xuwang@ecust.edu.cn)

School of Mechanical and Power Engineering, East China University of Science and Technology, Shanghai, China

PETER SCHIAVONE: [pschiavo@ualberta.ca](mailto:pschiavo@ualberta.ca)

Department of Mechanical Engineering, University of Alberta, Edmonton AB, Canada

# SUBMISSION GUIDELINES

## ORIGINALITY

Authors may submit manuscripts in PDF format online at the Submissions page. Submission of a manuscript acknowledges that the manuscript is original and has neither previously, nor simultaneously, in whole or in part, been submitted elsewhere. Information regarding the preparation of manuscripts is provided below. Correspondence by email is requested for convenience and speed. For further information, write to [contact@msp.org](mailto:contact@msp.org).

## LANGUAGE

Manuscripts must be in English. A brief abstract of about 150 words or less must be included. The abstract should be self-contained and not make any reference to the bibliography. Also required are keywords and subject classification for the article, and, for each author, postal address, affiliation (if appropriate), and email address if available. A home-page URL is optional.

## FORMAT

Authors can use their preferred manuscript-preparation software, including for example Microsoft Word or any variant of  $\text{T}_{\text{E}}\text{X}$ . The journal itself is produced in  $\text{L}^{\text{A}}\text{T}_{\text{E}}\text{X}$ , so accepted articles prepared using other software will be converted to  $\text{L}^{\text{A}}\text{T}_{\text{E}}\text{X}$  at production time. Authors wishing to prepare their document in  $\text{L}^{\text{A}}\text{T}_{\text{E}}\text{X}$  can follow the example file at [www.jomms.net](http://www.jomms.net) (but the use of other class files is acceptable). At submission time only a PDF file is required. After acceptance, authors must submit all source material (see especially Figures below).

## REFERENCES

Bibliographical references should be complete, including article titles and page ranges. All references in the bibliography should be cited in the text. The use of  $\text{BibT}_{\text{E}}\text{X}$  is preferred but not required. Tags will be converted to the house format (see a current issue for examples); however, for submission you may use the format of your choice. Links will be provided to all literature with known web locations; authors can supply their own links in addition to those provided by the editorial process.

## FIGURES

Figures must be of publication quality. After acceptance, you will need to submit the original source files in vector format for all diagrams and graphs in your manuscript: vector EPS or vector PDF files are the most useful. (EPS stands for Encapsulated PostScript.)

Most drawing and graphing packages—Mathematica, Adobe Illustrator, Corel Draw, MATLAB, etc.—allow the user to save files in one of these formats. Make sure that what you’re saving is vector graphics and not a bitmap. If you need help, please write to [graphics@msp.org](mailto:graphics@msp.org) with as many details as you can about how your graphics were generated.

Please also include the original data for any plots. This is particularly important if you are unable to save Excel-generated plots in vector format. Saving them as bitmaps is not useful; please send the Excel (.xls) spreadsheets instead. Bundle your figure files into a single archive (using zip, tar, rar or other format of your choice) and upload on the link you been given at acceptance time.

Each figure should be captioned and numbered so that it can float. Small figures occupying no more than three lines of vertical space can be kept in the text (“the curve looks like this:”). It is acceptable to submit a manuscript with all figures at the end, if their placement is specified in the text by means of comments such as “Place Figure 1 here”. The same considerations apply to tables.

## WHITE SPACE

Forced line breaks or page breaks should not be inserted in the document. There is no point in your trying to optimize line and page breaks in the original manuscript. The manuscript will be reformatted to use the journal’s preferred fonts and layout.

## PROOFS

Page proofs will be made available to authors (or to the designated corresponding author) at a Web site in PDF format. Failure to acknowledge the receipt of proofs or to return corrections within the requested deadline may cause publication to be postponed.

- Nonlinear impacting oscillations of pipe conveying pulsating fluid subjected to distributed motion constraints**  
WANG YIKUN, NI QIAO, WANG LIN, LUO YANGYANG and YAN HAO 563
- Micro and macro crack sensing in TRC beam under cyclic loading** YISKA GOLDFELD, TILL QUADFLIEG, STAV BEN-AAROSH and THOMAS GRIES 579
- Static analysis of nanobeams using Rayleigh–Ritz method**  
LAXMI BEHERA and S. CHAKRAVERTY 603
- Analysis of pedestrian-induced lateral vibration of a footbridge that considers feedback adjustment and time delay**  
JIA BUYU, CHEN ZHOU, YU XIAOLIN and YAN QUANSHENG 617
- Nearly exact and highly efficient elastic-plastic homogenization and/or direct numerical simulation of low-mass metallic systems with architected cellular microstructures** MARYAM TABATABAEI, DY LE and SATYA N. ATLURI 633
- Transient analysis of fracture initiation in a coupled thermoelastic solid**  
LOUIS M. BROCK 667
- Geometrically nonlinear Cosserat elasticity in the plane: applications to chirality**  
SEBASTIAN BAHAMONDE, CHRISTIAN G. BÖHMER and PATRIZIO NEFF 689
- Transient response of multilayered orthotropic strips with interfacial diffusion and sliding**  
XU WANG and PETER SCHIAVONE 711